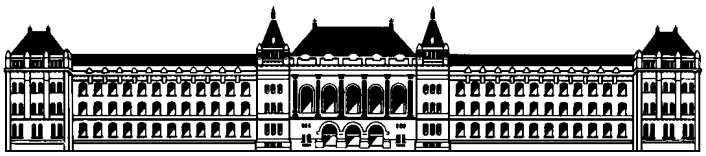

BUDAPEST UNIVERSITY OF TECHNOLOGY AND ECONOMICS
DEPARTMENT OF APPLIED MECHANICS

Dynamics of Stochastic Mechanical Systems with Delays

PhD Thesis

Author: **Henrik T. SYKORA**

Supervisor: **Dániel BACHRATHY**, PhD.

Submitted to
Géza Pattantyús-Ábrahám Doctoral School of Mechanical Engineering Sciences
Budapest University of Technology and Economics

Budapest, 2020

Acknowledgements

I would like to thank Dániel Bachrathy for his continuous support, inspiration and motivation he gave me. I would like also to thank my wife, Zsuzsanna Dobránszky for standing at my side and for the continuous encouragement and emotional support during the whole journey leading to this dissertation, and I also thank her family. I thank Attila Kovács for his remarks, comments and providing the "Oxford mathematician's perspective". I also thank my colleges Szabolcs Berezvai, Dávid Hajdu and the whole staff of the Department of Applied Mechanics for their support and the great time we spent together.

Furthermore, I am most grateful to my father for creating the possibility for me to go to university and be able to focus on my studies hundred percent, to my mother for her ceaseless support and aid, István Ács and Miklós Hamvas who were at our family's side in our most difficult times.

The research leading to these results has received funding from the European Research Council under the European Union's Seventh Framework Programme (FP7/2007-2013) ERC Advanced grant agreement No340889, supported by the Hungarian Scientific Research Fund (OTKA FK-124462; PD-124646), by the Hungarian Ministry of Human Capacities (NTP-NFTÖ-19-B-0127; BME FIKP-MI) and by the National Research, Development and Innovation Fund (NKFIH ÚNKP-18-3-I-BME-160; TUDFO/51757/2019-ITM Thematic Excellence Program).

Contents

Notations and Acronyms

Here are the most frequently used notations and abbreviations in this dissertation. Note that vectors of dimension d are treated as $d \times 1$ matrices (column vectors) and as a rule, the argument ω of random variables is omitted.

$\mathbb{P}(.)$	Probability of an event
x_t, y_n, z_k	Stochastic processes depending on (continuous or discrete) time
$x(t), y(n), z(k)$	Deterministic processes depending on (continuous or discrete) time
$\mathbf{I}$	Identity matrix
$\mathbf{x}^\top, \mathbf{X}^\top$	Transpose of the vector $\mathbf{x}$ or matrix $\mathbf{X}$
$\langle . \rangle$	Expectations value, ensemble average of a random variable
$\mathrm{StD}(.)$	Standard deviation of a random variable
$t, n, k, m, m_1, m_2, ...$	Variables denoting the continuous time t or the discrete times $n, k, m, m_1, m_2, ...$
$i, i_1, i_2, ...$	Indexes denoting the i-th element x_i of a vector $\mathbf{x}$ or the $i_1 i_2$-th element $X_{i_1 i_2}$ of a matrix $\mathbf{X}$
$j, j_1, j_2, j_\tau, ...$	Index used for multiple similar objects or for the j-th element of a set

PDF	Probability Density Function
SDE	Stochastic Differential Equation
DDE	Delay Differential Equation
SDDE	Stochastic Delay Differential Equation
MDBM	Multi Dimensional Bisection Method
MC simulation	Monte-Carlo simulation

Chapter 1

Introduction

There are several models in engineering and biology which lead to delay differential equations (DDE), e.g., the models of machine tool vibrations [2, 79, 94], delayed control loops [99], traffic dynamics [64], predator-prey systems [97] or neural networks [16]. During the investigation of such delayed dynamical systems stochastic effects are usually neglected, despite that stochastic excitations often influence the behaviour of these systems. The noise may appear not only as an external excitation, but also in the coefficients of the state variables. In case of construction of deterministic models that approximate stochastic systems, the usual approach is to consider the mean values of the measured system parameters that describe the process, while the measured variation is considered as the unwanted noise of the measurement [29]. This mean-value based approach is valid for linear systems only, and even in these cases, its result may be misleading regarding the stationary behaviour. A noise excitation can lead not only to change in stability properties, but it can also cause a so-called autonomous stochastic resonance or coherence resonance [53, 84].

For example, in manufacturing science, when machine tool vibrations are investigated usually this deterministic approximation is applied. When dealing with machine tool vibrations two main categories of vibrations are considered: the so-called chatter and forced vibrations [94]. Chatter is an instability phenomenon, caused by the time delay due to the surface regeneration effect. During this instability, self-induced oscillations occur, which can lead to poor surface quality and damage in the tool. The forced vibrations are the result of the time-varying cutting force, which can occur due to the changing size and shape of the chip, but can also be caused by high-frequency processes as chip formation and segmentation, shockwaves in the material, local inhomogeneities in the material properties [66, 67], shear plane oscillation, rough surface of the workpiece etc. However, these high-frequency variations are usually not considered [2, 59] in the constant parameters of the force characteristics describing the relationship between the chip size and the cutting force. Since these high speed phenomena are very complex processes, thus in some recent theoretical works [14, 43, 85] a stochastic noise excitation is used to take the effect of these unmodelled dynamics into account. Another example is in vehicular traffic, where the time delay originates from the drivers' reaction time, that typically varies stochastically [63], while the additive noise comes from the other vehicles whose motion the drivers need to respond to. In network control systems, delays may vary stochastically due to packet drops or capacity drops while in the meantime agents need to respond to the noisy environment [19, 35, 50, 60, 68–70]. In complex biological networks, like those within cells, external noise is ubiquitous, while stochastic delays may be used to model a sequence of reactions [30, 32].

However, if the stochastic effects are also considered, the range of tools used to analyze stability and stationary solutions is far more limited than the available tools for systems described by deterministic delay differential equations (DDE's). For some special, linear stochastic delay differential equations (SDDE's) with constant parameters, stochastic calculus can be utilised to study first and second moment stability [55]. Another approach is to use small perturbation of a critical parameter to investigate the stationary properties of the selected solution of the SDDE [14, 48]. In case of small delay, an alternative method is to approximate the system as a non-delayed stochastic differential equation (SDE) [31]. It is also possible to estimate the stationary probability density function (sPDF) of the phase angle in the polar-coordinate representation of the SDDE using Fokker-Planck equation [93]. This approach leads to a nonlinear deterministic system of equa-

tions for the dominant characteristic exponent, the average phase angle velocity, and the sPDF of the phase angle, which can be solved in an iterative way or by using the multidimensional bisection method [6, 7]. There are also methods to decide, if the necessary and sufficient conditions for exponential and second moment stability are satisfied, by utilizing Lyapunov functionals [57, 74]. However, the above-listed methods have the weaknesses of not only being problem-specific but usually applicable only for small degree-of-freedom dynamical systems with constant parameters.

The most general method to investigate SDDE's (including linear SDDE's with time-periodic parameters) is to numerically simulate them in the time domain using e.g., the Euler-Maruyama method [13] or the Milstein method [17, 76] generalised to SDDE's, and statistically analyze the calculated trajectories to determine stability and stationary beahviour. These integrated realizations then can be used to study their mean square (or in a more general case the p-th moment) to determine moment stability [8, 56] and stationary beahviour. A further application of these numerically obtained paths is based on data analysis, namely, the topological beahviour of the high-dimensional point cloud generated from the trajectories is investigated to detect instability near the boundaries of the stable parameter domain [43, 44]. Since these methods are based on Monte-Carlo simulations, they require high computational resources to provide the statistically reliable results. These methods have the weaknesses of not only being intuitive and problem specific, but usually applicable only for small degree of freedom dynamical systems.

This dissertation aims to investigate an approach which is able to efficiently characterise the stability and stationary behaviour of systems with delays subjected to parametric and additive noise perturbations. In Chapter 2 the basic mathematical concepts and the most important preliminaries are discussed, which are essential to investigate the stochastic systems with delays, especially in regards of stability and stationary behaviour. Chapter 3 introduces general and efficient method based on the semidiscretisation [37], which allows the analysis of stochastic delay differential equations (SDDEs) and systems with stochastic delays.

Based on this method a simple-to-use open-source package has been implemented in the Julia [12] programming language, and it has been released under the name of *StochasticSemiDiscretizationMethod.jl* [80]. Then, in Chapter 4 the usage and the convergence properties of the proposed methods are demonstrated through the analysis of some basic SDDE examples. In Chapter 5 the method is applied to numerically investigate engineering problems. First, the effect of the noisy cutting force on the dynamics of turning and milling processes is analysed, and it is shown how the stochastic models are able to predict some measured phenomena, which the deterministic models cannot explain. Then it is shown, how stochastic packet drops can influence the stability properties and the stationary behaviour of connected automated vehicles, and how the harmful effects of these packet losses can be compensated. Finally, in Chapter 6 the theoretical assumptions and predictions are compared to measurement results. Here it is proved that the stochastic component of the cutting force has to be taken into account, furthermore, it is demonstrated how the new theoretical results can be utilised for chatter detection during a milling operation.

Chapter 2

Mathematical Preliminaries

Disclaimer

To discuss stochastic differential equations (SDEs), especially stochastic delay differential equations (SDDEs) some of the fundamental concepts and tools of probability theory is needed. The goal of this chapter is not to introduce the reader to the subtleties of measure theory with rigorous definitions and proofs, but to give an intuition of the concepts necessary to understand the main theoretical contributions of this work. Note that this chapter is not an integral part of this dissertation, namely, some notation used in this section may be used in a different context in the following chapters, however, this chapter is regularly referred during the derivations in the subsequent chapters.

2.1 Basics Concepts from Probability Theory

Probability theory is the branch of mathematics which discusses events and mathematical models which have random outcomes. If an experiment is conduced (e.g.: rolls with a dice) and the outcome cannot be predicted, then the outcome can be called as a random event. For every experiment there exist a set of events Ω from which the outcome can take values (e.g.: the outcome of rolling with a regular dice is an integer from 1 to 6, so $\Omega = \{1, 2, 3, 4, 5, 6\}$). However, it is possible to describe these events not only using discrete values, but also by labelling them using values from a continuous set (e.g.: $\Omega = \mathbb{R}$ or even $\Omega = \mathbb{R}^d$). These random variables can characterise e.g. the life expectancy of a product, such as a lightbulb (here $\Omega = [0, \infty)$) or a measured length ($\Omega = [l_1, l_2]$).

2.1.1 Probability and Expectation

Let X denote a random variable, and restrict Chap. 2 to sets with a finite number of events labelled with real numbers, namely $\Omega_{\mathrm{d}} = \{\omega_{j_\omega} : \omega_{j_\omega} \in \mathbb{R}, j_\omega = 1, 2, 3, \ldots, N_\Omega,\ \omega_1 < \omega_2 < \ldots < \omega_{N_\Omega}\}$ or the infinite set $\Omega_{\mathrm{c}} = \mathbb{R}$.

The most important way to describe X is the probability of taking a value $\omega \in \Omega$, where this probability is denoted by $\mathbb{P}$. If the event space is the discrete Ω_{d}, then this probability takes a finite value, or weight $w_{j_\omega} \in [0, 1]$, namely

$$\mathbb{P}(X = \omega_{j_\omega}) = w_{j_\omega}. \tag{2.1.1}$$

However, if the continuous event space Ω_{c} is considered, then $\mathbb{P}(X = \omega) = 0$ for all $\omega \in \Omega$. To overcome this, instead of using probability as the fundamental quantity, the probability density function (PDF) is introduced, namely

$$f(\omega) = \mathbb{P}(\omega < X < \omega + \mathrm{d}\omega) \tag{2.1.2}$$

which represents the probability of the random variable X being located in the infinitesimal interval $[\omega, \omega + \mathrm{d}\omega]$. The other quantity which can be used for handling a random variable X is the cumulative distribution function (CDF)

$$F(\omega) = \mathbb{P}(X \leq \omega) \tag{2.1.3}$$

The connection between the two quantities is described by the relations

$$F(\omega) = \int_{-\infty}^{\omega} f(\hat{\omega})\mathrm{d}\hat{\omega} \quad \text{and} \quad f(\omega) = F'(\omega). \tag{2.1.4}$$

Furthermore, the CDF is normalised as

$$\lim_{\omega\to\infty} F(\omega) = \int_{-\infty}^{\infty} f(\omega)\mathrm{d}\omega = 1, \tag{2.1.5}$$

since the total probability of the entire event space has to add up to unity.

To describe discrete random variables with the help of continuous probability density functions, the Dirac delta $\delta(\omega)$ can be used, namely

$$f(\omega) = w_{j_\omega}\delta(\omega_{j_\omega} - \omega) \quad \text{where} \quad \omega_{j_\omega} \in \Omega_\mathrm{d}, \tag{2.1.6}$$

and the integral generating the cumulative distribution function reduces to the sum

$$F(\omega_{j_\omega}) = \sum_{j_1=1}^{j} w_{j_\omega}. \tag{2.1.7}$$

For example, the PDF of the one dimensional normal (or Gaussian) distribution is

$$f(\omega) = \frac{1}{\sigma\sqrt{2\pi}} e^{\frac{(\omega-\mu)^2}{2\sigma^2}}, \tag{2.1.8}$$

where μ and σ are the parameters of the distribution. If a random variable X is a normally distributed variable, than it is usually denoted as $X \sim \mathcal{N}(\mu, \sigma)$.

The next important quantity to describe a random variable X is its n-th moment, namely

$$\langle X^n \rangle = \int_\Omega \omega^n f(\omega)\mathrm{d}\omega, \tag{2.1.9}$$

where the operator $\langle . \rangle$ denotes the expectation value or the ensemble average (sometimes denoted as $\mathbb{E}(.)$). The first moment describes the mean $\overline{X}$ of the random variable X, while the standard deviation $\mathrm{StD}(X)$ can be calculated using the first and second moments:

$$\overline{X} = \langle X \rangle, \tag{2.1.10}$$

$$\overline{\overline{X}} = \langle X^2 \rangle, \tag{2.1.11}$$

$$\mathrm{StD}(X) = \sqrt{\langle X^2 \rangle - \langle X \rangle^2} = \sqrt{\overline{\overline{X}} - \overline{X}^2}, \tag{2.1.12}$$

where $\overline{\overline{X}}$ is also introduced to denote the second moment. For a normally distributed random variable $X \sim \mathcal{N}(\mu, \sigma)$ these quantities are

$$\langle X \rangle = \overline{X} = \mu, \quad \langle X^2 \rangle = \overline{\overline{X}} = \mu^2 + \sigma^2, \quad \mathrm{StD}(X) = \sigma. \tag{2.1.13}$$

So far introduced univariate random behaviour was introduced, but the above described quantities can be generalised straightforwardly to multivariate random numbers. For example, consider two $\mathbb{R}$-valued random variables X, Y with a PDF

$$f(x, y) = \mathbb{P}(x < X < x + \mathrm{d}x, y < Y < y + \mathrm{d}y) \tag{2.1.14}$$

and cumulative distribution function

$$F(x, y) = \int_{-\infty}^{y}\int_{-\infty}^{x} f(\hat{x}, \hat{y})\mathrm{d}\hat{x}\mathrm{d}\hat{y}. \tag{2.1.15}$$

In a multivariate context they are usually called joint PDF and joint CDF, respectively. If these variables are independent of each other, then the joint PDF can be multiplicatively separated as $f(x,y) = f_X(x)f_Y(y)$, and with this the joint CDF is

$$F(x,y) = \int_{-\infty}^{y}\int_{-\infty}^{x} f_X(\hat{x})f_Y(\hat{y})\mathrm{d}\hat{x}\mathrm{d}\hat{y} = \int_{-\infty}^{x} f_X(\hat{x})\mathrm{d}\hat{x}\int_{-\infty}^{y} f_Y(\hat{y})\mathrm{d}\hat{y} = F_X(x)F_Y(y). \tag{2.1.16}$$

This causes that the expectation value of the product of these two variables X and Y are calculated using multiple integrals, namely

$$\langle XY\rangle = \int_{-\infty}^{\infty}\int_{-\infty}^{\infty} xyf_X(x)f_Y(y)\mathrm{d}x\mathrm{d}y = \int_{-\infty}^{\infty} xf_X(x)\mathrm{d}x\int_{-\infty}^{\infty} yf_Y(y)\mathrm{d}y = \langle X\rangle\langle Y\rangle = \overline{X}\,\overline{Y} \tag{2.1.17}$$

If the independent random variables are added, due to the linearity of expectation, the mean and standard deviation of this sum can be calculated as

$$\langle X+Y\rangle = \langle X\rangle + \langle Y\rangle \quad \text{and} \quad \mathrm{StD}(X+Y) = \sqrt{\mathrm{StD}(X)^2 + \mathrm{StD}(Y)^2}. \tag{2.1.18}$$

When both of these random variables are normally distributed, namely $X \sim \mathcal{N}(\mu_X, \sigma_X)$ and $Y \sim \mathcal{N}(\mu_Y, \sigma_Y)$, then the sum of these two variables is also normally distributed, namely $X + Y \sim \mathcal{N}\Big(\mu_X + \mu_Y, \sqrt{\sigma_X^2 + \sigma_Y^2}\Big)$.

However, multiple normally distributed random variables are not necessary independent of each other. When these random variables are collected in a vector $\mathbf{X} \sim \mathcal{N}(\boldsymbol{\mu}_\mathbf{X}, \boldsymbol{\sigma}_\mathbf{X})$, $\boldsymbol{\mu}_\mathbf{X} \in \mathbb{R}^d$, $\boldsymbol{\sigma}_\mathbf{X} \in \mathbb{R}^{d\times d}$, which is called the multivariate or $\mathbb{R}^d$-valued random variable:

$$\mathbf{X} = \begin{pmatrix} X_1 & X_2 & \dots & X_d \end{pmatrix}^\top, \tag{2.1.19}$$

and has the multivariate probability distribution function $f_\mathbf{X} : \mathbb{R}^d \mapsto \mathbb{R}$, namely

$$f_\mathbf{X}(\mathbf{x}) = \frac{1}{(2\pi)^{\frac{d}{2}}\sqrt{\det(\boldsymbol{\Sigma}_\mathbf{X})}}\exp\left(-\frac{1}{2}(\mathbf{x}-\boldsymbol{\mu}_\mathbf{X})^\top\boldsymbol{\Sigma}_\mathbf{X}^{-1}(\mathbf{x}-\boldsymbol{\mu}_\mathbf{X})\right), \tag{2.1.20}$$

where $\boldsymbol{\Sigma}_\mathbf{X} = \boldsymbol{\sigma}_\mathbf{X}^\top\boldsymbol{\sigma}_\mathbf{X} = \boldsymbol{\Sigma}_\mathbf{X}^\top$. Note that in this case the first moment (or the mean) is expressed as a vector

$$\langle\mathbf{X}\rangle = \boldsymbol{\mu}_\mathbf{X} \in \mathbb{R}^d, \tag{2.1.21}$$

while the covariance (calculated with the help of the second moment) is the symmetric matrix

$$\mathrm{Cov}(\mathbf{X},\mathbf{X}) = \left\langle\mathbf{X}\mathbf{X}^\top\right\rangle - \langle\mathbf{X}\rangle\langle\mathbf{X}\rangle^\top = \boldsymbol{\Sigma}_\mathbf{X} \in \mathbb{R}^{d\times d}. \tag{2.1.22}$$

Due to the linearity of expectation, for any affine transformation it holds, that

$$\mathbf{Y} = \mathbf{a} + \mathbf{B}\mathbf{X} \tag{2.1.23}$$

has a mean

$$\langle\mathbf{Y}\rangle = \mathbf{a} + \mathbf{B}\boldsymbol{\mu}_\boldsymbol{X} \tag{2.1.24}$$

and covariance matrix

$$\mathrm{Cov}(\mathbf{Y},\mathbf{Y}) = \mathbf{B}\boldsymbol{\Sigma}_\mathbf{X}\mathbf{B}^\top, \tag{2.1.25}$$

where $\mathbf{a} \in \mathbb{R}^d$ and $\mathbf{B} \in \mathbb{R}^{d\times d}$. If $d = 1$, the scalar version of (2.1.23) is gained, namely

$$Y = a + BX \tag{2.1.26}$$

where $Y \sim \mathcal{N}(a + B\mu_X, B\sigma_X)$.

2.1.2 Stochastic Processes

A time dependent random variable X_t is called stochastic process, and in general has a time dependent PDF $f_X(t,x) = \mathbb{P}(x < X_t < x + \mathrm{d}x)$. Intuitively, X_t represents a collection of the process' observable realizations or trajectories. In this dissertation, to differentiate the stochastic and deterministic variables, the time dependence is denoted with a subscript t (e.g.: $\mathbf{X}_t$), or using parentheses (e.g.: $\mathbf{A}(t)$), respectively, as introduced by Arnold [5].

To model the information that is available at a given time point t_1 the filtration $(\mathcal{F}_t)_{t\in[0,t_1]}$ is used. For a stochastic process the probabilities at time t can be different on the previous history of a trajectory. This is encapsulated in the concept of the filtration $(\mathcal{F}_t)_{t\in[0,t_1]}$, which is the continuous analogue of the conditional probability. Intuitively, if the filtration $(\mathcal{F}_t)_{t\in[0,t_1]}$ is given, then the stochastic process X_t has already realised, and all of its previous value, or in other words, its trajectory is known up to time t_1. For example, if the time dependent PDF of a stochastic process is known, e.g.: $X_t \sim \mathcal{N}(\mu(t), \sigma(t))$, then its mean and standard deviation are

$$\langle X_t \rangle = \mu(t) \quad \text{and} \quad \mathrm{StD}(X_t) = \sigma(t). \tag{2.1.27}$$

However, if the filtration $(\mathcal{F}_t)_{t\in[0,t_1]}$ is given, then

$$\Big\langle X_t | (\mathcal{F}_t)_{t\in[0,t_1]} \Big\rangle = X(t) \quad \text{and} \quad \mathrm{StD}\Big(X_t | (\mathcal{F}_t)_{t\in[0,t_1]}\Big) = 0 \quad \text{for all} \quad t \in [0,t_1], \tag{2.1.28}$$

without any regard of the know time-dependent PDF of the process. That is, $X(t)$, $t \in [0,t_1]$ is a known and deterministic function of time, since it has already realised in the past and cannot be changed. Here $\langle .|. \rangle$ and $\mathrm{StD}(.|.)$ denotes the conditional expectation and standard deviation, respectively.

An important property of stochastic processes is stationarity, which characterise the time dependence of the PDF of a process; if a stochastic process is stationary, then its PDF does not change when shifted in time, namely

$$x_t \sim f(x,t) = f(x, t+\Delta t) \equiv f(x). \tag{2.1.29}$$

An other important property is ergodicity, which means that the ensemble average of a process (or other processes derived from the original one) is the same as the time average:

$$\int_\Omega x f(x) \mathrm{d}x = \lim_{T\to\infty} \frac{1}{T} \int_{t_0}^{t_0+T} x_t \mathrm{d}t. \tag{2.1.30}$$

Note that, stationary stochastic process is also ergodic, if the variable has the same distribution in time as its ensemble distribution. One can use this property to approximate the statistical properties of a stationary process x_t from a sufficiently long sample (realization) of the process.

2.1.3 The Wiener Process

Probably the most important stochastic process is the so-called Wiener process W_t, which is the most widely used process to model stochastic Gaussian white noise excitation, and is the main stochastic process used in stochastic calculus [5, 61]. The Wiener process is defined to have the following properties:

- $W_0 = 0$,
- its increments are normally distributed, with variation proportional to the elapsed time, namely $\Delta W_t := W_{t+\Delta t} - W_t \sim \mathcal{N}\Big(0, \sqrt{\Delta t}\Big)$,
- the increments for non-overlapping time intervals are independent.

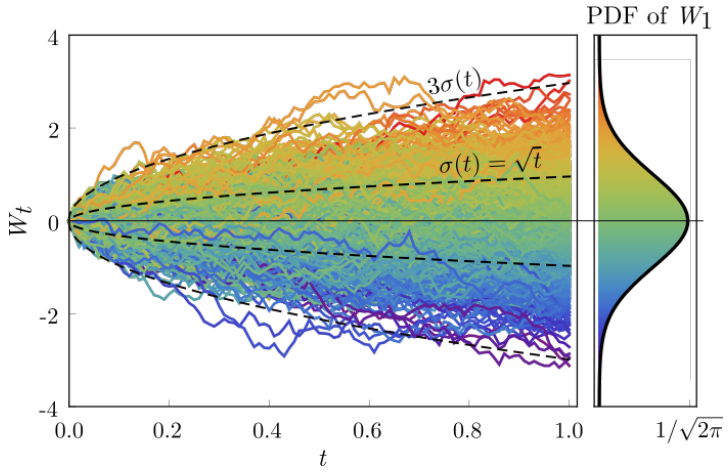

Figure 2.1. *Sample trajectories of the Wiener process along with the probability distribution function (PDF) of the Wiener process at time* $t = 1$.

These properties lead to the following corollaries

$$\langle W_t \rangle = 0, \tag{2.1.31}$$
$$\langle \Delta W_t \Delta W_t \rangle = \Delta t, \tag{2.1.32}$$
$$\langle \Delta W_{t_1} \Delta W_{t_2} \rangle = 0 \quad \text{if} \quad \Delta t < |t_1 - t_2|, \tag{2.1.33}$$
$$\langle W_{t_1} W_{t_2} \rangle = \min(t_1, t_2). \tag{2.1.34}$$

Furthermore, in case of a W_t process is realised up to t_1, if a $t_2 > t_1$ is investigated, its PDF can be written as $(W_{t_2}|\mathcal{F}_{t_1}) \sim \mathcal{N}\big(W_{t_1}, \sqrt{t_2 - t_1}\big)$, leading to

$$\langle W_{t_2}|\mathcal{F}_{t_1} \rangle = W(t_1). \tag{2.1.35}$$

These properties of the Wiener process make it an essential building block when modelling stochastic noise effects in engineering. First, it was used to model the driving force of the Brownian motion [54], where the motion of a particle excited by random impacts was investigated, since the Wiener process captures the resultant effect of these large number of high frequency stochastic impacts.

If one considers the central limit theorem [61], which states, that given $X_1, X_2, \ldots, X_N$ $\mathbb{R}$-valued independent stochastic variables with $\langle X_j \rangle = 0$ and $\mathrm{StD}(X_j) = 1$, $j = 1, 2, \ldots, N$, but otherwise arbitrarily distributed, the distribution of their sum convergences to a normal distributions, namely

$$S_N = \sum_{j=1}^{N} X_j \quad \text{and} \quad \lim_{N \to \infty} S_N \sim \mathcal{N}\Big(0, \sqrt{N}\Big). \tag{2.1.36}$$

During Brownian motion, it can be assumed that the number of random impacts exciting the particle is proportional to the length of the observed time interval, namely $N \propto \Delta t$. The Langevin equation describing the velocity v_t of a one-dimensional Brownian motion has the following form:

$$m\dot{v}_t = -\lambda v_t + \sigma \Gamma_t, \tag{2.1.37}$$

where m is the mass of the particle, λ is the viscosity of the medium where the particle is located, while σ describes the intensity of the Langevin force Γ_t, which is the process modelling the random impacts. Since mathematically Γ_t is not meaningful, the increment form is used

$$m\mathrm{d}v_t = -\lambda v_t \mathrm{d}t + \sigma \mathrm{d}W_t, \tag{2.1.38}$$

where

$$\mathrm{d}W_t := \int_t^{t+\mathrm{d}t} \Gamma_{\hat{t}} \mathrm{d}\hat{t}. \tag{2.1.39}$$

This integral can be intuitively interpreted, as Γ_t represents the high frequency discrete random impacts, which during the time interval $[t, t+\mathrm{d}t]$ accumulate into a normally distributed random variable $\mathrm{d}W_t$ with intensity $\mathrm{d}t$, similarly to (2.1.36). Note that Eq. (2.1.38) is a stochastic differential equation and in order to solve it, one needs to define the stochastic integral.

2.2 Basic Concepts of Stochastic Differential Equations

2.2.1 Stochastic Integrals

There exists two main definitions of the stochastic integral w.r.t. the Wiener process [61]. The first is the Itô definition:

$$\int_{t_0}^{T} g_t \mathrm{d}W_t = \lim_{\|\Delta\|\to 0} \sum_{t_j \in \Delta} g_{t_j} \Delta W_{t_j}, \tag{2.2.1}$$

where $\Delta = \{t_0, t_1, \ldots, t_N = T\}$ is a mesh on $[t_0, T]$, $\|\Delta\| = \max_j \{t_{j+1} - t_j\}$ and $\Delta W_{t_j} := \left(W_{t_{j+1}} - W_{t_j}\right)$. The other definition is the Stratonovich integral:

$$\int_{t_0}^{T} g_t \circ \mathrm{d}W_t = \lim_{\|\Delta\|\to 0} \sum_{t_j \in \Delta} \frac{g_{t_{j+1}} + g_{t_j}}{2} \Delta W_{t_j}. \tag{2.2.2}$$

In general the two definition produce different results, however if $g_t = g(t)$ is a sufficiently smooth deterministic function, then the two sum (2.2.1) and (2.2.2) defining the integrals converge to the same solution.

In order to numerically approximate the solution of a realization of the stochastic integral e.g. the Euler-Maruyama approximation [47] can be used:

$$\int_{t_0}^{T} g_t \mathrm{d}W_t \approx \sum_{t_j \in \Delta} g_{t_j} \xi_j \quad \text{or} \quad \int_{t_0}^{T} g_t \circ \mathrm{d}W_t \approx \sum_{t_j \in \Delta} \frac{g_{t_{j+1}} + g_{t_j}}{2} \xi_j, \tag{2.2.3}$$

where $\xi_j \sim \mathcal{N}(0, \sqrt{t_{j+1} - t_j})$ is a random variable generated at each time step t_j.

Despite of an integral being a stochastic integral, the formal solution, such as described in (2.2.1) or (2.2.2) is still a very important and useful representation. For example, the expectation value of the product of two Itô integrals can be calculated with the help of the Itô isometry [61] in case they are integrated w.r.t. the same Wiener process:

$$\begin{aligned}
\left\langle \int_{t_0}^{T} g_t \mathrm{d}W_t \int_{t_0}^{T} h_t \mathrm{d}W_t \right\rangle &= \left\langle \lim_{\|\Delta\|\to 0} \left(\sum_{t_j \in \Delta} g_{t_j} \Delta W_{t_j} \sum_{t_j \in \Delta} h_{t_j} \Delta W_{t_j} \right) \right\rangle = \\
&= \lim_{\|\Delta\|\to 0} \sum_{t_{j_1} \in \Delta} \sum_{t_{j_2} \in \Delta} \left\langle g_{t_{j_1}} h_{t_{j_2}} \Delta W_{t_{j_1}} \Delta W_{t_{j_2}} \right\rangle \\
&= \lim_{\|\Delta\|\to 0} \sum_{t_j \in \Delta} \left\langle g_{t_j} h_{t_j} \right\rangle (t_{j+1} - t_j) \\
&= \int_{t_0}^{T} \left\langle g_t h_t \right\rangle \mathrm{d}t.
\end{aligned} \tag{2.2.4}$$

The Itô isometry can also be used to show, that the Langevin force Γ_t from Eq. (2.1.37) is an appropriate representation of the Gaussian white noise excitation used to excite dynamical

systems. The term white noise is used to indicate, that the power that is fed into a dynamical system by Γ_t is constant for all frequencies, or in other words the power spectral density of Γ_t is constant. The power spectral density gives a good representation of the energy supplied to a system by a signal:

$$S(\omega) = \langle \hat{x}_\omega \hat{x}_\omega^* \rangle \,, \tag{2.2.5}$$

where $\hat{x}_\omega$ is the Fourier transform of a signal x_t, defined as

$$\hat{x}_\omega = \frac{1}{\sqrt{2T}} \int_{-T}^{T} e^{-i\omega t} x_t \mathrm{d}t. \tag{2.2.6}$$

In case of the signal being the Langevin force, namely $x_t = \Gamma_t$, the integral w.r.t. time t becomes an integral w.r.t. the Wiener process as in (2.1.39). Then, this stochastic integral is substituted into (2.2.5) to obtain

$$S(\omega) = \frac{1}{2T} \left\langle \int_{-T}^{T} e^{-i\omega t} \mathrm{d}W_t \int_{-T}^{T} e^{i\omega t} \mathrm{d}W_t \right\rangle = \frac{1}{2T} \int_{-T}^{T} \mathrm{d}t = 1 \,, \tag{2.2.7}$$

which is a constant, thus Γ_t is a white noise.

2.2.2 Stochastic Differential Equation

A stochastic differential equation (SDE) is a class of differential equations in which the right hand side of the equation has to be integrated w.r.t. one or more stochastic processes. The solution of these equations are also stochastic processes. In general, multiple types of stochastic processes can occur in a stochastic differential equation, however, in this dissertation only the Wiener process is considered, and the SDEs for an $\mathbb{R}^d$-valued stochastic process $\mathbf{x}_t$ have the form

$$\mathrm{d}\mathbf{x}_t = \mathbf{a}(\mathbf{x}_t, t)\mathrm{d}t + \mathbf{b}(\mathbf{x}_t, t)\mathrm{d}W_t, \tag{2.2.8}$$

where the stochastic effects are considered in the Itô sense. However, if one considers the stochastic effects in the Stratonovich case it can be transformed to an Itô SDE. If the SDE is given in the Stratonovich sense as

$$\mathrm{d}\mathbf{x}_t = \hat{\mathbf{a}}(\mathbf{x}_t, t)\mathrm{d}t + \hat{\mathbf{b}}(\mathbf{x}_t, t) \circ \mathrm{d}W_t, \tag{2.2.9}$$

then the corresponding Itô SDE is (2.2.8) with the transformed coefficient functions [5]

$$a_i(\mathbf{x}_t, t) = \hat{a}_i(\mathbf{x}_t, t) + \frac{1}{2} \sum_{i_1=1}^{d} \frac{\partial \hat{b}_i(\mathbf{x}_t, t)}{\partial x_{i_1}} \hat{b}_{i_1}(\mathbf{x}_t, t) \quad \text{and} \quad \hat{\mathbf{b}}(\mathbf{x}_t, t) = \mathbf{b}(\mathbf{x}_t, t). \tag{2.2.10}$$

Note that usually the coefficientfunction $\mathbf{a}(\mathbf{x}_t, t)$ of $\mathrm{d}t$ is called *drift term*, while the coefficient function $\mathbf{b}(\mathbf{x}_t, t)$ of $\mathrm{d}W_t$ is called *diffusion* term.

One of the simplest examples of a linear SDE is the following equation which generates the one dimensional $\mathbb{R}$-valued x_t Ornstein-Uhlenbeck process, which is an SDE with additive noise:

$$\mathrm{d}x_t = \mu x_t \mathrm{d}t + \sigma_0 \mathrm{d}W_t, \tag{2.2.11}$$

and its solution can be expressed as

$$x_t = x_0 e^{\mu t} + \sigma_0 \int_0^t e^{\mu(t-\hat{t})} \mathrm{d}W_{\hat{t}}. \tag{2.2.12}$$

The Ornstein-Uhlenbeck process has a time dependent normal distribution [5], namely

$$x_t \sim \mathcal{N}\left(x_0 e^{\mu t}, \frac{\sigma_0}{\sqrt{2\mu}} \sqrt{e^{2\mu t} - 1} \right). \tag{2.2.13}$$

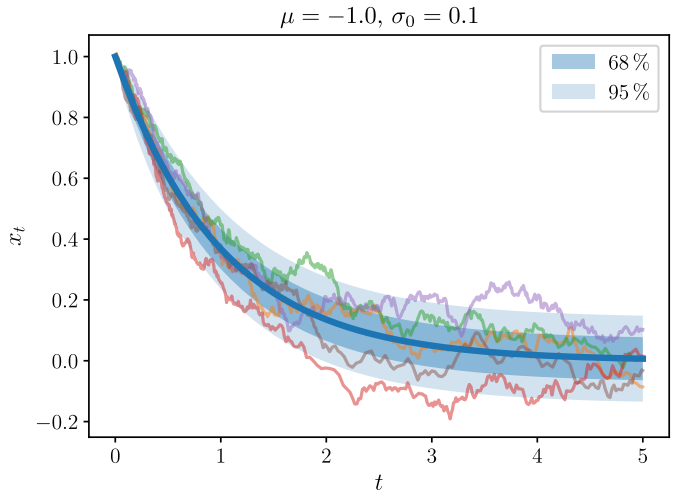

Figure 2.2. *Sample trajectories of the Ornstein-Uhlenbeck process for initial condition $x_0 = 1$. The shadings labelled by percentages denote the area where the corresponding percentage of the trajectories are located, furthermore, the darker blue line denotes the mean of the trajectories.*

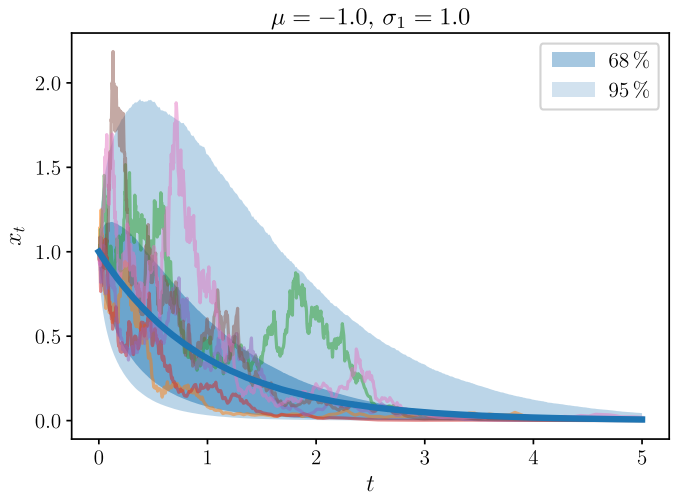

Figure 2.3. *Sample trajectories of the geometric Brownian motion process for initial condition $x_0 = 1$. The shadings labelled by percentages denote the area where the corresponding percentage of the trajectories are located, furthermore, the darker blue line denotes the mean of the trajectories.*

Another example of a linear SDE is the equation of a geometric Brownian motion with multiplicative noise, for which

$$\mathrm{d}x_t = \mu x_t \mathrm{d}t + \sigma_1 x_t \mathrm{d}W_t \tag{2.2.14}$$

and its solution is given by

$$x_t = x_0 e^{\left(\mu - \frac{\sigma_1^2}{2}\right)t + \sigma_1 W_t}. \tag{2.2.15}$$

In Fig 2.2 and 2.3 a small batch of sample realisations is shown for the Ornstein-Uhlenbeck process (2.2.12) and the geometric Brownian motion process (2.2.15), respectively. Along with the trajectories, based on Monte-Carlo simulations, some statistical properties of the realizations are shown, namely the mean, the area where the 68 % and where the 95 % of the trajectories are located. It can be observed that these areas are symmetric w.r.t. to the mean for the Ornstein-Uhlenbeck (as its PDF is a time dependent normal distribution (2.2.13)), however, these areas are

asymmetric for the geometric Brownian motion, while the mean is the same for both processes.

2.2.3 Stability of Stochastic Systems

In this section linear stochastic differential equations are considered in the form

$$\mathrm{d}\mathbf{x}_t = \mathbf{A}\mathbf{x}_t\mathrm{d}t + \boldsymbol{\alpha}\mathbf{x}_t\mathrm{d}W_t, \tag{2.2.16}$$

where $\mathbf{x}_t$ is the $\mathbb{R}^d$-valued stochastic state variable, and $\mathbf{A}, \boldsymbol{\alpha} \in \mathbb{R}^{d\times d}$ are coefficient matrices. For the solution process $\mathbf{x}_t$ of Eq. (2.2.16) there exists multiple stability definitions, from which a few important ones will be discussed in the following paragraphs.

A process is *first moment stable*, if the mean of the stochastic process is stable, namely

$$\lim_{t\to\infty} \langle \mathbf{x}_t \rangle = \mathbf{0}. \tag{2.2.17}$$

To demonstrate the first moment stability, the mean of the solution process (2.2.15) is investigated, where $d = 1$, $\mathbf{A} = \mu$ and $\boldsymbol{\alpha} = \sigma_1$, namely

$$\langle x_t \rangle = x_0 e^{\mu t}, \tag{2.2.18}$$

which is stable if

$$\mu < 0. \tag{2.2.19}$$

An other stability definition is the *almost surely (a.s.) exponential stability*, which is defined by the constant λ, where

$$\lambda = \left\langle \lim_{t\to\infty} \frac{1}{t} \log \|\mathbf{x}_t\|_2 \right\rangle. \tag{2.2.20}$$

and $\|.\|_2$ denotes the L_2 norm. The solution process $\mathbf{x}_t$ is a.s. exponentially stable if $\lambda < 0$, while it is a.s. exponentially unstable if $\lambda > 0$. Considering the solution of (2.2.15) one can determine the a.s. exponential stability by calculating λ from

$$\lambda = \mu - \frac{\sigma_1^2}{2}, \tag{2.2.21}$$

thus determining the stability criteria as:

$$\mu < \frac{\sigma_1^2}{2}. \tag{2.2.22}$$

The process $\mathbf{x}_t$ in (2.2.16) is *asymptotically mean square stable* [5] or *second moment stable*, if

$$\lim_{t\to\infty} \left\langle \|\mathbf{x}_t\|_2^2 \right\rangle = 0. \tag{2.2.23}$$

To investigate the asymptotically mean square stability of the geometric Brownian Motion process (2.2.15), its second moment has to be considered [5]:

$$\left\langle x_t^2 \right\rangle = x_0^2 e^{\left(2\mu+\sigma_1^2\right)t}. \tag{2.2.24}$$

From this, the stability criteria for asymptotically mean square stability can be deduced:

$$\mu < -\frac{\sigma_1^2}{2}. \tag{2.2.25}$$

Comparing the stability definitions one can see, that the different approaches to define stability lead to different results. From (2.2.19) one can see, that the first moment stability does not consider the stochastic effects when determining the stability of linear systems. From (2.2.22) it can be

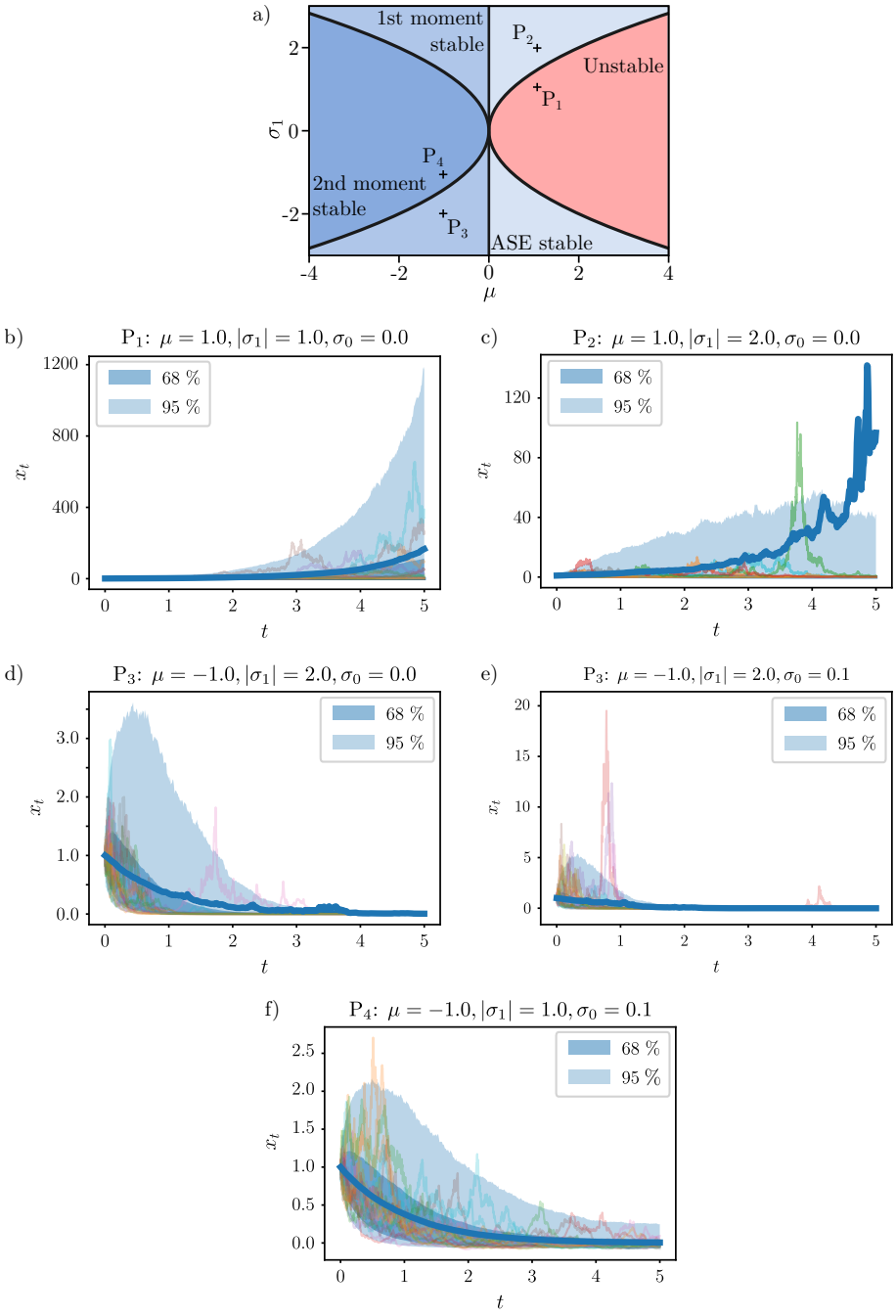

Figure 2.4. *a) Parameter regions determined by the different stability definitions b)-f) Sample trajectories for Eq.* (2.2.26) *with different parameter combinations and initial condition* $x_0 = 1$*. The shadings labelled by percentages denote the area where the corresponding percentage of the trajectories are located, furthermore, the darker, thick blue line denotes the mean of the trajectories.*

noted that the almost exponentially sure stability predicts that the noise exciting the system has a stabilising effect. However, the second moment stability forecasts the opposite, namely that the noise destabilises system (2.1.37).

To compare the different stability definitions, the original geometric Brownian motion is perturbed with an additive noise, namely

$$\mathrm{d}x_t = -\mu x_t \mathrm{d}t + (\sigma_1 x_t + \sigma_0)\mathrm{d}W_t. \tag{2.2.26}$$

This addition does not change the stability, however provides a perturbation to better illustrate the different behaviour for parameters satisfying different stability criteria as shown in Fig. 2.4. First, consider the case without the additive noise excitation, namely $\sigma_0 = 0$. If $\mu = 1, \sigma_1 = 1$ (Fig. 2.4a P_1), the system (2.2.26) is unstable w.r.t. to all of the stability definitions, and the trajectories of the system blow up as shown in Fig. 2.4b. In case of $\mu = 1, \sigma_1 = 2$ (Fig. 2.4a P_2) the parameters satisfy the condition of almost sure exponential stability. In Fig. 2.4c it can be observed, that the individual trajectories (thin lines) of the system decay over time, however the trajectories have bursts before doing so. If the ensemble average (thick line) of the trajectories is investigated, then it can be seen that it grows over time, due to these bursts. This stability definition is suitable to determine if the individual trajectories decay or persist over time. This is an essential property when investigating systems in population dynamics, where the state variable can represent for example the population of a bacteria. However, in case of engineering systems, where the state variable can represent e.g., a displacements or voltages, these occurring bursts can lead to catastrophic events. To avoid these bursts one has to consider the other stability definitions as well.

If $\mu = -1, \sigma_1 = -2$ (Fig. 2.4a P_3) the parameters are from the first moment stable region. In this case the mean process is stable (Fig. 2.4d), however, the aforementioned bursts are still present, but to a lesser extent. This phenomenon is amplified when even a small additive noise is present ($\sigma_0 = 0.1$ as in Fig. 2.4e) causing sudden bursts even after a long incubation period and it is especially undesired for engineering systems. To guarantee that these bursts do not occur, thus guaranteeing stochastic stability, a set of parameters has to be choosen from the mean square or second moment stable region, such as $\mu = -1, \sigma_1 = -1$ (Fig. 2.4 P_4) [77]. Since this dissertation considers engineering systems, the second moment stability definition will be used when investigating the stability of stochastic delay differential equations. Furthermore, in case of second moment stability defined in (2.2.25), the stationary second moment can be calculated. For system (2.2.26) this stationary second moment is

$$\lim_{t\to\infty} \left\langle x_t^2 \right\rangle = -\frac{\sigma_0^2}{2\mu + \sigma_1^2} \tag{2.2.27}$$

which takes a positive value in case of second moment stability defined in (2.2.25), since the denominator becomes negative.

2.2.4 White Noise-induced Resonance

Since the white noise process Γ_t has a constant power spectral density, as shown in (2.2.7), it has the potential to cause a resonance effect. To demonstrate this, consider the dimensionless equation of motion of the simple one degree of freedom linear oscillator subjected to white noise excitation:

$$\ddot{x}_t + 2\zeta\dot{x}_t + x_t = \sigma_0\Gamma_t, \tag{2.2.28}$$

where ζ is the damping coefficient and has the first order incremental form

$$\mathrm{d}\mathbf{x}_t = \mathbf{A}\dot{x}_t + \boldsymbol{\sigma}\mathrm{d}W_t, \quad \mathbf{x}_t = \begin{bmatrix} x_t \\ \dot{x}_t \end{bmatrix}, \quad \mathbf{A} = \begin{bmatrix} 0 & 1 \\ -1 & -2\zeta \end{bmatrix}, \quad \boldsymbol{\sigma} = \begin{bmatrix} 0 \\ \sigma_0 \end{bmatrix}. \tag{2.2.29}$$

The solution of (2.2.29) can be written [5] as

$$\mathbf{x}_t = e^{\mathbf{A}t}\mathbf{x}_0 + \int_0^t e^{\mathbf{A}(t-\hat{t})}\boldsymbol{\sigma}\mathrm{d}W_{\hat{t}}. \tag{2.2.30}$$

In case of a stable system with moderate damping ($0 < \zeta \ll 1$) the stationary moments are

$$\lim_{t\to\infty}\langle \mathbf{x}_t\rangle = \mathbf{0}, \qquad \lim_{t\to\infty}\left\langle \mathbf{x}_t\mathbf{x}_t^\top\right\rangle = \begin{pmatrix} \frac{\sigma_0^2}{4\zeta} & 0 \\ 0 & \frac{\sigma_0^2}{4\zeta} \end{pmatrix}. \tag{2.2.31}$$

Note that in case of small damping, even if the average tends to zero, there can persist a significant noisy motion.

This consequence can be derived using a different approach. The oscillator (2.2.29) is often characterised by using the absolute value of the frequency response function (resonance curve):

$$R(\omega) = \frac{1}{\sqrt{\left(1-\omega^2\right)^2 + 4\zeta^2\omega^2}}. \tag{2.2.32}$$

The resonance curve $R(\omega)$ describes the amplification rate of the mechanical system (2.2.29) for each frequency ω for a given force excitation. In case of a deterministic harmonic excitation, resonance occurs if the excitation frequency matches the natural frequency of the system.

Since the white noise Γ_t excites all the frequencies, the resonant excitation is unavoidable. The worst case, the maximum of the amplification described by the maximum of the resonance curve $R(\omega)$ is a good measure to investigate the maximal response of the system (2.2.29) given by

$$\max_\omega R(\omega) = \frac{1}{2\zeta\sqrt{1-\zeta^2}} \tag{2.2.33}$$

at $\omega = \sqrt{1-2\zeta^2}$, or for $0 < \zeta \ll 1$

$$\max_\omega R(\omega) \approx \frac{1}{2\zeta} \tag{2.2.34}$$

at $\omega \approx 1$, thus the noise is inversely proportional to the damping ζ.

Comparing the stationary second moment in (2.2.31) and the maximum amplification near small ζ values in (2.2.34) it can be seen, that the two quantity increase hyperbolically near the critical bifurcation parameter value $\zeta = 0$ (see Fig. 2.5). This observation can be utilised, to use the stationary second moment to qualitatively describe systems near critical parameters. In case of bifurcation analysis when the system changes from stable to unstable, e.g., in model (2.2.29) the bifurcation ζ goes through zero, before reaching the unstable zone the second moment of the vibration tends to infinity. In case of more complex models (e.g. a non-smooth, nonlinear model of turning in [23]), the bifurcation point of the trivial solution based on the linearised model can be used only as an approximation.

2.2.5 Stochastic Delay Differential Equations

A stochastic delay differential equation (SDDE) in the Itô sense is when the change of the $\mathbb{R}^d$-valued of a state $\mathbf{x}_t$ depends not only on the state $\mathbf{x}_t$ at current time t, but also on previous values. In general, these values can continuously cover a time segment via distributed delays, however, in this dissertation only point delays are considered. The distributed delays can be approximated as point delays using e.g. shifted Dirac delta distributions [39] or via Clenshaw-Curtis quadrature [96].

SDDEs with a single point delay can be given in the incremental form

$$\mathrm{d}\mathbf{x}_t = \mathbf{a}\left(\mathbf{x}_t, \mathbf{x}_{t-\tau}, t\right)\mathrm{d}t + \mathbf{b}\left(\mathbf{x}_t, \mathbf{x}_{t-\tau}, t\right)\mathrm{d}W_t, \qquad \mathbf{x}_t = \boldsymbol{\varphi}(t), t \in [-\tau, 0] \tag{2.2.35}$$

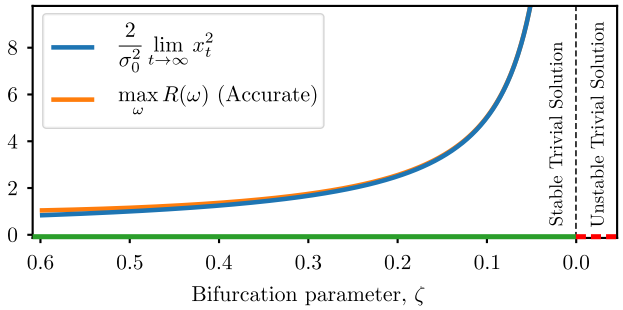

Figure 2.5. *Comparison of the stationary second moment and the maximum value of resonance curve for system* (2.2.29).

where $\mathbf{a}, \mathbf{b} : \mathbb{R}^d \times \mathbb{R}^d \times \mathbb{R} \to \mathbb{R}^d$ are smooth functions, $\tau > 0$ is the time delay, $\mathbf{x}_t$ is the $\mathbb{R}^d$-valued state variable at time t, $\mathbf{x}_{t-\tau}$ denotes the delayed state at time $t-\tau$, W_t is a standard Wiener process and the initial condition $\mathbf{x}_t = \boldsymbol{\varphi}(t)$, $t \in [-\tau, 0]$ is continuous with $\left\langle \|\boldsymbol{\varphi}(t)\|_{L^\infty}^2 \right\rangle < \infty$ on $t \in [-\tau, 0]$ and $\mathcal{F}_0$-measureable [18].

2.2.6 Linearisation of Stochastic Delay Differential Equations

In this dissertation such SDDEs are investgiated, where the noise acts as a perturbation on a deterministic system. When analysing the stochastic stability of the solution of these systems, first the equilibrium of the underlining deterministic system is determined, then its stability is investigated in the presence of the stochastic perturbation. To demonstrate the linearisation process consider the autonomous system

$$\dot{\mathbf{x}}(t) = \mathbf{a}(\mathbf{x}(t), \mathbf{x}(t-\tau)). \tag{2.2.36}$$

Assume that there exists a trivial solution $\mathbf{x}^*$ (equilibrium state) for Eq. (2.2.36). Without the loss of generality one can set $\mathbf{x}^* \equiv \mathbf{0}$ such that $\mathbf{a}(\mathbf{0}, \mathbf{0}) = \mathbf{0}$. Furthermore, presume that the conditions are fulfilled which guarantee that the differential equation linearised around the trivial solution $\mathbf{x}^*$ exhibits the same stability properties in the neighborhood of the equilibrium state as the original nonlinear equation [5, 45]. If there exist the coefficient matrices $\mathbf{A}$, $\mathbf{B} \in \mathbb{R}^{d\times d}$, such that

$$|\mathbf{a}(\boldsymbol{\xi}, \boldsymbol{\eta}) - \mathbf{A}\boldsymbol{\xi} - \mathbf{B}\boldsymbol{\eta}| = o(|\boldsymbol{\xi}| + |\boldsymbol{\eta}|), \qquad |\boldsymbol{\xi} + \boldsymbol{\eta}| \to 0 \tag{2.2.37}$$

then the investigation of the stability properties of

$$\dot{\mathbf{x}}(t) = \mathbf{A}\mathbf{x}(t) + \mathbf{B}\mathbf{x}(t-\tau) \tag{2.2.38}$$

can be used to prove the local stability of the trivial solution $\mathbf{x}^*$ of the nonlinear DDE (2.2.36).

To analyse the effect of stochastic perturbation on the stability properties, Eq. (2.2.36) is extended as follows:

$$\mathrm{d}\mathbf{x}_t = \mathbf{a}(\mathbf{x}_t, \mathbf{x}_{t-\tau})\,\mathrm{d}t + \mathbf{b}(\mathbf{x}_t, \mathbf{x}_{t-\tau})\,\mathrm{d}W_t + \boldsymbol{\sigma}\mathrm{d}W_t, \tag{2.2.39}$$

where function $\mathbf{b} \in C^1\left(\mathbb{R}^d \times \mathbb{R}^d, \mathbb{R}^d\right)$ has also the property of $\mathbf{b}(\mathbf{0}, \mathbf{0}) = \mathbf{0}$ and $\boldsymbol{\sigma} \in \mathbb{R}^d$ is a constant vector representing the intensity of the additive noise. In this case $\mathbf{x}_t$ is a d-dimensional stochastic process, thus the time dependence is in the subscript. The goal is to investigate whether the process $\mathbf{x}_t$ stays in a bounded region of the trivial solution $\mathbf{x}^*$ of Eq. (2.2.36). For this purpose the definition of the first and the conservative second moment stability is used [5] in the form of

$$\lim_{t\to\infty} |\langle \mathbf{x}_t \rangle| = 0, \quad \lim_{t\to\infty} \left| \left\langle \mathbf{x}_t \mathbf{x}_t^\top \right\rangle \right| \leq \varepsilon, \quad 0 < \varepsilon < \infty \tag{2.2.40}$$

for all $\mathbf{x}_t = \boldsymbol{\varphi}(t)$, $t \in [-\tau, 0]$. Similarly to a deterministic case, it is assumed that for matrices $\boldsymbol{\alpha}, \boldsymbol{\beta} \in \mathbb{R}^{d\times d}$, the condition

$$|\mathbf{b}(\boldsymbol{\xi}, \boldsymbol{\eta}) - \boldsymbol{\alpha}\boldsymbol{\xi} - \boldsymbol{\beta}\boldsymbol{\eta}| = o(|\boldsymbol{\xi}| + |\boldsymbol{\eta}|), \qquad |\boldsymbol{\xi} + \boldsymbol{\eta}| \to 0 \tag{2.2.41}$$

holds. Then the linear stochastic delay differential equation (SDDE) of the form

$$\mathrm{d}\mathbf{x}_t = (\mathbf{A}\mathbf{x}_t + \mathbf{B}\mathbf{x}_{t-\tau})\,\mathrm{d}t + (\boldsymbol{\alpha}\mathbf{x}_t + \boldsymbol{\beta}\mathbf{x}_{t-\tau} + \boldsymbol{\sigma})\,\mathrm{d}W_t \tag{2.2.42}$$

can be used to prove moment stability and to approximate the stationary beahviour of the process defined by the nonlinear SDDE Eq. (2.2.39). An appropriate way to construct the matrices $\mathbf{A}, \mathbf{B}, \boldsymbol{\alpha}$ and $\boldsymbol{\beta}$ is to use the first order Taylor expansion of $\mathbf{a}(\boldsymbol{\xi}, \boldsymbol{\eta})$ and $\mathbf{b}(\boldsymbol{\xi}, \boldsymbol{\eta})$ at the fixed point $\mathbf{x}^* = \mathbf{0}$.

One can generalise the linearisation to periodic nonlinear systems, however, then instead of an equilibrium point one has to consider a periodic solution with period T and linearise around this solution. This process leads to periodic coefficient matrices in the linear SDDE used for the stability analysis.

2.2.7 Numerical Integration of Stochastic Delay Differential Equations

There exist a wide range implementations of numerical methods to integrate DDEs and SDEs [34, 71, 75], however, there does not seem to be any widely used solver for SDDEs. In order to numerically calculate the trajectories of an SDDE (2.2.35) we created the Julia package *StochasticDelayDiffEq.jl* [91]. This package allows the use of the large number SDE solver algorithms implemented in the already existing *StochasticDiffEq.jl* [71] package. This is achieved by transforming the SDDE (2.2.35) into the SDE

$$\mathrm{d}\mathbf{x}_t = \hat{\mathbf{a}}(\mathbf{x}_t, t)\,\mathrm{d}t + \hat{\mathbf{b}}(\mathbf{x}_t, t)\,\mathrm{d}W_t. \tag{2.2.43}$$

Since all values $\mathbf{x}_s, s \in [-\tau, t]$ are available (even if through interpolation of the approximate discrete solution) at time t, the functions $\hat{\mathbf{a}}$ and $\hat{\mathbf{b}}$ can be defined by dynamically embedding the initial funcion $\boldsymbol{\varphi}$ and the already computed (approximated) $\mathbf{x}_t$ states into the functions $\hat{\mathbf{a}}$ and $\hat{\mathbf{b}}$ as a time dependent inhomogenity, namely

$$\hat{\mathbf{a}}(\mathbf{x}_t, t) = \mathbf{a}(\mathbf{x}_t, \boldsymbol{\phi}_{t-\tau}, t), \qquad \hat{\mathbf{b}}(\mathbf{x}_t, t) = \mathbf{b}(\mathbf{x}_t, \boldsymbol{\phi}_{t-\tau}, t), \tag{2.2.44}$$

where

$$\boldsymbol{\phi}_t = \begin{cases} \boldsymbol{\varphi}_t & t \le 0 \\ \mathbf{x}_t & t > 0 \end{cases}. \tag{2.2.45}$$

This representation is similar to the method of steps [9], however, it allows uninterrupted integration (with discontinuity handling) and the utilization of the solver algorithms and features of the already existing SDE ecosystem from *StochasticDiffEq.jl* [71]. Furthermore the use of this history function $\boldsymbol{\phi}$ allows the integration of more general SDDEs, e.g. with multiple point or with distributed delays.

For example, if the Euler-Maruyama method is chosen from the package as the integrator algorithm with time step $\Delta t = \tau/N_{\Delta t}$, where $N_{\Delta t} \in \mathbb{N}^+$, the approximation of the value $\mathbf{x}_{t_{n+1}} = \mathbf{x}_{(n+1)\,\Delta t}$ inherently reduces to:

$$\mathbf{x}_{t_{n+1}} \approx \mathbf{x}_{t_n} + \mathbf{a}(\mathbf{x}_n, \mathbf{x}_{n-N_{\Delta t}}, t_n)\,\Delta t + \mathbf{b}(\mathbf{x}_n, \mathbf{x}_{n-N_{\Delta t}}, t_n)\,\xi_n\,\sqrt{\Delta t}, \qquad \xi_n \sim \mathcal{N}(0,1), \tag{2.2.46}$$

which is shown to be convergent to the exact solution of (2.2.35) in [13].

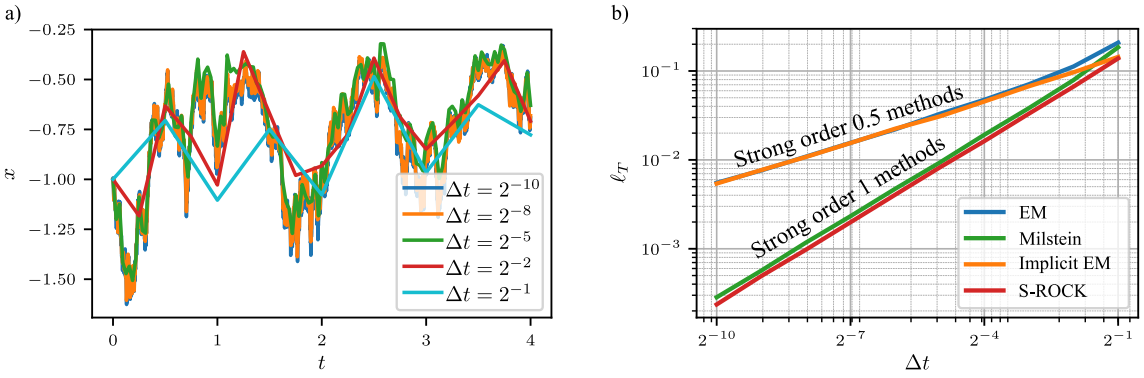

Figure 2.6. *Demonstration of the convergence of multiple methods for* $a(x_t, x_{t-1}, t) = x_t - \sin(x_{t-1})$, $b(x_t, x_{t-1}, t) = \sin(x_t)$ *and* $\varphi(t) = t - 1$. *The sample trajectories in a) are calculated with the Euler-Maruyama method using multiple time resolutions* Δt, *and with delay* $\tau = 1$, *while the trajectories are integrated up to time* $T = 4$. *For the convergence plots in b) the* ℓ_T *measure is used, defined in Eq.* (2.2.47).

Some examples are shown in Fig. 2.6, where numerical Monte-Carlo experiments were used to approximate the convergence of the solution at the final time point T approximated using different stochastic differential equation solver methods implemented in *StochasticDiffEq.jl* [71]. The analysis is conducted by studying the error measure

$$\ell_T(\Delta) = \left\langle \left\| \mathbf{x}_T^{\Delta t} - \mathbf{x}_T^{\Delta t_{\text{ref}}} \right\|_2 \right\rangle, \tag{2.2.47}$$

where $\mathbf{x}^{\Delta t}$ is the solution of the SDDE (2.2.35) approximated with time resolution Δt. To calculate the reference solution the time step $\Delta t_{\text{ref}} = 2^{-15}$ was used.

Due to its flexibility and its integration to the *DifferentialEquations.jl* [72] ecosystem, our *StochaticDelayDiffEq.jl* [91] package is used for all the Monte-Carlo simulations of SDDEs in this dissertation.

Chapter 3

Stochastic Semidiscretisation for Stochastic Delay Differential Equations

In this chapter an efficient method is provided to approximate the mean square stability of linear SDDEs through the analysis of the first and second moment dynamics of a discrete representation of the system. This method is the stochastic extension of the semidiscretisation method [39], where the terminology semidiscretisation is used in a similar sense as in case of partial differential equations [37] that is, only the delayed section of the state variable is discretised, while the time-derivatives are not. This is a kind of intermediate discretisation as opposed to the full discretisation, where time derivatives are also approximated, e.g., by finite difference schemes.

In paper [24], the basics of the moment mapping and the stability investigation method are laid down, but as opposed to the title of that paper, a full discretisation scheme is applied based on the Euler-Maruyama method. Due to its slow convergence properties and its high computational demand, it is not optimal for delayed problems especially with multiple state variables. In the present chapter, the numerical algorithm is derived based on semidiscretisation [37], which has higher-order convergence properties than the full discretisation based method mentioned above.

The chapter is partitioned into three sections. In Sec. 3.1 the semidiscretisation of linear SDDEs with constant coefficient matrices are considered, while in Sec. 3.2 the semidiscretisation method for linear SDDEs with periodic coefficient matrices are derived. Finally, in Sec. 3.3 it is shown how semidiscretisation can be utilised to analyse the stability and stationary behaviour of linear systems with stochastic delays subjected to additive noise.

3.1 Linear Systems with Constant Coefficient Matrices

Consider the linear SDDE (2.2.42) with constant coefficient matrices and constant delay given by

$$\mathrm{d}\mathbf{x}_t = (\mathbf{A}\mathbf{x}_t + \mathbf{B}\mathbf{x}_{t-\tau})\,\mathrm{d}t + (\boldsymbol{\alpha}\mathbf{x}_t + \boldsymbol{\beta}\mathbf{x}_{t-\tau} + \boldsymbol{\sigma})\,\mathrm{d}W_t, \tag{3.1.1}$$

where $\mathbf{A}$, $\mathbf{B}$, $\boldsymbol{\alpha}$ and $\boldsymbol{\beta} \in \mathbb{R}^{d\times d}$ are constant coefficient matrices, while $\boldsymbol{\sigma} \in \mathbb{R}^d$ is a constant coefficient vector and $\tau \in \mathbb{R}$ is a single time delay and $\mathbf{x}_t$ is the $\mathbb{R}^d$-valued stochastic state variable.

3.1.1 Zeroth-Order Stochastic Semidiscretisation

In order to numerically investigate the stationary solution of the SDDE (3.1.1), the state space of the continuous functions is reduced to a discrete one (see the sketch in Fig. 3.1). First, the SDDE (3.1.1) is approximated by considering the delayed term constant for a sufficiently short period of time Δt:

$$\mathrm{d}\mathbf{x}_t = \left(\mathbf{A}\mathbf{x}_t + \mathbf{B}\mathbf{x}_{t_{n-r}}\right)\mathrm{d}t + \left(\boldsymbol{\alpha}e^{\mathbf{A}(t-t_n)}\mathbf{x}_{t_n} + \boldsymbol{\beta}\mathbf{x}_{t_{n-r}} + \boldsymbol{\sigma}\right)\mathrm{d}W_t, \quad \text{where} \quad t \in [t_n, t_{n+1}], \tag{3.1.2}$$

which results in constant external excitation for $t \in [t_n, t_{n+1})$, $n \in \mathbb{N}$. Note that the discretised time t_n here denotes the incremented time t with the constant Δt for each n (which is not stochastic in this case, despite of the subscript notation), resulting $t_n = n\Delta t$.

The present multiplicative stochastic term has to be approximated since there exists no explicit analytic solution for the general linear SDE because the matrices $\mathbf{A}$ and $\boldsymbol{\alpha}$ are generally not exchangeable (see details in [5]). There are two simple ways to approximate the multiplicative term at present time: as a constant $\boldsymbol{\alpha}\mathbf{x}_{t_n}$, or as if it behaves according to the expected value $\boldsymbol{\alpha}e^{\mathbf{A}t}\mathbf{x}_{t_n}$ of the non-delayed equation. In Eq. (3.1.2), the latter approach is chosen for being a more accurate approximation as later detailed in Subsec. 3.1.3.

With the above assumptions, one can transform the SDDE (3.1.1) into the approximating difference equation given by

$$\mathbf{x}_{t_{n+1}} = (\mathbf{P}+\mathbf{Q})\,\mathbf{x}_{t_n} + (\mathbf{R}+\mathbf{S})\,\mathbf{x}_{t_n-\tau} + \mathbf{w}\,, \tag{3.1.3}$$

where the deterministic coefficient matrices $\mathbf{P}$ and $\mathbf{R}$ can be calculated explicitly from the deterministic part (the coefficients of $\mathrm{d}t$) of Eq. (3.1.2) according to [39]:

$$\mathbf{P} = e^{\mathbf{A}\Delta t}, \qquad \mathbf{R} = \mathbf{A}^{-1}\left(\mathbf{P}-\mathbf{I}\right)\mathbf{B}\,. \tag{3.1.4}$$

Since Eq. (3.1.2) is a linear stochastic differential equation with additive noise, the stochastic coefficient matrices $\mathbf{Q}$, $\mathbf{S}$ and the stochastic additive vector $\mathbf{w}$ originated in the coefficients $\boldsymbol{\alpha}$, $\boldsymbol{\beta}$, $\boldsymbol{\sigma}$ in Eq. (3.1.2) are represented [5] by the following Itô integrals:

$$\mathbf{Q} = \int_{t_n}^{t_{n+1}} e^{\mathbf{A}(t_{n+1}-s)}\boldsymbol{\alpha}e^{\mathbf{A}s}\mathrm{d}W_s\,, \qquad \mathbf{S} = \int_{t_n}^{t_{n+1}} e^{\mathbf{A}(t_{n+1}-s)}\boldsymbol{\beta}\mathrm{d}W_s\,, \tag{3.1.5}$$

$$\mathbf{w} = \int_{t_n}^{t_{n+1}} e^{\mathbf{A}(t_{n+1}-s)}\boldsymbol{\sigma}\mathrm{d}W_s\,. \tag{3.1.6}$$

Although these matrices cannot be calculated in closed form based on these formulas, but their first and second moments can be evaluated numerically as given in the subsequent subsection. Here, the time dependence of the stochastic matrices $\mathbf{Q}$ and $\mathbf{S}$, and vector $\mathbf{w}$ are omitted since their statistical properties do not change in time ($\mathbf{Q} := \mathbf{Q}_n$, $\mathbf{S} := \mathbf{S}_n$, $\mathbf{w} := \mathbf{w}_n$). In order to numerically investigate the stationary solution of the SDDE (3.1.1) the discretised state space vector $\mathbf{y}_n$ at time $t_n = n\Delta t$ is introduced (see Fig. 3.1):

$$\mathbf{y}_n = \begin{pmatrix}\mathbf{x}_{n\Delta t}^\top & \mathbf{x}_{(n-1)\Delta t}^\top & \cdots & \mathbf{x}_{(n-r)\Delta t}^\top\end{pmatrix}^\top, \tag{3.1.7}$$

with the discretisation resolution Δt chosen specifically to satisfy $r = \tau/\Delta t$.

This allows the solution of Eq. (3.1.3) to be written as a discrete stochastic map in the form [87]

$$\mathbf{y}_{n+1} = (\mathbf{F}+\mathbf{G})\,\mathbf{y}_n + \mathbf{g}\,, \tag{3.1.8}$$

where

$$\mathbf{F} = \begin{pmatrix} \mathbf{P} & \mathbf{0} & \cdots & \mathbf{0} & \mathbf{R} \\ \mathbf{I} & \mathbf{0} & \ldots & \mathbf{0} & \mathbf{0} \\ \mathbf{0} & \mathbf{I} & \ldots & \mathbf{0} & \mathbf{0} \\ \vdots & \vdots & \ddots & \vdots & \vdots \\ \mathbf{0} & \mathbf{0} & \cdots & \mathbf{I} & \mathbf{0} \end{pmatrix}, \quad \mathbf{G} = \begin{pmatrix} \mathbf{Q} & \mathbf{0} & \cdots & \mathbf{0} & \mathbf{S} \\ \mathbf{0} & \mathbf{0} & \cdots & \mathbf{0} & \mathbf{0} \\ \mathbf{0} & \mathbf{0} & \cdots & \mathbf{0} & \mathbf{0} \\ \vdots & \vdots & \ddots & \vdots & \vdots \\ \mathbf{0} & \mathbf{0} & \cdots & \mathbf{0} & \mathbf{0} \end{pmatrix}, \quad \mathbf{g} = \begin{pmatrix} \mathbf{w} \\ \mathbf{0} \\ \mathbf{0} \\ \vdots \\ \mathbf{0} \end{pmatrix}, \tag{3.1.9}$$

respectively. Similarly to $\mathbf{Q}$, $\mathbf{S}$ and $\mathbf{w}$ the time dependence of the matrix $\mathbf{G}$ and vector $\mathbf{g}$ is omitted due to their stochastic properties being independent of time. This is due to the renewal property of the stochastic integrals generating these matrices and vectors, since their properties only depend on the length of the time intervals of $[t_n, t_{n+1})$ and not on the current value of the discrete time n. Note that the matrix $\mathbf{F}$ is the same as that is already defined according to [39], while $\mathbf{G}$ can be built in a similar way, but its elements are stochastic integrals.

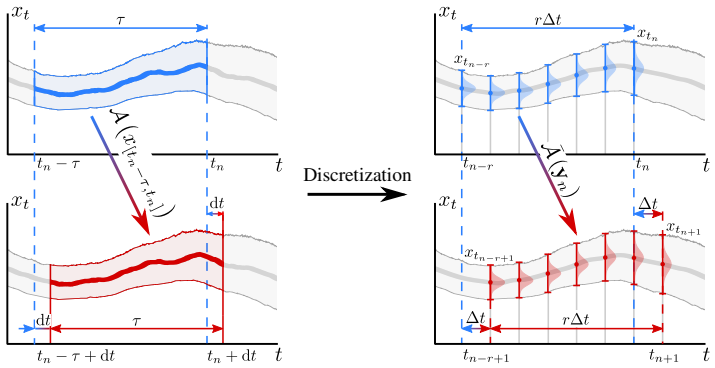

Figure 3.1. *Discretisation of the stochastic process, where* $\mathcal{A}\colon\ x_{[t_n-\tau,t_n]} \mapsto x_{[t_n+\mathrm{d}t-\tau,t_n+\mathrm{d}t]}$ *represents the operator which maps the function* x *forward for an infinitesimal time* $\mathrm{d}t$*. On the right side* $\bar{\mathcal{A}}\colon\ \mathbf{y}_n \mapsto \mathbf{y}_{n+1}$ *represents the discretised approximation of the operator* $\mathcal{A}$*, which maps the discretised function* x_t *stored in* $\mathbf{y}$ *(see Eq.* (3.1.7)*) at the finite time* Δt *forward.*

3.1.2 First and Second Moment Dynamics of Stochastic Maps

Since the stochastic map (3.1.8) contains the discrete approximate solution of Eq. (3.1.1) it can be utilised to approximate its first and second moment dynamics. This approach allows to also study the first and second moment stability and to give an estimate for the stationary second moment, which characterise the region where the solutions are located.

First Moment of the Stochastic Map

To approximate the first moment evolution of the SDDE (3.1.1), the expected value operator $\langle . \rangle$ is used on the stochastic map (3.1.8). Since $\mathbf{F}$ is defined to be deterministic and $\mathbf{G}$ describes the stochastic variations around $\mathbf{F}$, the first moment mapping is simply

$$\bar{\mathbf{y}}(n+1) = \mathbf{F}\bar{\mathbf{y}}(n), \tag{3.1.10}$$

where $\bar{\mathbf{y}}(n)$ is the first moment vector of the discretised state space, namely:

$$\bar{\mathbf{y}}(n) := \bar{\mathbf{y}}(n) = \left(\langle \mathbf{x}_{n\Delta t} \rangle^\top, \langle \mathbf{x}_{(n-1)\Delta t} \rangle^\top, \ldots, \langle \mathbf{x}_{(n-r)\Delta t} \rangle^\top \right)^\top. \tag{3.1.11}$$

The stochastic perturbation mapping matrix $\mathbf{G}$ defined in Eq. (3.1.9) using (3.1.5) is independent of $\mathbf{y}_n$, since for any function $f(.)$ the conditional expected value is equal to the expected value: $\langle f(\mathbf{G}) | (\mathcal{F}_t)_{t<n\Delta t} \rangle = \langle f(\mathbf{G}) \rangle$. It means, that the stochastic matrix process $\mathbf{G}$ does not depend on the history of the process up to $t = n\Delta t$ denoted with the filtration $(\mathcal{F}_t)_{t<n\Delta t}$. This is due to the fact, that the stochastic integrals are evaluated on the interval $(n\Delta t, (n+1)\Delta t]$.

The deterministic map (3.1.10) gives the underlying discrete deterministic delayed system of Eq. (3.1.1). The stability of the trivial solution, the fixed point $\bar{\mathbf{y}}_{\mathrm{st}} \equiv \mathbf{0}$ of the system (3.1.10) can be characterised by the spectral radius

$$\rho(\mathbf{F}) = \max_z \{ \mathrm{abs}(z),\ z \in \mathbb{C} : \det(\mathbf{F} - z\mathbf{I}) = 0 \} \tag{3.1.12}$$

of the mapping matrix $\mathbf{F}$ [37, 39]. Note that if the stochastic effects (the coefficients of $\mathrm{d}W_t$) are neglected during modelling, that is, the stochastic components are omitted from the governing Eq. (3.1.1), one ends up with the same deterministic mapping as Eq. (3.1.10); the stochastic effects do not influence the mean dynamics of a linear system.

When dealing with the moment stability of a linear SDDE, the second moment dynamics has to be investigated.

Second Moment of the Stochastic Map

To investigate the behaviour of the second moment the symmetric second moment matrix can be defined by

$$\overline{\overline{\mathbf{Y}}}(n) := \left\langle \mathbf{y}_n \mathbf{y}_n^\top \right\rangle = \begin{pmatrix} \overline{\overline{Y}}_{11}(n) & \overline{\overline{Y}}_{12}(n) & \dots & \overline{\overline{Y}}_{1,(r+1)d}(n) \\ \overline{\overline{Y}}_{12}(n) & \overline{\overline{Y}}_{22}(n) & \dots & \overline{\overline{Y}}_{2,(r+1)d}(n) \\ \vdots & \vdots & \ddots & \vdots \\ \overline{\overline{Y}}_{1,(r+1)d}(n) & \overline{\overline{Y}}_{2,(r+1)d}(n) & \dots & \overline{\overline{Y}}_{(r+1)d,(r+1)d}(n) \end{pmatrix}, \tag{3.1.13}$$

where

$$\overline{\overline{Y}}_{i_1 i_2}(n) = \overline{\overline{Y}}_{i_2 i_1}(n) := \langle y_{n,i_1} y_{n,i_2} \rangle \,. \tag{3.1.14}$$

To obtain the second moment matrix evolution, the outer product of both sides of the stochastic map (3.1.8) is taken:

$$\mathbf{y}_{n+1}\mathbf{y}_{n+1}^\top = (\mathbf{F}+\mathbf{G})\mathbf{y}_n\mathbf{y}_n^\top(\mathbf{F}+\mathbf{G})^\top + (\mathbf{F}+\mathbf{G})\mathbf{y}_n\mathbf{g}^\top + \mathbf{g}\mathbf{y}_n^\top(\mathbf{F}+\mathbf{G})^\top + \mathbf{g}\mathbf{g}^\top \,. \tag{3.1.15}$$

Utilizing Einstein's notation along with (3.1.14) and using the properties of the stochastic integrals [61] generating the elements of $\mathbf{G}$ and $\mathbf{g}$, the expected value of the squared map (3.1.15) can be written in the form

$$\overline{\overline{Y}}_{i_1 i_2}(n+1) = (F_{i_1 i_4}F_{i_2 i_3} + \langle G_{i_1 i_4}G_{i_2 i_3}\rangle)\overline{\overline{Y}}_{i_3 i_4}(n) + (\langle G_{i_1 i_3}g_{i_2} + G_{i_2 i_3}g_{i_1}\rangle)\,\bar{y}_{i_3}(n) + \langle g_{i_1}g_{i_2}\rangle \,. \tag{3.1.16}$$

The expected values in (3.1.16) can be computed using the Itô isometry [61,87], defined in (2.2.1). Furthermore, instead of the matrix-to-matrix map representation of the second moment map (3.1.16), the more convenient vector-to-vector map is used. An efficient vector-representation of the independent elements of the second moment matrix is

$$\bar{\bar{\mathbf{y}}}(n) := \left(\overline{\overline{Y}}_{11}(n), \overline{\overline{Y}}_{22}(n), \dots, \overline{\overline{Y}}_{12}(n), \overline{\overline{Y}}_{23}(n), \dots, \overline{\overline{Y}}_{1,(r+1)d}(n)\right)\top, \tag{3.1.17}$$

where the symmetric elements of the matrix $\overline{\overline{\mathbf{Y}}}(n)$ are only considered once. Using the above vector notation, the second moment map (3.1.16) can be written as

$$\bar{\bar{\mathbf{y}}}(n+1) = \mathbf{H}\bar{\bar{\mathbf{y}}}(n) + \mathbf{h}\bar{\mathbf{y}}(n) + \bar{\bar{\mathbf{g}}}, \tag{3.1.18}$$

where the coefficient matrices $\mathbf{H}$, $\mathbf{h}$ and vector $\bar{\bar{\mathbf{g}}}$ are calculated using the rules defined by Eq. (3.1.16).

To show the structure of the deterministic matrix $\mathbf{H}$ in Eq. (3.1.18) using the arrangement of the elements of the second moment matrix $\bar{\bar{\mathbf{y}}}(n)$ provided in Eqs. (3.1.17), the matrix $\mathbf{H}$ is partitioned into terms originating from matrix $\mathbf{F}$ and $\mathbf{G}$:

$$\mathbf{H} = \mathbf{H}_\mathbf{F} + \mathbf{H}_\mathbf{G}. \tag{3.1.19}$$

Note that, both $\mathbf{H}_\mathbf{F}$ and $\mathbf{H}_\mathbf{G}$ have identical structures, but since $\mathbf{G}$ is stochastic, the expectation value operator has to be used, e.g.: if $H_{\mathbf{F},11} = F_{11}^2$ then $H_{\mathbf{G},11} = \langle G_{11}^2 \rangle$.

In the case of $\mathbf{F} \in \mathbb{R}^{3\times3}$ and an $\mathbb{R}^{3\times3}$-valued $\mathbf{G}$, $\mathbf{H}_\mathbf{F}$ is the following:

$$\mathbf{H}_\mathbf{F} = \left(\begin{array}{ccc|ccc} F_{11}^2 & F_{12}^2 & F_{13}^2 & 2F_{11}F_{12} & 2F_{12}F_{13} & 2F_{11}F_{13} \\ F_{21}^2 & F_{22}^2 & F_{23}^2 & 2F_{21}F_{22} & 2F_{22}F_{23} & 2F_{21}F_{23} \\ F_{31}^2 & F_{32}^2 & F_{33}^2 & 2F_{31}F_{32} & 2F_{32}F_{33} & 2F_{31}F_{33} \\ \hline F_{11}F_{21} & F_{12}F_{22} & F_{13}F_{23} & F_{11}F_{22}+F_{12}F_{21} & F_{12}F_{23}+F_{13}F_{22} & F_{11}F_{23}+F_{13}F_{21} \\ F_{21}F_{31} & F_{22}F_{32} & F_{23}F_{33} & F_{21}F_{32}+F_{22}F_{31} & F_{22}F_{33}+F_{23}F_{32} & F_{21}F_{33}+F_{23}F_{31} \\ \hline F_{11}F_{31} & F_{12}F_{32} & F_{13}F_{33} & F_{11}F_{32}+F_{12}F_{31} & F_{12}F_{33}+F_{13}F_{32} & F_{11}F_{33}+F_{13}F_{31} \end{array}\right). \tag{3.1.20}$$

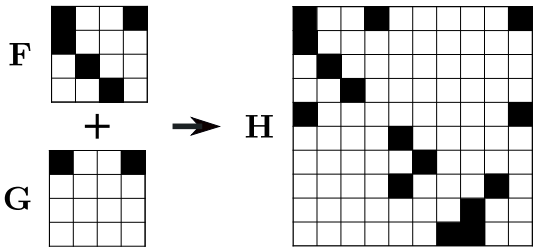

Figure 3.2. *The illustration of the structure of the second moment generator matrix* $\mathbf{H}$

In Fig. 3.2 the schematic structures of the deterministic, stochastic and second moment mapping matrices $\mathbf{F}$, $\mathbf{G}$ and $\mathbf{H}$ are presented for zeroth-order semidiscretisation with $r = 3$ (see Eqs. (3.1.16)-(3.1.18)).

The stability of the second moment process is determined by the spectral radius of $\mathbf{H}$: in case of $\rho(\mathbf{H}) > 1$, then the second moment of the process defined in Eq. (3.1.1) is unstable, and if $\rho(\mathbf{H}) < 1$ then it is stable and the process has a bounded stationary solution.

Note that the first moment process $\bar{\mathbf{y}}(n)$ appears in Eq. (3.1.18) as an additive excitation, independent of $\overline{\overline{\mathbf{Y}}}(n)$. According to Arnold [5], it can be shown that the second moment might be stable ($\rho(\mathbf{H}) < 1$) only if the first moment is stable ($\rho(\mathbf{F}) < 1$). Therefore, if the squared process is stable, then the stationary excitation from the first moment process decays: $\lim_{n\to\infty}\bar{\mathbf{y}}(n) = 0$, consequently the determination of the matrix $\mathbf{h}$ is needed neither for the stability investigation nor for the calculation of the stationary second moment. The additive term $\bar{\bar{\mathbf{g}}}$ is a bounded quantity originating from the stochastic integral of the additive process denoted by $\boldsymbol{\sigma}\mathrm{d}W_t$ in Eq. (3.1.1), and the stationary squared process $\bar{\bar{\mathbf{y}}}_{\mathrm{st}}$ can be calculated as

$$\bar{\bar{\mathbf{y}}}_{\mathrm{st}} = (\mathbf{I} - \mathbf{H})^{-1}\,\bar{\bar{\mathbf{g}}}\,. \tag{3.1.21}$$

For the calculation of $\mathbf{H}$, $\mathbf{h}$ and $\bar{\bar{\mathbf{g}}}$, one only needs the expected value of the product of the integrals in Eqs. (3.1.16)-(3.1.18), which can be approximated, e.g., with the help of Monte-Carlo (MC) simulations. However, in the subsequent section, a different, more efficient approach is presented to approximate the expected value of the products of the stochastic coefficients $\mathbf{G}$ and $\mathbf{g}$ to be used in the construction of mapping (3.1.18).

Evaluation of the Expected Values

To calculate the second moment mapping matrices $\mathbf{H}$, $\mathbf{h}$ and vector $\bar{\bar{\mathbf{g}}}$, there are terms originating in the stochastic matrix $\mathbf{G}$ and vector $\mathbf{g}$. The non-zero elements of matrix $\mathbf{G}$ can be written as a stochastic integral of the deterministic functions $t \mapsto f_{G,i_1i_2}(t)$ $i_1, i_2 = 1, 2, \ldots, (r+1)d$, defined by

$$\mathbf{Q} = \int_{t_n}^{t_{n+1}} e^{\mathbf{A}(t_{n+1}-t)}\boldsymbol{\alpha}e^{\mathbf{A}t}\mathrm{d}W_{t+n\Delta t} =: \int_{t_n}^{t_{n+1}} \begin{pmatrix} f_{G,11}(t) & \ldots & f_{G,1d}(t) \\ \vdots & \ddots & \vdots \\ f_{G,d1}(t) & \ldots & f_{G,dd}(t) \end{pmatrix} \mathrm{d}W_{t+n\Delta t}, \tag{3.1.22}$$

$$\mathbf{S} = \int_{t_n}^{t_{n+1}} e^{\mathbf{A}(t_{n+1}-t)}\boldsymbol{\beta}\mathrm{d}W_t =: \int_{t_n}^{t_{n+1}} \begin{pmatrix} f_{G,1\,rd+1}(t) & \ldots & f_{G,1\,rd+d}(t) \\ \vdots & \ddots & \vdots \\ f_{G,d\,rd+1}(t) & \ldots & f_{G,d\,rd+d}(t) \end{pmatrix} \mathrm{d}W_{t+n\Delta t}\,, \tag{3.1.23}$$

and $f_{G,i_1i_2}(t) \equiv 0$ where $G_{i_1i_2} = 0$ in Eq. (3.1.9). The elements of the vector $\mathbf{g}$ can be written similarly by means of

$$\mathbf{w} = \int_{t_n}^{t_{n+1}} e^{\mathbf{A}(t-t)}\boldsymbol{\sigma}\mathrm{d}W_t =: \int_{t_n}^{t_{n+1}} \begin{pmatrix} f_{g,1} \\ \vdots \\ f_{g,r} \end{pmatrix} \mathrm{d}W_t\,, \tag{3.1.24}$$

and $f_{g,i}(t) \equiv 0$ where $g_i = 0$ in Eq. (3.1.9).

The Itô isometry (2.2.4) [61] is used to evaluate the expected value of the products of the elements of the matrix $\mathbf{G}$ and the vector $\mathbf{g}$, as defined in Eq. (3.1.18).

$$\langle G_{i_1i_4}G_{i_2i_3}\rangle = \left\langle \int_{t_n}^{t_{n+1}} f_{G,i_1i_4}(t)\,\mathrm{d}W_t \int_{t_n}^{t_{n+1}} f_{G,i_2i_3}(t)\,\mathrm{d}W_t \right\rangle = \int_{t_n}^{t_{n+1}} f_{G,i_1i_4}(t)\, f_{G,i_2i_3}(t)\,\mathrm{d}t\,, \tag{3.1.25}$$

$$\langle G_{i_1i_3}g_{i_2}\rangle = \left\langle \int_{t_n}^{t_{n+1}} f_{G,i_1i_3}(t)\,\mathrm{d}W_t \int_{t_n}^{t_{n+1}} f_{g,i_2}(t)\,\mathrm{d}W_t \right\rangle = \int_{t_n}^{t_{n+1}} f_{G,i_1i_3}(t)\, f_{g,i_2}(t)\,\mathrm{d}t\,, \tag{3.1.26}$$

$$\langle g_{i_1}g_{i_2}\rangle = \left\langle \int_{t_n}^{t_{n+1}} f_{g,i_1}(t)\,\mathrm{d}W_t \int_{t_n}^{t_{n+1}} f_{g,i_2}(t)\,\mathrm{d}W_t \right\rangle = \int_{t_n}^{t_{n+1}} f_{g,i_1}(t)\, f_{g,i_2}(t)\,\mathrm{d}t\,. \tag{3.1.27}$$

During the numerical construction of the mapping matrix $\mathbf{H}$ in Eq. (3.1.16), the elements of $\mathbf{G}$ are not calculated directly; only the arguments of the integrals in Eq. (3.1.25)-(3.1.27) are computed at discrete points in the time intervals evaluated by an integration scheme (e.g.: trapezoidal or a quadrature). These are stored in a vectorised form, and during the second moment matrix calculation, they are multiplied with each other (according the definition in Eq. (3.1.16)), then weighted and summed according to the chosen integration scheme. This calculation has been implemented and used in my Julia package *StochasticSemidiscretisationMethod.jl*.

3.1.3 Improving the Accuracy of the Semidiscretisation in the Presence of Multiplicative Noise

To increase the accuracy of the discretisation in the presence of a multiplicative noise on the present state $\mathbf{x}_t$, the multiplicative term is approximated to behave according to the expected value $\boldsymbol{\alpha}e^{\mathbf{A}t}\mathbf{x}_{t_n}$ in Eq. (3.1.2) (as if $\mathbf{B} = \mathbf{0}$). To demonstrate the improvement in terms of accuracy, first consider the following linear SDE:

$$\mathrm{d}\mathbf{x}_t = \mathbf{A}\mathbf{x}_t\mathrm{d}t + \boldsymbol{\alpha}\mathbf{x}_t\mathrm{d}W_t. \tag{3.1.28}$$

In the general d dimensional case, it has no explicit solution [5]. In order to construct an analytical solution that improves the accuracy of our numerical method, the state vector $\mathbf{x}_t$ in the multiplicative term $\boldsymbol{\alpha}\mathbf{x}_t\mathrm{d}W_t$ is approximated by its expected value $\langle\mathbf{x}_t\rangle$, namely

$$\langle\mathrm{d}\mathbf{x}_t\rangle = \mathbf{A}\langle\mathbf{x}_t\rangle\,\mathrm{d}t \quad \Rightarrow \quad \langle\mathbf{x}_t\rangle = e^{\mathbf{A}t}\mathbf{x}_{t_0}\,. \tag{3.1.29}$$

This expectation value is substituted back into the multiplicative term $\mathbf{x}_t$ in (3.1.28) transforming it into an additive term. The solution then can be expressed in a closed form for the approximated linear SDE by

$$\mathrm{d}\mathbf{x}_t = \mathbf{A}\mathbf{x}_t\mathrm{d}t + \boldsymbol{\alpha}e^{\mathbf{A}t}\mathbf{x}_{t_0}\mathrm{d}W_t \quad \Rightarrow \quad \mathbf{x}_{t_0+\Delta t} = e^{\mathbf{A}\Delta t}\left(\mathbf{I} + \int_{t_0}^{t_0+\Delta t} e^{-\mathbf{A}s}\boldsymbol{\alpha}e^{\mathbf{A}s}\mathrm{d}W_s\right)\mathbf{x}_{t_0}\,, \tag{3.1.30}$$

where $t \in [t_0, t_0 + \Delta t)$.

To demonstrate the advantage of this approximation of second moment compared to the constant approximation, the following scalar example is used:

$$\mathrm{d}x_t = Ax_t\mathrm{d}t + \alpha x_t \mathrm{d}W_t, \tag{3.1.31}$$

which has the following exact solution [5, 61] for one discretisation time step going from t_0 to $t_0 + \Delta t$:

$$x_{t_0+\Delta t} = x_{t_0}\exp\left(\left(A - \frac{\alpha^2}{2}\right)\Delta t + \alpha\left(W_{t_0+\Delta t} - W_{t_0}\right)\right), \tag{3.1.32}$$

from which the first and second moments are [5, 61]:

$$\langle x_{t_0+\Delta t}\rangle = \langle x_{t_0}\rangle\, e^{A\Delta t}, \tag{3.1.33}$$

$$\langle x_{t_0+\Delta t}x_{t_0+\Delta t}\rangle = \langle x_{t_0}x_{t_0}\rangle\, e^{2A\Delta t+\alpha^2\Delta t}. \tag{3.1.34}$$

When the approximation of Eq. (3.1.31) is considered without the first moment correction in the multiplicative term, the approximation yields

$$\mathrm{d}\tilde{x}_t = A\tilde{x}_t\mathrm{d}t + \alpha\tilde{x}_{t_0}\mathrm{d}W_t \quad \text{where} \quad t \in [t_0, t_0+\Delta t)\,, \tag{3.1.35}$$

which has the following solution, first and second moment evolutions:

$$\tilde{x}_{t_0+\Delta t} = \tilde{x}_{t_0}e^{A\Delta t}\left(1 + \int_{t_0}^{t_0+\Delta t} e^{-At}\alpha\mathrm{d}W_t\right), \tag{3.1.36}$$

$$\langle \tilde{x}_{t_0+\Delta t}\rangle = \langle \tilde{x}_{t_0}\rangle\, e^{A\Delta t}, \tag{3.1.37}$$

$$\langle \tilde{x}_{t_0+\Delta t}\tilde{x}_{t_0+\Delta t}\rangle = \langle \tilde{x}_{t_0}\tilde{x}_{t_0}\rangle\left(e^{2A\Delta t} + \frac{\alpha^2\left(e^{2A\Delta t}-1\right)}{2A}\right), \tag{3.1.38}$$

respectively. When the first moment correction is applied in the approximation, the following SDE is obtained:

$$\mathrm{d}\bar{x}_t = A\bar{x}_t\mathrm{d}t + \alpha\bar{x}_t e^{As}\mathrm{d}W_t \quad \text{where} \quad t \in [t, t_0+\Delta t)\,, \tag{3.1.39}$$

and the corresponding solution, first and second moment evolutions are

$$\bar{x}_{t_0+\Delta t} = \bar{x}_{t_0}e^{A\Delta t}\left(1 + \int_{t_0}^{t_0+\Delta t} e^{-At}\alpha e^{At}\mathrm{d}W_t\right), \tag{3.1.40}$$

$$\langle \bar{x}_{t_0+\Delta t}\rangle = \langle \bar{x}_{t_0}\rangle\, e^{A\Delta t}, \tag{3.1.41}$$

$$\langle \bar{x}_{t_0+\Delta t}\bar{x}_{t_0+\Delta t}\rangle = \langle \bar{x}_{t_0}\bar{x}_{t_0}\rangle\, e^{2A\Delta t}\left(1+\alpha^2\Delta t\right). \tag{3.1.42}$$

Note that the first moment of both approximations provide the analytical solution. To compare the quality of the different approximations, the Taylor series of the second moments w.r.t. Δt are used. For the exact solution (3.1.34) it is

$$\langle x_{t_0+\Delta t}x_{t_0+\Delta t}\rangle = \langle x_{t_0}x_{t_0}\rangle\left(1 + \left(2A+\alpha^2\right)\Delta t + \left(2A^2 + 2A\alpha^2 + \frac{\alpha^4}{2}\right)\Delta t^2\right) + \mathcal{O}\big(\Delta t^3\big), \tag{3.1.43}$$

while for the non-corrected approximating solution (3.1.38) it reduces to

$$\langle \tilde{x}_{t_0+\Delta t}\tilde{x}_{t_0+\Delta t}\rangle = \langle \tilde{x}_{t_0}\tilde{x}_{t_0}\rangle\left(1 + \left(2A+\alpha^2\right)\Delta t + \left(2A^2 + A\alpha^2\right)\Delta t^2\right) + \mathcal{O}\big(\Delta t^3\big), \tag{3.1.44}$$

and for the corrected approximating solution (3.1.42) it reads as

$$\langle \bar{x}_{t_0+\Delta t}\bar{x}_{t_0+\Delta t}\rangle = \langle \bar{x}_{t_0}\bar{x}_{t_0}\rangle \left(1+\left(2A+\alpha^2\right)\Delta t+\left(2A^2+2A\alpha^2\right)\Delta t^2\right)+\mathcal{O}\big(\Delta t^3\big). \quad (3.1.45)$$

From the error of the non-corrected approximation

$$\langle x_{t_0+\Delta t}x_{t_0+\Delta t}\rangle - \langle \tilde{x}_{t_0+\Delta t}\tilde{x}_{t_0+\Delta t}\rangle = \left(A\alpha^2+\frac{1}{2}\alpha^4\right)\langle x_{t_0}x_{t_0}\rangle\,\Delta t^2+\mathcal{O}\big(\Delta t^3\big). \quad (3.1.46)$$

and from the error of the first moment corrected approximation

$$\langle x_{t_0+\Delta t}x_{t_0+\Delta t}\rangle - \langle \bar{x}_{t_0+\Delta t}\bar{x}_{t_0+\Delta t}\rangle = \frac{1}{2}\alpha^4\langle x_{t_0}x_{t_0}\rangle\,\Delta t^2+\mathcal{O}\big(\Delta t^3\big), \quad (3.1.47)$$

it can be seen, that the two methods have the same order in Δt. Ideally the second-order should match with the analytical, but to date we havent found such a correction. However, in case when the noise is used only as a perturbation, the multiplicative term α is typically at least an order of magnitude smaller than the term A, so the error of the corrected approximation in α is at least two order of magnitude smaller. Note that this extension has negligible effect on the computational time of the numerically determined integrals in Eq. (3.1.25). The beneficial effect of this approximation is further illustrated through numerical experiments in Sec. 4.2.

3.1.4 Higher-Order Semidiscretisation

To further improve the accuracy of the approximation of the mapping, Lagrange polynomials are used to approximate the delayed term [39]. The definition of the mapping matrices $\mathbf{F}$ and $\mathbf{G}$ are not limited to the zeroth-order semidiscretisation, but can also be built using this higher-order semidiscretisation. Note that the term "higher-order" refers to the order of the Lagrange polynomial used to approximate the delayed terms: during zeroth-order semidiscretisation a constant is used, when applying first-order semidiscretisation a linear approximation is fit, during the second-order approximation a parabola is applied, etc. This leads to additional terms in both the deterministic and the stochastic mapping matrices. In this case the delay resolution r is calculated by

$$r = \left\lfloor \frac{\tau}{\Delta t}+\frac{q}{2}\right\rfloor, \quad (3.1.48)$$

where $\lfloor . \rfloor$ denotes the floor operation, q is the order of the Lagrange polynomial

$$\mathbf{L}_t^{(q)} = \sum_{j_1=0}^{q} L^{(q,j_1)}(t)\mathbf{x}_{t-(n-r+j_1)\Delta t}\,, \quad (3.1.49)$$

and

$$L^{(q,j_1)}(t) = \left(\prod_{j_2=0,j_2\neq j_1}^{q}\frac{t-\tau-(n+j_2-r)\Delta t}{(j_1-j_2)\,\Delta t}\right), \quad \text{where} \quad t\in[t_n,t_{n+1})\,. \quad (3.1.50)$$

Using this, the approximation of Eq. 3.1.1 leads to

$$\mathrm{d}\mathbf{x}_t = \left(\mathbf{A}\mathbf{x}_t+\mathbf{B}\,\mathbf{L}_t^{(q)}\right)\mathrm{d}t+\left(\boldsymbol{\alpha}e^{\mathbf{A}s}\mathbf{x}_{t_n}+\boldsymbol{\beta}\,\mathbf{L}_t^{(q)}+\boldsymbol{\sigma}\right)\mathrm{d}W_t, \quad \text{where} \quad t\in[t_n,t_{n+1})\,, \quad (3.1.51)$$

with the discretised form

$$x_{t+\Delta t} = (\mathbf{P}+\mathbf{Q})\,\mathbf{x}_t+\sum_{j=0}^{q}(\mathbf{R}_j+\mathbf{S}_j)\,\mathbf{x}_{t-\tau+k\Delta t}+\mathbf{w}\,. \quad (3.1.52)$$

Example: first-order Semidiscretisation

In case of choosing $q = 1$, one approximates the delayed terms with a first-order polynomial. In terms of discretisation matrices, this leads to the following deterministic matrices:

$$\mathbf{P} = e^{\mathbf{A}\Delta t}, \tag{3.1.53}$$

$$\mathbf{R}_0 = \left(\mathbf{A}^{-1} + \frac{1}{\Delta t}\left(\mathbf{A}^{-2} - (\tau - (r-1)\Delta t)\,\mathbf{A}^{-1}\right)\left(\mathbf{I} - e^{\mathbf{A}\Delta t}\right)\right)\mathbf{B}, \tag{3.1.54}$$

$$\mathbf{R}_1 = \left(-\mathbf{A}^{-1} + \frac{1}{\Delta t}\left(-\mathbf{A}^{-2} + (\tau - r\Delta t)\,\mathbf{A}^{-1}\right)\left(\mathbf{I} - e^{\mathbf{A}\Delta t}\right)\right)\mathbf{B}, \tag{3.1.55}$$

stochastic matrices

$$\mathbf{Q} = \int_{t_n}^{t_{n+1}} e^{\mathbf{A}(t_{n+1}-t)}\boldsymbol{\alpha} e^{\mathbf{A}t}\mathrm{d}W_t, \tag{3.1.56}$$

$$\mathbf{S}_0 = \int_{t_n}^{t_{n+1}} e^{\mathbf{A}(t_{n+1}-t)} L_t^{(1,0)}(t)\boldsymbol{\beta}\mathrm{d}W_t, \tag{3.1.57}$$

$$\mathbf{S}_1 = \int_{t_n}^{t_{n+1}} e^{\mathbf{A}(t_{n+1}-t)} L_t^{(1,1)}(t)\boldsymbol{\beta}\mathrm{d}W_t, \tag{3.1.58}$$

and stochastic additive vector

$$\mathbf{w} = \int_{t_n}^{t_{n+1}} e^{\mathbf{A}(t_{n+1}-t)}\boldsymbol{\sigma}\mathrm{d}W_t. \tag{3.1.59}$$

The discretisation matrices and stochastic additive vector in Eq. (3.1.8) assume a similar structure to (3.1.9), namely:

$$\mathbf{F} = \begin{pmatrix} \mathbf{P} & \mathbf{0} & \cdots & \mathbf{R}_1 & \mathbf{R}_0 \\ \mathbf{I} & \mathbf{0} & \dots & \mathbf{0} & \mathbf{0} \\ \mathbf{0} & \mathbf{I} & \cdots & \mathbf{0} & \mathbf{0} \\ \vdots & \vdots & \ddots & \vdots & \vdots \\ \mathbf{0} & \mathbf{0} & \cdots & \mathbf{I} & \mathbf{0} \end{pmatrix}, \quad \mathbf{G} = \begin{pmatrix} \mathbf{Q} & \mathbf{0} & \cdots & \mathbf{S}_1 & \mathbf{S}_0 \\ \mathbf{0} & \mathbf{0} & \cdots & \mathbf{0} & \mathbf{0} \\ \vdots & \vdots & \ddots & \vdots & \vdots \\ \mathbf{0} & \mathbf{0} & \cdots & \mathbf{0} & \mathbf{0} \end{pmatrix}, \quad \mathbf{g} = \begin{pmatrix} \mathbf{w} \\ \mathbf{0} \\ \vdots \\ \mathbf{0} \end{pmatrix}. \tag{3.1.60}$$

3.1.5 Generalisation for Multiple Delays and Independent Noise Sources

To apply the semidiscretisation method for multiple delays and independent white-noise sources one has to use the form:

$$\mathrm{d}\mathbf{x}_t = \left(\mathbf{A}\mathbf{x}_t + \sum_{j_\tau=1}^{N_\tau}\mathbf{B}_{j_\tau}\mathbf{x}_{t-\tau_{j_\tau}}\right)\mathrm{d}t + \sum_{j_W=1}^{N_W}\left(\boldsymbol{\sigma}_{j_W} + \boldsymbol{\alpha}_{j_W}\mathbf{x}_t + \sum_{j_\tau=1}^{N_\tau}\boldsymbol{\beta}_{j_\tau,j_W}\mathbf{x}_{t-\tau_{j_\tau}}\right)dW_{j_W,t}, \tag{3.1.61}$$

where τ_{j_τ}, $j_\tau = 1,\dots,N_\tau$ are the time delays, $N_\tau \in \mathbb{N}^+$ is the number of time delays, and without the loss of generality, assume that $\tau_1 < \tau_2 < \ldots < \tau_{N_\tau}$. Furthermore, $j_W \in \mathbb{N}^+$ is the number of independent noise sources and $W_{j_W,t}$, $j_W = 1,\dots,N_W$ are the Wiener processes to model the Gaussian white noises, that is, $\mathbb{E}\left(\mathrm{d}W_{i_W,t_1}\mathrm{d}W_{j_W,t_2}\right) = \mathrm{d}t\,\delta_{i_W j_W}\mathbb{1}(t_1 = t_2)$ with $\delta_{i_W j_W}$ standing for the Kronecker symbol. The system in Eq. (3.1.61) can be transformed into the following mapping:

$$\mathbf{y}_{n+1} = \left(\mathbf{F} + \sum_{j_W=1}^{N_W}\mathbf{G}_{j_W}\right)\mathbf{y}_n + \sum_{j_W=1}^{N_W}\mathbf{g}_{j_W}, \tag{3.1.62}$$

where $\mathbf{F}$ is the deterministic mapping matrix while $\mathbf{G}_{j_W}$, $\mathbf{g}_{j_W}$ are the stochastic mapping matrices and additive noise vectors, respectively, each corresponding to the j_W-th noise source. To investigate the first moment stability, one should investigate the spectral radius of $\mathbf{F}$ as described in Eq. (3.1.10). The second moment stability is investigated with the mapping:

$$\begin{aligned}\overline{\overline{Y}}_{i_1 i_2}(n+1) = &\left(F_{i_1 i_4} F_{i_2 i_3} + \sum_{j_W=1}^{N_W} \langle G_{j_W,i_1 i_4} G_{j_W,i_2 i_3} \rangle \right) \overline{\overline{Y}}_{i_3 i_4}(n) \\ &+ \sum_{j_W=1}^{N_W} \left(\langle G_{j_W,i_1 i_3} g_{j_W,i_2} + G_{j_W,i_2 i_3} g_{j_W,,i_1} \rangle \right) \bar{y}_{i_3}(n) + \sum_{j_W=1}^{N_W} g_{j_W,i_1} g_{j_W,i_2}\end{aligned} \tag{3.1.63}$$

that is the generalised form of Eq. (3.1.16). In this case, however, the semidiscretisation method requires the introduction of different delay resolutions

$$r_{j_\tau} = \left\lfloor \frac{\tau_{j_\tau}}{\Delta t} + \frac{q}{2} \right\rfloor \tag{3.1.64}$$

for each time delay, where q is the order of the Lagrange polynomial (3.1.49). The dimension $(r+1)d$ of the generalised mapping (3.1.62) is determined by $r = \max_{j_\tau} \{r_{j_\tau}\} = r_{N_\tau}$.

3.2 Linear Systems with Periodic Coefficient Matrices and Delays

In the previous section a numerical method was derived, which allows to efficiently investigate the second moment stability of linear SDDEs with constant coefficients. However, in many cases, such as modelling milling processes or linearising a nonlinear SDDE around a periodic solution, these coefficients become periodic. To conduct second moment stability analysis on such systems, the stochastic semidiscretisation method needs to be generalised to periodic systems. First, consider the linear periodic stochastic delay differential equations (SDDE) in the incremental form:

$$\mathrm{d}\mathbf{x}_t = \big(\mathbf{A}(t)\mathbf{x}_t + \mathbf{B}(t)\mathbf{x}_{t-\tau(t)} + \mathbf{c}(t)\big)\,\mathrm{d}t + \big(\boldsymbol{\alpha}(t)\mathbf{x}_t + \boldsymbol{\beta}(t)\mathbf{x}_{t-\tau(t)} + \boldsymbol{\sigma}(t)\big)\,\mathrm{d}W_t, \tag{3.2.1}$$

where $t \mapsto \mathbf{x}_t$ is the $\mathbb{R}^d$-valued state variable. $\mathbf{A}(t)$, $\mathbf{B}(t)$, $\boldsymbol{\alpha}(t)$ and $\boldsymbol{\beta}(t) \in \mathbb{R}^{d\times d}$ are periodic coefficient matrices, while $\mathbf{c}(t)$ and $\boldsymbol{\sigma}(t) \in \mathbb{R}^d$ are periodic vectors and $\tau(t) \in \mathbb{R}$ is a periodic time delay, all with period T.

3.2.1 Zeroth-order Stochastic Semidiscretisation

In order to numerically investigate the stationary solution of the SDDE (3.2.1), the state space of the continuous functions is reduced to a discrete one (see the sketch in Fig. 3.3). First, the SDDE (3.2.1) is approximated by considering the delayed term constant for a sufficiently short period of time Δt:

$$\mathbf{x}_{t-\tau(t)} \approx \mathbf{x}_{t_{n-r(n)}}, \qquad t \in [t_n, t_{n+1}], \tag{3.2.2}$$

where

$$\bar{\tau}(n) = \frac{1}{\Delta t}\int_{t_n}^{t_{n+1}} \tau(t)\mathrm{d}t \quad \text{and} \quad r(n) = \left\lfloor \frac{\bar{\tau}(n)}{\Delta t} \right\rfloor, \tag{3.2.3}$$

and $n = 0, 1, 2, \ldots$ similarly as done in [87]. Similarly to the previous section, the discretised time t_n here denotes the incremented time t with the constant Δt for each n, resulting $t_n = n\Delta t$. However, in this case the time step Δt is chosen to satisfy $T = p\Delta t$, where $p \in \mathbb{N}^+$ is the period resolution. The next step is to consider the time average of the periodic coefficient matrix $\mathbf{A}(t)$ of the original SDDE (3.2.1) for each discretisation interval $t \in [t_n, t_{n+1}]$:

$$\bar{\mathbf{A}}(n) = \frac{1}{\Delta t}\int_{t_n}^{t_{n+1}} \mathbf{A}(t)\mathrm{d}t, \tag{3.2.4}$$

so $\bar{\mathbf{A}}(n)$ (along with $\bar{\tau}(n)$) is constant for each interval $[t_n, t_{n+1}]$. The multiplicative present state in the diffusion term is again approximated, since there exists no explicit analytic solution for the general linear SDE. Moreover, the approximation of the multiplicative diffusion term at the present time is again considered to behave similarly to the expected value of the non-delayed equation, as it is more accurate than a simple constant approximation (as shown in Sec. 3.1.3 [87]). However, opposed to [39] the coefficient $\mathbf{B}(t)$ of the delayed term $\mathbf{x}_{t-\tau(t)}$ is not approximated in the drift term, neither is $\boldsymbol{\beta}(t)$ in the diffusion term. This approach results in the linear SDE

$$\begin{aligned} \mathrm{d}\mathbf{x}_t = &\left(\bar{\mathbf{A}}(n)\mathbf{x}_t + \mathbf{B}(t)\mathbf{x}_{t_{n-r(n)}} + \mathbf{c}(t)\right)\mathrm{d}t + \\ &\left(\boldsymbol{\alpha}(t)e^{\bar{\mathbf{A}}(n)(t-t_n)}\mathbf{x}_{t_n} + \boldsymbol{\beta}(t)\mathbf{x}_{t_{n-r(n)}} + \boldsymbol{\sigma}(t)\right)\mathrm{d}W_t, \quad t \in [t_n, t_{n+1}]\,. \end{aligned} \tag{3.2.5}$$

Again the delay and the noise from the original SDDE (3.2.1) are discretised to behave as an external excitations, dependent only on the states $\mathbf{x}_{t_n}$ and $\mathbf{x}_{t_{n-r(n)}}$ at the beginning of these intervals. This way the solution of the linear SDE (3.2.5) can be written explicitly for the end of each time interval $[t_n, t_{n+1}]$ as:

$$\mathbf{x}_{t_{n+1}} = (\mathbf{P}(n) + \mathbf{Q}_n)\,\mathbf{x}_{t_n} + (\mathbf{R}(n) + \mathbf{S}_n)\,\mathbf{x}_{t_{n-r(n)}} + (\boldsymbol{v}(n) + \boldsymbol{w}_n)\,, \tag{3.2.6}$$

where

$$\mathbf{P}(n) = e^{\bar{\mathbf{A}}(n)\Delta t}\,, \qquad \mathbf{Q}_n = \int_{t_n}^{t_{n+1}} e^{\bar{\mathbf{A}}(n)(t_{n+1}-t)}\boldsymbol{\alpha}(t)e^{\bar{\mathbf{A}}(n)(t-t_n)}\mathrm{d}W_t\,, \tag{3.2.7}$$

$$\mathbf{R}(n) = \int_{t_n}^{t_{n+1}} e^{\bar{\mathbf{A}}(n)(t_{n+1}-t)}\mathbf{B}(t)\mathrm{d}t\,, \quad \mathbf{S}_n = \int_{t_n}^{t_{n+1}} e^{\bar{\mathbf{A}}(n)(t_{n+1}-t)}\boldsymbol{\beta}(t)\mathrm{d}W_t\,, \tag{3.2.8}$$

$$\mathbf{v}(n) = \int_{t_n}^{t_{n+1}} e^{\bar{\mathbf{A}}(n)(t_{n+1}-t)}\mathbf{c}(t)\mathrm{d}t\,, \qquad \mathbf{w}_n = \int_{t_n}^{t_{n+1}} e^{\bar{\mathbf{A}}(n)(t_{n+1}-t)}\boldsymbol{\sigma}(t)\mathrm{d}W_t\,. \tag{3.2.9}$$

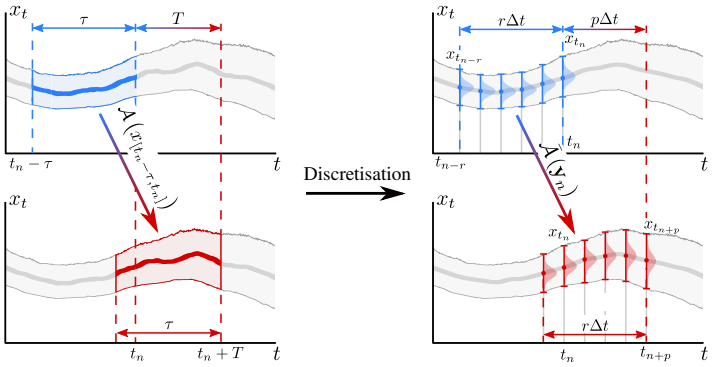

Figure 3.3. *Discretisation of the stochastic process, where $\mathcal{A} : x_{[t_n-\tau,t_n]} \mapsto x_{[t_n+T-\tau,t_n+T]}$ represents the operator which maps the function x_t forward by a principal period T. On the right side $\bar{\mathcal{A}} : \mathbf{y}_n \mapsto \mathbf{y}_{n+p}$ represents the discretised approximation of the operator $\mathcal{A}$, which maps the discretised function x_t stored in the vector $\mathbf{y}$) with the same time period T.*

In order to numerically investigate the stationary solution of the SDDE (3.2.1) the discretised state space vector $\mathbf{y}_n$ at time $t_n = n\Delta t$ is used as introduced in (3.1.7). However this time the mapping has to be applied for multiple time steps to cover a whole time-period (see Fig. 3.3) as it is needed in the Floquet theory to investigate stability [37, 39]. The solution of Eq. (3.2.6) is now written as a stochastic mapping with time dependent coefficients [83, 87]

$$\mathbf{y}_{n+1} = (\mathbf{F}(n) + \mathbf{G}_n)\,\mathbf{y}_n + (\mathbf{f}(n) + \mathbf{g}_n)\,, \tag{3.2.10}$$

where

$$\mathbf{F}(n) = \begin{array}{c} \begin{matrix} 1 & 2 & \cdots & r(n)+1 & \cdots & r & r+1 \end{matrix} \\ \begin{pmatrix} \mathbf{P}(n) & \mathbf{0} & \cdots & \mathbf{R}(n) & \cdots & \mathbf{0} & \mathbf{0} \\ \mathbf{I} & \mathbf{0} & \ldots & \mathbf{0} & \cdots & \mathbf{0} & \mathbf{0} \\ \vdots & \vdots & \ddots & \ddots & \cdots & \ddots & \vdots \\ \mathbf{0} & \mathbf{0} & \cdots & \cdots & \cdots & \mathbf{I} & \mathbf{0} \end{pmatrix} \end{array}, \tag{3.2.11}$$

$$\mathbf{G}_n = \begin{array}{c} \begin{matrix} 1 & 2 & \cdots & r(n)+1 & \cdots & r & r+1 \end{matrix} \\ \begin{pmatrix} \mathbf{Q}_n & \mathbf{0} & \cdots & \mathbf{S}_n & \cdots & \mathbf{0} & \mathbf{0} \\ \mathbf{0} & \mathbf{0} & \ldots & \mathbf{0} & \cdots & \mathbf{0} & \mathbf{0} \\ \vdots & \vdots & \ddots & \ddots & \cdots & \ddots & \vdots \\ \mathbf{0} & \mathbf{0} & \cdots & \cdots & \cdots & \mathbf{0} & \mathbf{0} \end{pmatrix} \end{array}, \tag{3.2.12}$$

while

$$\mathbf{f}(n) = \begin{pmatrix} \mathbf{v}(n)^\top & \mathbf{0}^\top & \ldots & \mathbf{0}^\top \end{pmatrix}^\top, \quad \mathbf{g}_n = \begin{pmatrix} \mathbf{w}_n^\top & \mathbf{0}^\top & \ldots & \mathbf{0}^\top \end{pmatrix}^\top. \tag{3.2.13}$$

Due to the periodic nature of the coefficients in Eq. (3.2.1) the deterministic part of mapping (3.2.10) itself is also periodic with the discrete period p:

$$\mathbf{F}(n) = \mathbf{F}(n+p) \quad \text{and} \quad \mathbf{f}(n) = \mathbf{f}(n+p), \tag{3.2.14}$$

while the stochastic coefficients $\mathbf{G}_n$ and $\mathbf{g}_n$ are periodic in distribution:

$$\mathbf{G}_n \overset{\text{dist}}{=} \mathbf{G}_{n+p} \quad \text{and} \quad \mathbf{g}_n \overset{\text{dist}}{=} \mathbf{g}_{n+p}. \tag{3.2.15}$$

This originates from their periodic statistical properties, since their elements are constructed by stochastic integrals containing the periodic functions $\boldsymbol{\alpha}(t)$, $\boldsymbol{\beta}(t)$ and $\boldsymbol{\sigma}(t)$.

To obtain a stochastic mapping for a whole time period T, a whole mapping period p has to be considered by substituting Eq. (3.2.10) for p steps. This leads to the one-period map

$$\mathbf{y}_{n+p} = \left(\overset{\curvearrowleft}{\prod_{m=0}^{p-1}} \left(\mathbf{F}\left(n+m\right) + \mathbf{G}_{n+m} \right) \right) \mathbf{y}_n + \sum_{m=0}^{p-1} \left(\mathbf{f}_{n+m}^{\text{red}} + \mathbf{g}_{n+m}^{\text{red}} \right), \tag{3.2.16}$$

interpreted as an identity matrix $\mathbf{I}$. The symbol $\curvearrowleft$ is used to emphasise, that the matrices in the products are multiplied from the left as the index increases, e.g.,

$$\overset{\curvearrowleft}{\prod_{i=1}^{3}} A_i = A_3 A_2 A_1. \tag{3.2.17}$$

The reduced additive vectors $\mathbf{f}_{n+m}^{\text{red}}$ and $\mathbf{g}_{n+m}^{\text{red}}$ are defined as

$$\mathbf{f}_{n+m}^{\text{red}} = \left(\overset{\curvearrowleft}{\prod_{m_0=m+1}^{p-1}} \left(\mathbf{F}(n+m_0) + \mathbf{G}_{n+m_0} \right) \right) \mathbf{f}(n+m), \tag{3.2.18}$$

$$\mathbf{g}_{n+m}^{\text{red}} = \left(\overset{\curvearrowleft}{\prod_{m_0=m+1}^{p-1}} \left(\mathbf{F}(n+m_0) + \mathbf{G}_{n+m_0} \right) \right) \mathbf{g}_{n+m}. \tag{3.2.19}$$

Note that the one-period map (3.2.16) has constant deterministic and independent and identically distributed stochastic coefficient matrices and additive vectors, furthermore, $\mathbf{f}_{n+m}^{\text{red}}$ becomes stochastic. In case of $m = p-2$ the products in Eqs. (3.2.18) and (3.2.19) become empty products (since m_0 cannot take values), thus the product results in the indentity matrix $\mathbf{I}$.

There are multiple ways to utilise the stochastic one-period map (3.2.16). Since the elements of the coefficient matrices are defined using stochastic Itô integrals, their joint distribution can be determined, using the fact that they form a multivariate normal distribution with zero mean and computable covariance matrix. Then this joint distribution can be used to generate random matrices for direct simulation of the trajectories or to calculate e.g. the expected value of different quantities determined with the help of these coefficient matrices and vectors. However, in this section they are only used to obtain the maps describing the first and second moment dynamics, then the stability and the fixed points of these mappings are investigated.

3.2.2 First and Second Moment Dynamics of Periodic Stochastic Maps

Since the one-period map (3.2.16) contains the discrete approximate solution of Eq. (3.2.1) it can be utilised for an approximate moment stability investigation. To give a sufficient condition for stochastic stability of linear stochastic differential equations, the first and second moment are studied [5]. Furthermore, the fixed point of the moment mappings are used to approximate the stationary first and second moment of the process defined by (3.2.1), which characterise the region where the solutions are located.

First Moment of the One-period Map

To investigate the behaviour of the first and second moment of the approximating one-period map (3.2.16) the expected value operator $\langle . \rangle$ is used. It is important to emphasise, that $\langle . \rangle$ refers to the ensemble average of a process in contrast with the time average, such as in Eqs. (3.2.4)-(3.2.3). The first moment map over a discrete period p can be obtained for $\bar{\mathbf{y}}(n)$ by taking the expected value of the stochastic one-period map (3.2.16):

$$\bar{\mathbf{y}}(n+p) = \mathbf{F}^{(n,p)}\bar{\mathbf{y}}(n) + \mathbf{f}^{(n,p)}, \tag{3.2.20}$$

where

$$\mathbf{F}^{(n,p)} = \overset{\curvearrowleft}{\prod_{m=0}^{p-1}} \mathbf{F}(n+m), \tag{3.2.21}$$

$$\mathbf{f}^{(n,p)} = \sum_{m_1=0}^{p-1} \left(\overset{\curvearrowleft}{\prod_{m_2=m_1+1}^{p-1}} \mathbf{F}(n+m_2) \right) \mathbf{f}(n+m_1). \tag{3.2.22}$$

Note that the matrix $\mathbf{G}_{n+m}$ and vector $\mathbf{g}_{n+m}$ are not present in Eqs. (3.2.20)-(3.2.22). Since the elements of the matrix $\mathbf{G}_{n+m}$ and vector $\mathbf{g}_{n+m}$ are constructed using stochastic Itô integrals on the interval $[t_{n+m}, t_{n+m+1}]$, they are independent of the values in y_n, which contains the states up to t_n as well as from the Itô integrals on other intervals contained in $\mathbf{G}_{n+m_0}$ and $\mathbf{g}_{n+m_0}$:

$$\langle \mathbf{G}_n \rangle = \mathbf{0}, \ \langle \mathbf{g}_n \rangle = \mathbf{0}, \qquad \text{for all} \quad n, \tag{3.2.23}$$

$$\langle \mathbf{G}_{n+m}\mathbf{y}_n \rangle = \langle \mathbf{G}_{n+m} \rangle \langle \mathbf{y}_n \rangle = \mathbf{0}, \qquad \text{for all} \quad m \geq 0, \tag{3.2.24}$$

$$\langle \mathbf{G}_{n+m}\mathbf{G}_n \rangle = \langle \mathbf{G}_{n+m} \rangle \langle \mathbf{G}_n \rangle = \mathbf{0}, \qquad \text{for all} \quad m \neq 0, \tag{3.2.25}$$

$$\langle \mathbf{G}_{n+m_1}\mathbf{g}_{n+m_2} \rangle = \langle \mathbf{G}_{n+m_1} \rangle \langle \mathbf{g}_{n+m_2} \rangle = \mathbf{0}, \qquad \text{for all} \quad m_1 \neq m_2. \tag{3.2.26}$$

Another approach to obtain the first moment mapping (3.2.20) is to take the expected value of a single mapping step described in Eq. (3.2.10), and then applying the resultant deterministic mapping over a discrete period p. This results in the same mapping as in Eq. (3.2.20) due to the linear nature of both the original stochastic mapping and the underlying SDDE (3.2.1). Note that the mapping matrix $\mathbf{F}^{(n,p)}$ is the approximation of the *monodromy matrix* (or *principal matrix* of *Floquet transition matrix*) $\overline{\mathbf{\Phi}}(t_n, T)$ as in [37,39] for the first moment of SDDE (3.2.1), for which the convergence properties are analyzed [41].

The first moment stability is characterised by the spectral radius (maximum magnitude of the eigenvalues) of the mapping matrix $\mathbf{F}^{(n,p)}$; if $\rho\big(\mathbf{F}^{(n,p)}\big) < 1$ the mapping is first moment stable, if $\rho\big(\mathbf{F}^{(n,p)}\big) > 1$ it is first moment unstable. Furthermore, if the mapping (3.2.20) is stable, the periodic stationary first moment ($\bar{\mathbf{y}}_{\mathrm{st}}(n) = \bar{\mathbf{y}}_{\mathrm{st}}(n+p)$) can be obtained by

$$\bar{\mathbf{y}}_{\mathrm{st}}(n) = \left(\mathbf{I} - \mathbf{F}^{(n,p)}\right)^{-1} \mathbf{f}^{(n,p)}, \tag{3.2.27}$$

which is the discrete approximation of the stationary periodic mean solution, on which the stochastic motion is superimposed. Note that due to linearity, if the stochastic effects in Eq. (3.2.1) (the coefficients of $\mathrm{d}W_t$) are neglected, then the beahviour and stability properties of the obtained deterministic system is identical to the beahviour of the above described first moment.

To study the effects of stochastic perturbations on the stability of the system (3.2.5), the second moment stability has to be considered.

Second Moment of the one-period map

To investigate the behaviour of the second moment the symmetric second moment matrix can be used again, defined by (3.1.13) and (3.1.14). To investigate the second moment matrix evolution, the outer product of both sides of the stochastic mapping (3.2.10) is taken

$$\begin{aligned}\mathbf{y}_{n+1}\mathbf{y}_{n+1}^{\top} = &(\mathbf{F}(n)+\mathbf{G}_n)\mathbf{y}_n\mathbf{y}_n^{\top}(\mathbf{F}(n)+\mathbf{G}_n)^{\top}\\ &+(\mathbf{F}(n)+\mathbf{G}_n)\mathbf{y}_n(\mathbf{f}(n)+\mathbf{g}_n)^{\top}+(\mathbf{f}(n)+\mathbf{g}_n)\mathbf{y}_n^{\top}(\mathbf{F}(n)+\mathbf{G}_n)^{\top}\\ &+(\mathbf{f}(n)+\mathbf{g}_n)(\mathbf{f}(n)+\mathbf{g}_n)^{\top},\end{aligned} \tag{3.2.28}$$

similarly to (3.1.15) Performing the multiplications in (3.2.28) and using the properties of the stochastic integrals [61] generating the elements of $\mathbf{G}_n$ and $\mathbf{g}_n$, the expected value of the squared process mapping can be written, utilizing Einstein's notation along with (3.1.14), in the form [87]

$$\begin{aligned}\overline{\overline{Y}}_{i_1i_2}(n+1) = &\left(F_{i_1i_4}(n)F_{i_2i_3}(n)+\langle G_{n,i_1i_4}G_{n,i_2i_3}\rangle\right)\overline{\overline{Y}}_{i_3i_4}(n)\\ &+\left((F_{i_1i_3}(n)f_{i_2}(n)+F_{i_2i_3}(n)f_{i_1}(n))+\langle G_{n,i_1i_3}g_{n,i_2}+G_{n,i_2i_3}g_{n,i_1}\rangle\right)\bar{y}_{i_3}(n)\\ &+\left(f_{i_1}(n)f_{i_2}(n)+\langle g_{n,i_1}g_{n,i_2}\rangle\right).\end{aligned} \tag{3.2.29}$$

The expected values in (3.2.29) can be computed using the Itô isometry [61, 87] as discussed in Sec. 3.1.2. Similarly to (3.1.18), instead of the matrix-to-matrix mapping representation of the second moment mapping (3.2.29), the more convenient vector-to-vector mapping is used, utilizing the efficient vector-representation of the independent elements of the second moment matrix defined in (3.1.17). Using the vector notation, the second moment mapping (3.2.29) can be written as

$$\bar{\bar{\mathbf{y}}}(n+1) = \mathbf{H}(n)\bar{\bar{\mathbf{y}}}(n) + \mathbf{h}(n)\bar{\mathbf{y}}(n) + \left(\bar{\bar{\mathbf{f}}}(n) + \bar{\bar{\mathbf{g}}}(n)\right), \tag{3.2.30}$$

where the coefficient matrices $\mathbf{H}(n)$, $\mathbf{h}(n)$ and vectors $\bar{\bar{\mathbf{f}}}(n)$ and $\bar{\bar{\mathbf{g}}}(n)$ are calculated using the rules defined by Eq. (3.2.29), similarly as for (3.1.18) in the case of constant coefficients. Due

to the independence of the discrete time intervals, the periodic second moment mapping can be derived from Eq. (3.2.30) as

$$\bar{\bar{\mathbf{y}}}(n+p) = \mathbf{H}^{(n,p)}\bar{\bar{\mathbf{y}}}(n) + \overline{\mathbf{h}\bar{\mathbf{y}}}^{(n,p)} + \overline{\bar{\mathbf{f}}\bar{\mathbf{g}}}^{(n,p)}, \tag{3.2.31}$$

where

$$\mathbf{H}^{(n,p)} = \prod_{m=0}^{\overset{\curvearrowleft}{p-1}} \mathbf{H}(n+m), \tag{3.2.32}$$

$$\overline{\mathbf{h}\bar{\mathbf{y}}}^{(n,p)} = \sum_{m_1=0}^{p-1} \left(\prod_{m_2=m_1+1}^{\overset{\curvearrowleft}{p-1}} \mathbf{H}(n+m_2) \right) \mathbf{h}(n+m_1)\bar{\mathbf{y}}(n+m_1), \tag{3.2.33}$$

$$\overline{\bar{\mathbf{f}}\bar{\mathbf{g}}}^{(n,p)} = \sum_{m_1=0}^{p-1} \left(\prod_{m_2=m_1+1}^{\overset{\curvearrowleft}{p-1}} \mathbf{H}(n+m_2) \right) \left(\bar{\bar{\mathbf{f}}}(n+m_1) + \bar{\bar{\mathbf{g}}}(n+m_1) \right). \tag{3.2.34}$$

Similarly to the first moment mapping, the matrix $\mathbf{H}^{(n,p)}$ behaves as a monodromy matrix $\bar{\bar{\mathbf{\Phi}}}(t_n, T)$ for the second moment process, therefore, the stability of the second moment process can be investigated using the spectral radius $\rho(\mathbf{H}^{(n,p)})$: if $\rho(\mathbf{H}^{(n,p)}) > 1$ then the mapping is unstable, if $\rho(\mathbf{H}^{(n,p)}) < 1$ then it is stable and and has a bounded stationary solution. This periodic stationary second moment vector $\left(\bar{\bar{\mathbf{y}}}_{\text{st}}(n) = \bar{\bar{\mathbf{y}}}_{\text{st}}(n+p)\right)$ can be determined as

$$\bar{\bar{\mathbf{y}}}_{\text{st}}(n) = \left(\mathbf{I} - \mathbf{H}^{(n,p)} \right)^{-1} \left(\overline{\mathbf{h}\bar{\mathbf{y}}}_{\text{st}}^{(n,p)} + \overline{\bar{\mathbf{f}}\bar{\mathbf{g}}}^{(n,p)} \right), \tag{3.2.35}$$

where

$$\overline{\mathbf{h}\bar{\mathbf{y}}}_{\text{st}}^{(n,p)} = \sum_{m_1=0}^{p-1} \left(\prod_{m_2=m_1+1}^{\overset{\curvearrowleft}{p-1}} \mathbf{H}(n+m_2) \right) \mathbf{h}(n+m_1)\bar{\mathbf{y}}_{\text{st}}(n+m_1). \tag{3.2.36}$$

Note that the first moment process $\bar{\mathbf{y}}(n)$ has to be stable $\left(\rho(\mathbf{F}^{(n,p)}) < 1\right)$, in order to have a bounded stationary first moment $\bar{\mathbf{y}}_{\text{st}}(n)$, which is necessary for the existence of a stationary second moment $\bar{\bar{\mathbf{y}}}_{\text{st}}(n)$. However, the condition $\rho(\mathbf{H}^{(n,p)}) < 1$ for the stability of the second moment process $\bar{\bar{\mathbf{y}}}(n)$ already implies that the first moment is stable and $\rho(\mathbf{F}^{(n,p)}) < 1$ is satisfied. In case of a sufficently small Δt (leading to a sufficiently large period resolution p and delay resolution r), the stability of the first two moments of the discretised form of Eq. (3.2.1) provides enough information to decide if it has a stationary solution, and the continuous process $\mathbf{x}_t$ stays in a bounded region of the stationary mean approximated by $\bar{\mathbf{y}}_{\text{st}}(n)$. Note that for determining stochastic stability the investigation of higher-order moment stability is not necessary, since it does not provide any additional information despite of the complexity of its calculation.

Note that when creating the approximating SDE such as (3.2.5), instead of using only a constant $\mathbf{x}_{t_{n-r(n)}}$, the Lagrange-polynomials can be utilised [39, 87] (as described in 3.2.3) to approximate the delayed state more accurately. This leads to a potentially higher-order convergence for the spectral radii of the moment mapping matrices $\mathbf{F}^{(n,p)}$, $\mathbf{H}^{(n,p)}$ and the stationary first and second moments $\bar{\mathbf{y}}_{\text{st}}(n)$, $\bar{\bar{\mathbf{y}}}_{\text{st}}(n)$. The use of semidiscretisation method with higher-order polynomials results in the same mapping as in (3.2.10), only the elements of the mapping matrices $\mathbf{F}(n)$, $\mathbf{G}_n$ are changed. This approach leads to the same stochastic and moment mappings as described in Eqs. (3.2.10)-(3.2.36). The details of the generation of the individual mapping matrices and their convergence properties are described in Sec. 3.1 and in [87].

3.2.3 Higher-order Semidiscretisation

To improve the accuracy and convergence of the approximation of the stochastic mapping (3.2.10), q-th order Lagrange polynomials are utilised [39, 87]. The term higher-order again refers to the order of the Lagrange polynomial used to approximate the delayed terms. This leads to additional terms in both the deterministic and the stochastic mapping matrices. Here, the time dependent delay resolution r is corrected with the order q of the Lagrange polynomial as

$$r(n) = \left\lfloor \frac{\bar{\tau}(n)}{\Delta t} + \frac{q}{2} \right\rfloor, \qquad r = \max_{n\in\{0,1,\dots,p-1\}} r(n). \tag{3.2.37}$$

In this case, the Lagrange polynomial is used to approximate the delay terms, and has the following form:

$$\mathbf{L}_t^{(q)} = \sum_{j_1=0}^{q} L^{(q,j_1)}(t)\mathbf{x}_{t-(n-r(n)+j_1)\Delta t}\,, \tag{3.2.38}$$

and

$$L^{(q,j_1)}(t) = \left(\prod_{j_2=0, j_2\neq j_1}^{q} \frac{t-\bar{\tau}(n)-(n+j_2-r(n))\Delta t}{(j_1-j_2)\,\Delta t} \right) \quad \text{where} \quad t\in[t_n, t_{n+1})\,. \tag{3.2.39}$$

Using this, the approximation of Eq. (3.2.1) leads to

$$\begin{aligned} \mathrm{d}\mathbf{x}_t = &\left(\bar{\mathbf{A}}(n)\mathbf{x}_t + \mathbf{B}(t)\,\mathbf{L}_t^{(q)} + \mathbf{c}(t)\right)\mathrm{d}t \\ &+ \left(\boldsymbol{\alpha}(t)e^{\bar{\mathbf{A}}(n)t}\mathbf{x}_{t_n} + \boldsymbol{\beta}(t)\,\mathbf{L}_t^{(q)} + \boldsymbol{\sigma}(t)\right)\mathrm{d}W_t, \\ &\qquad\qquad \text{where} \quad t\in[t_n, t_{n+1})\,, \end{aligned} \tag{3.2.40}$$

with the discretised form

$$\begin{aligned} \mathbf{x}_{t_{n+1}} = &\left(\mathbf{P}(n)+\mathbf{Q}(n)\right)\mathbf{x}_{t_n} + \mathbf{v}(n) \\ &+ \sum_{k=0}^{q}\left(\mathbf{R}_k(n)+\mathbf{S}_k(n)\right)\mathbf{x}_{t_{n-r(n)+k}} + \mathbf{w}(n)\,. \end{aligned} \tag{3.2.41}$$

The discretised mapping matrices $\mathbf{F}(n)$ and $\mathbf{G}_n$ will have the structure

$$\mathbf{F}(n) = \begin{array}{c} \begin{matrix} 1 & 2 & \cdots & r(n)+q+1 & \cdots & r(n)+1 & \cdots & r & r+1 \end{matrix} \\ \begin{pmatrix} \mathbf{P}(n) & \mathbf{0} & \cdots & \mathbf{R}_q(n) & \cdots & \mathbf{R}_0(n) & \cdots & \mathbf{0} & \mathbf{0} \\ \mathbf{I} & \mathbf{0} & \cdots & \cdots & \cdots & \mathbf{0} & \cdots & \mathbf{0} & \mathbf{0} \\ \vdots & \vdots & \ddots & \ddots & \ddots & \ddots & \cdots & \vdots & \vdots \\ \mathbf{0} & \mathbf{0} & \cdots & \cdots & \cdots & \cdots & \cdots & \mathbf{I} & \mathbf{0} \end{pmatrix} \end{array}, \tag{3.2.42}$$

$$\mathbf{G}_n = \begin{array}{c} \begin{matrix} 1 & 2 & \cdots & r(n)+q+1 & \cdots & r(n)+1 & \cdots & r & r+1 \end{matrix} \\ \begin{pmatrix} \mathbf{Q}_n & \mathbf{0} & \cdots & \mathbf{S}_{q,n} & \cdots & \mathbf{S}_{0,nj,n} & \cdots & \mathbf{0} & \mathbf{0} \\ \mathbf{0} & \mathbf{0} & \cdots & \cdots & \cdots & \mathbf{0} & \cdots & \mathbf{0} & \mathbf{0} \\ \vdots & \vdots & \ddots & \ddots & \ddots & \ddots & \cdots & \vdots & \vdots \\ \mathbf{0} & \mathbf{0} & \cdots & \cdots & \cdots & \cdots & \cdots & \mathbf{0} & \mathbf{0} \end{pmatrix} \end{array}, \tag{3.2.43}$$

where

$$\mathbf{R}_{j,n} = \int_{t_n}^{t_{n+1}} e^{\bar{\mathbf{A}}(n)(t_{n+1}-t)} L_t^{(q,j)}\mathbf{B}(t)\mathrm{d}t, \qquad j=0,1,\dots,q, \tag{3.2.44}$$

$$\mathbf{S}_{j,n} = \int_{t_n}^{t_{n+1}} e^{\bar{\mathbf{A}}(n)(t_{n+1}-t)} L_t^{(q,j)}\boldsymbol{\beta}(t)\mathrm{d}W_t\,, \qquad j=0,1,\dots,q. \tag{3.2.45}$$

3.2.4 Generalisation for Multiple Delays and Independent Noise Sources

To apply the semidiscretisation method for multiple delays and independent white-noise sources one has to use the form:

$$\begin{aligned} \mathrm{d}\mathbf{x}_t = &\left(\mathbf{A}(t)\mathbf{x}_t + \sum_{j_\tau=1}^{N_\tau} \mathbf{B}_{j_\tau}(t)\mathbf{x}_{t-\tau_{j_\tau}(t)} + \mathbf{c}(t) \right) \mathrm{d}t \\ &+ \sum_{j_W=1}^{N_W} \left(\boldsymbol{\alpha}_{j_W}(t)\mathbf{x}_t + \sum_{j_\tau=1}^{N_\tau} \boldsymbol{\beta}_{j_\tau,j_W}(t)\mathbf{x}_{t-\tau_{j_\tau}} + \boldsymbol{\sigma}_{j_W}(t) \right) dW_{j_W,t}, \end{aligned} \tag{3.2.46}$$

where τ_{j_τ}, $j_\tau = 1,\dots,N_\tau$ are the time delays, $N_\tau \in \mathbb{N}^+$ is the number of time delays. Furthermore, $j_W \in \mathbb{N}^+$ is the number of noise sources and $W_{j_W,t}$, $j_W = 1,\dots,N_W$ are the Wiener processes to model the Gaussian white noises, that is, $\mathbb{E}\left(\mathrm{d}W_{i_W,t_1}\mathrm{d}W_{j_W,t_2}\right) = \mathrm{d}t\,\delta_{i_W j_W}\mathbb{1}(t_1 = t_2)$ with $\delta_{i_W j_W}$ standing for the Kronecker symbol. The system in Eq. (3.2.46) can be transformed into the following mapping:

$$\mathbf{y}_{n+1} = \left(\mathbf{F}(n) + \sum_{j_W=1}^{N_W} \mathbf{G}_{j_W,n} \right) \mathbf{y}_n + \left(\mathbf{f}(n) + \sum_{j_W=1}^{N_W} \mathbf{g}_{j_W,n} \right), \tag{3.2.47}$$

where $\mathbf{F}(n)$, $\mathbf{f}(n)$is the deterministic mapping matrix and additive vector while $\mathbf{G}_{j_W,n}$, $\mathbf{g}_{j_W,n}$ are the stochastic mapping matrices and additive noise vectors, respectively, each corresponding to the j_W-th noise source. To investigate the first moment stability, one should investigate the spectral radius of $\mathbf{F}^{n\dots p}$ as described in Eq. (3.2.20). The second moment stability is investigated with the mapping:

$$\begin{aligned} \overline{\overline{Y}}_{i_1 i_2}(n+1) = &\left(F_{i_1 i_4}(n)F_{i_2 i_3}(n) + \sum_{j_W=1}^{N_W} \langle G_{j_W,n,i_1 i_4} G_{j_W,n,i_2 i_3} \rangle \right) \overline{\overline{Y}}_{i_3 i_4}(n) \\ &+ \left(F_{i_1 i_3}(n)f_{i_2}(n) + F_{i_2 i_3}(n)f_{i_1}(n) \right) \bar{y}_{i_3}(n) \\ &+ \sum_{j_W=1}^{N_W} \langle G_{j_W,n,i_1 i_3} g_{j_W,n,i_2} + G_{j_W,n,i_2 i_3} g_{j_W,n,i_1} \rangle \, \bar{y}_{i_3}(n) \\ &+ \left(f_{i_1}(n)f_{i_2}(n) + \sum_{j_W=1}^{N_W} \langle g_{j_W,n,i_1} g_{j_W,n,i_2} \rangle \right). \end{aligned} \tag{3.2.48}$$

that is the generalised form of Eq. (3.2.29). In this case, however, the semidiscretisation method requires the introduction of different delay resolutions for each time delay given by

$$r_{j_\tau}(n) = \left\lfloor \frac{\bar{\tau}_{j_\tau}(n)}{\Delta t} + \frac{q}{2} \right\rfloor, \tag{3.2.49}$$

where q is the order of the Lagrange polynomial (3.2.38). The dimension $(r+1)d$ of the generalised mapping (3.2.47) is determined by

$$r = \max_{n\in\{0,1,\dots,p-1\}} \left(\max_{j_\tau} \{ r_{j_\tau}(n) \} \right). \tag{3.2.50}$$

3.3 Linear Systems with Stochastic Delays and Additive Noise

In the previous sections such SDDEs were explored, where the stochasticity was in the coefficients of the state variables, however the delay was considered deterministic. However there are systems,

where the delay can vary stochastically, e.g., wirelessly connected control systems, where information packet losses can occur. Therefore, in this section linear systems with stochastic delay and additive noise are considered in the special form :

$$\mathrm{d}\mathbf{x}_t = \big(\mathbf{A}\mathbf{x}_t + \mathbf{B}\mathbf{x}_{t-\tau_0} + \mathbf{B}_\mathrm{s}\mathbf{x}_{t-\tau_{\mathrm{s},t}} + (\bar{\tau}_\mathrm{s} - \tau_{\mathrm{s},t})\,\boldsymbol{\sigma}_\tau\big)\mathrm{d}t + \boldsymbol{\sigma}\mathrm{d}W_t, \tag{3.3.1}$$

where t is the time, $\mathbf{x}$ is the $\mathbb{R}^d$-valued state vector, τ_0 and $\tau_{\mathrm{s},t}$ represent the constant and the stochastically varying delays, respectively, $\mathbf{A}, \mathbf{B}, \mathbf{B}_\mathrm{s} \in \mathbb{R}^{d\times d}$ are the coefficient matrices and $\boldsymbol{\sigma}$, $\boldsymbol{\sigma}_\tau \in \mathbb{R}^d$ are the intensity vectors of the Wiener process and delay induced noise processes, respectively. The Wiener process models the usual Gaussian white noise excitation, while the delay induced noise process is significant when analysing systems, that model e.g., traffic dynamics [92] as shown later in Sec. 5.4.

The delay process $\tau_{\mathrm{s},t}$ is considered to have piecewise constant trajectories. In particular, the delay is assumed to stay constant for a holding time T_τ before potentially taking on a new value from a finite set $\{\tau_1, \tau_2, \ldots, \tau_{J_\tau}\}$, such that $\tau_1 < \tau_2 < \ldots < \tau_{J_\tau}$; see Fig. 3.4 for a sample realization of this process.

Note that this sorting constraint is not valid for τ_0. The delays are assumed to be independent

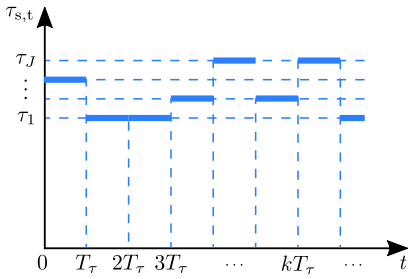

Figure 3.4. *A sample realization of the delay process $\tau_{\mathrm{s},t}$.*

and identically distributed (IID) across the holding intervals. The probabilities of the delays can be described as

$$\mathbb{P}(\tau_{\mathrm{s},t} = \tau_{j_\tau}) = w_{j_\tau}, \quad \tau_{j_\tau} \in \{\tau_1, \tau_2, \ldots, \tau_{J_\tau}\}, \tag{3.3.2}$$

while remaining constant for each interval $t \in (kT_\tau, (k+1)T_\tau]$. Note that the delay induced noise $(\bar{\tau}_\mathrm{s} - \tau_{\mathrm{s},t})\,\boldsymbol{\sigma}_\tau)$ is normalised to have zero mean with the help of the ensemble average of the delay process, namely

$$\bar{\tau}_\mathrm{s} = \langle \tau_{\mathrm{s},t} \rangle = \sum_{j_\tau=1}^{J_\tau} w_{j_\tau}\tau_{j_\tau}. \tag{3.3.3}$$

3.3.1 Zeroth-Order Semidiscretisation

In order to numerically investigate the stability and stationary solution of the delayed system in Eq. (3.3.1), the continuous time dynamics can be approximated by a discrete one. System (3.3.1) is discretised using zeroth-order semidiscretisation [39, 73], however it can be done by utilising higher-order semidiscretisation similarly as shown in Subsec. 3.1.4.

The approximating SDE of Equation (3.3.1) can be written as:

$$\mathrm{d}\mathbf{x}_t \approx \Big(\mathbf{A}\mathbf{x}_t + \mathbf{B}\mathbf{x}_{t_{n-r_0}} + \mathbf{B}_\mathrm{s}\mathbf{x}_{t_{n-r_{\mathrm{s},n}}} + (\bar{\tau}_\mathrm{s} - \tau_{\mathrm{s},t})\,\boldsymbol{\sigma}_\tau\Big)\mathrm{d}t + \boldsymbol{\sigma}\mathrm{d}W_t, \qquad t \in [t_n, t_{n+1}) \tag{3.3.4}$$

where $n \in \mathbb{N}$ counts the time step up to $t_n = n\Delta t$ under the time resolution $\Delta t = T_\tau/\ell$; see Fig. 3.5.

Note that is ℓ is chosen such that $\Delta t < \tau_{j_\tau}$, $j_\tau = 1, \ldots, J_\tau$. The discretised delay is given by

$$r_0 = \left\lfloor \frac{\tau_0}{\Delta t} \right\rfloor \quad \text{and} \quad r_{\mathrm{s},n} = \left\lfloor \frac{\tau_{\mathrm{s},n\Delta t}}{\Delta t} \right\rfloor, \tag{3.3.5}$$

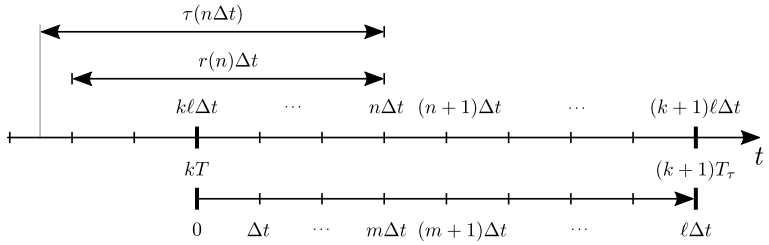

Figure 3.5. *Sketch of the time discretisation used for the construction of the stochastic map. The discrete time $n \in \mathbb{N}$ denotes the n-th time step taken with Δt, $k \in \mathbb{N}$ denotes the k-th holding interval, while $m = 0, 1, \ldots, m$ denotes the time step m taken with Δt relative to the beginning of each holding interval.*

while $r_{\mathrm{s},n}$ follows a similar stochastic process as $\tau_{\mathrm{s},n\Delta t}$, that is,

$$\mathbb{P}\left(r_{\mathrm{s},n} = r_{j_\tau}\right) = \mathbb{P}(\tau_{\mathrm{s},t_n} = \tau_{j_\tau}) = w_{j_\tau}, \tag{3.3.6}$$

where $r_{j_\tau} = \left\lfloor \frac{\tau_{j_\tau}}{\Delta t} \right\rfloor$, $j_\tau = 1, \ldots, J_\tau$; cf. (3.3.2). The differential equation (3.3.4) can be solved analytically for one period of length Δt:

$$\mathbf{x}_{t_{n+1}} = \mathbf{P}\mathbf{x}_{t_n} + \mathbf{R}\mathbf{x}_{t_n-\tau_0} + \mathbf{R}_{\mathrm{s}}\mathbf{x}_{t_n-\tau_{\mathrm{s},t_n}} + \mathbf{w}_{\tau,n} + \mathbf{w}, \tag{3.3.7}$$

where $\mathbf{P}$, $\mathbf{R}$ and $\mathbf{w}$ are computed according to Eqs. (3.1.4) and (3.1.6), respectively. The coefficient matrix $\mathbf{R}_{\mathrm{s}}$ of the stochastically delayed term $\mathbf{x}_{t-\tau_{s,t_n}}$ and the additive disturbance vector $\mathbf{w}_{\tau,n}$ originating from the delay induced excitation can be calculated as

$$\mathbf{R}_{\mathrm{s}} = \int_{t_n}^{t_{n+1}} \mathrm{e}^{\mathbf{A}(t_n-t)}\mathbf{B}_{\mathrm{s}}\mathrm{d}t = \mathbf{A}^{-1}\left(\mathbf{P}-\mathbf{I}\right)\mathbf{B}_{\mathrm{s}}, \tag{3.3.8}$$

$$\mathbf{w}_{\tau,n} = \int_{t_n}^{t_{n+1}} \mathrm{e}^{\mathbf{A}(t_n-t)}(\bar{\tau}_{\mathrm{s}} - \tau_{\mathrm{s},t})\,\boldsymbol{\sigma}_\tau \mathrm{d}t = \mathbf{A}^{-1}\left(\mathbf{P}-\mathbf{I}\right)\boldsymbol{\sigma}_\tau(\bar{\tau}_{\mathrm{s}} - \tau_{\mathrm{s},n}), \tag{3.3.9}$$

since $\tau_{\mathrm{s},n}$ stays constant on the Δt long interval $[t_n, t_{n+1})$. By utilizing the augmented vector $\mathbf{y}_n$ defined in (3.1.7), the system (3.3.7) can be written in the compact form

$$\mathbf{y}_n = (\mathbf{F} + \mathbf{F}_{\mathrm{s},n})\mathbf{y}_n + (\mathbf{g}_{\tau,n} + \mathbf{g}), \tag{3.3.10}$$

where $\mathbf{F}$ and $\mathbf{g}$ are given by (3.1.9), while

$$\mathbf{F}_{\mathrm{s},n} = \begin{array}{c} \begin{array}{ccccccc} 1 & 2 & \cdots & r_{\mathrm{s},n}{+}1 & \cdots & r & r{+}1 \end{array} \\ \begin{pmatrix} \mathbf{0} & \mathbf{0} & \cdots & \mathbf{R}_{\mathrm{s},n} & \cdots & \mathbf{0} & \mathbf{0} \\ \mathbf{0} & \mathbf{0} & \cdots & \mathbf{0} & \cdots & \mathbf{0} & \mathbf{0} \\ \vdots & \vdots & \cdots & \ddots & \cdots & \ddots & \vdots \\ \mathbf{0} & \mathbf{0} & \cdots & \cdots & \cdots & \mathbf{0} & \mathbf{0} \end{pmatrix} \end{array}, \qquad \mathbf{g}_{\tau,n} = \begin{pmatrix} \mathbf{w}_{\tau,n} \\ \mathbf{0} \\ \vdots \\ \mathbf{0} \end{pmatrix}. \tag{3.3.11}$$

where the size r is defined as

$$r = \max\left\{r_{J_\tau}, r_0\right\}. \tag{3.3.12}$$

Note that the in (3.3.11) the block matrix $\mathbf{R}_{\mathrm{s},n}$ is in the $(r_{\mathrm{s},n}+1)^{\mathrm{th}}$ block-column of matrix $\mathbf{F}_{\mathrm{s},n}$. In other words, the position of the block matrix $\mathbf{R}_{\mathrm{s},n}$ in the first block-row of $\mathbf{F}_{\mathrm{s},n}$ depends on the instantaneous value of the delay, that is, $\tau_{\mathrm{s},n} = \tau_{j_\tau}$ in the time interval $(kT, (k+1)T_\tau]$, then $r_{\mathrm{s},n} = r_{j_\tau}$. In this case, $\mathbf{F}_{\mathrm{s},n}$ can be substituted by $\mathbf{F}_{j_\tau}$, namely

$$\mathbf{F}_{j_\tau} = \langle \mathbf{F}_{\mathrm{s},n} | \tau_{\mathrm{s},t_n} = \tau_{j_\tau} \rangle \tag{3.3.13}$$

and, based on (3.3.6), $\mathbf{F}_{\mathrm{s},n}$ is IID and follows the probability distribution

$$\mathbb{P}\left(\mathbf{F}_{\mathrm{s},n} = \mathbf{F}_{j_\tau}\right) = \mathbb{P}(\tau_{\mathrm{s},t_n} = \tau_j) = w_{j_\tau}\,. \tag{3.3.14}$$

Note that the delay value $\tau_{\mathrm{s},n}$ does not change during one holding period $T_\tau = \ell\Delta t$; see Fig. 3.4. Therefore, defining the state vector

$$\mathbf{z}_k = \mathbf{y}_{k\ell}\,, \qquad k = 0, 1, 2, \ldots \tag{3.3.15}$$

for each holding period and applying (3.3.10) iteratively, the system dynamics can be written as

$$\mathbf{z}_{k+1} = \mathbf{K}_k\mathbf{z}_k + \mathbf{l}_k \tag{3.3.16}$$

where

$$\mathbf{K}_k = \left(\mathbf{F} + \mathbf{F}_{\mathrm{s},k\ell}\right)^\ell, \tag{3.3.17}$$

$$\mathbf{l}_k = (\mathbf{l}_{W,k} + \mathbf{l}_{\tau,k}), \tag{3.3.18}$$

$$\mathbf{l}_{W,k} = \sum_{m=0}^{\ell-1} \left(\mathbf{F} + \mathbf{F}_{\mathrm{s},k\ell}\right)^{\ell-1-m}\mathbf{g}, \tag{3.3.19}$$

$$\mathbf{l}_{\tau,k} = \sum_{m=0}^{\ell-1} \left(\mathbf{F} + \mathbf{F}_{\mathrm{s},k\ell}\right)^{\ell-1-m}\mathbf{g}_{\tau,k\ell+m} = \hat{\mathbf{F}}_k\mathbf{g}_{\tau,k\ell}\,. \tag{3.3.20}$$

where

$$\hat{\mathbf{F}}_k := \sum_{m=0}^{\ell-1} \left(\mathbf{F} + \mathbf{F}_{\mathrm{s},k\ell}\right)^{\ell-1-m}. \tag{3.3.21}$$

To calculate the mapping matrix $\mathbf{K}_k$ and additive vectors $\mathbf{l}_{\tau,k}$ and $\mathbf{l}_{W,k}$ one needs the only the value of $\mathbf{F}_{\mathrm{s},k\ell}$ and $\mathbf{g}_{\tau,k\ell}$ at the beginning at each holding interval, namely

$$\mathbf{F}_{\mathrm{s},k\ell+m} = \mathbf{F}_{\mathrm{s},k\ell}, \quad \mathbf{g}_{\tau,k\ell+m} = \mathbf{g}_{\tau,k\ell}, \qquad m \in [0, \ell)\,, \tag{3.3.22}$$

and from this it follows, that

$$\mathbb{P}\left(\mathbf{K}_k = \left(\mathbf{F} + \mathbf{F}_{j_\tau}\right)^\ell\right) = \mathbb{P}\left(\mathbf{F}_{\mathrm{s},n} = \mathbf{F}_{j_\tau}\right) = \mathbb{P}(\tau_{\mathrm{s},t} = \tau_{j_\tau}) = w_{j_\tau}. \tag{3.3.23}$$

It is important to Note that even if it is not denoted in (3.3.19), the additive vector $\mathbf{g}$ originating from the Wiener process is different for every $m = 0, 1, 2, \ldots, \ell - 1$, as emphasised when $\mathbf{g}$ is defined in Eq. (3.1.9), thus the same simplification for $\mathbf{l}_{W,k}$ cannot be used as for $\mathbf{l}_{\tau,k}$). However, this is not true for $\mathbf{g}_{\tau,k\ell+m}$, since the vector $\mathbf{w}_{\tau,n}$ generatiting $\mathbf{g}_{\tau,k\ell+m}$ has time dependent probability, which depends on the current value of k, namely

$$\mathbb{P}\left(\mathbf{w}_{\tau,n} = \mathbf{A}^{-1}\left(\mathbf{P} - \mathbf{I}\right)\boldsymbol{\sigma}_\tau(\bar{\tau}_{\mathrm{s}} - \tau_i) \,|\, \tau_{\mathrm{s},t_{k\ell}} = \tau_j, n \in [k\ell, (k+1)\ell)\right) = \delta_{ij}, \tag{3.3.24}$$

where $\delta_{ij} = \mathbb{1}(i = j)$ is the Kronecker delta.

3.3.2 First and Second Moment Dynamics over a Holding Period

First Moment of the Mapping over a Holding Period

When considering the mean dynamics of (3.3.16) it reduces to

$$\bar{\mathbf{z}}(k+1) = \overline{\mathbf{K}}\bar{\mathbf{z}}(k) + \bar{\mathbf{l}}_\tau, \tag{3.3.25}$$

where $\bar{\mathbf{z}}(k) := \langle \mathbf{z}_k \rangle$, $\overline{\mathbf{K}} := \langle \mathbf{K} \rangle$ and $\bar{\mathbf{l}}_\tau := \langle \mathbf{l}_k \rangle = \langle \mathbf{l}_{W,k} + \mathbf{l}_{\tau,k} \rangle = \langle \mathbf{l}_\tau \rangle$. Since $\mathbf{l}_{W,k}$ is generated by stochastic Itô integrals its expectation value is zero. However, the computation of these expectation values differ from the case, when the stochasticity in the coefficient matrices and the additive vectors were originating from a Wiener process. The value of the coefficient matrix $\mathbf{K}_k$ only depends on the delay $\tau_{\mathrm{s},t}$ in the interval $(kT_\tau, (k+1)T_\tau]$ while $\mathbf{l}_k$, depends both on the delay in the interval $(kT_\tau, (k+1)T_\tau]$ and the Wiener process W_t. The process $\tau_{\mathrm{s},t}$ takes values at beginning at each holding interval at time $t = kT_\tau$ independent of the previous holding interval, thus $\mathbf{K}_k$ is independent of $\mathbf{z}_k$ and their expectation can be calculated separately, leading to

$$\overline{\mathbf{K}} = \langle \mathbf{K}_k \rangle = \sum_{j_\tau=1}^{J_\tau} \mathbb{P}(\tau_{\mathrm{s},t} = \tau_{j_\tau}) \, \langle \mathbf{K}_k | \tau_{\mathrm{s},t_{k\ell}} = \tau_{j_\tau} \rangle = \sum_{j=1}^{J_\tau} w_{j_\tau} (\mathbf{F} + \mathbf{F}_{j_\tau})^\ell. \tag{3.3.26}$$

The mean of the additive term $\mathbf{l}_{\tau,k}$ can be calculated as

$$\begin{aligned} \bar{\mathbf{l}}_\tau &= \left\langle \sum_{m=0}^{\ell-1} (\mathbf{F} + \mathbf{F}_{\mathrm{s},k\ell})^{\ell-1-m} \mathbf{g}_{\tau,k\ell+m} \right\rangle \\ &= \sum_{j_\tau=1}^{J_\tau} w_{j_\tau} \left(\sum_{m=0}^{\ell-1} (\mathbf{F} + \mathbf{F}_{j_\tau})^{\ell-1-m} \right) \langle \mathbf{g}_{\tau,k\ell} | \tau_{\mathrm{s},t_{k\ell}} = \tau_{j_\tau} \rangle \,, \end{aligned} \tag{3.3.27}$$

where

$$\langle \mathbf{g}_{\tau,k\ell} | \tau_{\mathrm{s},t_{k\ell}} = \tau_{j_\tau} \rangle = \begin{pmatrix} \mathbf{A}^{-1} \left(\mathbf{P} - \mathbf{I} \right) \boldsymbol{\sigma}_\tau (\bar{\tau}_\mathrm{s} - \tau_{j_\tau}) \\ \mathbf{0} \\ \vdots \\ \mathbf{0} \end{pmatrix}. \tag{3.3.28}$$

Since $\mathbf{g}$ is independent of the coefficient matrices $\mathbf{F}$ and $\mathbf{F}_{\mathrm{s},k\ell}$ and has zero mean, namely $\langle \mathbf{g} \rangle = \mathbf{0}$, it does not affect the mean dynamics. From Eq. (3.3.25) it can be concluded, that the mean $\bar{\mathbf{z}}_k$ converges to

$$\bar{\mathbf{z}}_\mathrm{st} = \left(\mathbf{I} - \overline{\mathbf{K}} \right)^{-1} \bar{\mathbf{l}}_\tau \tag{3.3.29}$$

as $k \to \infty$, if and only if the process (3.3.1) is first moment stable, namely

$$\rho\left(\overline{\mathbf{K}}\right) < 1. \tag{3.3.30}$$

Second Moment of the Mapping over a Holding Period

To derive the second moment evolution, the dynamics of the squared process is investigated, namely

$$\begin{aligned} \mathbf{z}_{k+1} \mathbf{z}_{k+1}^\top = \mathbf{K}_k \mathbf{z}_k \mathbf{z}_k^\top \mathbf{K}_k^\top + \mathbf{K}_k \mathbf{z}_k (\mathbf{l}_{\tau,k} + \mathbf{l}_{W,k})^\top + \\ (\mathbf{l}_{\tau,k} + \mathbf{l}_{W,k}) \mathbf{z}_k^\top \mathbf{K}_k^\top + (\mathbf{l}_{\tau,k} + \mathbf{l}_{W,k}) (\mathbf{l}_{\tau,k} + \mathbf{l}_{W,k})^\top. \end{aligned} \tag{3.3.31}$$

Performing the multiplications in (3.3.31) and using Einstein's notation, the second moment map can be given as

$$\begin{aligned} \overline{\overline{Z}}_{i_1 i_2}(k+1) = \langle K_{k,i_1 i_4} K_{k,i_2 i_3} \rangle \, \overline{\overline{Z}}_{i_3 i_4}(k) \\ + \left(\langle K_{k,i_1 i_4} l_{\tau,k,i_2} + K_{k,i_2 i_4} l_{\tau,k,i_1} \rangle \right) \bar{z}_{i_4}(k) \\ + \left(\langle l_{\tau,k,i_1} l_{\tau,k,i_2} \rangle + \langle l_{W,k,i_1} l_{W,k,i_2} \rangle \right), \end{aligned} \tag{3.3.32}$$

where $\overline{\overline{Z}}_{i_1 i_2}(k) = \overline{\overline{Y}}_{i_1 i_2}(k\ell)$. The expected values in this equation can be calculated with

$$\langle K_{k,i_1 i_4} K_{k,i_2 i_3} \rangle = \sum_{j_\tau=1}^{J_\tau} w_{j_\tau} \langle K_{k,i_1 i_4} K_{k,i_2 i_3} | \tau_{\mathrm{s},t_{k\ell}} = \tau_{j_\tau} \rangle , \tag{3.3.33}$$

$$\langle K_{k,i_1 i_3} l_{\tau,k,i_2} \rangle = \sum_{j_\tau=1}^{J_\tau} w_{j_\tau} \langle K_{k,i_1 i_3} l_{\tau,k,i_2} | \tau_{\mathrm{s},t_{k\ell}} = \tau_{j_\tau} \rangle , \tag{3.3.34}$$

$$\langle l_{\tau,k,i_1} l_{\tau,k,i_2} \rangle = \sum_{j_\tau=1}^{J_\tau} w_{j_\tau} \langle l_{\tau,k,i_1} l_{\tau,k,i_2} | \tau_{\mathrm{s},t_{k\ell}} = \tau_{j_\tau} \rangle . \tag{3.3.35}$$

All the expectation values containing first-order terms from the additive vector $\mathbf{l}_{W,k}$ disappear, since $\mathbf{l}_{W,k}$ contains integrals with respect to the Wiener process and they are all have zero mean. However, expectations containing second-order terms from $\mathbf{l}_{W,k}$ lead to composite expected values, and one has to consider both the expectation w.r.t. the stochastic time-delay and the expectation of Itô integrals as it can be derived from (3.3.19):

$$\begin{aligned} \langle l_{W,k,i_1} l_{W,k,i_2} \rangle &= \left\langle \hat{F}_{k,i_1 i_4} \hat{F}_{k,i_2 i_3} \right\rangle \langle g_{i_3} g_{i_4} \rangle \\ &= \left(\sum_{j_\tau=1}^{J_\tau} w_{j_\tau} \left\langle \hat{F}_{k,i_1 i_4} \hat{F}_{k,i_2 i_3} | \tau_{\mathrm{s},t_{k\ell}} = \tau_{j_\tau} \right\rangle \right) \langle g_{i_3} g_{i_4} \rangle . \end{aligned} \tag{3.3.36}$$

Here a major simplification was used: despite $\mathbf{g}$ depends on the discrete time n, its distribution, hence its second moment $\mathbf{g}\mathbf{g}^\top$ does not. This allows one to factor out $\mathbf{g}\mathbf{g}^\top$ and use the matrix $\hat{\mathbf{F}}$ defined in (3.3.21) for the second moment calculation of $\mathbf{l}_W$, similarly to the definition and the second moment calculation of $\mathbf{l}_{\tau,k}$.

Using the notation $\bar{\bar{\mathbf{z}}}(k) = \bar{\bar{\mathbf{y}}}(k\ell)$ the second moment evolution can be given in the vector-to-vector map form as

$$\bar{\bar{\mathbf{z}}}(k+1) = \overline{\overline{\mathbf{K}}} \bar{\bar{\mathbf{z}}}(k) + \bar{\mathbf{k}} \bar{\mathbf{z}}(k) + \left(\bar{\bar{\mathbf{l}}}_\tau + \bar{\bar{\mathbf{l}}}_W \right), \tag{3.3.37}$$

similarly to (3.2.28) or (3.1.15). To determine if the second moment stability of (3.3.37) one has to investigate if $\rho\left(\overline{\overline{\mathbf{K}}}\right) < 1$ holds, and if the squared process is stable it converges to the fixed point

$$\bar{\bar{\mathbf{z}}}_{\mathrm{st}} = \left(\mathbf{I} - \overline{\overline{\mathbf{K}}} \right)^{-1} \left(\bar{\mathbf{k}} \bar{\mathbf{z}}_{\mathrm{st}} + \left(\bar{\bar{\mathbf{l}}}_\tau + \bar{\bar{\mathbf{l}}}_W \right) \right), \quad \text{as} \quad k \to \infty, \tag{3.3.38}$$

approximating the stationary second moment of (3.3.1).

Chapter 4

Numerical Case Studies

In the previous chapter the construction of the stochastic semidiscretisation method has been given to investigate the stationary behaviour of the linear SDDEs defined in Eqs. (3.1.1), (3.2.1) and (3.3.1). In the following sections, the convergence properties of the described method are investigated numerically for different simple SDDEs. In Sec. 4.1 a scalar first order delayed equation, the stochastic Hayes equation is investigated for which an analytic solution exists, thus it can be tested, that the results gained by the discrete mapping converge to this exact solution. In Sec. 4.2 the second order problem, the stochastic delay oscillator is investigated. In case of this example, the advantages of the semidiscretisation method are emphasised, namely the convergence of both the spectral radius and the stationary solution are compared to the full-discretisation. Next, in Sec. 4.3 the stochastic delayed Mathieu equation is analysed, which is a second order periodic problem. For this equation it can be demonstrated, how the method can be utilised to approximate the stability and characterise the stationary solution of periodic systems. Finally, in Sec. 4.4 a scalar system with stochastic delays is investigated, and it is shown, that such system produce periodic stationary behaviour even if the system is subjected to white noise.

4.1 Stochastic Hayes Equation

The Hayes equation is one of the simplest scalar examples to investigate the behaviour of DDEs [49, 78]. In this case its stochastic version is used, namely:

$$\mathrm{d}x_t = Ax_t\mathrm{d}t + \beta x_{t-1}\mathrm{d}W_t + \sigma\mathrm{d}W_t\,, \tag{4.1.1}$$

with initial condition:

$$x_t = \phi_t\,, \quad t \in [-1, 0]\,, \tag{4.1.2}$$

where $A,\ \beta,\ \sigma \in \mathbb{R}$. Note that the delay can be chosen to be 1 without loss of generality.

4.1.1 Analytical Solution

The stability properties of Eq. (4.1.1) can be determined analytically. The solution of Eq. (4.1.1) can be written in the following form [55]:

$$x_t = e^{At}x_0 + \int_0^t \left(e^{A(t-\hat{t})}\beta x_{\hat{t}-1} + e^{A(t-\hat{t})}\sigma\right)\mathrm{d}W_{\hat{t}}. \tag{4.1.3}$$

The mean dynamics is

$$\langle x_t\rangle = e^{At}x_0\,, \tag{4.1.4}$$

which converges to 0 if the proportional parameter $A < 0$. This means that the system is first moment stable:

$$\lim_{t\to\infty}\langle x_t\rangle = \lim_{t\to\infty}\langle x_{t-1}\rangle = 0. \tag{4.1.5}$$

Still, it is necessary to further investigate the stationary behaviour of the process in Eq. (4.1.1); the second moment $M(t) = \langle x_t x_t\rangle$ of the solution (4.1.3) needs to be evaluated using the Itô

isometry [61]:

$$M(t) = e^{2At}M_0 + \frac{\sigma^2}{2A}\left(e^{2At} - 1\right) + \int_0^t \left(\beta^2 e^{2A(t-\hat{t})}M(\hat{t}-1) + 2e^{2A(t-\hat{t})}\sigma\beta\left\langle x_{\hat{t}-1}\right\rangle\right)\mathrm{d}\hat{t}\,. \tag{4.1.6}$$

A large enough time instant t_0 is chosen to have $e^{2At_0} \to 0$, $\langle x_{t-1}\rangle \to 0$, so the solution converged to the stationary second moment $M_{\mathrm{st}} = \lim_{t\to\infty} M(t)$. If $0 \ll t_0 \ll t$ then

$$M_{\mathrm{st}} = -\frac{\sigma^2}{2A} + \int_{t_0}^t \beta^2 e^{2A(t-\hat{t})}\mathrm{d}\hat{t}M_{\mathrm{st}}, \tag{4.1.7}$$

from which

$$M_{\mathrm{st}} = -\frac{\sigma^2}{2A+\beta^2}. \tag{4.1.8}$$

Since M_{st} has to be non-negative and σ^2 is always positive, the second moment is stable only if:

$$A < -\frac{\beta^2}{2}, \tag{4.1.9}$$

which is a stricter condition than the $A < 0$ for the first moment stability in Eq. (4.1.5).

Note that these analytical results and also the decay rate of the transient part can be calculated by means of Itô's lemma [5, 61], too. The squared process of the stochastic Hayes equation Eq. (4.1.1) assumes the form:

$$\mathrm{d}x_t^2 = \left(2Ax_t^2 + \beta^2 x_{t-1}^2 + \sigma^2 + 2\beta\sigma x_{t-1}\right)\mathrm{d}t + \left(\beta x_{t-1} + \sigma\right)\mathrm{d}W_t\,. \tag{4.1.10}$$

Taking the expected value of the squared process Eq. (4.1.10) and transforming the resulting increment equation into differential form lead to the following deterministic DDE:

$$\dot{M}(t) = 2AM(t) + \beta^2 M(t-1) + 2\beta\sigma\left\langle x_{t-1}\right\rangle + \sigma^2. \tag{4.1.11}$$

Note that after the substitution of Eq. (4.1.5) into Eq. (4.1.11), the calculated stationary solution is equivalent to the result described in Eq. (4.1.8). Furthermore, it is possible to determine the characteristic exponents of the perturbed second moment $\tilde{M}(t) = M(t) - M_{\mathrm{st}}$ and the following homogeneous DDE [78] is obtained:

$$\dot{\tilde{M}}(t) = 2A\tilde{M}_t + \beta^2\tilde{M}(t-1). \tag{4.1.12}$$

Using the exponential trial solution

$$\tilde{M}(t) = ce^{\lambda t}, \tag{4.1.13}$$

one arrives at the following characteristic equation:

$$\lambda - 2A - \beta^2 e^{-\lambda} = 0. \tag{4.1.14}$$

The characteristic exponent λ can be partitioned as $\lambda = \gamma + \mathrm{i}\omega$, $\gamma, \omega \in \mathbb{R}$, where γ and ω are related to the decay rate and to the angular frequency of the transient second moment, respectively. To determine the stability boundaries, one has to substitute $\gamma = 0$ into Eq. (4.1.14), and separate the real and complex terms, and find the roots of the corresponding implicit equations [78]:

$$2A + \beta^2\cos\omega = 0, \tag{4.1.15}$$

$$\omega + \beta^2\sin\omega = 0. \tag{4.1.16}$$

The analytic solution of Eqs. (4.1.15)-(4.1.16) are the following parametric curves in case of Hopf bifurcation ($\omega \neq 0$):

$$A = \frac{\omega}{2\tan(\omega)}, \qquad \beta = \pm\sqrt{-\frac{\omega}{\sin(\omega)}}, \qquad \omega \in [(2k-1)\pi, 2k\pi), k \in \mathbb{Z}, \tag{4.1.17}$$

while in case of fold bifurcation ($\omega = 0$) it gives

$$A = -\frac{\beta^2}{2}. \tag{4.1.18}$$

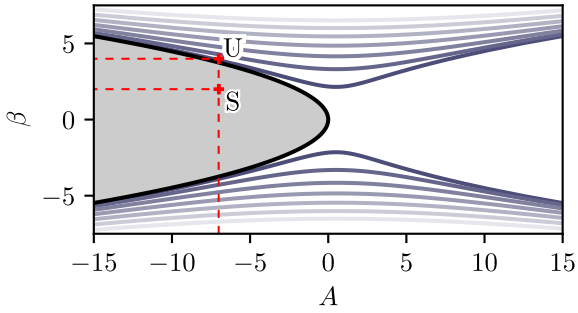

Figure 4.1. *Stable area (gray) and the bifurcation curves defined by Eqs.* (4.1.15)-(4.1.18)

Fig. 4.1 presents the critical parameter lines defined by Eq. (4.1.17)-(4.1.18). Note that the stability boundary is defined by a fold-type bifurcation only (denoted by the shaded region). Assuming that the characteristic root is real ($\omega = 0$), it is possible to write γ as the function of A and β:

$$\gamma = 2A + W_0\left(\beta^2 e^{-2A}\right), \tag{4.1.19}$$

which characterises the decay rate [100] of the second moment process $M(t)$. In this formula, W_0 is the main branch of the Lambert W function [1], which is by definition the function $W(z)$ which satisfies $W(z)e^{W(z)} = z$.

4.1.2 Testing the Monte-Carlo Simulations of the Stochastic Hayes Equation

The above described results are compared to numerical simulations. In Fig. 4.2, the first- and second moment evolutions are obtained by the deterministic equations Eqs. (4.1.4) and (4.1.11), and these are compared to the statistical evaluation of MC simulations, where the expected value and the standard deviation of the trajectories are presented on the basis of 10^4 realisations of the SDDE (4.1.1) calculated by using the Euler-Maruyama from *StochasticDelayDiffEq.jl* [91]. To validate the results obtained through the Monte-Carlo simulations, the DDE (4.1.11) was also numerically integrated using the Tsitouras 5/4 Runge-Kutta method from the Julia package *DifferentialEquations.jl* [72]. In Fig. 4.2 it can be seen, that the deterministic solution matches well to the mean values and deviations of the MC simulations. Note that the analytic method gives almost everywhere smooth curves for the moment evolutions, while the MC simulations give only somewhat noisy curves and with orders of magnitude higher computation time, due to the large but finite number of realisations used for the MC simulations.

This shows, that the MC simulations can be used for validation purposes, and the 10^4 – 10^5 number of trajectories are enough to approximate the moment solutions. However the results gained through the MC calculations are “noisy”, due to the finite number of trajectories used for the averaging to obtain the first and second moments.

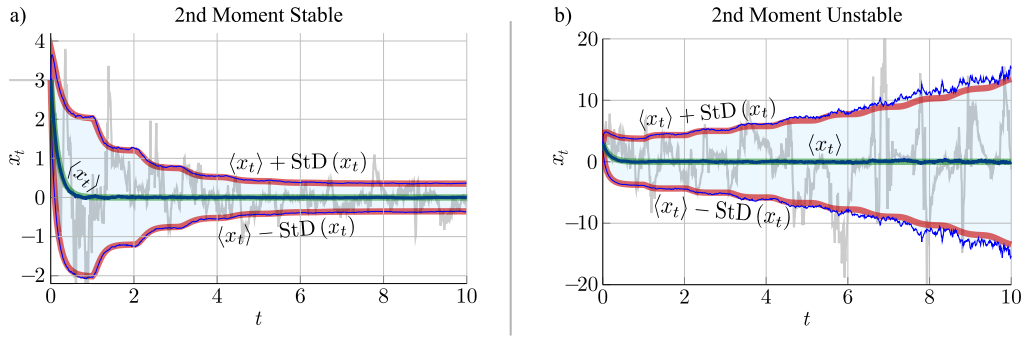

Figure 4.2. *The first moment (green curve) and its envelopes (red curves) calculated by means of Eqs.* (4.1.4) *and* (4.1.11)*, respectively, are compared to the statistical evaluation of MC simulations: the dark thick blue line represents the mean and the thin blue lines and the light blue areas represents the standard deviation of* 10^4 *realisations. Panel (a) shows a stable case* ($A = -6,\ \beta = 2$*, denoted by parameter point "S" in the stability chart of Fig 4.1). Panel (b) shows a second moment unstable case* ($A = -6,\ \beta = 4$*, denoted with point "U" in Fig 4.1).* $\bar{x}(t) = \langle x_t \rangle$, $\sigma_x(t) = \sqrt{M(t) - \bar{x}(t)^2}$ *and initial function* $\phi_t \equiv 3$, $t \in [-1, 0]$*. The gray trajectories show one selected realisation in the MC simulation.*

4.1.3 Zeroth-order Semidiscretisation of the Stochastic Hayes Equation

To illustrate the construction of the second moment mapping defined in Eq. (3.1.16), the Y_{11} element of the second moment mapping of the stochastic Hayes equation is given using two separate approach. First the original stochastic Hayes equation from Eq. (4.1.1)) is considered:

$$\mathrm{d}x_t = Ax_t\mathrm{d}t + \beta x_{t-1}\mathrm{d}W_t + \sigma\mathrm{d}W_t\,. \tag{4.1.20}$$

Its zeroth-order semidiscretised form similar to Eq. (3.1.1) is

$$\mathrm{d}x_t = Ax_t\mathrm{d}t + \beta x_{t_{n-r}}\mathrm{d}W_t + \sigma\mathrm{d}W_t \quad \text{where} \quad t \in [t_n, t_{n+1}\Delta t] \tag{4.1.21}$$

The calculated stochastic mapping matrices and vector using Eqs. (3.1.4), (3.1.5), (3.1.6) and (3.1.9):

$$\mathbf{F} = \begin{pmatrix} F_{11} & 0 & \cdots & 0 \\ 1 & 0 & \cdots & 0 \\ & & & \\ 0 & \ddots & & \vdots \\ 0 & \cdots & 1 & 0 \end{pmatrix}, \qquad \mathbf{G} = \begin{pmatrix} 0 & 0 & \cdots & G_{1,r+1} \\ 0 & 0 & \cdots & 0 \\ & & & \\ 0 & \ddots & & \vdots \\ 0 & \cdots & & 0 \end{pmatrix}, \qquad \mathbf{g} = \begin{pmatrix} g_1 \\ 0 \\ \vdots \\ 0 \end{pmatrix}, \tag{4.1.22}$$

where

$$F_{11} = e^{A\Delta t}, \qquad G_{1,r+1} = \beta \int_{t_n}^{t_{n+1}} e^{A(t_{n+1}-s)}\mathrm{d}W_s, \qquad g_1 = \sigma \int_{t_n}^{t_{n+1}} e^{A(t_{n+1}-t)}\mathrm{d}W_t\,. \tag{4.1.23}$$

The elements of the second moment matrix which will be used are the following:

$$\langle x_{t_n-1} \rangle := \bar{y}_{r+1}(n), \qquad \langle x_{t_n} x_{t_n} \rangle := \overline{\overline{Y}}_{11}(n), \qquad \langle x_{t_{n-r}} x_{t_{n-r}} \rangle := \overline{\overline{Y}}_{r+1,r+1}(n) \tag{4.1.24}$$

Approximating the moment evolution using the semidiscretisation matrices in (3.1.18) and the stepping definitions from Eq. (3.1.16) lead to the mapping for $\overline{\overline{Y}}_{11}(n+1)$:

$$\overline{\overline{Y}}_{11}(n+1) = F_{11}^2\overline{\overline{Y}}_{11}(n) + G_{1,r+1}^2\overline{\overline{Y}}_{r+1,r+1}(n) + 2G_{1,r+1}g_1\left\langle x_{t_{n-r}} \right\rangle + g_1^2\,. \tag{4.1.25}$$

Substituting the matrix elements from Eq. (4.1.22) into Eq. (4.1.25) and the Ito integral is performed as in Eqs. (3.1.25)-(3.1.27) leads to the mapping

$$\begin{aligned}\overline{\overline{Y}}_{11}(n+1) = e^{2A\Delta t}\overline{\overline{Y}}_{11}(n) + \frac{\beta^2\left(e^{2A\Delta t}-1\right)}{2A}\overline{\overline{Y}}_{r+1,r+1}(n) \\ + \frac{\beta\sigma\left(e^{2A\Delta t}-1\right)}{A}\left\langle x_{(n\Delta t-p)\Delta t}\right\rangle + \frac{\sigma^2\left(e^{2A\Delta t}-1\right)}{2A}.\end{aligned} \tag{4.1.26}$$

To show the correctness of this result a second approach is used; the zeroth-order deterministic semidiscretization [39] is applied to the analytically derived second moment equation Eq. (4.1.13):

$$\dot{M}(t) = 2AM(t) + \beta^2 M(t-1) + 2\beta\sigma\left\langle x_{t-1}\right\rangle + \sigma^2, \tag{4.1.27}$$

yielding:

$$\dot{M}(t) \approx 2AM(t) + \beta^2 M\left(t_{n-r}\right) + 2\beta\sigma\left\langle x_{t_{n-r}}\right\rangle + \sigma^2 \quad \text{where} \quad t \in [t_n, t_{n+1}]\,. \tag{4.1.28}$$

Solving the above linear differential equation on the time interval $t \in [t_n, t_{n+1}]$ leads to:

$$\begin{aligned}M\left(t_{n+1}\right) = e^{2A\Delta t}M\left(t_n\right) + \frac{\beta^2\left(e^{2A\Delta t}-1\right)}{2A}M\left(t_{n-r}\right) \\ + \frac{\beta\sigma\left(e^{2A\Delta t}-1\right)}{A}\left\langle x_{(n\Delta t-p)\Delta t}\right\rangle + \frac{\sigma^2\left(e^{2A\Delta t}-1\right)}{2A}\end{aligned} \tag{4.1.29}$$

which gives the same result as Eq. (4.1.26) since

$$M(t_n) := \overline{\overline{Y}}_{11}(n), \qquad M(t_{n-r}) := \overline{\overline{Y}}_{r+1,r+1}(n)\,. \tag{4.1.30}$$

thus the semidiscretisation of the second moment equation is equivalent to the second moment of the stochastic semidiscretisation (4.1.1).

4.1.4 Convergence of the Stochastic Semidiscretisation

When the semidiscretisation method is applied, the mapping described in Eq. (3.1.16) is constructed numerically. With the help of Eqs. (4.1.8), (4.1.18) and (4.1.19), the convergence of the stochastic semidiscretisation method is investigated by means of the spectral radius of the second moment mapping matrix $\mathbf{H}$, the stationary second moment and also the stability chart. Since there is no deterministic delayed term in the stochastic Hayes equation (4.1.1), the convergence of the spectral radius of the first moment is not analysed here (for details see in [39]); in this case the semidiscretisation method provides the analytic solution, while the full-discretisation converges only in first order.

A properly chosen discretisation has to satisfy the following criterion:

$$\lim_{r\to\infty}\rho\left(\mathbf{H}\right)^r = e^{\gamma\tau}. \tag{4.1.31}$$

The expression $e^{\gamma\tau}$ describes the change of the amplitude in one delay period, while the spectral radius $\rho\left(\mathbf{H}\right)$ only characterises it within the numerical timestep $\Delta t = 1/r$. To compare them, one has to use the r-th power of the spectral radius. To characterise the convergence of the method, the relative error

$$\delta_{\rho,2}(r) = \frac{\left|e^{\gamma\tau} - \rho\left(\mathbf{H}\right)^r\right|}{e^{\gamma\tau}} \tag{4.1.32}$$

between the numerical result and the analytic solution is used. The semidiscretisation method is also compared to the full-discretisation method. The computation of the full-discretisated mapping matrices can be computed by adjusting the elements of the matrices in (4.1.23), namely: $F_{11,\text{full}} =$

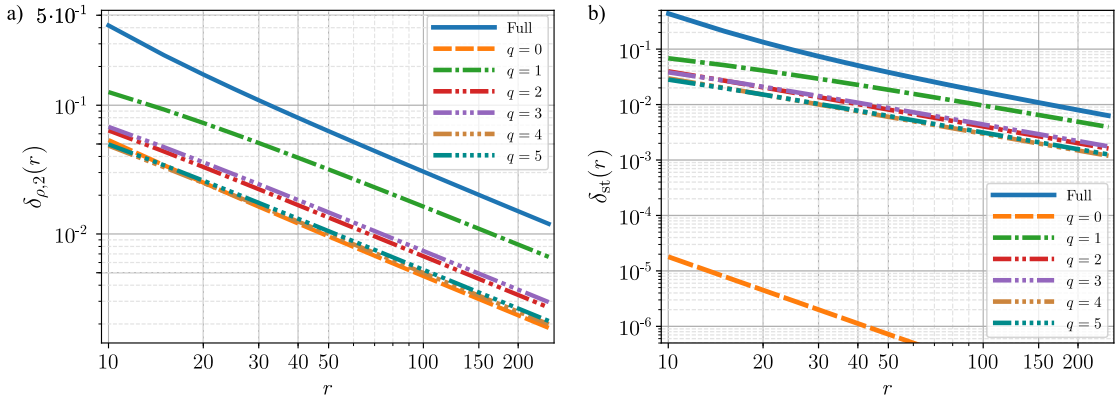

Figure 4.3. *Relative error of the spectral radius of (a) the second moment mapping matrix and (b) the stationary second momentf as a function of the delay resolution r, for the stochastic Hayes equation Eq. (4.1.1) for different order q of semidiscretisation and the full-discretisation method [24]. The numerical parameters are $A = -6$, $\beta = 2$, $\sigma = 1$, $e^{\gamma\tau} \approx 0.3640$ and $M_{\mathrm{st}} = 0.125$. The order q refers to the order of the Lagrange polynomial used to approximate the delayed terms. The numerical values of the convergence rates are given in Tab. 4.1*

.

$(1 + A)\Delta t$, $G_{1,r+1,\mathrm{full}} = \beta\,(W_{t_{n+1}} - W_{t_n})$ and $g_1 = \sigma\,(W_{t_{n+1}} - W_{t_n})$, and then computing the first and second moment mapping matrices needed for the computation of stability and the steady-state second moment.

Fig. 4.3a shows that the convergence rate of the full-discretisation method [24] and the proposed semidiscretisation methods of different order are the same w.r.t. r, and the errors $\delta_{\rho,2}(r)$ differ only in a constant multiplier. In this scalar case, the semidiscretisation method provides an order of magnitude more accurate approximation than the full-discretisation method. This is important, since the number of elements of the second moment mapping matrix $\mathbf{H}$ is proportional to r^4, and the zeroth-order semidiscretisation method achieves 1 % accuracy at $r = 50$, while the full-discretisation method cannot achieve this even with $r = 250$.

To investigate the convergence of the stationary second moment matrix, the following relative error is defined:

$$\delta_{\mathrm{st}}(r) = \frac{\left| M_{\mathrm{st}} - \overline{\overline{Y}}_{\mathrm{st},11} \right|}{M_{\mathrm{st}}}. \tag{4.1.33}$$

Note that in this scalar case, all the diagonal elements of the second moment matrix $\overline{\overline{\mathbf{Y}}}(n)$ in the stationary solution $\overline{\overline{\mathbf{Y}}}_{\mathrm{st}}$ are the same. Therefore in Eq. (4.1.33), only the first element $\overline{\overline{Y}}_{\mathrm{st},11} = \lim_{t\to\infty} \langle x_t x_t \rangle$ of the stationary second moment vector $\overline{\overline{\mathbf{y}}}_{\mathrm{st}}$ from Eq. (3.1.21) is compared to the analytic solution M_{st} (Eq. (4.1.8)).

In Fig. 4.3b, the better convergence of the stochastic semidiscretisation method can be observed again. The different order methods show a slightly smaller error, although the rate of convergence is almost the same. Furthermore, the relative error for the spectral radius and the stationary second moment show similar tendency.

In Fig. 4.4, the numerically calculated stability boundaries, defined by the spectral radius $\rho(\mathbf{H})$ of the discretised system, are compared to the stability boundary determined analytically from Eq. (4.1.18). The stability boundary $\rho\,(H) = 1$ of the discretised system is determined with the help of the multi-dimensional bisection method (MDBM) [7]. It can be seen, that the smaller A in the discrete system is, the worse the approximation of the analytic stability chart is, so in the general case, the use of higher-order method is useful to reach a certain desired accuracy.

At the moment, we could not find a mathematical explanation for the extremely good convergence of the zeroth-order semidiscretisation compared to the higher-order ones. This might be due

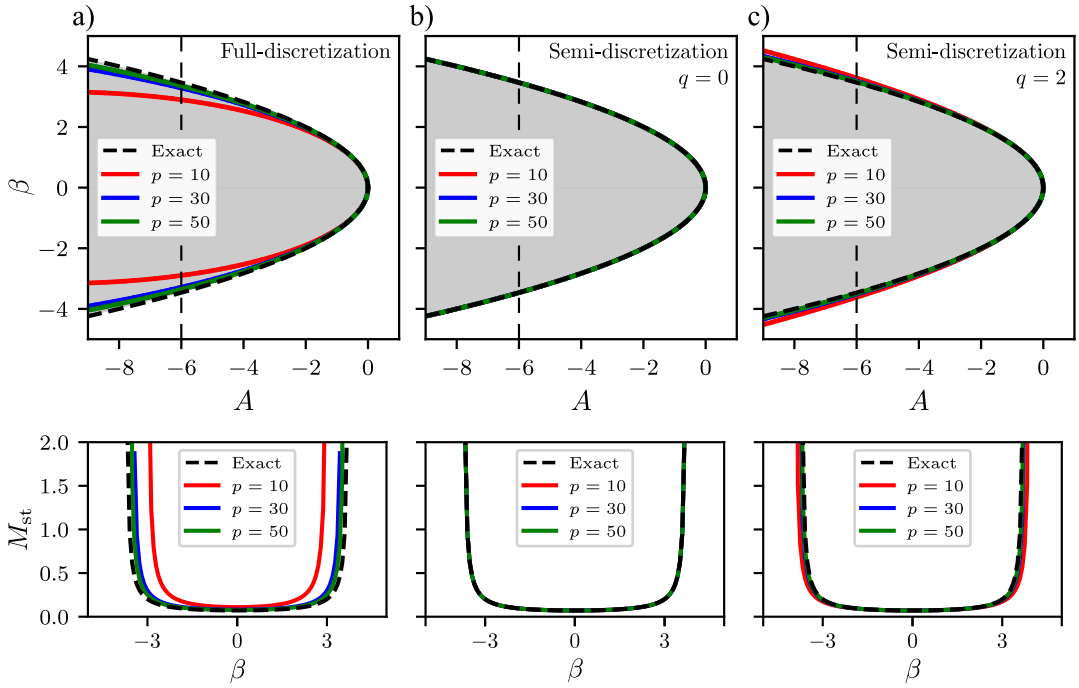

Figure 4.4. *Convergence of the stability chart (upper panel) and the stationary second moment (lower panel) using (a) full-discretisation (b) zeroth-order semidiscretisation (c) second-order semidiscretisation. The order q refers to the order of the Lagrange polynomial used to approximate the delayed terms. The vertical dashed lines in the stability charts represent the paramater $A = -6$ along which the stationary second moments were calculated*

to the special simple mathematical form of the Hayes equation. This is the reason why the method is tested on a more general problem in the next section.

4.2 Stochastic Delayed Oscillator

The stochastic delayed oscillator of the form

$$\dot{x}_t = v_t \tag{4.2.1}$$

$$\dot{v}_t + 2\zeta v_t + A x_t = B x_{t-2\pi} + (\alpha x_t + \beta x_{t-2\pi} + \sigma)\, \Gamma_t \tag{4.2.2}$$

is an essential mathematical model in many engineering problems like machine tool vibrations [53, 84]. This can be transformed into Eq. (3.1.1) with $\tau = 2\pi$ and

$$\begin{aligned} \mathbf{x}_t &= \begin{pmatrix} x_t \\ v_t \end{pmatrix}, \quad & \mathbf{A} &= \begin{pmatrix} 0 & 1 \\ -A & -2\zeta \end{pmatrix}, \quad & \mathbf{B} &= \begin{pmatrix} 0 & 0 \\ B & 0 \end{pmatrix}, \\ \boldsymbol{\alpha} &= \begin{pmatrix} 0 & 0 \\ \alpha & 0 \end{pmatrix}, \quad & \boldsymbol{\beta} &= \begin{pmatrix} 0 & 0 \\ \beta & 0 \end{pmatrix}, \quad & \boldsymbol{\sigma} &= \begin{pmatrix} 0 \\ \sigma \end{pmatrix}. \end{aligned} \tag{4.2.3}$$

In this multidimensional case, the explicit solution like Eq. (4.1.3) for the Hayes equation is not available [5]. In Fig. 4.5 two examples are shown for the evolution of the first and second moments together with an individual realisation of the process in Eq. (4.2.1)-(4.2.3). The cases of stable and unstable second moments show good agreement between the statistical analysis of independent MC simulations and the spectral radius and the stationary solution computed with the stochastic semidiscretisation.

For comparison, the reference values of the stationary second moment $\bar{\bar{\mathbf{y}}}_{\mathrm{st}}$ and the spectral radii of the first moment mapping matrix $\mathbf{F}$ and second moment mapping matrix $\mathbf{H}$ are calculated using

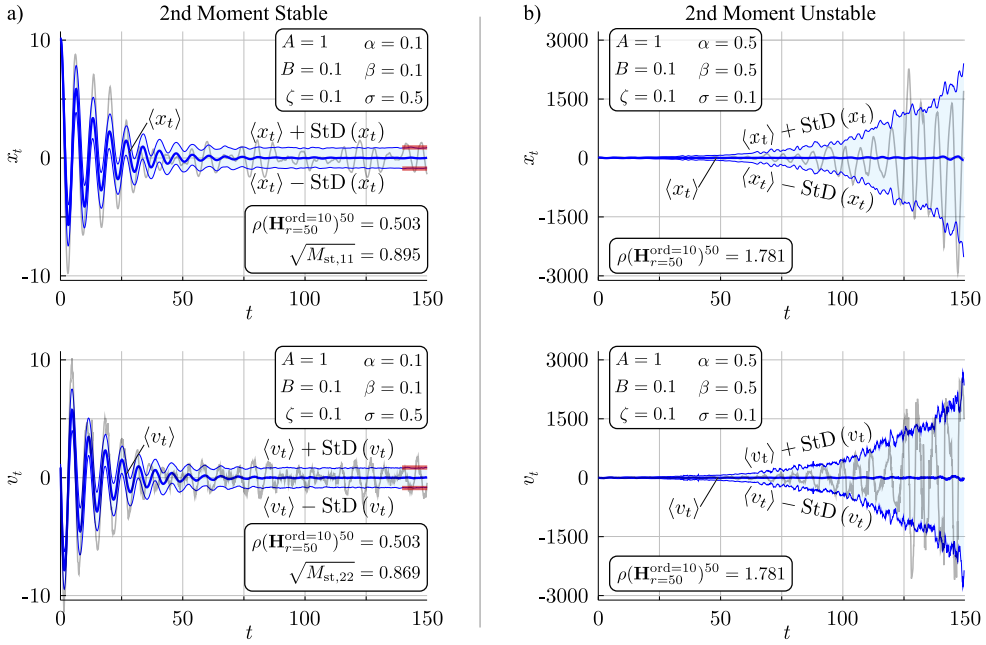

Figure 4.5. *First moment stable processes are shown for stable second moment in panel (a) and for unstable second moment in panel (b). The gray lines represent typical realisations of the process. The thick blue lines show the mean, while the thin blue lines and light blue areas show the standard deviation of 10^4 realisations obtained by MC simulations. The red lines in panel (a) represent the stable stationary second moment calculated with stochastic semidiscretisation.*

the 10^{th}-order semidiscretisation method with as high resolution r as our computational capacity allowed:

$$\rho_1^{\mathrm{ref}} = \rho\left(\mathbf{F}_{r=200}\right)^{200}, \tag{4.2.4}$$

$$\rho_2^{\mathrm{ref}} = \rho\left(\mathbf{H}_{r=200}\right)^{200}, \tag{4.2.5}$$

$$\overline{\overline{\mathbf{y}}}_{\mathrm{st}}^{\mathrm{ref}} = \left(\mathbf{I} - \mathbf{H}_{r=130}\right)^{-1} \mathbf{c}_{r=130}\,. \tag{4.2.6}$$

Selecting these reference values, the relative errors δ are defined as a function of the resolution parameter r:

$$\delta_{\rho,1}(r) = \frac{\left|\rho_1^{\mathrm{ref}} - \rho\left(\mathbf{F}\right)^r\right|}{\left(\rho_1^{\mathrm{ref}}\right)}, \tag{4.2.7}$$

$$\delta_{\rho,2}(r) = \frac{\left|\rho_2^{\mathrm{ref}} - \rho\left(\mathbf{H}\right)^r\right|}{\left(\rho_2^{\mathrm{ref}}\right)}, \tag{4.2.8}$$

$$\delta_{\mathrm{st}}(r) = \frac{\left|\overline{\overline{Y}}_{\mathrm{st},11}^{\mathrm{ref}} - \overline{\overline{Y}}_{\mathrm{st},11}\right|}{\overline{\overline{Y}}_{\mathrm{st},11}^{\mathrm{ref}}}, \tag{4.2.9}$$

where $\overline{\overline{Y}}_{\mathrm{st},11}^{\mathrm{ref}}$ is the first element of $\overline{\overline{\mathbf{y}}}_{\mathrm{st}}^{\mathrm{ref}}$ defined in (4.2.6).

In Figs. 4.6, 4.7 and 4.8, the convergence properties of the spectral radii of the first and the second moment mapping matrices and similarly, those of the stationary second moment can be observed, respectively.

The convergence rate c_r is calculated by fitting of

$$\delta(r) = Kr^{-c_r} \tag{4.2.10}$$

for $r > 50$ onto the error functions showed in Figs. 4.6, 4.7 and 4.8. The corresponding numerical values of c_r are given in Tab. 4.1.

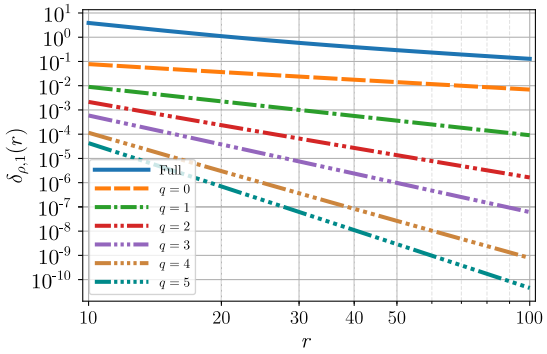

Figure 4.6. *Relative error of the spectral radius of the first moment matrix* $\mathbf{F}$ *for the delayed oscillator using the numerical parameters* $A = 1$, $B = 0.1$. *The order* q *refers to the order of the Lagrange polynomial used to approximate the delayed terms. See the approximated convergence rates in Tab. 4.1*

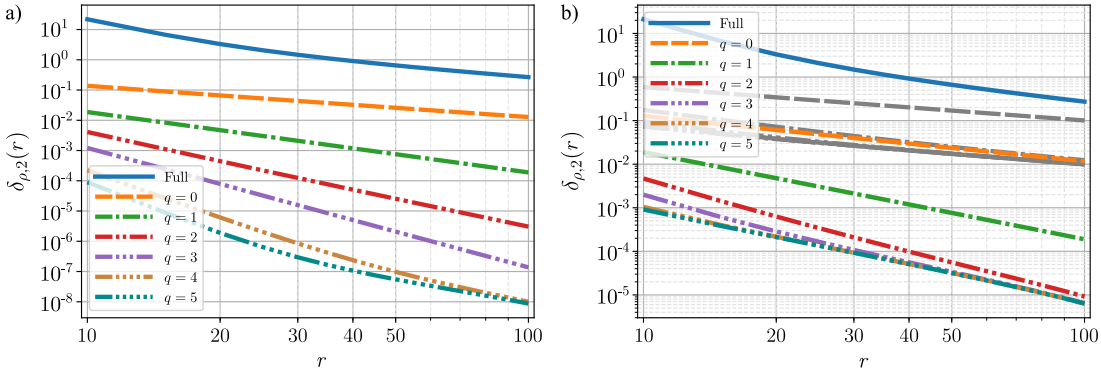

Figure 4.7. *Relative error of the spectral radius of the second moment matrix* $\mathbf{H}$ *for the delayed oscillator* (4.2.3) *with numerical parameters* $A = 1.0$, $B = 0.1$, $\beta = 0.1$ *and stochastic proportional coefficient (a)* $\alpha = 0$ *and (b)* $\alpha = 0.1$. *The order* q *refers to the order of the Lagrange polynomial used to approximate the delayed terms. The gray lines correspond to the results obtained without the correction term presented in Sec. 3.1.3. Note that the uncorrected zeroth-order semidiscretisation* ($q = 0$) *only differs in a constant multiplier* ($\sim 10\times$) *from the corrected one, while the lines corresponding uncorrected higher-order* ($q \geq 1$) *semidiscretisation cluster around the corrected zeroth-order result. The corresponding convergence rates are given numerically in Tab. 4.1*

It can be seen in Fig. 4.6, that the first moment's spectral radius behaves as expected [39]: the increase of both the interpolation order of the delayed states and the resolution parameter r decreases the error $\delta_{\rho,1}$; the convergence rate c_r increases by 1 as the interpolation order increases by 1. The spectral radius of the second moment mapping matrix behaves similarly as it can be observed in Fig. 4.7 for two different cases. In case of no multiplicative noise at the actual time t (that is for $\alpha = 0$ in Fig. 4.7a), the 1-by-1 increase of the interpolation order leads to the increase of the convergence rate only by 1 (instead of 2) due to the magnitude $\sqrt{\mathrm{d}t}$ property of the Wiener process [47]. However, it can be concluded from Fig. 4.7b that the convergence of the spectral radius of the second moment is limited for $\alpha \neq 0$ due to the error introduced by the multiplicative noise term $\boldsymbol{\alpha}\mathbf{e}^{\mathbf{A}\mathbf{t}}\mathbf{x}_{t_n}\mathrm{d}W_t$ (as discussed in Sec. 3.1.3). In this case, the use of a maximum second order interpolation of the delayed terms is suggested, since the increase in calculation time is not accompanied by significant improvement in accuracy.

In Fig. 4.8, the convergence of the stationary second moment $M_{\mathrm{st},11} = \lim_{t\to\infty}\left\langle x_t^2\right\rangle$ can be seen. One can observe that the results gained with the full-discretisation method are divergent for $r \lesssim 35 - 38$ (see the dashed blue line). Here, $\rho\left(\mathbf{H}\right) > 1$ implies that Eq. (3.1.21) does not hold

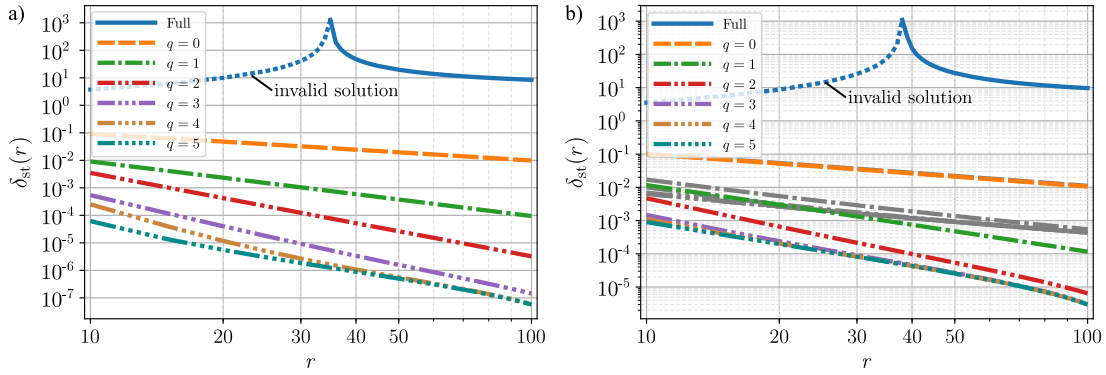

Figure 4.8. *Relative error of the spectral radius of the stationary second moment $M_{\mathrm{st},11}$ for the delay oscillator (4.2.3) with numerical parameters $A = 1.0$, $B = 0.1$, $\beta = 0.1$ and stochastic proportional coefficient (a) $\alpha = 0$ and (b) $\alpha = 0.1$. The dashed line refers to an invalid (negative) stationary solution. The gray lines correspond to the results obtained without the correction term presented in Sec. 3.1.3. Note that the uncorrected zeroth-order semidiscretisation ($q = 0$) does not differ from the corrected one, while the lines corresponding uncorrected higher-order ($q \geq 1$) semidiscretisation does not increase in convergence order compared to the zeroth-order, and only differs from it in a constant multiplier. The order q refers to the order of the Lagrange polynomial used to approximate the delayed terms. The corresponding convergence rates are given numerically in Tab. 4.1*

any more because it can lead to a negative second moment:

$$\lim_{n\to\infty} \left\langle y_{n-m,i}^2 \right\rangle < 0, \quad \text{for all} \quad m = 0, 1, 2 \ldots r \quad \text{and} \quad i = 1, 2, ..., (r+1)d, \tag{4.2.11}$$

meaning that there exists no stationary distribution of the unstable approximation. The fast convergence is especially important near the stability boundaries; this is crucial if the original system is stable but the low resolution approximate mapping is still unstable, like in the case explained above for full-discretisation. Consequently, the calculated (invalid) stationary second moment of the approximation first converges to $-\infty$ as the resolution r is increased, leading to a seemingly ill-working numerical method. However, the expected convergence rate can be reached in these cases for very large and computationally costly discretisation resolution r.

Test case	Quantity	Fig.	FD	n-th order SSD					
				0	1	2	3	4	5
Stochastic Hayes	$\delta_{\rho,2}(r)$	4.3a	1.03	1.02	0.97	1.00	1.00	1.00	1.00
	$\delta_{\mathrm{st}}(r)$	4.3b	1.08	2.00	0.97	1.01	0.99	1.00	1.00
Delayed oscillator	$\delta_{\rho,1}(r)$	4.6	1.18	1.02	2.00	3.06	4.00	5.08	6.00
	$\delta_{\rho,2}(r)$, $\alpha = 0.0$	4.7a	1.28	1.01	2.00	3.06	3.95	5.23	5.71
	$\delta_{\mathrm{st}}(r)$, $\alpha = 0.0$	4.8a	-	0.99	2.00	3.02	3.42	3.14	3.01
	$\delta_{\rho,2}(r)$, $\alpha = 0.1$	4.7b	1.28	1.02	2.01	2.59	2.38	2.32	2.32
	$\delta_{\mathrm{st}}(r)$, $\alpha = 0.1$	4.8b	-	0.99	2.04	2.99	2.97	2.95	2.95

Table 4.1. *Convergence rate c_{r} of the different discretisation methods, by fitting $\delta(r) = Kr^{-c_{\mathrm{r}}}$ function for resolution parameter $r > 50$ (FD – full-discretisation method, SSD – stochastic semidiscretisation method)*

4.3 Stochastic Delayed Mathieu Equation

In this section the moment stability and stationary moments of the stochastic delayed Mathieu equation is investigated, which contains multiplicative noise in both the present and past position

and present velocity along with a constant additive term. Consider the stochastic delay differential equation in the Itô sense:

$$\begin{aligned}\ddot{x}_t + a_1(1+\alpha_1\Gamma_t)\dot{x}_t + (\delta + \varepsilon\cos(\omega t))\,(1+\alpha_0\Gamma_t)x_t \\ = b_0(1+\beta_0\Gamma_t)x_{t-2\pi} + \sigma\Gamma_t,\end{aligned} \tag{4.3.1}$$

where the principal period is $T = 2\pi/\omega$, while the delay $\tau(t) \equiv 2\pi$ can be set without the loss of generality. The Gaussian white noise process is described with the help of the Langevin force Γ_t. The first order incremental form of the stochastic delayed Mathieu equation (4.3.1) can be written as

$$\mathrm{d}\mathbf{x}_t = (\mathbf{A}(t)\mathbf{x}_t + \mathbf{B}(t)\mathbf{x}_{t-2\pi})\,\mathrm{d}t + (\boldsymbol{\alpha}(t)\mathbf{x}_t + \boldsymbol{\beta}(t)\mathbf{x}_{t-2\pi} + \boldsymbol{\sigma})\,\mathrm{d}W_t, \tag{4.3.2}$$

where

$$\mathbf{A}(t) = \begin{pmatrix} 0 & 1 \\ -(\delta + \varepsilon\cos(\omega t)) & -a_1 \end{pmatrix}, \quad \mathbf{B}(t) \equiv \begin{pmatrix} 0 & 0 \\ b_0 & 0 \end{pmatrix}, \tag{4.3.3}$$

$$\boldsymbol{\alpha}(t) = \begin{pmatrix} 0 & 0 \\ -\alpha_0(\delta + \varepsilon\cos(\omega t)) & -\alpha_1 a_1 \end{pmatrix}, \quad \boldsymbol{\beta}(t) = \beta_0\mathbf{B}(t), \quad \boldsymbol{\sigma} = \begin{pmatrix} 0 \\ \sigma \end{pmatrix}. \tag{4.3.4}$$

To reduce the number of the parameters during the moment stability investigation the values of α_1, α_0, β_0 are set to a common value σ_0:

$$\alpha_1 \equiv \alpha_0 \equiv \beta_0 \equiv \sigma_0\,. \tag{4.3.5}$$

To conduct numerical experiments to investigate the convergence properties of the approximation of the stability properties, the error measure $\delta^p_{\rho,2}(\hat{p})$ is introduced:

$$\delta^p_{\rho,2}(\hat{p}) = \left| \frac{\rho\big(\mathbf{H}^{(n,p)}|_{p=\hat{p}}\big) - \rho\big(\mathbf{H}^{(n,p)}|_{p=p_{\mathrm{ref}}}\big)}{\rho\big(\mathbf{H}^{(n,p)}|_{p=p_{\mathrm{ref}}}\big)} \right|. \tag{4.3.6}$$

In Figure 4.9 the convergence rate and some computational properties of the spectral radius $\rho\big(\mathbf{H}^{(n,p)}\big)$ is shown through the error measure $\delta^p_{\rho,2}(\hat{p})$ for the numerical parameters $a_1 = 0.2$, $\delta = 3.25$, $b_0 = -0.2$, $\sigma_0 = 0.2$, $\omega = 0.5$, $\varepsilon = 2$, $\sigma_0 = 0.2$ and for different q Lagrange polynomial orders. The reference solution $\rho\big(\mathbf{H}^{(n,p)}\big)$ is calculated with period resolution $p_{\mathrm{ref}} = 200$ and $q = 7$th order Lagrange polynomial was used to approximate the delay term. In Figure 4.9a the error measure $\delta^p_{\rho,2}(\hat{p})$ is shown. To give an approximation of the convergence of $\delta^p_{\rho,2}(\hat{p})$, black lines are given with slopes corresponding to 1st, 2nd and 3rd order convergences. It can be observed, that the results computed with $q = 0$th order converge approximately with order 1, the results obtained using $q = 1$st, 2nd and 3rd order semidiscretization converge approximately with order 2, while the results computed with $q = 4$th and 5th order semidiscretization converge approximately with order 3 to the reference solution.

Furthermore, to benchmark the computational costs of the spectral radius calculation 50 sample calculations were conducted for each p and q parameter pairs and the required computational time, and the memory usage was recorded for every sample. During a benchmark sample, the whole process of the construction of the deterministic and stochastic mapping matrices, the multiplications over a mapping period, and the largest eigenvalue computation was included. The benchmarks were conducted on a workstation computer with dual Intel Xeon Gold 6154 processors and 192 GB RAM. In Figure 4.9b, the error measure $\delta^p_{\rho,2}(\hat{p})$ is shown with respect to the median of the computation time. It can be observed that if the Lagrange polynomial order q of the semidiscretization is increased, significantly higher accuracy can be achieved for the same computational time. In Figure 4.9c and d, the relative time and memory required for the calculations are shown, where the reference median computation time is $808.094\,\mu\mathrm{s}$ and reference

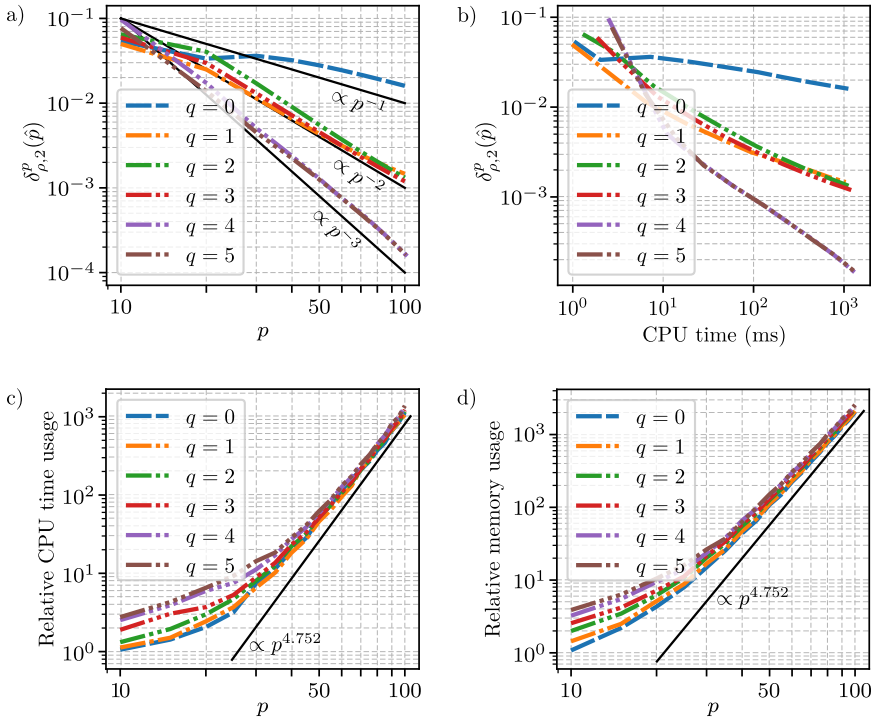

Figure 4.9. *Convergence properties of the spectral radius* $\rho(\mathbf{H})$ *with numerical parameters* $a_1 = 0.2$, $\delta = 3.25$, $b_0 = -0.2$, $\sigma_0 = 0.2$, $\omega = 0.5$, $\varepsilon = 2$, $\sigma_0 = 0.2$*: relative error* ℓ_ρ *of the spectral radius with respect to the a) period resolution* p *and b) the computational time needed, where the reference spectral radius is obtained using semidiscretization with* $q = 7$ *and* $p_{\text{ref}} = 200$*. In panels c) and d) the relative computation time and memory usage is shown, respectively, with reference median computation time* 808.094 µs *and reference median memory requirement* 808.59 *KiB. These values correspond to* $q = 0$ *and* $p = 10$

.

median memory requirement is 808.59 KiB, which occurs at $p = 10$ and $q = 0$. Here it can be seen that the additional computation required by the higher q order semidiscretization is only significant for small p period resolutions. However, for large period resolutions p the eigenvalue computation of the sparse matrix describing $\mathbf{H}^{(n,p)}$ is the dominant source of the computational cost. Since the complexity of the eigenvalue decomposition for a matrix $\mathbf{A} \in \mathbb{R}^{n\times n}$ is approximately $\mathcal{O}(n^{2.376})$ [20, 65], and the size n_H of matrix $\mathbf{H}^{(n,p)} \in \mathbb{R}^{n_H \times n_H}$ can be calculated as $n_H = \sum_{i=1}^{p} i = (p^2 + p)/2$, thus the complexity of the spectral radius calculation becomes $\mathcal{O}(p^{4.752})$. In Figures 4.9c and d, this complexity can be observed in both the computational time and the memory usage for all Lagrange polynomial order q.

In Figure 4.10 the convergence of the second moment stability chart is shown for the semidiscretisation for different period resolutions p and Lagrange polynomial order q with parameters $a_1 = 0.1$, $\omega = 1$, $\varepsilon = 1$, $\sigma_0 = 0.275$. Since in this example the principal period $T = 2\pi/\omega$ is equal to the time delay $\tau = 2\pi$ (the frequency of the periodic term $\omega = 1$), for Lagrange polynomial order $q = 0$ and $q = 1$ the delay resolution r and period resolution p are equal, namely $r = \lfloor \tau/\Delta t + q/2 \rfloor = p$. The diagrams were constructed using MDBM [7] with an initial 25×16 grid for the parameters δ and b_0, respectively, followed by 5 halving iterations (the final grid is of size 800×512). As the analytical stability boundaries for this particular periodic SDDE are not known, a reference stability chart is created for the convergence analysis with $p = 80$, $q = 7$. The figure shows how the boundaries for the different approximations approach the reference boundaries denoted with the dashed black lines. It can be seen that the stability curves obtained with higher q values converge significantly better than $q = 0$ even for small period resolution p.

In Figure 4.11 second moment stability charts for different parameter combinations are shown.

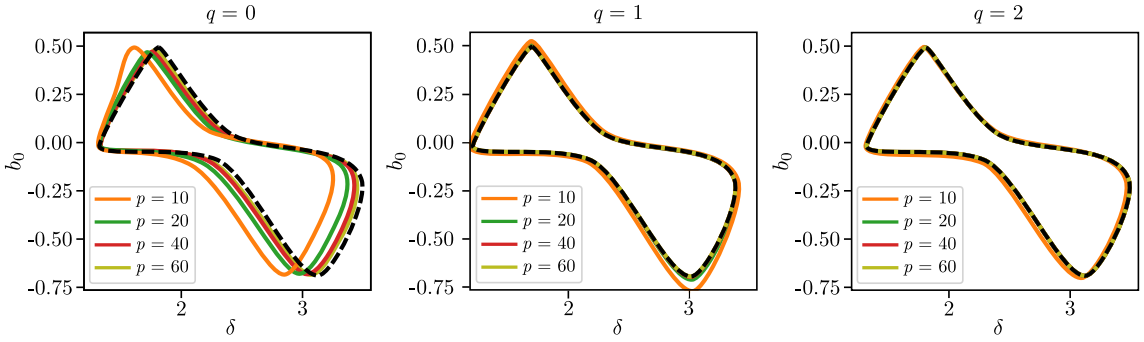

Figure 4.10. *Convergence of the second moment stability boundary with parameters* $a_1 = 0.1$, $\omega = 1$, $\varepsilon = 1$, $\sigma_0 = 0.275$. *The reference stability boundary is denoted with the dashed black lines, obtained using a semidiscretisation with* $q = 7$ *and* $p = 80$.

During the calculations of these diagrams a fifth order $(q = 5)$ Lagrange polynomial was used to approximate the delay state during semidiscretisation along with a sufficiently large period resolution $p = 80$. Similarly to Figure 4.10 the stability boundaries were found using MDBM [7] with an initial 25×16 grid for the parameter plane (δ, b_0) followed by 5 halving iterations. It is important to emphasise that for cases where the time delay τ does not equal to the principal period T, the period resolution p does not equal to the delay resolution r, even in cases $q = 0$ and 1. It can be observed, that in the undamped $(a_1 = 0)$ and deterministic cases (first row, blue lines for $\sigma_0 = 0$) the stability regions have a special structure, namely there are stable islands bounded by straight lines [37]. As the intensity of the stochastic terms are increased, these islands are decreasing, first only slowly near the corners, then the stable regions completely disappear in an accelerating manner. However, if damping is added $(a_1 = 0.2)$ these island are joined and the system described by (4.3.1) becomes much more robust against the noise. For the cases in which the ratio τ/T is not an integer (e.g. in the last row where $\tau/T = 0.5$), due to the interaction of the time-delayed term and the parametric excitation the stability charts become complex and intricate, which gets simplified as the increasing noise intensity decreases the significance of this interaction.

Note that these second moment stability boundaries are robust, meaning if there is no additive noise $(\sigma = 0)$ exciting the system (4.3.1), then it gives only a sufficient condition for stochastic stability (the process can be stable outside of the calculated stable domain). However, if one has to consider additive noise $(\sigma \neq 0)$, then the parameters taken from the stable region calculated with this approach guarantees that the trajectories describing the solution will stay in a finitely bounded region and there exist a stationary second moment.

Next the stationary periodic second moment determined using Eq. (3.2.35) derived from the stochastic semidiscretisation method and it is compared to results obtained with statistical evaluation of direct Monte-Carlo simulations of (4.3.1). The comparisons were conducted using the parameters $a_1 = 0.2$, $\varepsilon = 2$, $\delta = 3.25$, $b_0 = -0.2$, $\sigma_0 = 0.2$, additive noise intensity $\sigma = 1$ and three different parametric excitation frequencies: $\omega = 2, 1$ and 0.5 (denoted by black $\times$-s in Fig 4.11). The Monte-Carlo simulations were conducted using the Euler-Maruyama method for SDDE-s with time step relative to the principal period of the system $\Delta t^{MC} = T/2000 = 2\pi/2000\,\omega$ with the *StochasticDelayDiffEq.jl*. The system (4.3.1) was integrated for 600 periods, while 80 individual trajectories were calculated. To ensure that the initial conditions are not influencing the results, the first 100 periods were dropped from each trajectory, leaving $500 \times 80 = 40000$ periods altogether, providing statistically sufficient number of periods to average over.

The comparison is shown in Fig. 4.12: since the stationary first moment is zero (no additive determinist excitation is present) the convergence of the stationary periodic standard deviation is presented only. Furthermore, a more compact notation is introduced for the periodic stationary

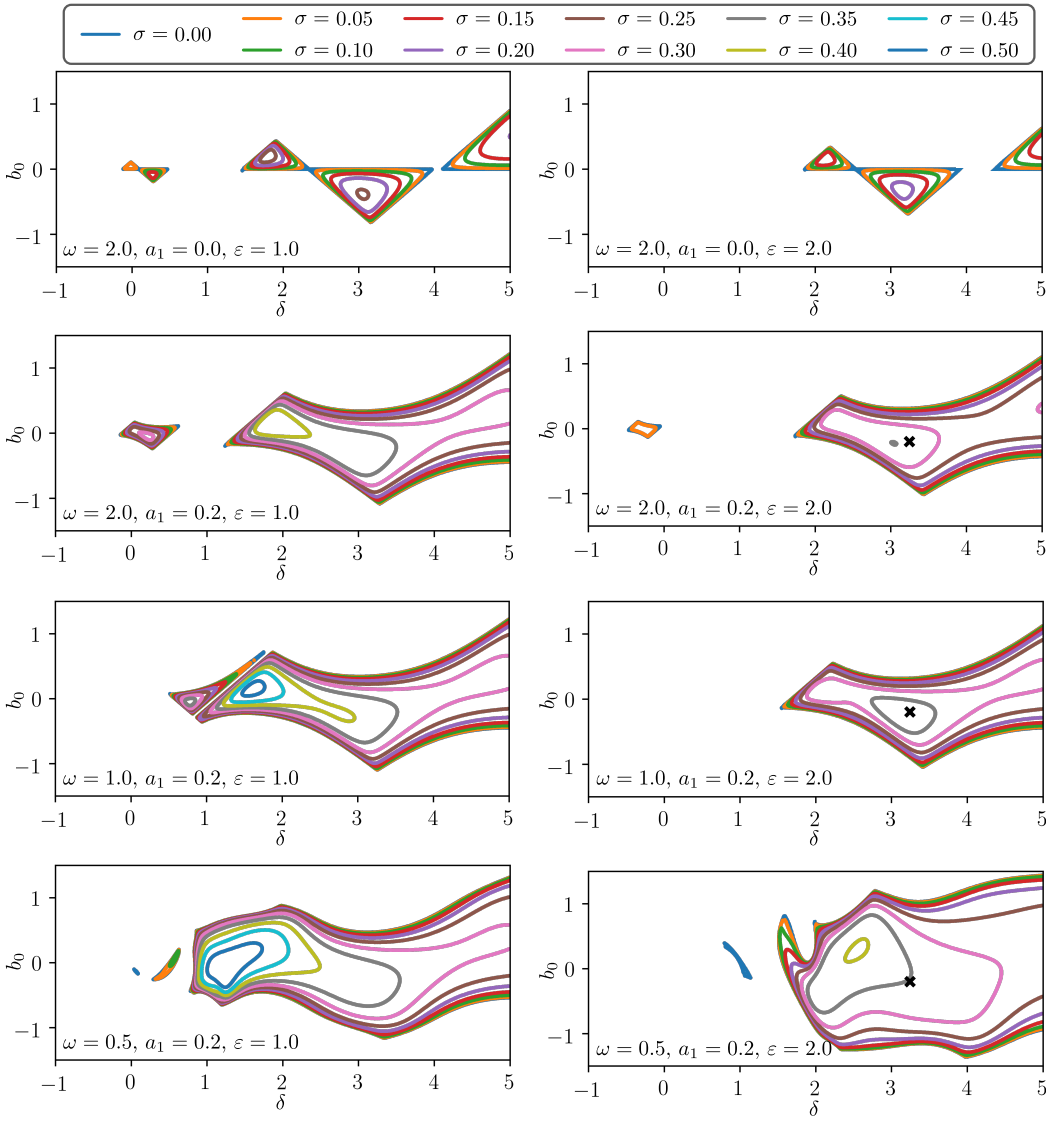

Figure 4.11. *Second moment stability charts for Eq.* (4.3.1) *for different values of* ε, ω *and* a_1. *The period resolution is* $p = 80$ *and the delayed state is approximated with a* $q = 5$ *order polynomial for all cases.*

standard deviation:

$$\mathrm{StD}_x^{\mathrm{st}}(s) = \lim_{k\to\infty} \mathrm{StD}(x_{kT+s}) \quad \text{where} \quad s \in [-T, 0]. \tag{4.3.7}$$

In the figure the red $\times$-s denote the reference solution obtained via Monte-Carlo simulations, plotted with time density being $\Delta t_{\mathrm{plot}}^{\mathrm{MC}} = T/20$. The convergence w.r.t. the period resolution p and w.r.t. the order of the Lagrange polynomial approximating the delay state q is shown in the left and right columns, respectively. When the convergence w.r.t. the period resolution p is shown, the polynomial order is fixed to $q = 0$, while when the convergence is investigated w.r.t. the order q the resolution is fixed to $p = 20$. In the left column it can be seen, that the zeroth-order stochastic semidiscretisation method converges to the reference solution even for smaller period resolutions ($p = 20$), but the accuracy can be further improved if higher-order stochastic semidiscretisations are applied as it can be seen in the right column.

Next, to further demonstrate the convergence of the introduced stochastic semidiscretisation method the mean-square error of the stationary second moment compared to a reference solution is investigated, namely

$$l_2(p) = \sqrt{\frac{1}{p} \sum_{t_n \in \Delta(p)} \left(\mathrm{StD}_{x,p}^{\mathrm{st}}(t_n) - \mathrm{StD}_{x,\mathrm{ref}}^{\mathrm{st}}(t_n)\right)^2}, \tag{4.3.8}$$

where $\Delta(p) = \{-T, \dots, -2T/p, -T/p\}$.

In Fig. 4.13a-c the $\ell_2(p)$ error is shown for period resolutions $p = 2, 4, 8, \dots, 128$ and for $q = 0, 1, \dots, 5$. The reference periodic stationary standard deviation was computed using a higher-order semidiscretization with $q = 7$ and $p = 256$.

To give an approximation of the convergence of the ℓ_2 error in the presented p-range black lines are given with slopes corresponding to 1st, 2nd order convergences. It can be observed that the results computed with $q = 0$th order converge approximately with order 1, the results obtained using higher-order semidiscretization converge approximately with order 2 to the reference solution. One reason for the limited convergence rate can be caused by the averaged constant $\bar{\mathbf{A}}(n)$ term in the approximating SDE (3.2.5), as similar beahviour is shown for the deterministic semidiscretization in [41]. Another factor is the approximation of the multiplicative present state, which lowers the convergence rate that can be achieved even for one mapping step, as shown in [87].

Furthermore, to analyse the performance of the method to determine the stationary second moment, 50 samples of benchmark runs were conducted for each point of p and q of the stationary second moment calculation, where the required computational time and the memory usage was recorded for every sample. During a benchmark run, the whole process of the construction of the deterministic and stochastic mapping matrices and vectors, the multiplications over a mapping period, and the LU decomposition needed to solve equation (3.2.36) is included. In Figure 4.13d and e the relative time and memory required for the calculations are shown, where the reference median computation time is 0.328 ms, and reference median memory requirement is 403.95 KiB, which occurs at $p = 10$ and $q = 0$. Here it can be seen that for large period resolutions p the matrix operations are the dominant source of the computational costs, similarly as in the case of the spectral radius calculations, demonstrated in Figure 4.9c-d. Based on [22] the complexity of the LU decomposition on a parallel processor is between $\mathcal{O}(n^2)$ and $\mathcal{O}(n^3)$ for a problem of size n, so in our case it should be between $\mathcal{O}(p^4)$ and $\mathcal{O}(p^6)$. The trends observable in Fig 4.13d and e coincide with this prediction. The additional computation requirements by the higher q order semidiscretization are not significant even for small p period resolutions.

Note that for higher p values, the computation of stationary quantities is challenging due to the high memory demand of the stochastic semidiscretization method $\left(\sim p^4\right)$ [87].

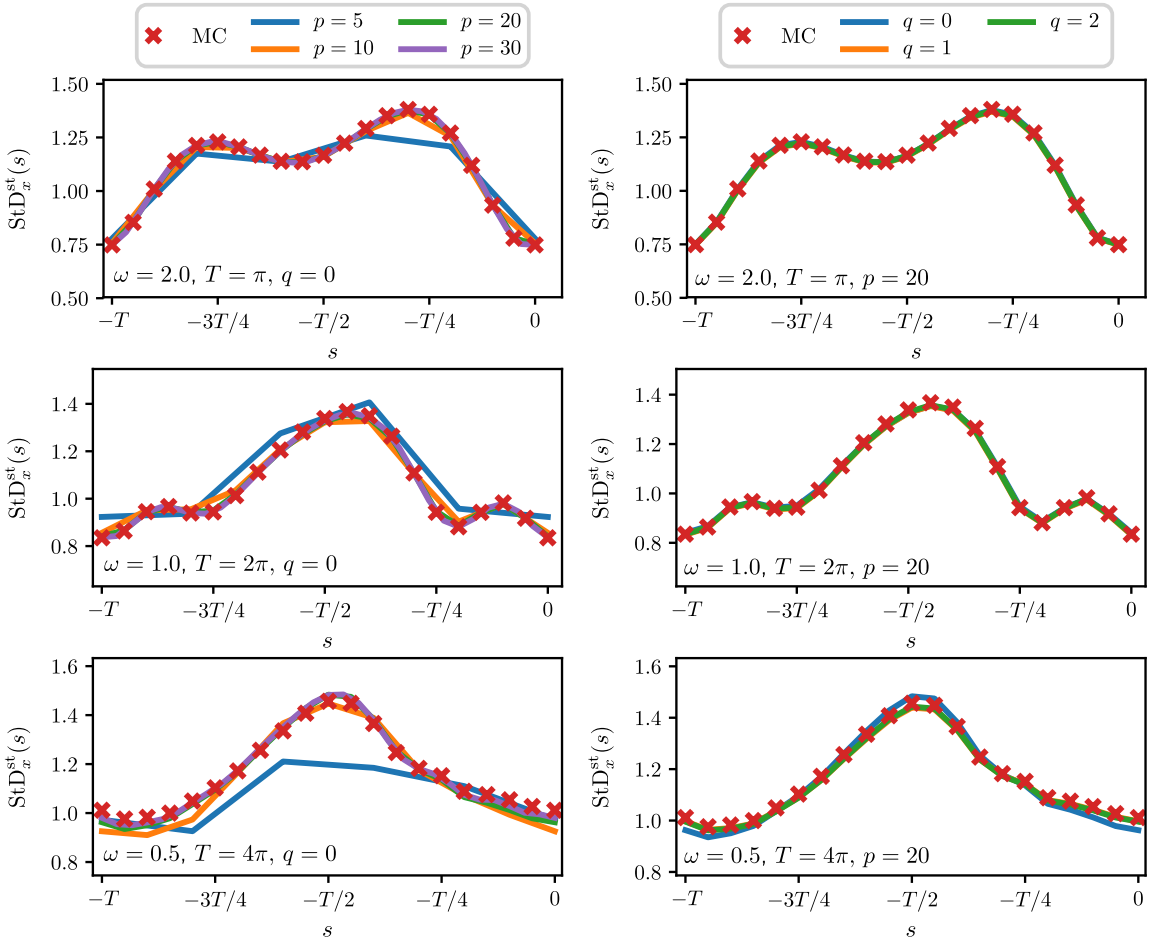

Figure 4.12. *Comparison of the stationary periodic standard deviations obtained with the stochastic semidiscretisation method (denoted by lines) with the results obtained through Monte-Carlo simulations (denoted by the red $\times$-s). The stationary standard deviations are calculated for different values of ω and for $a_1 = 0.2$, $\delta = 3.25$, $b_0 = -0.2$, $\sigma_0 = 0.2$ and $\varepsilon = 2$ (black $\times$-s in Fig 4.11).*

To compare the performance of the stochastic semidiscretization method to the Monte-Carlo simulations, the computational time required for the Monte-Carlo simulations was also measured, and compared to the median computational time requirements of the stochastic semidiscretization method. In Figure 4.14 the ℓ_2 error measure is shown with respect to the computational time for the stochastic semidiscretization method and for the Monte-Carlo simulations with different number of averaged periods, denoted with the numbers on the black lines and different time size $\Delta t^{\mathrm{MC}} \in \{T/2^8, T/2^9, \dots, T/2^{14}\}$. The reference solution was calculated with stochastic semidiscretization with $q = 7$ and $p = 256$. In this figure, it can be observed that the error in the Monte-Carlo simulation is slightly influenced by the number of the averaged periods, however, the effect of the time step Δ^{MC} of the Euler-Maruyama method is the dominant factor. More importantly, it is also apparent that stochastic semidiscretization can provide the same accuracy as the Monte-Carlo simulations orders of magnitudes faster; e.g., the stochastic semidiscretization can lead to $\ell_2 = 10^{-3}$ error using 4 magnitudes less computational resource then the applied Monte-Carlo method.

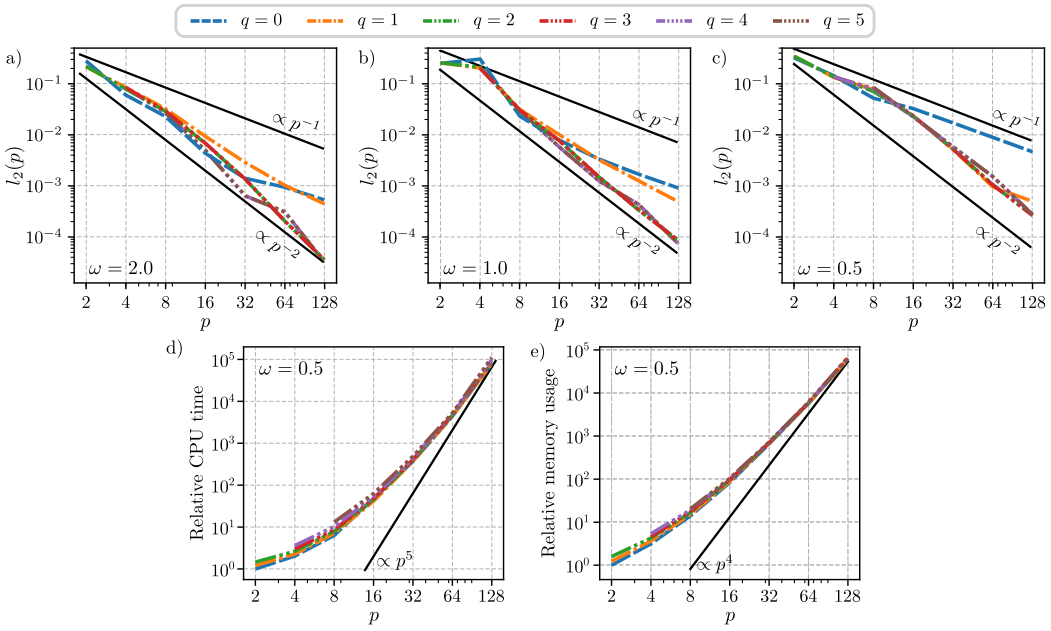

Figure 4.13. *Panels a)-c) show the $\ell_2(p)$ error defined by (4.3.8) computed utilising the stationary second moment of the stochastic delayed Mathieu equation (4.3.1) with numerical parameters $a_1 = 0.2$, $\delta = 3.25$, $b_0 = -0.2$, $\sigma_0 = 0.2$, $\varepsilon = 2$ and $\sigma = 1$ (black $\times$-s in Fig 4.11) and reference solution computed using $q = 7$ and $p = 256$. Panels d) and e) show the median relative computation time and median memory usage of the computations, respectively, based on 50 benchmarking runs for each point. The reference median computation time is 0.328 ms, while the reference median memory requirement for the calculations is 403.95 KiB. These values correspond to $q = 0$ and $p = 2$.*

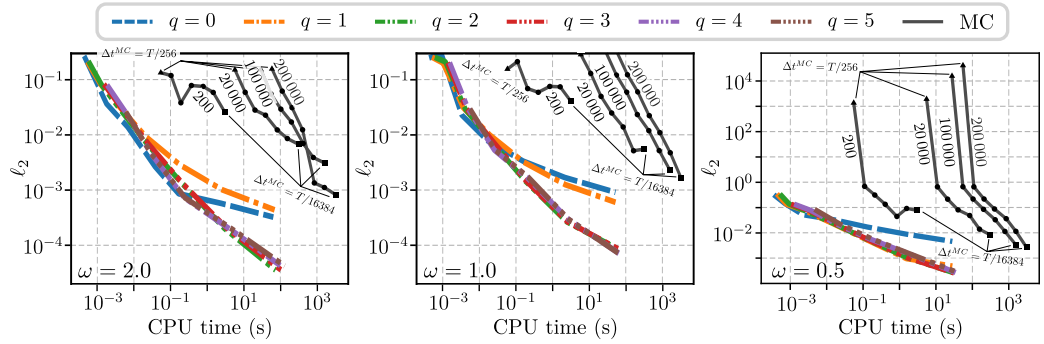

Figure 4.14. *The ℓ_2 error defined by (4.3.8) for the stochastic delayed Mathieu equation with numerical parameters $a_1 = 0.2$, $\delta = 3.25$, $b_0 = -0.2$, $\sigma_0 = 0.2$, $\varepsilon = 2$ and $\sigma = 1$ (black $\times$-s in Fig 4.11) with respect to the required median computation time. The reference solution was computed using the stochastic semidiscretization method with $q = 7$ and $p = 256$. The results are compared to the the Monte-Carlo simulations denoted with black lines. The numbers on the black lines are corresponding to the number of the averaged periods used when statisticially evaluating the Monte-Carlo simulations*

4.4 Hayes Equation with Stochastic Delays

To illustrate the dynamics and stability analysis of the mean and the second moment established in Sec. 3.3 the scalar Hayes equation with stochastic delays is considered. Assuming additive noise that is the sum of a Gaussian noise and a delay induced noise

$$\mathrm{d}x_t = \big(ax_t + bx_{t-\tau_{\mathrm{s},t}} + \sigma_\tau\left(\tau_{\mathrm{s},t} - \bar{\tau}_{\mathrm{s}}\right)\big)\mathrm{d}t + \sigma \mathrm{d}W_t, \tag{4.4.1}$$

is obtained, where $a, b, \sigma_\tau, \sigma \in \mathbb{R}$. The delay $\tau(t)$ is assumed to take one of the values $\tau_1 = 0.2$, $\tau_2 = 0.3$, or $\tau_3 = 0.4$ at each holding period with equal probability $w_{j_\tau} = 1/3$, $j_\tau = 1, 2, 3$ resulting the mean delay $\bar{\tau}_{\mathrm{s}} = \sum_{j_\tau=1}^{J_\tau=3} w_j \tau_{j_\tau} = 0.3$.

To investigate the stability properties and the stationary first and second moments of (4.4.1) the systems (3.3.25) and (3.3.31) are constructed. The condition $\rho\big(\overline{\mathbf{K}}\big) < 1$ is used to calculate mean stability while $\rho\Big(\overline{\overline{\mathbf{K}}}\Big) < 1$ is required for second moment stability. The stationary mean and second moment are given in (3.3.29) and (3.3.38).

The stochastic mapping matrices using Eqs. (3.1.4), (3.1.9) and (3.3.11) are calculated as:

$$\mathbf{F} = \begin{pmatrix} \mathrm{e}^{a\Delta t} & 0 & \cdots & 0 \\ 1 & 0 & \cdots & 0 \\ 0 & \ddots & & \vdots \\ 0 & \cdots & 1 & 0 \end{pmatrix}, \quad \mathbf{F}_{\mathrm{s},n} = \begin{matrix} \\ \\ \\ \\ \end{matrix} \begin{matrix} \begin{matrix} 1 & 2 & \cdots & r_{\mathrm{s},n}+1 & \cdots & r+1 \end{matrix} \\ \begin{pmatrix} 0 & 0 & \cdots & \frac{b}{a}\left(\mathrm{e}^{a\Delta t} - 1\right) & \cdots & 0 \\ 0 & 0 & 0 & \cdots & 0 & 0 \\ \vdots & \vdots & \vdots & \ddots & \vdots & \vdots \\ 0 & 0 & 0 & \cdots & 0 & 0 \end{pmatrix} \end{matrix}, \tag{4.4.2}$$

where $r_{\mathrm{s},n} = \lfloor \tau_{\mathrm{s},t_n}/\Delta t \rfloor$ and $r = r_{J_\tau} = \lfloor \tau_{J_\tau}/\Delta t \rfloor$; cf.(3.3.5) and (3.3.12). From (3.3.9) and (3.1.6) the stochastic mapping vectors are

$$\mathbf{g} = \begin{pmatrix} \int_{t_n}^{t_{n+1}} \mathrm{e}^{a(\Delta t - t)} \sigma \mathrm{d}W_t \\ 0 \\ \vdots \\ 0 \end{pmatrix}, \qquad \mathbf{g}_{\tau,n} = \begin{pmatrix} \frac{\sigma_\tau}{a}\left(\mathrm{e}^{a\Delta t} - 1\right)\left(\tau_{\mathrm{s},t_n} - \bar{\tau}_{\mathrm{s}}\right) \\ 0 \\ \vdots \\ 0 \end{pmatrix}. \tag{4.4.3}$$

Given the terms in (4.4.2)-(4.4.3), to use condition for the stability of the first moment $\rho\big(\overline{\mathbf{K}}\big) < 1$ one can obtain $\overline{\mathbf{K}}$ from (3.3.17) and (3.3.26), and to use condition for the stability of the second moment $\rho\Big(\overline{\overline{\mathbf{K}}}\Big) < 1$ one can obtain $\overline{\overline{\mathbf{K}}}$ from (3.3.33). For the stationary mean $\bar{\mathbf{z}}_{\mathrm{st}}$ and second moment $\bar{\bar{\mathbf{z}}}_{\mathrm{st}}$ in (3.3.29) and (3.3.38), one can obtain $\bar{\mathbf{l}}_\tau$ from (3.3.27) and $\bar{\mathbf{k}}$, $\bar{\bar{\mathbf{l}}}_\tau$ and $\bar{\bar{\mathbf{l}}}_W$ from (3.3.34), (3.3.35), and (3.3.36).

To generate the results below the time step $\Delta t = 0.01$ is used. This is sufficiently small to approximate well the stability boundaries of this example (see also the discussion in [30] where this example is taken from).

The left panel in Fig. 4.15 shows the stability boundaries in the (a, b) parameter space for holding times $T_\tau = 0.1, 0.3, 0.5$, and 1 as indicated by color. Notice that the holding time values are chosen such that they span a relatively large range with respect to the delay values, i.e., $T_\tau = 0.1$ is smaller than all the delays, $T_\tau = 0.3$ is the mean delay, and $T_\tau = 0.5$ and 1 are larger than all the delays. Dashed lines indicate mean stability boundaries while solid lines bound the second moment stability regions. That is, on the left side of the dashed lines the mean converges to the stationary solution (3.3.29) while on the right side is diverges to infinity. Similarly, on the left side of the solid lines the second moment converges to the stationary solution 3.3.38 and it diverges on the right side of these boundaries.

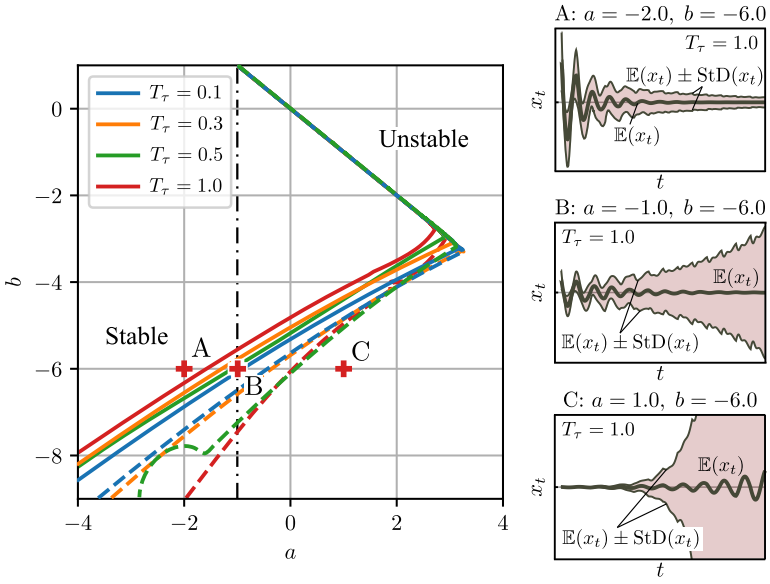

Figure 4.15. *(Left) Mean (dashed) and second moment (solid) stability boundaries for the Hayes equation* (4.4.1) *for different values of the holding time T_τ as indicated by color. The charts were determined using $\Delta t = 0.01$ and using MDBM [7]. (Right) Numerical simulation results for points A,B,C when $T_\tau = 1$ with the mean and standard deviations highlighted.*

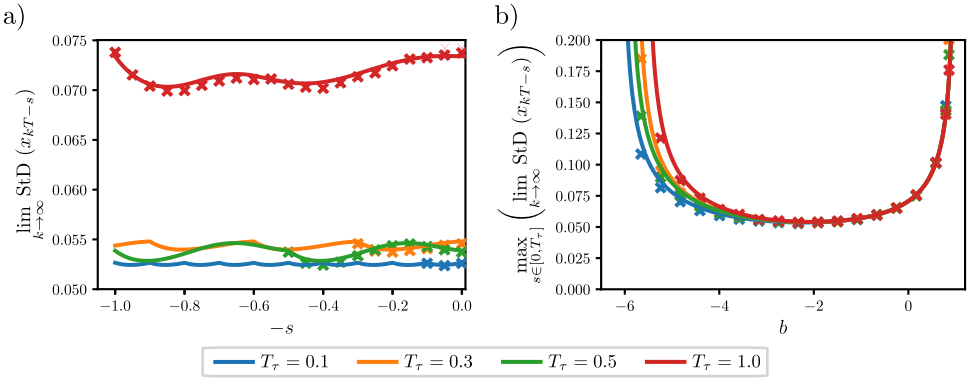

Figure 4.16. *a) Stationary standard deviation over a holding period T_τ for the Hayes equation* (4.4.1) *with parameters $a = -1$, $b = -4.5$ and white noise excitation ($\sigma_\tau = 0$, $\sigma = 1$). b) The maximum values of the stationary standard deviation over a holding time along the dashed-dotted line in Fig. 4.15. The continuous line denotes results obtained with semidiscretisation while the $\times$-s are obtained by MC simulations.*

The right panel in Fig. 4.15 shows three different moment realizations to demonstrate the three types of stability states: moment stable (case A), first moment stable – second moment unstable (case B), and moment unstable (case C). In order to illustrate the behaviour of the dynamical system (4.4.1) in the different parameter domains the ensemble standard deviation $\mathrm{StD}(x_t)$ is used. It can be observed, that when the system (4.4.1) is moment stable (case A), then both the first and second moments converge. However, as the parameters are moved towards the unstable areas first the second moment diverges (case B), then the first moment also loses stability (case C).

Next, to validate the result obtained with semidiscretisation the stationary mean and standard deviation are calculated utilizing (3.3.38) with time resolution $\Delta t = 0.01$, and the results are compared with statistical evaluations of the mean and second moment obtained by MC simulations of system (4.4.1). For these simulations, the Euler-Maruyama method is used with a time step $\delta t = 0.001$.

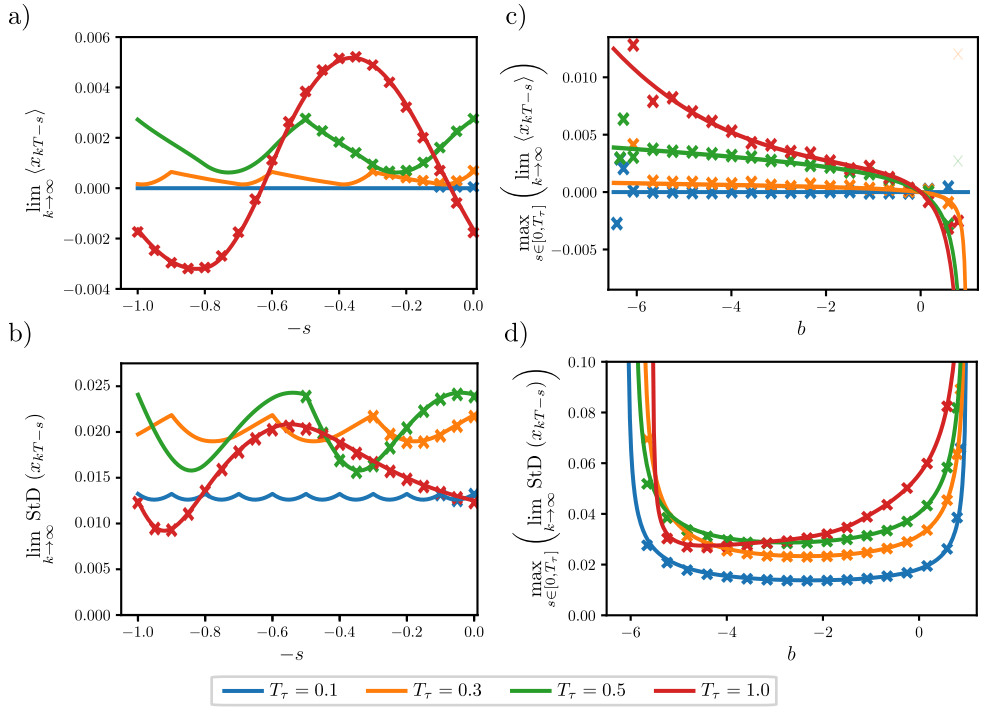

Figure 4.17. *a) Stationary mean and b) standard deviation over a holding period T_τ for the Hayes equation (4.4.1) with parameters $a = -1$, $b = -4.5$ and delay excitation ($\sigma_\tau = 1$, $\sigma = 0$). Maximum values of c) the mean and d) the stationary standard deviation along the dashed-dotted line in Fig. 4.15. The continuous line denotes results obtained with semidiscretisation while the $\times$-s denote the results obtained by MC simulations.*

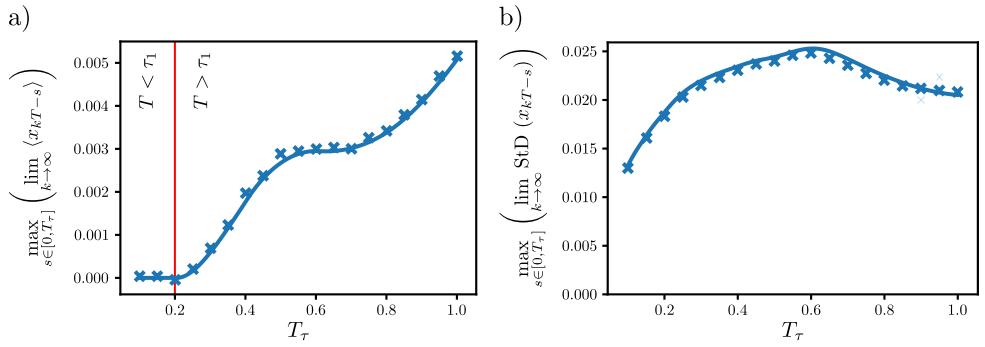

Figure 4.18. *Maxima of the a) stationary mean and b) standard deviation over a holding period T_τ for the Hayes equation (4.4.1) with parameters $a = -1$, $b = -4.5$ and different T_τ holding times for delay excitation ($\sigma_\tau = 1$, $\sigma = 0$). The continuous line denotes results obtained with semidiscretisation while the $\times$-s denote the results obtained by MC simulations. Note that first moment is zero for $T_\tau < \tau_1$.*

In Fig. 4.16(a) the stationary standard deviations are shown over as a function of time for different holding times when the additive noise is purely due to the white noise excitation, i.e., $\sigma_\tau = 0$ and $\sigma = 1$ in (4.4.1). The results are shown up to $s = 1$ for all holding times, that is, the augmented vector (3.1.7) includes the time history up to the largest holding time $T_\tau = 1$. The results of the semidiscretisation (solid lines) are compared with the results obtained by MC simulations ($\times$-s). Notice that the stationary standard deviation gained by both methods show periodic variation with period T_τ due to the periodic switching of the delay process $\tau_{s,t}$, even though the additive noise gives no periodic excitation [21].

In Fig. 4.16(b) we show the maximum value of the stationary standard deviation within a

holding interval while setting $a = -1$ and varying b within $[-6.5, 1]$; see the vertical dashed-dotted line in the stability chart in Fig. 4.15. As the parameters of the system approach the stability boundary, the effect of the noise on the stationary standard deviation is magnified, leading to the so-called stochastic coherence resonance; see [14, 53, 84]. Note that the stationary mean is constantly zero for any holding time T_τ. This is due to the fact that the white noise excitation is independent of the random delay fluctuations. This can also be verified by observing that $\mathbf{l}_{\tau,k} \equiv \mathbf{0}$ in (3.3.25) and $\bar{\mathbf{l}}_\tau \equiv \mathbf{0}$ in (3.3.29), because $\mathbf{g}_{\tau,n} \equiv \mathbf{0}$ in (3.3.11) due to $\sigma_\tau = 0$.

In Fig. 4.17(a)-(b) the stationary mean and standard deviation are shown as function of time over a holding time interval for the delay induced noise scenario ($\sigma_\tau = 1$ and $\sigma = 0$ in (4.4.1)). Notice that since the delay $\tau_{\mathrm{s},t}$ switches at every kT_τ, the stationary beahviour shows a periodic beahviour with period T_τ. This can be observed in both the stationary mean and standard deviation. In Fig. 4.17(c)-(d) the maximum value of the stationary mean and standard deviation over a holding interval are depicted for the delay induced noise case when considering parameters $a = -1$, $b \in [-6.5, 1]$. In Fig. 4.17(d) the stochastic resonance can be observed again for the parameters in the vicinity of the stability boundaries. Meanwhile a stability loss can be observed for the stationary first moment in Fig. 4.17(c) near $b = 1$ (upper stability boundary) only.

In Fig. 4.18 the maxima of the stationary moments are shown as a function of the holding time T_τ. In Fig. 4.18(a) it can be observed, that if the holding time T_τ is larger than the smallest delay value τ_1, the stationary mean is not zero any more. In particular, examining $\bar{\mathbf{l}}_\tau$ in (3.3.27) one can see that for $T_\tau > \tau_1$ the quantity $\bar{\mathbf{l}}_\tau$ is non-zero yielding non-zero stationary mean, even though the excitation term $\sigma_\tau(\tau_{\mathrm{s},t} - \bar{\tau}_\mathrm{s})$ has a zero expected value. The stationary standard deviation does not show any special behaviour with respect to the holding time T_τ around the smallest delay value τ_1, however it decreases as T_τ increases. This can be due to the reason, that as T_τ takes greater values, the delay induced noise causes resonance-like phenomenon. However, if T_τ is further increased, the same time delay is held for longer time allowing the variations around the temporary equilibrium state to settle before the next additive time delay induced switching in $\sigma_\tau(\tau_{\mathrm{s},t} - \bar{\tau}_\mathrm{s})$ perturbs system (4.4.1) again.

Notice that the MC simulations approximate the results obtained via semidiscretisation well. However, the latter approach only requires a few matrix multiplications and solving a system of linear equations, which are orders of magnitudes faster than calculating thousands of realizations and statistically evaluating them. This suggests that the proposed method is a very efficient tool to investigate the beahviour of such systems, especially for higher dimensional state variables.

Chapter 5

Engineering Applications

In this chapter some engineering applications are given, which rely on the analysis of stochastic delay differential equations. The examples in Secs. 5.1, 5.2 and 5.3 are discussing the effect of stochastic cutting force (see the typically measured force signal in Fig. 6.2) on the stability and stationary behaviour of cutting processes such as turning and milling. These sections show, how in the field of machine tool vibrations the stochastic perturbation on the cutting force can lead to large amplitude vibrations, which can be falsely identified as the self excited oscillation called chatter. However, it is also shown, how the robustness of a turning operation against white noise excitation can be made worse by increasing the stable parameter region. Furthermore, it is discussed, how the noise-induced resonance can be utilised, to predict chatter before it forms.

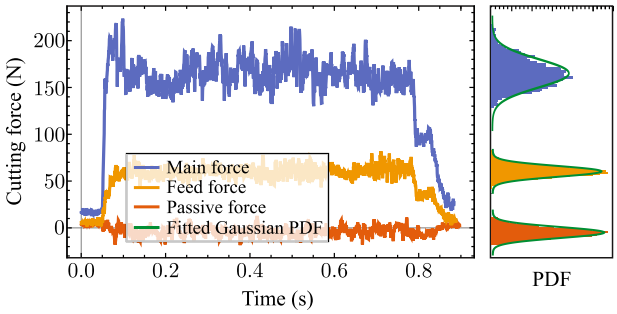

Figure 5.1. *Examples of force signal components and the corresponding probability density functions (PDFs) measured during a turning operation.*

Finally, Sec. 5.4 investigates how stochastic effects influence a connected control system, namely a scenario is analysed when a connected automated vehicle (CAV) follows a connected human driven vehicle (CHV). The CHV measures its position and velocity and broadcasts it through wireless communication, while the CAV listens and adjusts its velocity correspondingly. However, during this communication packet losses can occur, which are modelled as stochastic time delays in the corresponding delay differential equation.

The chapter is organised the following way. In Sec. 5.1 the effect of stochastic perturbation of the deterministic turning models are investigated through the stability and stationary moment analysis of turning models. In Sec. 5.2 it is investigated, how spindle variation affects surface roughness in presence of a noisy cutting force. In Sec. 5.3 the difficulties of chatter detection during milling is accurately explained through the stochastic model of milling, and a possible measure is given to quantify chatter. In Sec. 5.4 a topic related to control theory is discussed, namely the effects of stochastic packet losses on a connected automated vehicle control.

5.1 Stochastic Model of Turning

To demonstrate the effect of the stochastic cutting force on the dynamics of cutting processes [84], the simple one degree of freedom regenerative model of orthogonal turning is used [94, 95]:

$$\ddot{z}_t + 2\zeta\omega_{\mathrm{n}}\dot{z}_t + \omega_{\mathrm{n}}^2 z_t = \frac{1}{m}F_t. \tag{5.1.1}$$

In this model, the cutting tool is considered as a linear oscillator with natural frequency $\omega_{\mathrm{n}} = \sqrt{k/m}$ and damping coefficient $\zeta = c/m$, where m, k and c are the modal mass, stiffness and the viscous damping, respectively.

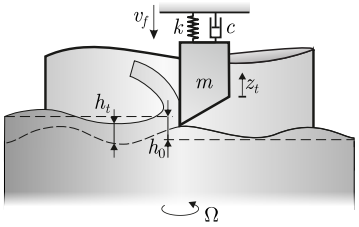

Figure 5.2. *Mechanical model of orthogonal turning*

This oscillator is excited by the stochastic cutting force F_t which can be partitioned into a deterministic mean cutting force F_{m} and a stochastic force perturbation F_σ, namely

$$F_t = F_{\mathrm{m}}(h_t) + F_{\sigma,t} \tag{5.1.2}$$

The deterministic mean cutting force F_{m} depends on the chip thickness h, which is described by the surface regeneration effect, calculated using the actual and a delayed tool position [78]:

$$h_t = h_0 + z_{t-\tau} - z_t, \tag{5.1.3}$$

where h_0 is the nominal chip thickness. The delay τ is corresponds to the the spindle speed of the workpiece, namely $\tau = \Omega/2\pi$, where Ω is the spindle's angular frequency.

To analyse the small amplitude vibration around the stationary position of the tool, it is assumed, that the mean cutting force F_{m} depends on the chip thickness h according to the widely used deterministic shifted linear cutting force model [2, 40, 41, 94, 95]:

$$F_{\mathrm{m}}(h_t) = K_{\mathrm{z}}\left(h^* + h_t\right), \tag{5.1.4}$$

where K_{z} is the resultant cutting force coefficient, which includes the average effects of the material properties as well as the chip width w, while h^* is the shift parameter. Based on preliminary measurements (see Chap. 6 and [27, 85]) it is assumed, that the stochastic cutting force perturbation F_σ is a Gaussian white noise process and its intensity is proportional to the mean cutting force with ration σ_0, namely

$$F_{\sigma,t} = \sigma_0 F_{\mathrm{m}}(h_t)\Gamma_t. \tag{5.1.5}$$

With these assumptions, the stochastic cutting force is described as:

$$F_t = K_{\mathrm{z}}\left(h^* + h_t\right)\,\left(1 + \sigma_0\Gamma_t\right). \tag{5.1.6}$$

Substituting Eqs. (5.1.3) and (5.1.6) into (5.1.1) leads to

$$\begin{aligned} \ddot{z}_t + 2\zeta\omega_{\mathrm{n}}\dot{z}_t + \omega_{\mathrm{n}}^2 z_t & \\ &= H(h^* + h_0 + z_{t-\tau} - z_t) \\ &+ \sigma_0 H(h^* + h_0 + z_{t-\tau} - z_t)\Gamma_t, \end{aligned} \tag{5.1.7}$$

where $H = K_{\mathrm{z}}/m$. To investigate the stochastic perturbation of the mean stationary solution $\langle z_{\mathrm{st}}\rangle = \left(H/\omega_{\mathrm{n}}^2\right)(h^* + h_0)$ a stochastic perturbation process x_t is introduced:

$$z_t = \langle z_{\mathrm{st}}\rangle + (h^* + h_0)\, x_t. \tag{5.1.8}$$

Note that x_t has zero mean $\langle x_t \rangle = 0$. This x_t process describes the motion of the tool around its stationary solution and is normalised with the shifted-nominal chip thickness. Substituting (5.1.8) into (5.1.7) leads to

$$\begin{aligned} \ddot{x}_t + 2\zeta\omega_\mathrm{n}\dot{x}_t + \omega_\mathrm{n}^2 x_t & \\ = H(x_{t-\tau} - x_t) & \\ + \sigma_0 H(1 + x_{t-\tau} - x_t)\Gamma_t. & \end{aligned} \tag{5.1.9}$$

This perturbation equation can be rewritten into the usual representation of a stochastic differential equation, the first order incremental form [5, 61] as in Sec. 3.1:

$$\begin{aligned} \mathrm{d}\mathbf{x}_t = & (\mathbf{A}\mathbf{x}_t + \mathbf{B}\mathbf{x}_{t-\tau})\,\mathrm{d}t \\ & + (\boldsymbol{\alpha}\mathbf{x}_t + \boldsymbol{\beta}\mathbf{x}_{t-\tau} + \boldsymbol{\sigma})\,\mathrm{d}W_t, \end{aligned} \tag{5.1.10}$$

where

$$\begin{gathered} \mathbf{x}_t = \begin{pmatrix} x_t \\ \dot{x}_t \end{pmatrix}, \ \mathbf{A} = \begin{pmatrix} 0 & 1 \\ -\left(\omega_\mathrm{n}^2 + H\right) & -2\zeta\omega_\mathrm{n} \end{pmatrix}, \ \mathbf{B} = \begin{pmatrix} 0 & 0 \\ H & 0 \end{pmatrix}, \\ \boldsymbol{\alpha} = \begin{pmatrix} 0 & 0 \\ -\sigma_0 H & 0 \end{pmatrix}, \ \boldsymbol{\beta} = \begin{pmatrix} 0 & 0 \\ \sigma_0 H & 0 \end{pmatrix}, \ \boldsymbol{\sigma} = \begin{pmatrix} 0 \\ \sigma_0 H \end{pmatrix}. \end{gathered} \tag{5.1.11}$$

In Fig. 5.3a the stability chart is shown, where the unstable and stable areas are denoted with white and blue colors, respectively. The calculations where conducted using the damping $\zeta = 0.1$ and as an overestimation of the stochastic effects $\sigma_0 = 0.1$ (which corresponds to a $10\ \%$ multiplicative noise intensity compared to the mean cutting force). To see effect of the noise originating from the cutting force, the stability boundary for the deterministic case is plotted with dashed line based on the analytical solution presented in [78].

When comparing the stability boundaries gained with the stochastic and deterministic models, it can be observed, that the change in stability is insignificant, the deterministic model is sufficient for the stability calculations. However, if one considers the stationary vibrations caused by the small stochastic cutting force, the noise intensity in the vibrations can be amplified. This can dramatically increase the surface roughness, since this vibration is directly copied onto the surface, and it can lead to additional loads on the tool.

To characterise the intensity of these stochastic vibrations, the stationary standard deviation of the displacement perturbation x_t is defined:

$$\sigma_{x,\mathrm{st}} := \lim_{t\to\infty} \mathrm{StD}\big(x_t^2\big). \tag{5.1.12}$$

By defining a limit (e.g.: based on a prescribed surface quality requirement), the stationary second moment chart can be given by the contour lines of (5.1.12). In Fig. 5.3a, two contours are given for 15 and 30 times dimensionless noise amplification, namely $\sigma_{x,\mathrm{st}}/\big(\sigma_0 H\omega_\mathrm{n}^2\big) = 15$ and 30. The darker blue areas correspond to the parameter regions, where the noise amplification is limited by these values. Although the stability limit (both the deterministic and stochastic) provides stability pockets with optimal and high material removal rates, these optimums cannot be utilised, due to the large stationary stochastic vibrations.

In Fig. 5.3b the stationary second moment is illustrated along the parameter line $H/\omega_\mathrm{n}^2 = 0.3$. These vibrations are extremely amplified near the stability borders; this phenomena is called the stochastic coherence resonance [52]. Note that these theoretical predictions are only valid for small amplitude vibrations, due to the unmodelled nonlinear nature of the cutting force characteristics [2] and the fly-over effect [23]. If in the stable parameter region the vibrations reach a sufficiently large stationary second moment (and therefore large amplitudes), the chatter vibration can occur before the machining would lose the stability predicted with the help of deterministic linear models. This means, that the measurable stability boundaries are potentially shifted towards smaller chip widths

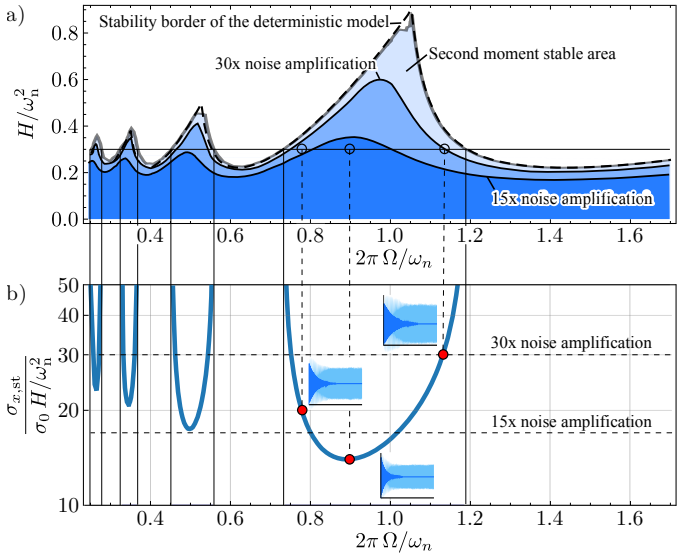

Figure 5.3. *a) Second moment stability chart (blue area) along with stationary second moment limiting charts (darker blue areas) with parameter $\sigma_0 = 0.1$, compared to the deterministic stability borders. b) Noise magnification in the stationary solution along $H/\omega_n^2 = 0.3$. There are three small figures inside illustrating how the first moment decays (dark blue) while the standard deviation of the vibrations persist (light blue) for different spindle speeds Ω based on MC simulations.*

by the stochastic nature of the cutting force. In Fig. 5.3b it can be seen, that as the spindle speed Ω is chosen from the immediate proximity of the stability boundary the effect of the stochastic noise is significantly magnified even though, the intensity of the noise stays constant. This phenomenon can be due to the fact, that the white noise excites through the whole frequency spectrum, and the characteristic damping of the dynamical system representing the turning process decreases, reaching zero at the stability boundary. This means, that even if the presence of the additive stochastic effect is small, it can cause significant vibrations due to the noise-induced resonance, despite of the system being asymptotically stable.

5.2 Stochastic Model of Turning with Spindle Speed Variation

To further demonstrate the application of the periodic stochastic semidiscretisation to a practical problem, the stability and stationary behaviour of a turning operation is investigated. To improve the stability properties of the cutting process, that is to increase the domain from where stable machining parameters can be selected and the chatter [94] phenomena can be avoided, one possibility is to vary the spindle speed in a sinusoidal manner [38]. Similarly to Sec. 5.1, the usual mechanical model of the turning process [94] is shown in Fig. 5.4, while the corresponding governing deterministic equation of motion describing the dynamics is

$$m\ddot{z}(t) + c\dot{z}(t) + kz(t) = F(t). \tag{5.2.1}$$

In this analysis a nonlinear mean cutting force model is assumed as in [23], namely

$$F(t) = K_z\, w\, h^{q_c}(t) \quad \text{where} \quad h(t) = h_0(t) + z(t-\tau(t)) - z(t). \tag{5.2.2}$$

The system (5.2.1) models the cutting tool as a linear oscillator, which is excited by the cutting force $F(t)$ described in by the cutting force characteristics in Eq. (5.2.2) [23]. In Eq. (5.2.1) the parameters m, c and k denote the modal mass, damping and stiffness of the cutting tool, respectively, while in Eq. (5.2.2) K_z and q_c are parameters of the cutting force model, w is the

chip width, $h(t)$ is the time varying chip thickness. In case of constant feed velocity v_f (see Fig. 5.4) and time periodic spindle speed $\Omega(t)$ the nominal chip thickness $h_0(t)$ becomes also time periodic. The time delay $\tau(t)$ originates from the regenerative nature of turning, namely the position of the tool is copied to the machined surface during vibration, and it effects the cutting force one revolution later through the chip thickness. The time dependence of the delay $\tau(t)$ comes from the variable spindle speed described by:

$$\Omega(t) = \Omega_0 + \Omega_1 \cos(\omega_\tau t), \quad \text{where} \quad \omega_\tau = \text{RVF} \cdot \Omega_0 \tag{5.2.3}$$

and the parameter RVF is the ratio of the modulation frequency ω_τ and the mean spindle speed Ω_0. In [39] it is shown, that the corresponding time delay $\tau(t)$ can be approximated as

$$\tau(t) \approx \tau_0 + \tau_1 \cos(\omega_\tau t), \quad \text{where} \quad \tau_0 = \frac{2\pi}{\Omega_0} \quad \text{and} \quad \tau_1 = \tau_0 \cdot \text{RVA}. \tag{5.2.4}$$

Here the notation RVA $:= \Omega_1/\Omega_0$ represents the ratio of the amplitude Ω_1 and the mean value Ω_0. Due to the varying spindle speed the nominal chip thickness $h_0(t)$ varies in time, and it can be described with the help of the feed rate v_f and the varying time delay $\tau(t)$:

$$h_0(t) = v_f \tau(t), \tag{5.2.5}$$

leading to

$$F(t) = K_\text{z}\, w\, (v_f \tau(t) + z(t - \tau(t)) - z(t))^q. \tag{5.2.6}$$

Linearizing the cutting force around $z(t - \tau(t)) - z(t) = 0$ and dividing by the modal mass m gives

$$\frac{1}{m} F(t) \approx \omega_\text{n}^2 \left(H_1 \left(\frac{\tau(t)}{\tau_0} \right)^{q_\text{c}-1} (z(t - \tau(t)) - z(t)) + H_0 \left(\frac{\tau(t)}{\tau_0} \right)^q \right), \tag{5.2.7}$$

where

$$H_1 = \frac{K_\text{z}\, w\, q}{m\omega_\text{n}^2} (v_f \tau_0)^{q_\text{c}-1}, \quad H_0 = \frac{K_\text{z}\, w}{m\omega_\text{n}^2} (v_f \tau_0)^q = \frac{H_1}{q_\text{c}} v_f \tau_0 \tag{5.2.8}$$

and $\omega_\text{n} = \sqrt{k/m}$ is the natural frequency.

To approximate the stochastic and high frequency effects in the cutting force [85], such as chip fragmentation, shock-waves and inhomogeneous material properties, a Gaussian white noise with relative intensity σ_0 is introduced through the cutting force coefficient by replacing the constant cutting force coefficient K_z with the time dependent

$$K_{\text{z},t} := K_\text{z} (1 + \sigma_0 \Gamma_t), \tag{5.2.9}$$

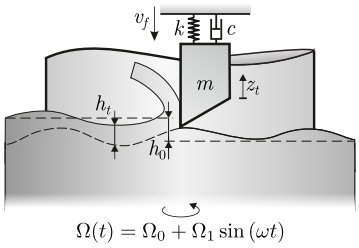

Figure 5.4. *One degree of freedom mechanical model of orthogonal turning with periodic (sinusoidal) spindle speed variation*

which leads to the same partitioning in the cutting force as introduced in (5.1.2). When substituting it into the linearised cutting force model (5.2.7) the equation of motion (5.2.1) becomes a SDDE:

$$\begin{aligned}
&\ddot{z}_t + 2\zeta\omega_\mathrm{n}\dot{z}_t + \omega_\mathrm{n}^2 z_t = \\
&\quad = \omega_\mathrm{n}^2 \left(H_1 \left(\frac{\tau(t)}{\tau_0} \right)^{q_\mathrm{c}-1} (z_{t-\tau(t)} - z_t) + H_0 \left(\frac{\tau(t)}{\tau_0} \right)^{q} \right) \\
&\quad + \sigma_0 \omega_\mathrm{n}^2 \left(H_1 \left(\frac{\tau(t)}{\tau_0} \right)^{q_\mathrm{c}-1} (z_{t-\tau(t)} - z_t) + H_0 \left(\frac{\tau(t)}{\tau_0} \right)^{q} \right) \Gamma_t,
\end{aligned} \tag{5.2.10}$$

where $\zeta = c/(2m\omega_\mathrm{n})$ is the damping coefficient.

To reduce the parameters of the system the dimensionless time $\hat{t} = \omega_\mathrm{n} t$ and displacement $x_{\hat{t}} = z_{\hat{t}}/v_f\tau_0$ are introduced. Substituting these dimensionless variables into Eq. (5.2.10) leads to

$$\begin{aligned}
&x''_{\hat{t}} + 2\zeta x'_{\hat{t}} + x_{\hat{t}} = \\
&\quad = \left(H_1 \left(\frac{\hat{\tau}(\hat{t})}{\hat{\tau}_0} \right)^{q_\mathrm{c}-1} (x_{\hat{t}-\hat{\tau}(\hat{t})} - x_{\hat{t}}) + \frac{H_1}{q_\mathrm{c}} \left(\frac{\hat{\tau}(\hat{t})}{\hat{\tau}_0} \right)^{q} \right) \\
&\quad + \hat{\sigma}_0 \left(H_1 \left(\frac{\hat{\tau}(\hat{t})}{\hat{\tau}_0} \right)^{q_\mathrm{c}-1} (x_{\hat{t}-\hat{\tau}(\hat{t})} - x_{\hat{t}}) + \frac{H_1}{q_\mathrm{c}} \left(\frac{\hat{\tau}(\hat{t})}{\hat{\tau}_0} \right)^{q} \right) \Gamma_{\hat{t}},
\end{aligned} \tag{5.2.11}$$

where

$$\hat{\tau}(t) = \hat{\tau}_0 \left(1 + \mathrm{RVA} \cos\Big(\mathrm{RVF}\, \hat{\Omega}_0\, \hat{t} \Big) \right), \quad \text{with} \quad \hat{\Omega}_0 = \frac{\Omega_0}{\omega_\mathrm{n}}, \quad \hat{\tau}_0 = \omega_\mathrm{n}\tau_0 \tag{5.2.12}$$

and $\square'$ denotes the derivative w.r.t. the dimensionless time $\hat{t}$. Furthermore the coefficent $\hat{\sigma}_0 := \sigma_0/\omega_\mathrm{n}^{5/2}$ is the relative intensity of the rescaled Gaussian white noise process $\Gamma_{\hat{t}}$. For the dimensionless equation of motion (5.2.11) the coefficient matrices of the first order form (3.2.1) are given by:

$$\mathbf{A}(\hat{t}) = \begin{pmatrix} 0 & 1 \\ -1 - H_1 \left(\frac{\hat{\tau}(\hat{t})}{\hat{\tau}_0} \right)^{q_\mathrm{c}-1} & -2\zeta \end{pmatrix}, \tag{5.2.13}$$

$$\mathbf{B}(\hat{t}) = \begin{pmatrix} 0 & 0 \\ H_1 \left(\frac{\hat{\tau}(\hat{t})}{\hat{\tau}_0} \right)^{q_\mathrm{c}-1} & 0 \end{pmatrix}, \qquad \mathbf{c}(\hat{t}) = \begin{pmatrix} 0 \\ \frac{H_1}{q_\mathrm{c}} \left(\frac{\hat{\tau}(\hat{t})}{\hat{\tau}_0} \right)^{q_\mathrm{c}} \end{pmatrix}, \tag{5.2.14}$$

$$\boldsymbol{\alpha}(\hat{t}) = \begin{pmatrix} 0 & 0 \\ -\hat{\sigma}_0 H_1 \left(\frac{\hat{\tau}(\hat{t})}{\hat{\tau}_0} \right)^{q_\mathrm{c}-1} & 0 \end{pmatrix}, \tag{5.2.15}$$

$$\boldsymbol{\beta}(\hat{t}) = \hat{\sigma}_0 \mathbf{B}(\hat{t}), \qquad \boldsymbol{\sigma}(\hat{t}) = \hat{\sigma}_0 \mathbf{c}(\hat{t}), \tag{5.2.16}$$

and the state space vector is

$$\mathbf{x}_{\hat{t}} = \left[x_{\hat{t}}, x'_{\hat{t}} \right]^\top. \tag{5.2.17}$$

To apply the dimensionless parameters in the Eq. (5.2.11) to investigate the effect of the spindle speed variation on the stability and the surface quality, a small number of realistic machining parameters are introduced to connect the mathematical model to the application. First, the damping ratio was set to $\zeta = 0.02$, then a cutting force model, the three-quarter rule is used, with $q_\mathrm{c} = 3/4$ [94]. Furthermore, it is a safe assumption to consider the noise intensity in the cutting force coefficient to be $\hat{\sigma}_0 = 0.1$. Another important parameter is the mean nominal chip thickness

$\bar{h}_0 = v_f \tau_0$, since this scales the dimensionless tool position $x_{\hat{t}}$. In this analysis a realistic value, $\bar{h}_0 = 100\,\mu$m is used.

To guarantee acceptable surface quality, the roughness profile parameter Ra is the commonly used metric, which describes the arithmetic mean value of the magnitude of the measured surface profile ordinates [58]. However, this value cannot be directly calculated using the theorem described in this paper, so the roughness parameter Rq is used, which refers to the root mean square of the surface profile ordinates. For a roughing operation it could be sufficient to select Rq 13.75, referring to the standard deviation of the surface roughness profile peaks being at maximum $13.75\,\mu$m, which approximately corresponds to a Ra 12.5 value [42]. If $h_0 = 100\,\mu$m is chosen, then the Rq 13.75 translates to

$$\max_{s\in[-\hat{T},0]} \mathrm{StD}_x^{\mathrm{st}}(s) = 0.1375 \quad \text{where} \quad \hat{T} = \frac{2\pi}{\mathrm{RVF}\,\hat{\Omega}_0} = \frac{\hat{\tau}_0}{\mathrm{RVF}}\,, \tag{5.2.18}$$

while $\mathrm{StD}_x^{\mathrm{st}}(s)$ is defined in (4.3.7).

To evaluate (5.2.18) one needs to calculate both the stationary first and second moments. However, the variation of the first moment is only considered in the stationary standard deviation, and is not considered separately, since it does not describe surface quality, only the final exact shape of the resulting workpiece, which is not investigated in this study.

In Fig. 5.5 the second moment stability and the surface quality charts (where the stationary second moment is limited by the condition of Rq 13.75) are shown for modulation frequencies $\mathrm{RVF} = \omega_\tau/\Omega_1 = 0.5$ and 0.1, while the corresponding curves for the constant spindle speed turning are given with the dashed lines. The diagrams were determined using $q = 5$ order stochastic semidiscretisation with period resolution $p = 50$ for all cases. The boundaries were found using a MDBM with an initial 21×11 grid for the parameter plane of the dimensionless spindle speed $\hat{\Omega}_0$ and the dimensionless effective cutting force coefficient H_1 followed by 4 halving iteration, resulting in a final grid of 336×176.

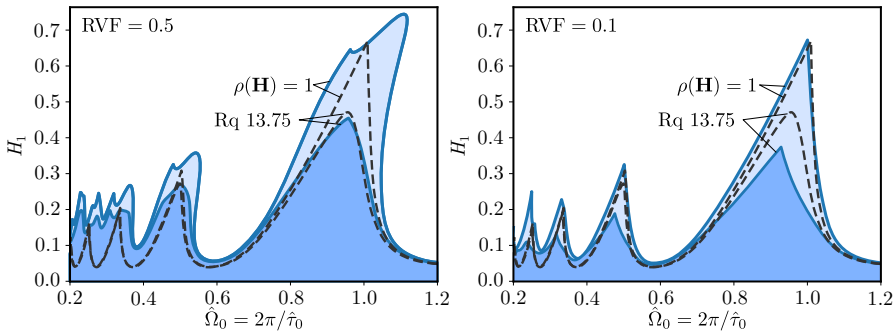

Figure 5.5. *Second moment stability and Rq* 13.75 *limiting charts for turning process with sinusoidal spindle speed modulation with RVA* $= \Omega_1/\Omega_0 = 0.1$. *The dashed lines indicate the corresponding boundaries associated with constant spindle speed turning. Under the curves denoted with* $\rho(\mathbf{H}) = 1$ *and Rq* 13.75 *the process is second moment stable and the maximum of the stationary standard deviation is smaller then the limit* 13.75 μm, *respectively.*

From this analysis it can be deduced, that the application of spindle speed variation with a relatively fast modulation frequency RVF $= 0.5$ (left panel of Fig. 5.5) significantly increases the stable parameter domain even for the high-speed range. This stabilizing effect is more pronounced for lower spindle speeds, where the "stability pockets" merge creating a domain robust against uncertainty in the mean spindle speed Ω_0. This second moment stability chart is almost identical to the traditional (deterministic) stability chart [39, 84], due to the relatively small noise intensity. This effect can also be observed in Fig. 4.11. The surface quality chart behaves similarly, the Rq 13.75 limiting curve follows the change of the stability chart for lower spindle speeds, however,

higher speeds, the application of spindle speed variation with RVF $= 0.5$ does not provide any advantage.

For a more realistic frequency ratio RVF $= 0.1$ the improvement in stability is only significant in the lower spindle speed domains, as it can be observed on the right panel of Fig. 5.5. However, if the surface quality is also considered, the effect is not so obviously positive. Although the bottom of the "instability lobes" rise, causing increased robustness, the peak of the "spikes", inside which the preferable high material removal rates can be achieved, become significantly lower.

5.3 Stochastic Model of Milling

Another problem which leads to periodic delay differential equations is the mechanical modelling of milling. It is essential also in case of milling operations to design the machining process carefully, so the regenerative chatter does not occur during the material removal process. To ensure a stable machining while increasing the material removal rate, there are endeavours to utilise automatic chatter detection during machining, however the quantification of chatter is in most practical cases is still based on empirical expertise [4, 25, 51].

The deterministic models used for the mathematical modelling of milling operations provide capable methods to predict parameter regions where chatter can be avoided, and are used to design tool edge geometries which increase productivity, however, there are some phenomena that they cannot explain. One such phenomena is the rise of chatter peaks in the FFT of the measured stationary vibration signal, which is not connected to the excitation frequencies, and these even occur in stable parameter domains, which is not present in any deterministic model. In this section a mathematically well established explanation is given to this phenomenon, and some remarks are made, how noise-induced resonance can be utilised in machine tool chatter detection.

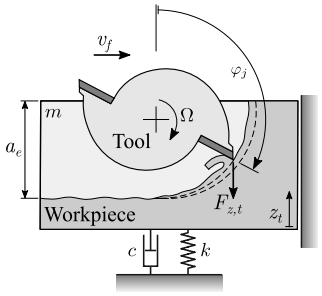

Figure 5.6. *One degree of freedom mechanical model of milling*

First the usual mechanical model of milling is briefly given, based on [46]. The governing deterministic equation of motion describing the dynamics of mechanical model shown in Fig. 5.6 is

$$m\ddot{z}(t) + c\dot{z}(t) + kz(t) = -F_z(t), \tag{5.3.1}$$

where $F_z(t)$ denotes the deterministic cutting force component in the z direction, while m, c and k are the modal mass, damping and stiffness, respectively. In [46] the cutting force is given with the help of the linear cutting force model as

$$F_z(t) = a_p \sum_{j=1}^{N} (-K_{\tan} \sin\varphi_j(t) + K_{\mathrm{rad}} \cos\varphi_j(t)) g_j(t) h_j(t), \tag{5.3.2}$$

where a_p is the axial depth of cut, $K_{\tan}$ and K_{rad} are the tangential and radial cutting force coefficients, respectively, ϕ_j is the angular position of the tooth j. The chip thickness $h_j(t)$ at tooth j can be approximated as

$$h_j(t) \approx f_z \sin\varphi_j(t) + (z(t) - z(t-\tau)) \cos\varphi_j(t), \tag{5.3.3}$$

where $f_z = v_f\tau$ is the feed per tooth in the feed direction and $\tau = 2\pi/(N\Omega)$, while N is the number of teeth. The screen function $g_j(t)$ shows whether the tool cuts into the material and can be given as

$$g_j(t) = \begin{cases} 1, & \text{if } \varphi_{\text{en}} < (\varphi_j(t) \bmod 2\pi) < \varphi_{\text{ex}}, \\ 0, & \text{otherwise}, \end{cases} \tag{5.3.4}$$

where φ_{en} denotes the angular position where the tooth enters into the material, while φ_{ex} is where the tooth leaves the workpiece. Similarly to (5.2.9), the stochastic cutting force coefficients are introduced as

$$K_{\text{tan,t}} = K_{\text{tan}}(1 + \sigma_0\Gamma_t) \quad \text{and} \quad K_{\text{rad,t}} = K_{\text{rad}}(1 + \sigma_0\Gamma_t). \tag{5.3.5}$$

The cutting force with the introduced stochastic coefficients reduces to

$$\begin{aligned} F_{z,t} = &- a_p \sum_{j=1}^{N} (-K_{\text{tan}} \sin\varphi_j(t) + K_{\text{rad}} \cos\varphi_j(t)) g_j(t) h_{j,t} \\ &- a_p\sigma_0 \sum_{j=1}^{N} (-K_{\text{tan}} \sin\varphi_j(t) + K_{\text{rad}} \cos\varphi_j(t)) g_j(t) h_{j,t}\Gamma_{j,t} \end{aligned} \tag{5.3.6}$$

Note that the chip thickness $h_{j,t}$ becomes also stochastic and there are multiple independent stochastic noises $\Gamma_{j,t}$ driving this equation, corresponding to each tooth. The SDDE describing the motion of the milling process is

$$\begin{aligned} m\ddot{z}_t + c\dot{z}_t + kz_t = &- a_p \sum_{j=1}^{N} (-K_{\text{tan}} \sin\varphi_j(t) + K_{\text{rad}} \cos\varphi_j(t)) g_j(t) h_{j,t} \\ &- a_p\sigma_0 \sum_{j=1}^{N} (-K_{\text{tan}} \sin\varphi_j(t) + K_{\text{rad}} \cos\varphi_j(t)) g_j(t) h_{j,t}\Gamma_{j,t}. \end{aligned} \tag{5.3.7}$$

The solution of (5.3.1) with the stochastic cutting force defined in (5.3.6) can be partitioned into a dimensionless periodic deterministic $x_{\text{p}}(t)$ and into a dimensionless stochastic $x_t$component as

$$z_t = f_z\,(x_{\text{p}}(t) + x_t), \tag{5.3.8}$$

where $x_{\text{p}}(t) = x_{\text{p}}(t-\tau)$ and $\langle x_t \rangle = 0$. Furthermore, one can introduce the dimensionless time $\hat{t} = \omega_{\text{n}}t$, where $\omega_{\text{n}} = k/m$ is the natural frequency. Substituting (5.3.3) and (5.3.8) into (5.3.7) leads to the dimensionless equation of motion

$$\begin{aligned} \big(x_{\text{p}}''(\hat{t}) + \zeta x_{\text{p}}'(\hat{t}) + x_{\text{p}}(\hat{t})\big) + \big(x_{\hat{t}}'' + \zeta x_{\hat{t}}' + x_{\hat{t}}\big) = \\ - H\big(G_{\text{s}}(\hat{t}) + G_{\text{c}}(\hat{t})(x_{\hat{t}} + x_{\hat{t}-\hat{\tau}})\big) \\ - \sum_{j=1}^{N} \hat{\sigma} H\big(G_{\text{s},j}(\hat{t}) + G_{\text{c},j}(\hat{t})(x_{\hat{t}} + x_{\hat{t}-\hat{\tau}})\big)\Gamma_{j,t}, \end{aligned} \tag{5.3.9}$$

where $2\zeta\omega_{\text{n}} = c/m$, $\hat{\tau} = 2\pi/\big(N\hat{\Omega}\big)$, $\hat{\Omega} = \Omega/\omega_{\text{n}}$, $H = a_pK_{\text{tan}}/\big(m\omega_{\text{n}}^2\big)$ and $\hat{\sigma} = \sqrt{\omega_{\text{n}}}\sigma_0$ due to the rescaling properties of the Wiener process [61]:

$$\Gamma_t = \sqrt{\omega_{\text{n}}}\Gamma_{\hat{t}} \quad \text{and} \quad \mathrm{d}W_t = \frac{1}{\sqrt{\omega_{\text{n}}}}\mathrm{d}W_{\hat{t}}. \tag{5.3.10}$$

The periodic coefficients can be expressed as $G_{\text{c}}(\hat{t}) = \sum_{j=1}^{N} G_{\text{c},j}(\hat{t})$, $G_{\text{s}}(\hat{t}) = \sum_{j=1}^{N} G_{\text{s},j}(\hat{t})$ and

$$G_{\text{c},j}(\hat{t}) = \big(-\sin\varphi_j(\hat{t}) + r\cos\varphi_j(\hat{t})\big)\cos\varphi_j(\hat{t})g_j(\hat{t}), \tag{5.3.11}$$

$$G_{\text{s},j}(\hat{t}) = \big(-\sin\varphi_j(\hat{t}) + r\cos\varphi_j(\hat{t})\big)\sin\phi_j(\hat{t})g_j(\hat{t}), \tag{5.3.12}$$

where $r = K_{\mathrm{rad}}/K_{\mathrm{tan}}$. Assuming constant spindle speed, the angular positions $\varphi_j(\hat{t})$ can be written as

$$\varphi_j(\hat{t}) = \hat{\Omega}\hat{t} - (j-1)\frac{2\pi}{N}. \tag{5.3.13}$$

The differential equation for the deterministic periodic solution $x_{\mathrm{p}}(\hat{t})$ can be obtained by taking the expectation value of Eq. (5.3.9). The first order incremental form of the resulting equation is

$$\mathrm{d}\mathbf{x}_{\mathrm{p}}(\hat{t}) = \big(\mathbf{A}_0\mathbf{x}_{\mathrm{p}}(\hat{t}) + \mathbf{c}(\hat{t})\big)\mathrm{d}\hat{t}, \tag{5.3.14}$$

where

$$\mathrm{d}\mathbf{x}_{\mathrm{p}}(\hat{t}) = \begin{pmatrix} x_{\mathrm{p}}(\hat{t}) \\ x'_{\mathrm{p}}(\hat{t}) \end{pmatrix}, \qquad \mathbf{A}_0 = \begin{pmatrix} 0 & 1 \\ -1 & -2\zeta \end{pmatrix}, \qquad \mathbf{c}(\hat{t}) = \begin{pmatrix} 0 \\ -HG_{\mathrm{s}}(\hat{t}) \end{pmatrix}. \tag{5.3.15}$$

Subtracting (5.3.14) from (5.3.9) the equation of motion for the stochastic perturbation x_t can be obtained in the first order form

$$\begin{aligned} \mathrm{d}\mathbf{x}_{\hat{t}} =& \big(\mathbf{A}(\hat{t})\mathbf{x}_{\hat{t}} + \mathbf{B}(\hat{t})\mathbf{x}_{\hat{t}-\hat{\tau}}\big)\mathrm{d}\hat{t} \\ &+ \sum_{j=1}^{N} \big(\boldsymbol{\alpha}_j(\hat{t})\mathbf{x}_{\hat{t}} + \boldsymbol{\beta}_j(\hat{t})\mathbf{x}_{\hat{t}-\hat{\tau}} + \boldsymbol{\sigma}_j(\hat{t})\big)\mathrm{d}W_{j,\hat{t}}\,, \end{aligned} \tag{5.3.16}$$

where

$$\begin{gathered} \mathrm{d}\mathbf{x}_{\hat{t}} = \begin{pmatrix} x_{\hat{t}} \\ x'_{\hat{t}} \end{pmatrix}, \qquad \mathbf{A}(\hat{t}) = \mathbf{A}_0 + \begin{pmatrix} 0 & 0 \\ -HG_{\mathrm{c}}(\hat{t}) & 0 \end{pmatrix}, \qquad \mathbf{B}(\hat{t}) = \begin{pmatrix} 0 & 0 \\ HG_{\mathrm{c}}(\hat{t}) & 0 \end{pmatrix}, \\ \boldsymbol{\alpha}_j(\hat{t}) = \begin{pmatrix} 0 & 0 \\ -\hat{\sigma}HG_{\mathrm{c},j}(\hat{t}) & 0 \end{pmatrix}, \quad \boldsymbol{\beta}_j(\hat{t}) = \begin{pmatrix} 0 & 0 \\ \hat{\sigma}HG_{\mathrm{c},j}(\hat{t}) & 0 \end{pmatrix}, \quad \boldsymbol{\sigma}_j(\hat{t}) = \begin{pmatrix} 0 \\ -\hat{\sigma}HG_{\mathrm{s},j}(\hat{t}) \end{pmatrix}. \end{gathered} \tag{5.3.17}$$

To investigate the behaviour of milling subjected to stochastic cutting force excitation, one needs (5.3.14) to determine the stationary deterministic periodic first moment $x_{\mathrm{p}}(\hat{t})$, while (5.3.16) allows the first and second moment stability investigation of this periodic solution and the calculation of the stationary periodic second moment of the process $x_{\hat{t}}$. The deterministic periodic first moment $x_{\mathrm{p}}(\hat{t})$ can be utilised to qualify the stationary mean behaviour: the peak-to-peak (P2P) amplitude of $x_{\mathrm{p}}(\hat{t})$ is used for this purpose, namely,

$$\mathrm{P2P}\big(x_{\mathrm{p}}(\hat{t})\big) = \max_{t\in[0,T]}\big(x_{\mathrm{p}}(\hat{t})\big) - \min_{t\in[0,T]}\big(x_{\mathrm{p}}(\hat{t})\big). \tag{5.3.18}$$

To investigate the noise-induced resonance near the stability borders, the maximum and the time average of the stationary standard deviation is used,

$$\max_{t\in[0,T]} \mathrm{StD}_x^{\mathrm{st}}(t) \quad \text{and} \quad \operatorname*{mean}_{t\in[0,T]} \mathrm{StD}_x^{\mathrm{st}}(t), \tag{5.3.19}$$

respectively. These indicators can be directly computed with the stochastic semidiscretisation method.

However, during measurements the chatter peaks are analysed in the measured Fourier spectrum. To determine the theoretical counterpart of this Fourier spectrum, Eq. (5.3.9) is utilised to calculate realisations of the milling process. Then, the stationary section of the trajectory (after the transient vibrations decayed, which is assumed to surely happen after 5000 natural period $2\pi/\omega_n$) are decomposed into the deterministic periodic solution $x_{\mathrm{p}}(\hat{t})$ and into the stochastic perturbation $x_{\hat{t}}$. To investigate the noise-induced resonance, the Fourier transform of the stochastic perturbation $x_{\hat{t}}$ is investigated in the stationary section, namely

$$\ell_{\mathrm{peak}} = \max_{\omega} |\mathrm{FFT}(x_{\hat{t}})|. \tag{5.3.20}$$

The draft of this decomposition is illustrated in Fig. 5.7. In Fig. 5.7a) the original stationary trajectory is shown, while b) and c) show the periodic deterministic and the stationary stochastic perturbation components, respectively. Along with the trajectories, the magnitude of the Fourier transform of the stationary trajectory z_t and the decomposed trajectories $f_z x_{\mathrm{p}}(\hat{t})$ and $f_z x_{\hat{t}}$ is shown in Fig. 5.7d)-e). As during a real measurement, when taking the Fourier transform of z_t peaks can be observed at the excitation frequency and its higher harmonics and an additional peak at the chatter frequency (around the natural frequency ω_{n}. When analysing the Fourier transform of the decomposed vibrations the peaks at the excitation frequencies appear only in the deterministic periodic component. However, in the Fourier transform of the stochastic component x_t of the simulated trajectory it can be observed, that the well defined peak at the natural frequency ω_n is present, while there is no peak at the excitation frequencies. This can only be due to the noise-induced resonance.

To investigate the effect of machining parameters on the indicators described in (5.3.18), (5.3.19) and (5.3.20) a numerical analysis was conducted. For this analysis of the stochastic model of milling some numerical parameters were chosen, based on [46]. The modal parameters were identified through impact modal tests, the modal mass, damping and natural frequency are $m = 2.701$ kg, $\zeta = 0.71$ % and $\omega_n = 259.96$ Hz, respectively. The milling operation is assumed to be conducted with a straight-edged two-flooted tool ($N = 2$) with diameter $D = 16$ mm and with a feed per tooth $f_z = 0.1$ mm. In this case study down-milling operation is considered with radial immersion $a_e = 2$ mm, which results in $\varphi_{\mathrm{en}} = 138.6°$ and $\varphi_{\mathrm{ex}} = 180°$. Finally, the cutting force characteristic was determined for this configuration through a series of cutting test at the Department of Applied Mechanics (Budapest University of Technology and Economics), and the radial and tangential cutting force coefficients are $K_{\mathrm{rad}} = 0.175 \cdot 10^9$ N/m^2 and $K_{\tan} = 1.095 \cdot 10^9$ N/m^2, respectively, resulting in $r = 0.16$, as defined in (5.3.11). The intensity of the noise component in the cutting force is assumed as small as $\sigma_0 = 0.5$ %. During semidiscretisation the period resolution $p = 50$ and the Lagrange polynomial order $q = 3$ was chosen, while the trajectories for the analysis of the Fourier spectra were calculated using the stabilised SROCK [71] method (through the *StochasticDelayDiffEq.jl* package) with time step $\delta t = 10^{-3} \cdot 2\pi/\omega_n \approx 3.847 \cdot 10^{-6}$ s.

Since the noise has a very low intensity in the cutting force, it has no significant effect on the stability of milling (as in Secs. 5.1 and 5.2), thus the semidiscretised first and second moment (3.2.20) both can be used to determine stability on the parameter region $a_p \in [0, 4\ \mathrm{mm}]$ and $\Omega \in [1000\ \mathrm{rpm}, 10000\ \mathrm{rpm}]$, as shown in Fig. 5.8. To analyse the P2P of the stationary periodic first and maximum and mean values of the second moments, the fix point (3.2.27) of the first moment map (3.2.20) and the fix point (3.2.35) of the second moment map (3.2.31) was used, and the axial depth of cut was fixed for $a_p = 2$ mm and the analysis was conducted on spindle speed interval $\Omega \in [4800\ \mathrm{rpm}, 8600\ \mathrm{rpm}]$.

First, the behaviour of the FRF peak ℓ_{peak} is investigated as the stability boundary $\Omega = 8457$ rpm is approached. In Fig. (5.9) the growth of this peak is illustrated: the peaks of the deterministic component slightly decrease, while peak of the stochastic component increases significantly. It shows, that the noise-induced resonance is amplified near the border of the stable milling parameters, since the characteristic damping becomes 0 when losing stability, similarly as it has been illustrated in Subsec. 2.2.4.

These amplitude changes are plotted for the spindle speed range $\Omega \in [4800\ \mathrm{rpm}, 8600\ \mathrm{rpm}]$ in Figs. 5.10b and c. To compare the results of the stochastic semi discretisation and the MC simulations, the P2P of the stationary deterministic periodic first moment $x_{\mathrm{p}}(\hat{t})$, the peak heights ℓ_{peak} and the mean and maximum values of the stationary standard deviation of the noise perturbation $x_{\hat{t}}$ are plotted together in Fig. 5.10. Note that P2P of the stationary first moment in Fig. 5.10b do not show any particular behaviour near the stability borders, only its magnitude grows at the resonant spindle speed $\Omega = \omega_n/N$. The peak heights ℓ_{peak} in the Fourier spectrum of the stochas-

tic perturbation x_t blow up near the stability borders as shown in Fig. 5.10c. Furthermore, both the maximum and the mean of the stationary standard deviation $\mathrm{StD}(x_t)$ in Fig. 5.10d blow up near the stability borders, due to noise-induced resonance, similarly to the peak height ℓ_{peak}. Note that only the maximum value can be used to detect deterministic resonance, the mean standard deviation is insensitive to it.

Note that the square root of the peaks ℓ_{peak} is shown for eyeballing purposes, and to allow the direct comparison with the standard deviations.

Based on the results described in this section, the measurement difficulties in the chatter detection close to the stability boundary can be explained and predicted. It is shown that by filtering the noisy components from the measured signal important information is eliminated, since based on deterministic values e.g., the averaged P2P values, the forthcoming chatter cannot be predicted and detected. While utilising the stochastic effects, a model based quantification of chatter prediction is possible.

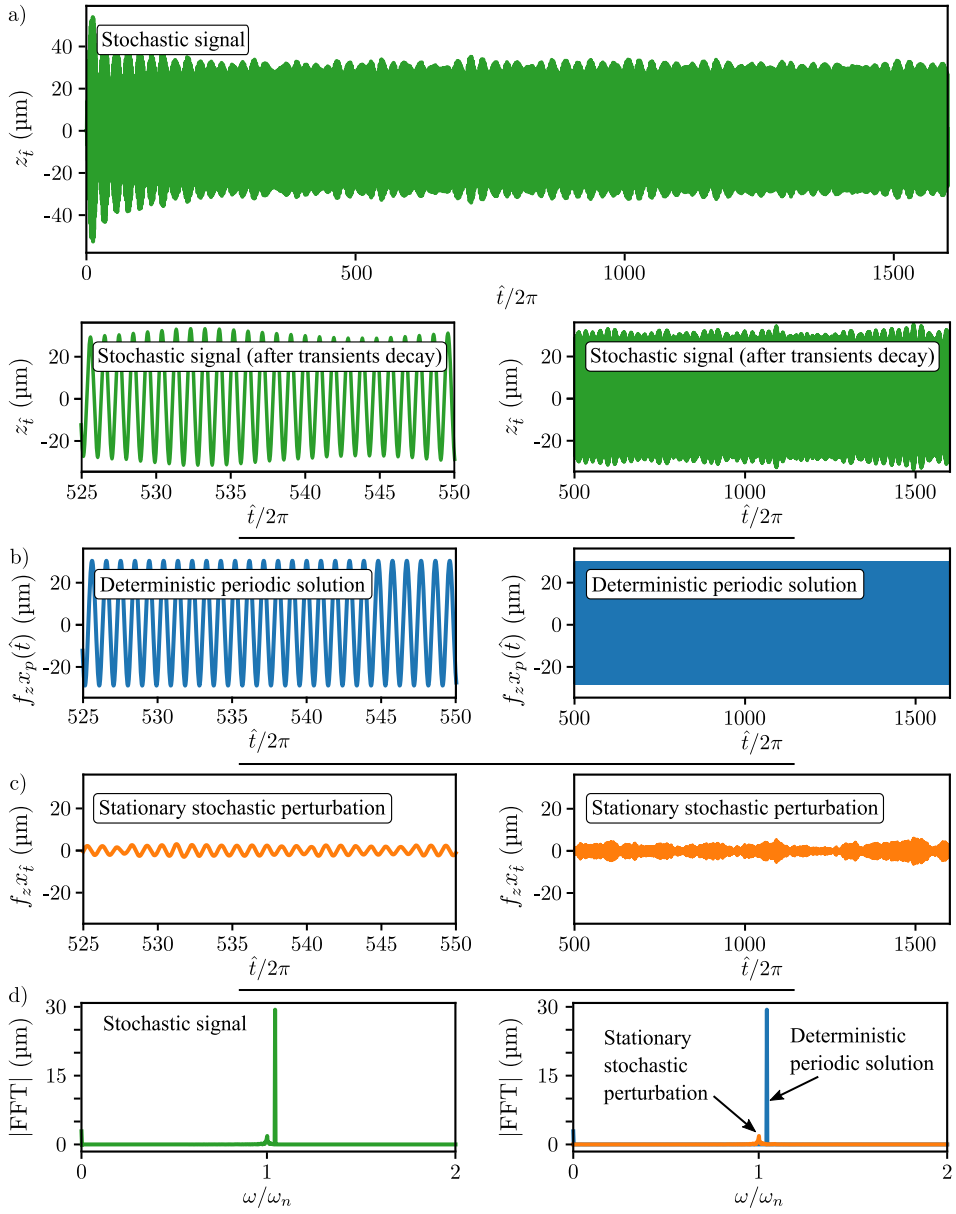

Figure 5.7. *Draft of the trajectory decomposition of the stationary trajectories: a) the entire stochastic signal, b) deterministic periodic component, c) stationary stochastic component. In panels d) the Fourier spectrum of the simulated trajectory and the decomposed trajectories can be seen.*

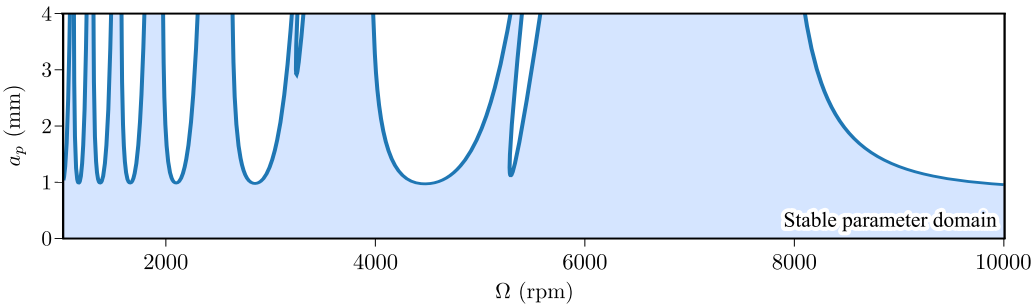

Figure 5.8. *First moment stability chart of a milling operation. The shaded area denotes the stable parameter region*

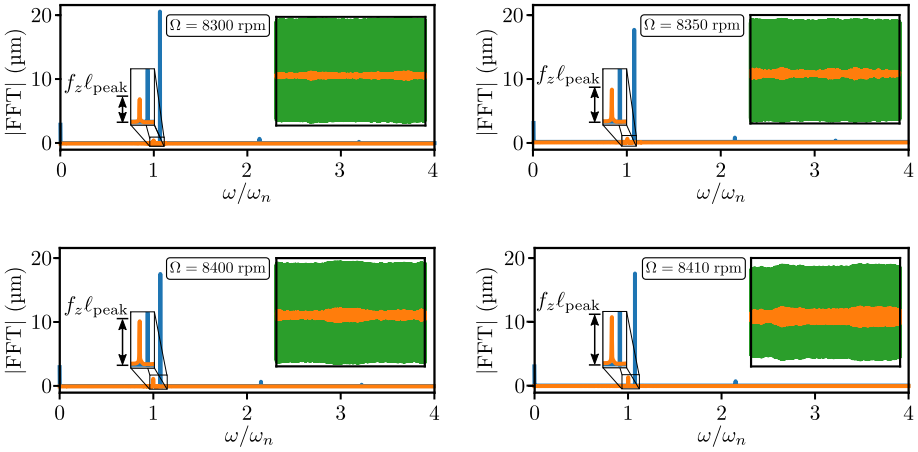

Figure 5.9. *Examples of the Fourier transforms of the decomposed stationary trajectories. The blue peaks denote the Fourier transforms of the periodic deterministic solution, while the orange peaks denotes the Fourier transforms of the noise perturbation. For each Fourier transforms the draft of the simulated trajectory is given in green, while the orange trajectory denotes the the noise perturbation component of the trajectory. The spindle speed* Ω *in each panel correspond to Fig. 5.10.*

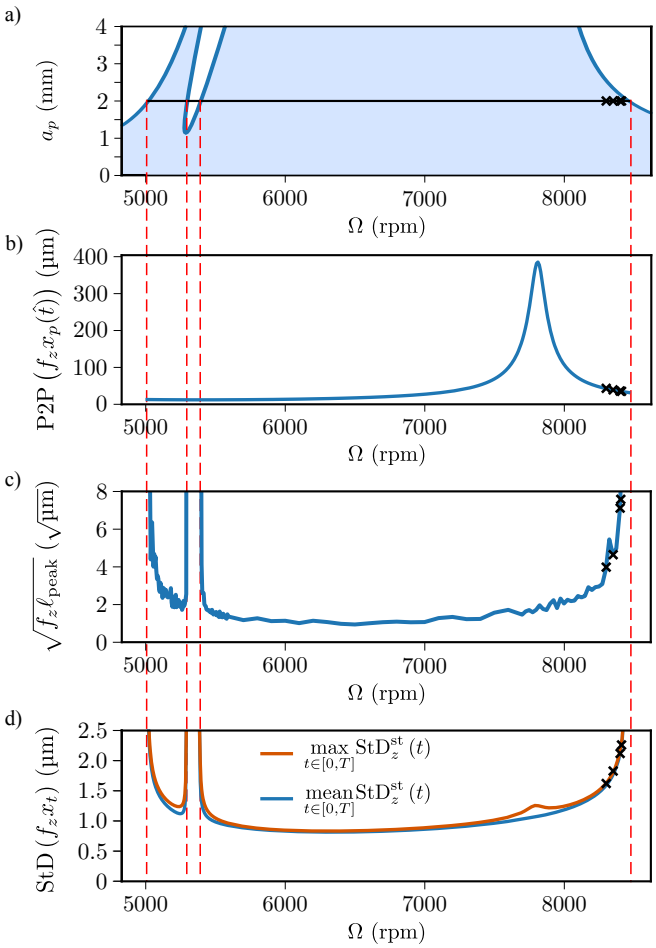

Figure 5.10. *Stability analysis of a milling operation. Panel a) shows the first moment stability chart, where the shaded area denotes the stable parameters, panel b) shows the P2P values of the deterministic periodic solution, panel c) shows the standard deviation of the stochastic perturbation, while panel d) illustrates the behaviour of the peak height* ℓ_{peak} *of the Fourier spectrum of the stochastic perturbation* x_t*. The black* $\times$*-s denote the results corresponding to the spindle speeds* Ω *used for Fig 5.9.*

5.4 Stochastic Effects in Connected Vehicle Systems

In this section the influence of stochastic time delay and addtive noise on connected vehicle systems is considered. In particular, the focus is on the longitudinal dynamics of a connected automated vehicle (CAV) following a connected human driven vehicle (CHV) that broadcasts its position data (measured e.g.: with GPS) and speed via wireless vehicle-to-vehicle (V2V) communication. When receiving the packets the CAV can respond to the motion of the CHV by adjusting the throttle or applying the brakes. This is referred as connected cruise control and the effects of time delays in such systems have been investigated both theoretically and experimentally [28, 62].

There are two sources of delay in the this example. On one hand, the actuator delay of the CAV is typically constant and in the range of 0.3-0.6 seconds. On the other hand, the communication delay is in the range of 0.1-0.3 sec and this changes stochastically based on the random nature of packet scheduling algorithms and the packet drops in wireless communication.

The stochastically delayed differential equation describing the motion of the CAV can be written as in [33]:

$$\begin{aligned} \dot{s}_t &= v_t, \\ \dot{v}_t &= \alpha \left(V \left(s_{\mathrm{h},t-\tau_{\mathrm{h},t}} - s_{t-\tau_t} - l \right) - v_{t-\tau_t} \right) + \\ &\quad + \beta \left(v_{\mathrm{h},t-\tau_{\mathrm{h},t}} - v_{t-\tau_t} \right) . \end{aligned} \tag{5.4.1}$$

Here the dot stands for differentiation with respect to time t, s and s_{h} denote the positions of the rear bumpers of the CAV and the CHV ahead while v and v_{h} denote their velocities, respectively; see Fig. 5.11(a). The length of the CAV is denoted with l and the headway is defined by

$$h = s_{\mathrm{h}} - s - l \, . \tag{5.4.2}$$

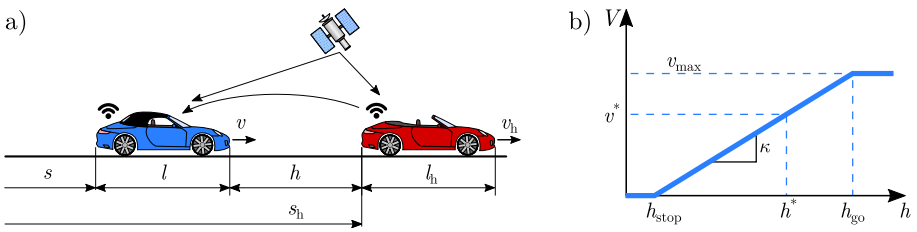

Figure 5.11. *Connected car-following example: a) Sketch of a connected automated vehicle following a connected human-driven vehicle and b) the range policy* (5.4.3).

In (5.4.1), the gains α and β are used to correct velocity errors, τ represents the actuator delay of the CAV, while τ_{h} incorporates the communication delay as well as the actuator delay. The effect of the packet losses are modelled as stochastically switching delays, that is $\tau_h \in \{\tau_1, \ldots, \tau_{J_\tau}\}$ with probabilites w_j, $j = 1, \ldots, J_\tau$ and with holding time T_τ, which is related to the communication frequency. Note, that this is only a continuous approximation of the real delay process. This approach allows the analysis of the stability and stationary behaviour of the CAV model with the tools established in Secs. 3.3 and 4.4.

The desired velocity is determined by the nonlinear range policy function

$$V(h) = \begin{cases} 0 & \text{if} \quad h \leq h_{\mathrm{st}} \, , \\ \kappa \, (h - h_{\mathrm{stop}}) & \text{if} \quad h_{\mathrm{stop}} < h < h_{\mathrm{go}} \, , \\ v_{\max} & \text{if} \quad h \geq h_{\mathrm{go}} \, , \end{cases} \tag{5.4.3}$$

shown in Fig. 5.11(b), where $\kappa = v_{\max}/(h_{\mathrm{go}} - h_{\mathrm{stop}})$. That is, the desired velocity is zero for small headways ($h \leq h_{\mathrm{st}}$ and equal to the speed limit $v_{\max}$ for large headways ($h \geq h_{\mathrm{go}}$). Between

these, the desired velocity increases with the headway linearly, with gradient κ. Note that when $h_{\text{stop}} = 0$, the quantity $1/\kappa$ is often referred to as the time headway.

In a steady state traffic flow with average velocity v^* and vehicle starting positions s_{h^*} and s^* the CHV's velocity is assumed to have the expectation value $\langle v_1(t) \rangle = v^*$ which allows to partition its position and velocity as

$$\begin{pmatrix} s_{\text{h},t} \\ v_{\text{h},t} \end{pmatrix} = \begin{pmatrix} v^* \\ 0 \end{pmatrix} t + \begin{pmatrix} s^*_{\text{h}} \\ v^* \end{pmatrix} + \begin{pmatrix} x_{\text{h}s,t} \\ x_{\text{h}v,t} \end{pmatrix}. \tag{5.4.4}$$

To describe the sum of the measurement error and the perturbation of the motion of the lead vehicle, $\mathbf{x}_{\text{h}} := (x_{\text{h}s},\, x_{\text{h}v})^\top$ is defined, that is, $\langle \mathbf{x}_1 \rangle = \mathbf{0}$. In the case of the CAV the same partitioning leads to

$$\begin{pmatrix} s_t \\ v_t \end{pmatrix} = \begin{pmatrix} v^* \\ 0 \end{pmatrix} t + \begin{pmatrix} s^* \\ v^* \end{pmatrix} + \begin{pmatrix} x_{s,t} \\ x_{v,t} \end{pmatrix}, \tag{5.4.5}$$

where the vector $\mathbf{x} := (x_s,\, x_v)^\top$ collects the position and velocity perturbations of the CAV. Note that for connected cars the holding time is always smaller than the minimum time delay of the system, that is $T_\tau < \tau_1$, leading to $\langle \mathbf{x}_t \rangle = \mathbf{0}$ (see Fig. 4.18).

Substituting the definitions of the positions and the velocities of the vehicles from (5.4.4) and (5.4.5) into (5.4.1), using the range policy (5.4.3), and taking the expected value of the resulting equation, the stationary average headway distance can be determined:

$$\lim_{t\to\infty} \langle h_t \rangle = \lim_{t\to\infty} \langle s_{\text{h},t} - s_t - l \rangle = s^*_{\text{h}} - s^* - l = V^{-1}(v^*) + (\bar{\tau}_{\text{h}} - \bar{\tau})\, v^*. \tag{5.4.6}$$

Here $\bar{\tau}$ and $\bar{\tau}_{\text{h}}$ denote the average values of the delays and V^{-1} is only unique for $0 < v^* < v_{\max}$; cf. (5.4.3). This shows that the average mismatch between the delays may result in an (undesired) increase of the stationary headway.

To characterise the quality of the CAV control in case of a dense, but continuously flowing traffic scenario ($h_{\text{stop}} < h(t) < h_{\text{go}}$), the dynamics describing the perturbation on the middle linear section of the range policy $V(h)$, namely the linear system

$$\dot{\mathbf{x}}_t = \mathbf{A}\mathbf{x}_t + \mathbf{B}\mathbf{x}_{t-\tau_t} + \mathbf{B}_{\text{h}}\mathbf{x}_{\text{h},t-\tau_{\text{h},t}} - ((\tau_t - \bar{\tau})\mathbf{B} + (\tau_{\text{h},t} - \bar{\tau}_{\text{h}})\mathbf{B}_{\text{h}})\mathbf{v}^* \tag{5.4.7}$$

has to be investigated, where

$$\mathbf{A} = \begin{pmatrix} 0 & 1 \\ 0 & 0 \end{pmatrix}, \quad \mathbf{B} = \begin{pmatrix} 0 & 0 \\ -\alpha\kappa & -(\alpha+\beta) \end{pmatrix}, \quad \mathbf{B}_{\text{h}} = \begin{pmatrix} 0 & 0 \\ \alpha\kappa & \beta \end{pmatrix}, \quad \mathbf{v}^* = \begin{pmatrix} v^* \\ 0 \end{pmatrix}. \tag{5.4.8}$$

Note that in (5.4.7) the terms containing $\mathbf{x}_{\text{h},t-\tau_{\text{h},t}}$ and $\mathbf{v}^*$ act as excitations on the system. Furthermore, it is assumed, that the perturbation $\mathbf{x}$ is small and will not produce such motions, that cause the headway h to leave the interval $[h_{\text{stop}}, h_{\text{go}}]$.

5.4.1 Effect of Delay Matching on Connected Cruise Control

It was shown in Eq. (5.4.6) that a mismatch between the delays τ and τ_{h} results in a shift from the desired stationary solution. Since the packets sent via V2V communication are time stamped one may add some delay to the actuation delay τ so it matches τ_{h}. This means that the CAV uses its own position and velocity (not affected by the packet loss) which was obtained at the time when the state of the CHV was measured. Here we utilise the analytical techniques established above to evaluate the performance of the CAV when we apply vs. do not apply such delay matching.

In case of delay matching the controller sets

$$\tau_t = \tau_{\text{h},t}, \tag{5.4.9}$$

and, since $\mathbf{v}^*$ is in the nullspace of the sum $\mathbf{B} + \mathbf{B}_\mathrm{h}$, the linear system (5.4.7) simplifies to

$$\dot{\mathbf{x}}_t = \mathbf{A}\mathbf{x}_t + \mathbf{B}\mathbf{x}_{t-\tau_{\mathrm{h},t}} + \mathbf{B}_\mathrm{h}\mathbf{x}_{\mathrm{h},t-\tau_{\mathrm{h},t}}. \tag{5.4.10}$$

In case of no delay matching the actuation delay is left constant, that is,

$$\tau_t \equiv \tau = \bar{\tau} \tag{5.4.11}$$

and (5.4.7) becomes

$$\dot{\mathbf{x}}_t = \mathbf{A}\mathbf{x}_t + \mathbf{B}\mathbf{x}_{t-\tau} + \mathbf{B}_\mathrm{h}\mathbf{x}_{\mathrm{h},t-\tau_{\mathrm{h},t}} - \mathbf{B}_\mathrm{h}\mathbf{v}^* \cdot (\tau_{\mathrm{h},t} - \bar{\tau}_\mathrm{h}), \tag{5.4.12}$$

with no stochasticity in the delay τ. The Eqs. (5.4.10) and (5.4.12) are compatible with the form given in (3.3.1).

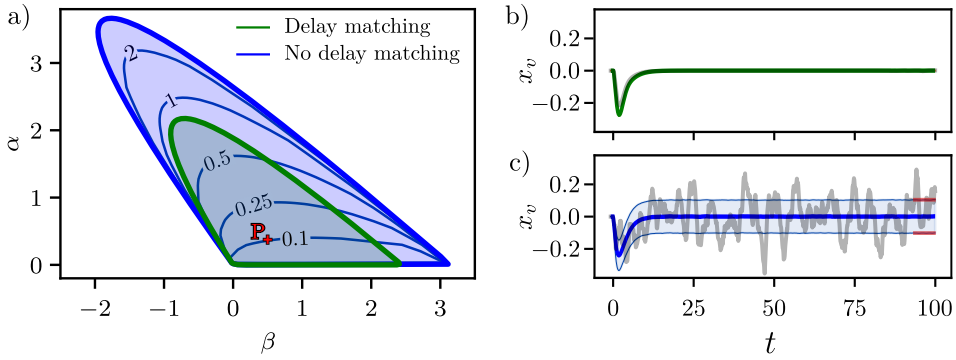

Figure 5.12. *Performance of connected cruise control without added noise. a) Second moment stability charts with the stable parameter domains shaded. The lines with the numbers denote contours of stationary standard deviations of $x_v(t)$. b) and c): The results of Monte Carlo simulations conducted for gain parameters $\alpha = 0.4$ and $\beta = 0.5$ (marked as P on the stability chart) the mean and the standard deviation are highlighted by the coloured lines and a sample realisation with gray line. The red lines represent the stable stationary second moment calculated with semidiscretisation.*

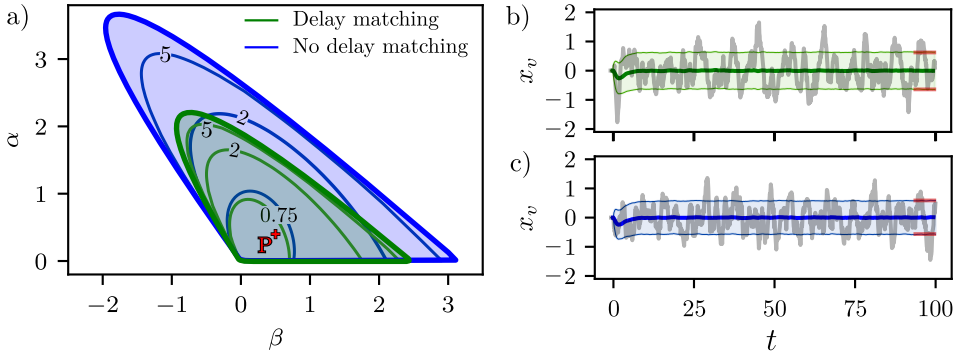

Figure 5.13. *Performance of connected cruise control with added white noise. The same notations are used as in Fig. 5.12.*

For simplicity the case when the leading vehicle is moving with a constant speed is considered, that is, $\mathbf{x}_{\mathrm{h},t} \equiv \mathbf{0}$. In this case (5.4.10) has no additive noise while (5.4.12) is only excited by the delay noise. When presenting the results we use the realistic parameters $\kappa = 0.6$ 1/s, stationary velocity $v^* = 20$ m/s, actuation delay $\tau = 0.5$ s and holding time $T_\tau = 0.1$ s. It is also assumed that the stochastic delay $\tau_{\mathrm{h},t}$ can take values from the set $\tau_{\mathrm{h},t} \in \{0.55\,\mathrm{s}, 0.65\,\mathrm{s}, 0.75\,\mathrm{s}\}$ with probabilities $w_i \in \{0.25, 0.5, 0.25\}$, respectively.

The stability charts are plotted in the plane of the control gains α and β in Fig. 5.12a by utilizing $\rho\left(\overline{\overline{\mathbf{K}}}\right) < 1$. Notice that the stability domain is smaller for the case with delay matching due to the fact that τ is increased in this case. However, since there is no added noise in this case we obtain $\lim_{t\to\infty} x_s^2 = 0$ and $\lim_{t\to\infty} x_v^2 = 0$ for the stationary second moments. This is illustrated by the numerical simulation in Fig. 5.12b corresponding to point P located at $(\alpha, \beta) = (0.4, 0.5)$ in the stability chart. The simulated trajectories (grey curve) approach zero quickly bringing the mean (thick green curve) and the standard deviation (thin green curve) to zero too.

When no delay matching is used, the stable domain is larger but, due to the delay induced noise added to the system, the stationary second moment is not zero. The contours of the stationary second moment of the velocity perturbation $\lim_{t\to\infty} x_v^2$ are calculated using (3.3.38) are shown in Fig. 5.12a. The numerical simulations in Fig. 5.12c illustrate the dynamics for point P marked in the stability chart. The sample trajectory (grey curve) shows that the velocity of the CAV keeps changing in time so that the mean (thick blue curve) approaches zero while the standard deviation approaches the constant value calculated using stochastic semidiscretisation.

Remark that while delay matching reduces the size of the stability domain one may still have a large range of gain parameters to choose from. In particular, in the experimentally realistic range of $\alpha \in [0, 1], \beta \in [0, 1]$ stability is still ensured. Furthermore, the delay matching eliminates the unwanted stationary oscillations that lead to "jerky ride", which typically has a negative effect on driver comfort and energy consumption. Note that in case of no delay matching the delay induced noise is magnified to an extent, where Eq. (5.4.7) is not valid anymore (the range policy $V(h)$ can saturate). However, in terms of control design these parameter regions should be avoided and instead of the stability boundary, to limit the amplitude of the perturbation $\mathbf{x}$, the stationary second moment contours should be considered when choosing control parameters for the CAV.

The positive effects of delay matching can also be observed when the CHV ahead varies its velocity slowly (that is typical in real traffic situations) [10]. In order to evaluate the effects for more severe motion perturbations, the perturbation dynamics of the CHV is modelled using white noise, that is,

$$\mathbf{x}_{\mathrm{h},t-\tau_{\mathrm{h},t}} := (\Gamma_{1,t}, \Gamma_{2,t})^\top. \tag{5.4.13}$$

where $\Gamma_{1,t}$ and $\Gamma_{2,t}$ are uncorrelated Gaussian white noise. This is indeed an overestimation of the severity of perturbations but provides a way to compare the behaviour with and without delay matching. This leads to a noise excitation from 3 different noise sources in (3.3.1) with intensities

$$(\boldsymbol{\sigma}_1, \boldsymbol{\sigma}_2) := \mathbf{B}_\mathrm{h}, \qquad \boldsymbol{\sigma}_\tau = \begin{cases} \mathbf{0}, & \text{in case of delay matching} \\ \mathbf{B}_\mathrm{h}\mathbf{v}^*, & \text{in case of no delay matching} \end{cases} \tag{5.4.14}$$

where $\boldsymbol{\sigma}_1$ and $\boldsymbol{\sigma}_2$ are the noise intensity vectors of the Gaussian white noise processes $\Gamma_{1,t}$ and $\Gamma_{2,t}$, respectively. The effect of multiple additive Gaussian white noise processes can be taken into account similarly as described in Sec. 3.1.5 or 3.2.4

The results are summarised in Fig. 5.13 where panel (a) depicts the stability charts. The stability boundaries are identical to those in Fig. 5.12a as these are still obtained by $\rho\left(\overline{\overline{\mathbf{K}}}\right) < 1$ while the contours for the stationary second moment of the velocity perturbation calculated by (3.3.38) change due to the added white noise. Notice that the contours obtained for the delay matching case are quite similar to those obtained without delayed matching for small gain values, including the experimentally realistic range $\alpha \in [0, 1], \beta \in [0, 1]$. For point P at $(\alpha, \beta) = (0.4, 0.5)$ this behaviour is also illustrated by the numerical simulations shown in panels (b) and (c). This means that when responding to severe perturbations using delay matching neither improves nor degrades the performance of the CAV.

Note that the stationary second moment analysis presented in Fig. 5.13 again corresponds to the linear system only, where $h_{\mathrm{stop}} < h < h_{\mathrm{go}}$. Close to the stability boundary where noise-induced resonance can be observed, the large amplitudes of the perturbation $\mathbf{x}$ can be saturated

due to the nonlinear range policy $V(h)$. However, this effect is not considered in this study, and this parameter region should be avoided during control design.

Chapter 6

Experimental results

In the previous chapter the variations of the cutting force was modelled with the help of white noise processes. The main goal of the measurements conducted in this chapter is to show, that from modelling perspective it is a sufficient approximation to use a Gaussian random process to model the effects of high frequency phenomena in the cutting force.

6.1 Stochastic Cutting Force Model

In this section the magnitude of the noise relative to the mean cutting force is estimated through a series of measurements. The measurement layout is shown in Fig. 6.1. The measurement was conducted on an NCT EmR-610Ms milling machine, where the workpiece was clamped into the spindle, and the tool was fixed on the table. The cutting force was measured with a Kistler Dynamometer 9129AA and the data were acquired using a 5080A charge amplifier and two NI-9234 Input Modules in a NI cDAQ-9178 Chassis at 51200 Hz sampling rate.

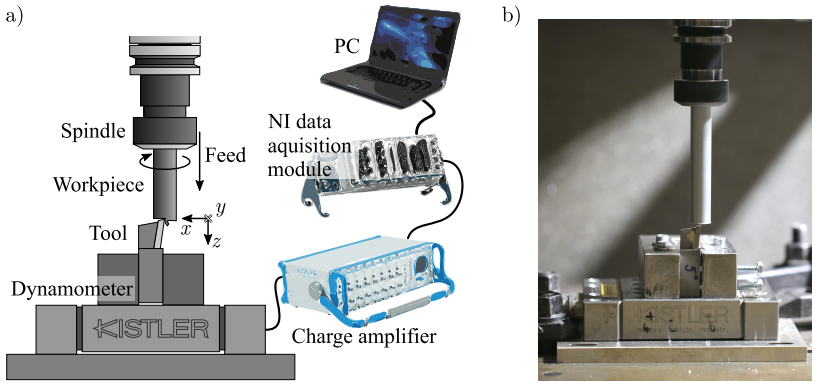

Figure 6.1. *The schematic figure a) and the experimental setup b) for the cutting force tests.*

During the measurements all three direction was measured: the main cutting force F_{main} (x direction in Fig. 6.1), F_{feed} (z direction in Fig. 6.1) and F_{passive} (y direction in Fig. 6.1). The main and the feed cutting force components are assumed to be generated by the same stochastic process Γ_t with the same relative intensity, namely

$$F_{j,t} = \bar{F}_j(1 + \sigma_F \Gamma_t) \quad \text{where} \quad j = \text{main, feed,} \tag{6.1.1}$$

where Γ_t is an unknown noise process with $\langle \Gamma_t \rangle = 0$ and $\text{StD}(\Gamma_t) = 1$. Note that both $\bar{F}_j$ and σ_F can depend on the cutting parameters, e.g.,chip width, chip thickness, cutting velocity or the rake angle of the tool. The mean component $\bar{F}_j$ is usually described by a deterministic cutting force model e.g., as presented in [3,23]. In this section no cutting force model will be fitted on the measured cutting force, only the relation between the mean cutting force $\bar{F}_j$ and the relative noise intensity σ_F is investigated.

The analysed cutting tests were performed on an AL 2024-T351 tube with 16 mm diameter and 1.5 mm wall thickness as the workpiece, and the cutting was conducted with a custom made tool with 5° rake angle and ($\sim 10^\circ$) clearance angle. The chip thickness h was varied between 0.2

mm and 0.0005 mm with exponentially decreasing and increasing steps. The orthogonal turning layout allowed to realise the prescribed chip thickness with high precision, even for the small chip thicknesses. This is due to the workpiece having high stiffness in the feed direction, and the chip thickness was controlled by adjusting the feed rate and the spindle speed.

A single force section was measured for around 1–2 s at a sampling rate 51200 Hz and there was a 0.1 s pause after every step to separate the signal sections while avoiding the cooling of the cutting tool. Due to the fast-varying, stationary and ergodic characteristic of the cutting force, the time length 1–2 s of the measurements were sufficient to determine the parameters of the stochastic cutting force. A typical measured signal with the usually occurring force distributions is shown in Fig. 6.2. During the measurements different cutting velocities $v_c = 50\,\mathrm{m/min}$, $100\,\mathrm{m/min}$, $175\,\mathrm{m/min}$, $250\,\mathrm{m/min}$, $300\,\mathrm{m/min}$, and rake angles $\alpha_r = 5°$, $10°$, $15°$, $30°$, $35°$, $40°$ were applied while the relief angle was $10°$ for each tool. The tool edge radius was measured using a microscope for each tool, and all of them were found to be smaller than $35\,\mu\mathrm{m}$. The initial fast wearing of the tools had already taken place before starting the experiments of this work (and measuring the edge radii), and no noticeable toolwear was found during the cutting force measurements.

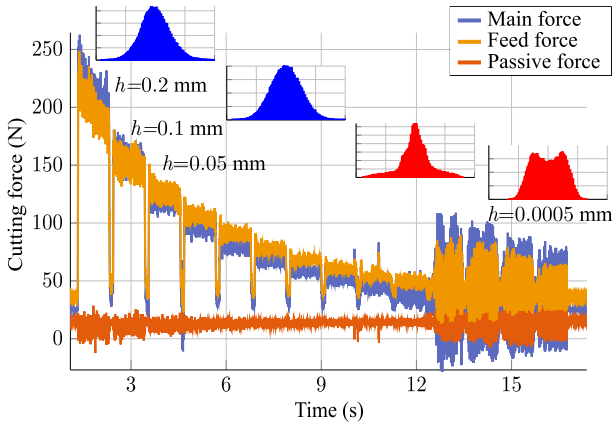

Figure 6.2. *Example of a measured force signal for exponentially decreasing chip thicknesses h with the usually occurring force distributions (blue: considered as Gaussian, red: not considered as Gaussian) with parameters $v_c = 250\,\mathrm{m/min}$.*

Due to the measurement setup, not only the stochastic effects are contained in the variation of the cutting force. There is a slow change due to the heating of the cutting tool and the workpiece, and a periodic component corresponding to the spindle rotation. To compensate the thermal effects, an exponentially decreasing function $\theta(t)$ is used:

$$\theta(t) = a + b\exp(ct), \tag{6.1.2}$$

where a, b and $c < 0$ are fitted parameters, using the measured time signal $F_{\mathrm{meas},j,t}$ where j refers to the cutting force component ($j \in \{\mathrm{mean}, \mathrm{feed}\}$). The thermal compensated force signal is calculated as follows:

$$F_{\theta,j,t} = F_{\mathrm{meas},j,t}\frac{a}{\theta(t)}, \tag{6.1.3}$$

where $F_{\theta,j,t}$ denotes the thermal compensated force signal. Fig. 6.3 shows the effect of this compensation for a single measurement point.

Next, the Fourier transformation is applied to the thermal compensated force signal $F_{\theta,j,t}$, denoted with $\hat{F}_{\theta,j,\omega}$. In $|\hat{F}_{\theta,j,\omega}|$ there are peaks at the frequencies corresponding to the spindle speed and its multiples (see Fig. 6.4). This originates form the inhomogeneous wall thickness and the eccentricity of the workpiece. To eliminate these effects on $|\hat{F}_{\theta,j,\omega}|$ of the measured signal, a

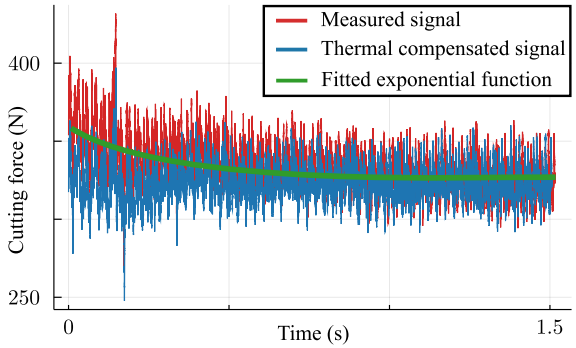

Figure 6.3. *The effect of the thermal compensation (example)*

filter similar to the so-called Comb-filter is applied:

$$H_c(\omega) = \frac{1}{2}\mathrm{abs}(1 - \exp\left(i\frac{\omega}{\Omega}\right)), \tag{6.1.4}$$

where Ω is the spindle speed. Using the product of the Fourier spectrum $|\hat{F}_{\theta,j,\omega}|$ and the Comb-filter $H_c(f)$, the Fourier spectrum $|\hat{F}_{\mathrm{comb},j,\omega}|$ is gained:

$$|\hat{F}_{j,\omega}| = |\hat{F}_{\theta,j,\omega}|H_c(\omega). \tag{6.1.5}$$

$|\hat{F}_{j,\omega}|$ represents the Fourier spectra of the variation of the measured cutting force originating from the high frequency deterministic and stochastic effects. With the combination of the original phase

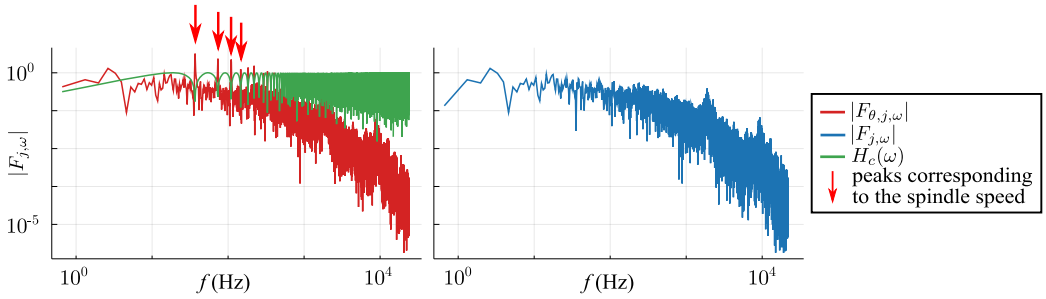

Figure 6.4. *The effect of the comb filter on the Fourier spectrum*

angle $\mathrm{ang}(\hat{F}_{\theta,j,\omega})$ and the Fourier spectrum of the comb filtered $|\hat{F}_{j,\omega}|$ the stochastic cutting force $F_{j,t}$ is reconstructed using inverse Fourier transformation.

Taking the time average and the standard deviation of each measured and processed force signal $F_{j,t}$ one gains

$$\langle F_{j,t}\rangle = \bar{F}_j \quad \text{and} \quad \mathrm{StD}(F_{j,t}) = \sigma_F \bar{F}_j, \qquad j \in \{\mathrm{mean}, \mathrm{feed}\}. \tag{6.1.6}$$

Next, the noise process Γ_t is assumed to behave according an Ornstein-Uhlenbeck process, which is a first order filtered noise:

$$\mathrm{d}\Gamma_t = -\mu_1 \Gamma_t \mathrm{d}t + \sqrt{2\mu_1}\mathrm{d}W_t. \tag{6.1.7}$$

Comparing (6.1.7) to (2.2.26) it can be concluded, that when substituting the parameters of the drift and diffusion terms to the stationary second moment (2.2.27) one obtains $\lim_{t\to\infty}\langle \Gamma_t^2\rangle = 1$, thus the stationary deviation $\mathrm{StD}(\Gamma_t) = 1$. This means, that the process Γ_t generated by (6.1.7) can be used as the noise process to model the stochastic variations of the cutting force $F_{j,t}$. With this approach all the information of the mean and relative noise intensity is contained in $\bar{F}_j$ and

σ_F, respectively, while the nature of the noise process can be described with one single parameter μ_1. This parameter can be determined by fitting the power spectral density (2.2.5) [98]

$$S_\gamma(\omega) = \frac{2\mu_1}{\mu_1^2 + \omega^2} \tag{6.1.8}$$

to the power spectral density (PSD) $S^{\text{meas}}_{\gamma,\omega}$ of the measured noise process $\gamma^{\text{meas}}_{j,t}$ which is

$$S^{\text{meas}}_{\gamma,\omega} := \hat{\gamma}^{\text{meas}}_{j,\omega} \hat{\gamma}^{\text{meas}\,*}_{j,\omega}, \tag{6.1.9}$$

where

$$\gamma^{\text{meas}}_{j,t} := \frac{F_{j,t} - \bar{F}_j}{\sigma_F \bar{F}_j}, \tag{6.1.10}$$

and

$$\hat{\gamma}^{\text{meas}}_{j,\omega} = \frac{1}{\sqrt{T}} \int_0^T e^{-i\omega t} \gamma^{\text{meas}}_{j,t} \mathrm{d}t, \tag{6.1.11}$$

where T is the length of the measurement $F_{j,t}$.

The force signals $\Gamma^{\text{meas}}_{j,t}$ were categorised by their distribution, whether the force perturbations can be considered as a Gaussian noise or not. This is necessary to check that the assumption that the behaviour of the process $\Gamma^{\text{meas}}_{j,t}$ can be approximated by Ornstein-Uhlenbeck process is even possible, since that is a Gaussian process. This was done by visual inspection of the force distributions for each signal, since a hypothesis test would have been to restrictive: a distribution can qualify as a Gaussian distribution from an engineering point of view while not satisfying the conditions of a normality test. In Fig. 6.5, the usually occurring distributions are compared to the probability density function of the standard normal distribution, along with a label, if it is considered as a normally distributed noise or not. In Fig. 6.5a a typical normally distributed force signal can be seen. However, in Fig. 6.5b, the distribution is not perfectly Gaussian, but in practice this is still an acceptable approximation from an engineering point of view. In Fig. 6.5c and 6.5d, the nonlinear nature of the force characteristics or some deterministic resonance phenomena distorts the probability density function in a way, that it loses its Gaussian form.

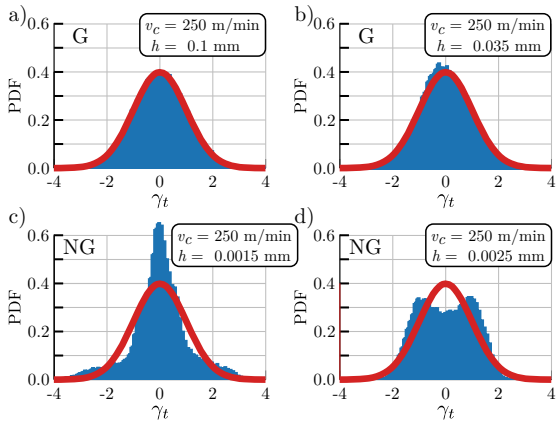

Figure 6.5. *The usually occurring standardised distributions among the measured signals: G denotes distributions considered as Gaussian while NG denotes distributions that were not considered as Gaussian. The red lines represent the reference probability density function of the standard normal distribution.*

However, if one wants to use the stochastic cutting force for example, to see how it affects the stability and stationary behaviour of machining processes, the filtered noise approach leads to a nonlinear system, for which the stochastic semidiscretisation introduced in Chap. 3 cannot be used. To overcome this, one may use an approximating white noise process Γ_t. Since, the white noise

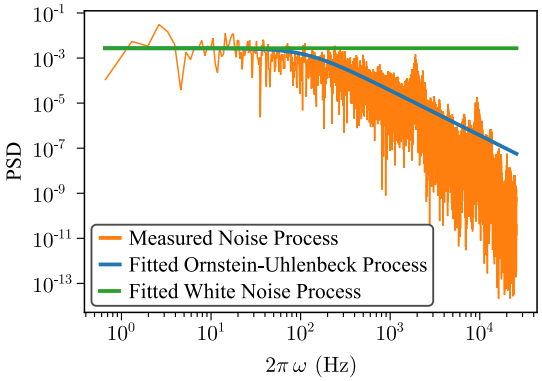

Figure 6.6. *Power spectral density of the measured noise process γ_t^{meas} along with the PSDs of the fitted Ornstein-Uhlenbeck and the fitted white noise processes*

has $\langle \Gamma_{t_1} \Gamma_{t_2} \rangle = \delta(t_1 - t_2)$, where $\delta(.)$ represents the Dirac-delta, the previously determined noise intensity $\sigma_F \bar{F}_j$ cannot be used for the intensity of the white noise Γ_t, thus a $\sigma_0 \bar{F}_j$ is introduced. This intensity σ_0 of the white noise process Γ_t is calculated with the help of the PSD of the stochastic process Γ_t. Since the PSD of the first order filter does not change significantly up to its cutoff frequency μ_1, the intensity σ_0 is calculated with the help of the maximum of the fitted PSD at $\omega = 0$, namely

$$\sigma_0^2 = \sigma_F^2 S_\gamma(0) = \frac{2\sigma_F^2}{\mu_1}, \tag{6.1.12}$$

thus leading to

$$\sigma_0 = \frac{\sqrt{2}}{\sqrt{\mu_1}} \sigma_F. \tag{6.1.13}$$

An example comparison of the PSDs of the measured noise process, the fitted Ornstein-Uhlenbeck process (6.1.7) and the white noise processes is shown in Fig. 6.6.

In Fig. 6.7 the above described measured quantities $\bar{F}_j$, σ_F, μ_1 and σ_0 are shown as a function of the chip width h for different cutting velocities v_c. The mean measured cutting force $\bar{F}_j$ (both the feed and main force components) follow the usual deterministic cutting force characteristics w.r.t. the chip thickness h [3], as it is shown in Fig. 6.7a. In addition, it can be also seen in Fig. 6.7b, that the relative intensity σ_F of the noise process Γ_t, relative to the mean, tends to a constant value independent from the cutting velocity v_c for chip thicknesses above $h = 0.025$–0.1 mm. In this range all the signals produced Gaussian distribution for all cutting velocities $v_c \geq 100$ m/min. This means, that for conventional chip thicknesses this noise can be considered as a multiplicative noise with relative intensity $\sigma_F \approx 5$ %. This multiplicative nature shows, that the noise is present in the cutting force and it is not related to measurement errors. In Fig. 6.7c the cutoff frequency μ_1 of the Ornstein-Uhlenbeck process can be seen, while Fig. 6.7d shows the behaviour of the relative white noise intensity σ_0. A general observation is, that the parameter μ_1 increases with the cutting velocity v_c, and during the fitting it is capped at $\mu_1 = 3.5\,\text{kHz} = 2\pi \times 3500\,\text{rad/s}$, which is the natural frequency of the dynamometer Kistler 9129AA. This capping is denoted with the black dashed line in Fig. 6.7 b). Furthermore, the parameter μ_1 is significantly higher than the usual natural frequency of the mechanical system excited by the noise Γ_t, thus the white noise approach is a proper approximation. The relative white noise intensity σ_0 tends to a constant value as well for larger chip thicknesses, however, this value is considerably smaller than σ_F. Nonetheless, considering $\sigma_0 = 0.1$–1 % is a safe assumption w.r.t. to stability and stationary second moment, even though it might be a slight overestimation of the actual intensity.

Note that even though the parameters for the main and the feed cutting forces (left and right columns of Fig. 6.7) were calculated independently, they show almost the same numerical values

for σ_F, μ_1 and σ_0. Thus the simplification, that the same noise process generates both cutting force components is adequate.

It can be concluded, that the modelling of deterministic and stochastic high frequency phenomena in the cutting forces can be approximated by a Gaussian noise process, which is a mathematically concise and efficient approach, especially compared to finite element methods [11]. For large chip thickness, the distribution of the measured force is Gaussian: a Gaussian stochastic process is superimposed on the mean force. Furthermore, in Fig. 6.7b, it can be observed that the intensity σ_F of the noise process Γ_t, as well as the equivalent white noise intensity σ_0 tends to a constant value above $h \approx 0.025\ \mathrm{mm}$. Thus for conventional chip thicknesses the noise component of the cutting force can be considered as a multiplicative noise $\sigma_F \bar{F}_j \Gamma_t$ during e.g. Monte-Carlo simulations, or as a white noise $\sigma_0 \bar{F}_j \Gamma_t$ for calculations like the stochastic semidiscretisation.

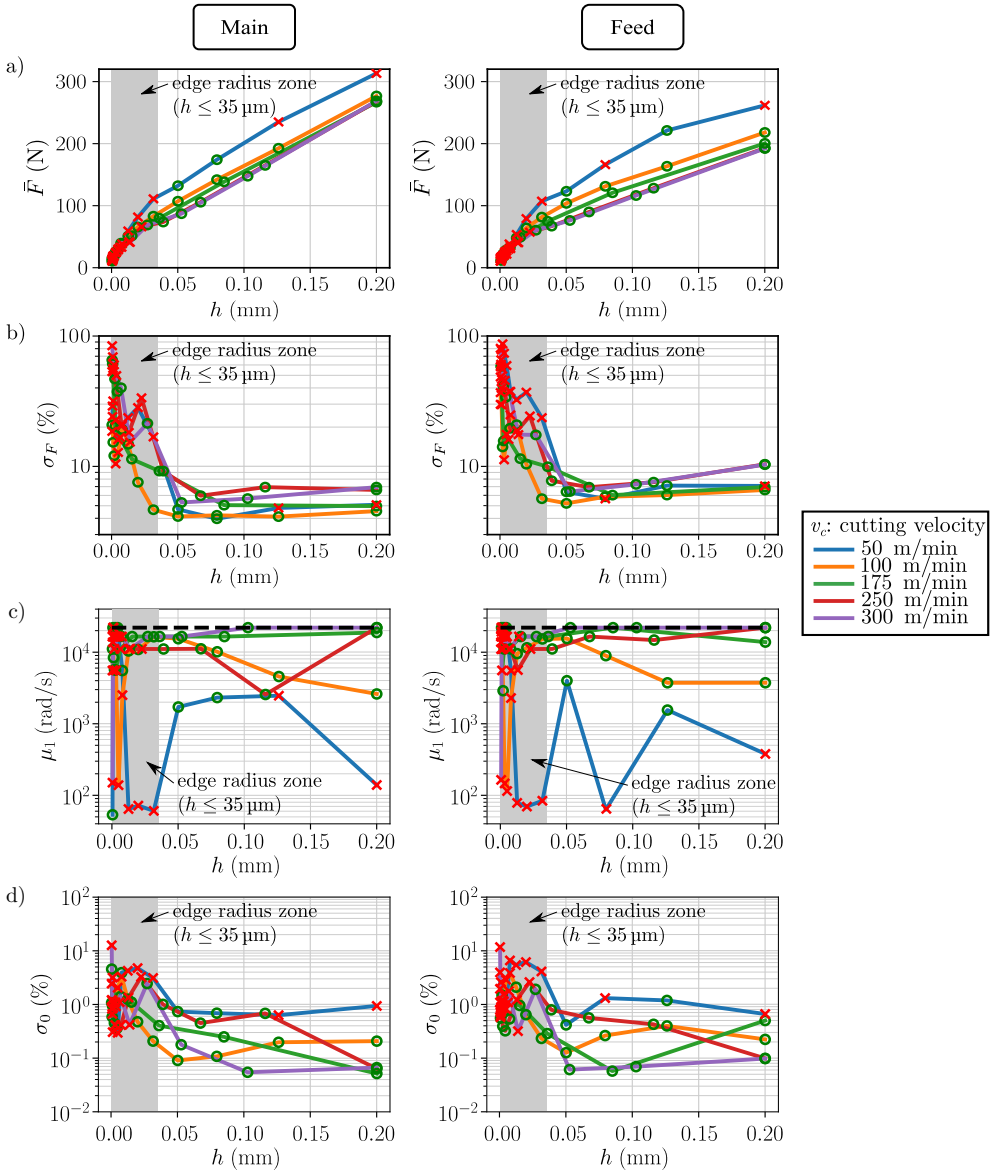

Figure 6.7. *a) The average cutting force, b) the relative cutting force noise intensity c) the cutoff frequency of the approximating Ornstein-Uhlenbeck process (capping due to the natural frequency of the dynamometer denoted with dashed black line) and d) the relative equivalent white noise intensity. In the gray areas the stochastic cutting force model based on the proposed filtered noise processes is not valid, due to the effect of the tool edge radius.*

6.2 Stochastic Effects during Chatter Detection during Milling

In this section it is experimentally investigated, how the theoretical results in Sec. 5.3 translate into practice. Namely, how well the stochastic milling model can describe the qualitative behaviour of the milling process. The stationary second moment of the measured displacements as well as the peak growth of the Fourier spectrum of the measured signal is investigated as the spindle speed Ω of the milling is varied.

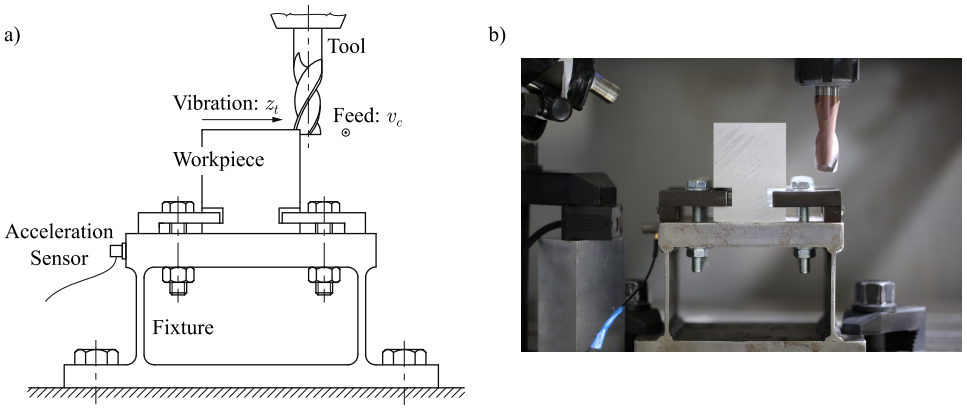

Figure 6.8. *The schematic figure a) and the experimental setup b) for milling with single-degree-of-freedom experimental setup as presented in [46].*

For the measurements, the same experimental setup is applied, as in [46] (see Fig. 6.8). During the measurements the milled workpiece is clamped onto a specially prepared flexure, that was designed to be flexible only in one direction, thus it can mimic the dynamics of a single-degree-of-freedom system. The milling tool is considered to be rigid, because it is significantly more stiff, than the flexible direction of this flexure. The feed direction of the milling is chosen to be perpendicular to z (as shown in Fig. 6.8), leading to the same setup that's dynamics is described by Eq. (5.3.7) in Sec. 5.3. Note that in [46] it is thoroughly demonstrated, that the deterministic part of this mechanical model is capable of capturing the stability properties.

During the analysis of the vibrations, no external perturbations were applied on the system, only the vibrations of the workpiece (caused by the milling force) were measured by means of a piezoelectric accelerometer. To analyse the displacement signal, the measured acceleration is integrated in frequency domain and an appropriate high-pass filter was used. Furthermore, from the measured signal, only the section is used, where the radial immersion, thus the entering and exiting angles φ_{en} and φ_{ex} are constant, and the transient vibrations have decayed.

After the integration, the measured displacement z_t is decomposed into a deterministic $f_z x_p(t)$ and into a stochastic $f_z x_t$ component. To obtain the deterministic component $f_z x_p(t)$, the tooth passing frequency ω_{tp} has to be accurately determined, since the periodic averaging has to be conducted w.r.t. its period $T_{\mathrm{tp}} = 2\pi/\omega_{\mathrm{tp}}$. In the ideal case the tooth passing frequency could be determined from the nominal spindle speed Ω of the tool as

$$\omega_{\mathrm{tp}} = N\Omega. \tag{6.2.1}$$

However, in practice this frequency is not accurate enough, since there is a small deviation ($\sim 0.1\ \%$) between the prescribed Ω and the realised $\tilde{\Omega}$ spindle speeds. The actual spindle speed $\tilde{\Omega}$ is determined using the same approach as in [46]. Since the cutting force exciting the workpiece is not a smooth function, the Fourier spectrum of the corresponding periodic forced vibrations contains the peaks at the tooth passing frequency ω_{tp} and at its integer multiplies. The nominal spindle speed is used as an initial guess to initiate the calculation of the realised spindle speed $\tilde{\Omega}$, which is determined by detecting the 50^{th} higher harmonic of the tooth passing frequency ω_{tp}.

With this approach, the realised spindle speed $\tilde{\Omega}$ (and therefore the corresponding ω_{tp}) is obtained accurately enough to allow the calculation of the periodic solution $f_z x_{\mathrm{p}}(t)$ and the periodic standard deviation $\mathrm{StD}(f_z x_t)$ through periodic averaging and periodic standard deviation calculation, respectively, where the stochastic perturbation $f_z x_t$ is obtained by

$$f_z x_t = z_t - f_z x_{\mathrm{p}}(t). \tag{6.2.2}$$

The stochastic perturbation can be used to predict noise-induced resonance through the calculation of the maximum and mean of periodic standard deviation of $f_z x_t$. Another approach is to take its Fourier spectrum $|\hat{x}_\omega|$ and determine its maximum peak height ℓ_{peak} near $\omega = \omega_{\mathrm{n}}$, where ω_{n} is the natural frequency of the workpiece-flexure composition. According to the theoretical results in Sec. 5.3, as the border of the stable parameter region is approached, the above described quantities increase hyperbolically.

The chatter detection strategy described above is applied to a similar case study as in Sec. 5.3, where the axial depth of cut is fixed to $a_p = 2\,\mathrm{mm}$, while the spindle speed is varied in the range $\Omega \in [4500\ \mathrm{rpm}, 8218\ \mathrm{rpm}]$ with average steps of $100\,\mathrm{rpm}$ and near the stability borders with extremely small steps 2–$5\,\mathrm{rpm}$. The modal parameters, the cutting force characteristics are presented in Sec. 5.3. The milling operations are conducted with a two-flooted tool ($N = 2$) with diameter $D = 16\ \mathrm{mm}$, helix angle $\beta = 30°$, and the feed per tooth was chosen as $f_z = 0.1\ \mathrm{mm}$. Furthermore, these down-milling tests were conducted along a straight path, with radial immersion $a_e = 2\ \mathrm{mm}$, which results in $\varphi_{\mathrm{en}} \approx 138.6°$ and $\varphi_{\mathrm{ex}} = 180°$. The parameters of the calculations in Sec. 5.3 are chosen to be similar to these measurements, thus a direct qualitative comparison can be made with the theoretical results obtained there. Note that the effect of the helix angle $\beta = 30°$ is negligible due to the small axial immersion a_p.

The measurements were carried out on an NCT EmR-610Ms milling machine, where the workpiece was clamped onto the flexible flexure. The vibrations were acquired with PCB 352C23 type acceleration sensor and the vibration data was collected with a NI-9234 Input Module in a NI cDAQ-9178 Chassis at 51200 Hz sampling rate.

In Fig. 6.9 some properties of the measured signal is shown, namely the peak-to-peak value $\mathrm{P2P}(f_z x_p(t))$ of the mean periodic displacement $f_z x_p(t)$, the $f_z \ell_{\mathrm{peak}}$ of the FFT of stochastic signal $f_z x_t$ and the maximum and mean values of the standard deviation $\mathrm{StD}(f_z x_t)$, respectively. These properties of the measured signals show similarity to the theoretical results shown in Sec. 5.3. The peak-to-peak value $\mathrm{P2P}(f_z x_p(t))$ does not show any particular behaviour near the stability borders and its magnitude grows at the resonant spindle speed $\Omega = \omega_{\mathrm{n}}/N$, which is expected, also based on the deterministic models. However, in contrast to the theoretical results, there are increased $\mathrm{P2P}(f_z x_p(t))$ values around $\sim 5300-5500$ rpm, which corresponds to a flip bifurcation predicted by theoretical models at that spindle speed [36]. Since there is a period doubling effect, this can be due to measurement inaccuracies, such as the run-out of the tool and the varying spindle speed. Due to spindle speed not being perfectly constant during a milling operation and even a small variation of spindle speed makes it impossible to perfectly decompose the measured signal into a mean periodic and into a stochastic component.

The peak heights ℓ_{peak} in the Fourier spectrum of the stochastic component x_t blow up at all the stability borders as predicted in the theory. Discrepancies at the resonant spindle speed might be due to the above mentioned measurement problems, which cause a small portion of the deterministic component still being present in the stochastic component x_t, and this leads to the increase in the peak height ℓ_{peak}. Note that this increase is only relatively large, since in absolute value it is only a 4–5 µm (compared to the mean's peak height which is ~ 350 µm). Some examples for the growth of the $f_z \ell_{\mathrm{peak}}$ at the stability borders is shown in Fig. 6.10, where the measured signal and its FFT is presented.

Furthermore, both the maximum and the mean of the stationary standard deviation $\mathrm{StD}(x_t)$ in Fig. 5.10c-d blow up at all the stability borders, due to the noise-induced resonance, similarly to the peak height ℓ_{peak}.

As for the standard deviations, the difference between the maximum and the mean is only approximately a multiplier, but they show the same behaviour, while the theoretical results predict a slight difference at the resonant spindle speed. This can be also the consequence of the varying spindle speed, since during the averaging, the effects causing the different behaviour in the maximum and mean of the $\mathrm{StD}(f_z x_t)$ are mitigated by this small variation of the spindle speed. Nonetheless, the standard deviation $\mathrm{StD}(f_z x_t)$ is a good chatter indicators, since it does not produce a false positive result and show the same type of behaviour near the stability borders, as predicted by the theory.

However, the measurement of such a small standard deviation is challenging during a real practical scenario, due to the measurement is being overloaded by noise related to the measurement, while the $f_z \ell_{\mathrm{peak}}$ can be still well tracked, thus the state-of-the-art approaches are based on this quantity.

As a summary, the stochastic analysis of the milling process can provide a qualitative description of the noise component in the stable domain, which can be utilised to detect the emerging chatter. For quantitative comparison, the intensity of the noise process as well as the other parameter of the model can be tuned. However, the intensity σ_0 should be decreased in the theoretical model (5.3.7) to fit the calculated peak values ℓ_{peak} and standard deviations $\mathrm{StD}(f_z x_t)$ to their measured counterparts, while based on the visual inspection of the time signals presented in Fig. 6.11 this intensity σ_0 should be increased, relative to the measured intensity presented in Sec. 6.1. Furthermore, near the stability borders, due to the noise-induced resonance, the theoretical model is really sensitive [15, 53] to a slight change of the model, e.g., including a varying spindle speed, the run-out the tool, the effect of the helical edge geometry and the fly-overs even at small amplitude vibrations.

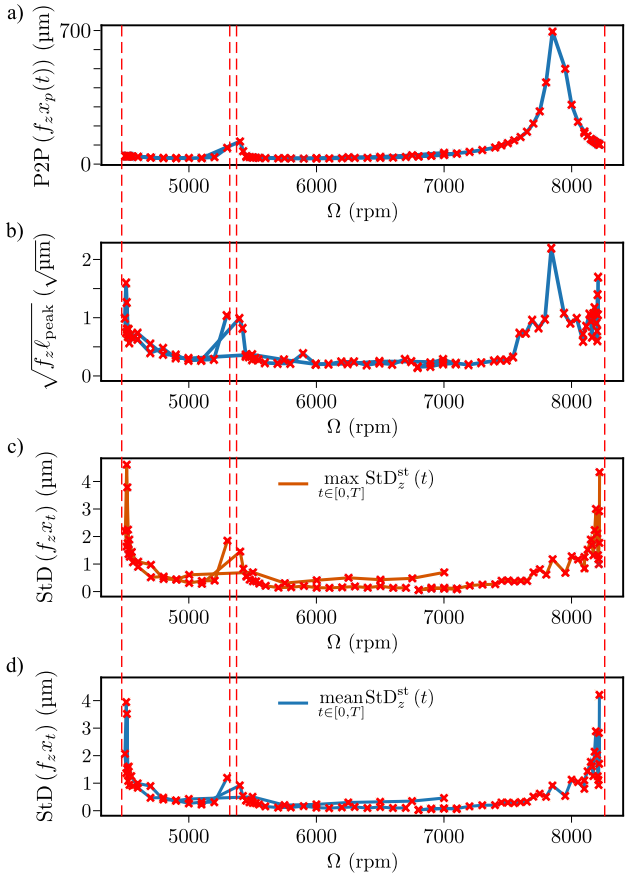

Figure 6.9. *Measured quantities during the milling operation. Panel a) shows the P2P values of the mean periodic solution, panel b) illustrates the behaviour of the peak height $f_z \ell_{\text{peak}}$ of the Fourier spectrum of the stochastic component $f_z x_t$ while panel c) and d) shows the maximum and mean values of the standard deviation of the stochastic component of the vibrations, respectively.*

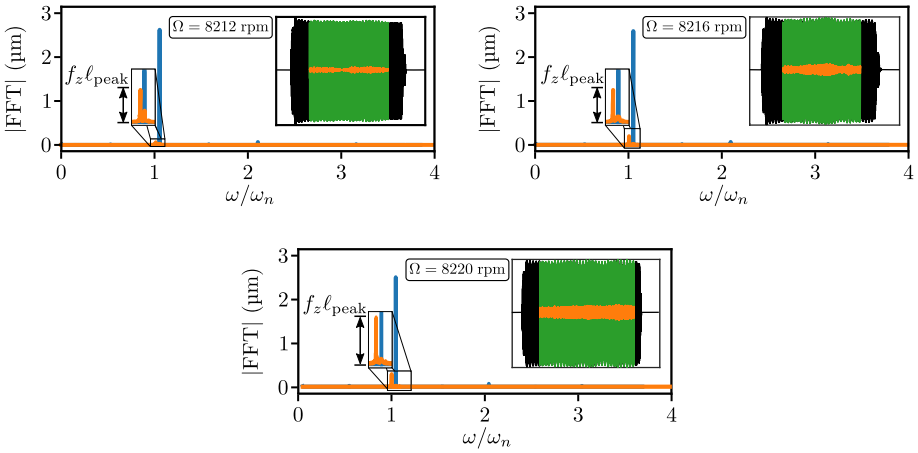

Figure 6.10. *Examples of the Fourier transforms of the decomposed measured vibrations. The blue peaks denote the Fourier transforms of the periodic deterministic solution, while the orange peaks denote the Fourier transforms of the noise perturbation. For each Fourier transforms the measured displacement is given in green, the stochastic component is shown with the orange trajectory. The spindle speed Ω in each panel correspond to the nominal spindle speed*

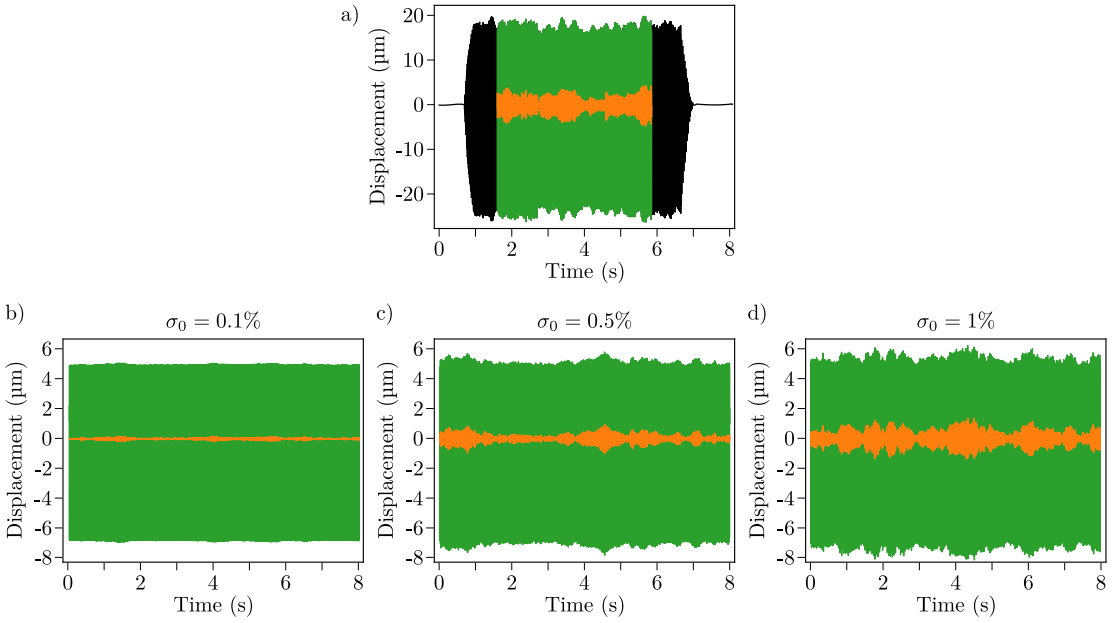

Figure 6.11. *Comparison of the a) measured signal at* $\Omega = 4600$ rpm *with simulated signals b)-d) with parameters used in Sec. 5.3 at* $\Omega = 5100$ rpm *(both spindle speed is in the domain of stable milling, and* ~ 100 rpm *from the stability border.*

Chapter 7

Main Results

There are several models in engineering and biology which lead to delay differential equations (DDE), e.g., the models of machine tool vibrations [2, 79, 94], delayed control loops [99], traffic dynamics [64], predator-prey systems [97] or neural networks [16]. During the investigation of such delayed dynamical systems stochastic effects are usually neglected, despite that stochastic excitations often influence the behaviour of these systems. The noise may appear not only as an external excitation, but also in the coefficients of the state variables. In case of construction of deterministic models that approximate stochastic systems, the usual approach is to consider the mean values of the measured system parameters that describe the process, while the measured variation is considered as the unwanted noise of the measurement [29]. This mean-value based approach is valid for linear systems only, and even in these cases, its result may be misleading regarding the steady-state behaviour. A noise excitation can lead not only to change in stability properties, but it can also cause a so-called autonomous stochastic resonance or coherence resonance [53, 84].

For example, in manufacturing science, when machine tool vibrations are investigated usually this deterministic approximation is applied. When dealing with machine tool vibrations two main categories of vibrations are considered: the so-called chatter and forced vibrations [94]. Chatter is an instability phenomenon, caused by the time delay due to the surface regeneration effect. During this instability, self-induced oscillations occur, which can lead to poor surface quality and damage in the tool. The forced vibrations are the result of the time-varying cutting force, which can occur due to the changing size and shape of the chip, but can also be caused by high-frequency processes as chip formation and segmentation, shockwaves in the material, local inhomogeneities in the material properties [66, 67], shear plane oscillation, rough surface of the workpiece etc. However, these high-frequency variations are usually not considered [2, 59] in the constant parameters of the force characteristics describing the relationship between the chip size and the cutting force. Since these high speed phenomena are very complex processes, thus in some recent theoretical works [14, 43, 85] a stochastic noise excitation is used to take the effect of these unmodelled dynamics into account.

Another example is in vehicular traffic, where the time delay originates from the drivers' reaction time, that typically varies stochastically [63], while the additive noise comes from the other vehicles whose motion the drivers need to respond to. In network control systems, delays may vary stochastically due to packet drops or capacity drops while in the meantime agents need to respond to the noisy environment [19, 35, 50, 60, 68–70]. In complex biological networks, like those within cells, external noise is ubiquitous, while stochastic delays may be used to model a sequence of reactions [30, 32].

This dissertation aims to investigate an approach which is able to efficiently characterise the stability and steady-state behaviour of systems with delays subjected to parametric and additive noise perturbations. For this purpose this dissertation discusses the first and second moment stability and the steady-state first and second moment of linear stochastic delay differential equations (SDDEs). After a brief and gentle introduction to the core mathematical tools in Chapter 2, the stochastic semidiscretisation was constructed in Chapter 3 for periodic linear SDDEs. Next, the stochastic maps derived with the stochastic semidiscretisation were used to construct the first and second moment maps. These moment maps then were utilised to investigate the first and second moment stability of the original SDDE, as well as the steady-state first and second moments were

approximated, allowing the prediction of the white noise-induced resonance. Furthermore, the semidiscretisation of delay differential equations (DDEs) with stochastic delay was generalised to allow the steady-state first and second moment analysis of these systems subjected to noise excitation.

In Chapter 4 the convergence of the stochastic semidiscretisation was investigated through numerical case studies (stochastic Hayes equation, stochastic delay oscillator, stochastic delayed Mathieu equation, Hayes equation with stochastic delays). Furthermore, it was shown that SDDEs with periodic coefficients and delays, as well as DDEs with stochastic delays have periodic steady-state first and second moments. Chapter 5 discusses the application of the method to engineering problems, namely the effect of the noisy cutting force on the dynamics of turning and milling. It was shown, that the noise in the cutting force can cause large amplitude vibrations during machining processes even before the cutting process looses stability, and that the spindle speed variation during turning can negatively influence the turning's robustness against noise-induced resonance, even though the stability properties are improved. Furthermore, it was shown how the statistical properties of the vibrations in the stable parameter domain, such as the standard deviation of the measured displacement, can be used to predict the formation of chatter during a machining operation. In the last section of this chapter it is also shown, that how stochastic packet drops can influence the stability properties and the steady-state behaviour of connected automated vehicles. Moreover, it was demonstrated how the harmful effects of these packet losses can be eliminated at the cost of a minor deterioration in the size of the stable parameter domain.

In Chapter 6 the theoretical assumptions and predictions are compared to measurement results. First, it is proved that there is a significant stochastic component of the cutting force through a set of cutting force measurements, furthermore, the equivalent white noise intensity of this noise component is determined. Finally, it is investigated, how the quantities studied during the theoretical analysis of milling processes compare to measurements. It is demonstrated through an experiment on a specially prepared milling setup, that the stochastic model of milling is capable of capturing the behaviour of the quantities which predict the formulation of chatter.

Main Result 1

Thesis statement 1: Stochastic delay differential equations as stochastic differential equations for numerical integration

Consider stochastic delay differential equations (SDDE) with a single point delay given in the incremental form

$$\begin{aligned} \mathrm{d}\mathbf{x}_t &= \mathbf{a}\left(\mathbf{x}_t, \mathbf{x}_{t-\tau}, t\right)\mathrm{d}t + \mathbf{b}\left(\mathbf{x}_t, \mathbf{x}_{t-\tau}, t\right)\mathrm{d}W_t, \\ \mathbf{x}_t &= \boldsymbol{\varphi}(t), t \in [-\tau, 0], \end{aligned} \tag{R1.1}$$

where $\mathbf{a}, \mathbf{b} : \mathbb{R}^d \times \mathbb{R}^d \times \mathbb{R} \to \mathbb{R}^d$ are smooth functions, $\tau > 0$ is the time delay, $\mathbf{x}_t$ is the $\mathbb{R}^d$-valued state variable at time t, $\mathbf{x}_{t-\tau}$ denotes the delayed state at time $t-\tau$, W_t is a standard Wiener process and the initial condition $\mathbf{x}_t = \boldsymbol{\varphi}(t)$, $t \in [-\tau, 0]$ is continuous with $\left\langle \|\boldsymbol{\varphi}(t)\|^2_{L^\infty} \right\rangle < \infty$ on $t \in [-\tau, 0]$ and $\mathcal{F}_0$-measureable.

SDDE (R1.1) can be numerically integrated by transforming it into the stochastic differential equation (SDE) of the form

$$\mathrm{d}\mathbf{x}_t = \hat{\mathbf{a}}\left(\mathbf{x}_t, t\right)\mathrm{d}t + \hat{\mathbf{b}}\left(\mathbf{x}_t, t\right)\mathrm{d}W_t.$$

Since at time t all values $\mathbf{x}_s, s \in [-\tau, t]$ are available (e.g., it can be approximated by the interpolation of the approximate discrete solution), the functions $\hat{\mathbf{a}}$ and $\hat{\mathbf{b}}$ can be defined by dynamically embedding the initial function $\boldsymbol{\varphi}$ and the already computed (approximated) $\mathbf{x}_t$ states into the functions $\mathbf{a}$ and $\mathbf{b}$ as a time dependent inhomogenity, namely

$$\hat{\mathbf{a}}(\mathbf{x}_t, t) = \mathbf{a}(\mathbf{x}_t, \boldsymbol{\phi}_{t-\tau}, t), \qquad \hat{\mathbf{b}}(\mathbf{x}_t, t) = \mathbf{b}(\mathbf{x}_t, \boldsymbol{\phi}_{t-\tau}, t),$$

where the history embedding function is

$$\boldsymbol{\phi}_t = \begin{cases} \boldsymbol{\varphi}_t & t \leq 0 \\ \mathbf{x}_t & t > 0 \end{cases}.$$

This representation (with discontinuity handling originating from the intial state) allows uninterrupted numerical integration and the utilization of the solver algorithms and features of already existing SDE ecosystems.

To implement this approach the *StochasticDelayDiffEq.jl* package is created for the Julia programming language, and made available in its package ecosystem. The package can be used for the numerical simulations of stochastic delay differential equations, by being able to utilise a wide range of stochastic integrators from the *StochasticDiffEq.jl* package, e.g., the Euler-Maruyama method, the implicit Runge-Kutta Milstein method, or even stabilised SROCK methods. Furthermore, the package can use the features of the *DifferentialEquations.jl* ecosystem, such as the built-in Monte-Carlo simulation interface.

Corresponding sections:

- Sec. 2.2.5
- Sec. 2.2.7

Corresponding publications:

- Software
  StochasticDelayDiffEq.jl
  SciML, *github.com/SciML/StochasticDelayDiffEq.jl*

Main Result 2

Thesis statement 2: Stochastic Semidiscretization Method

Consider the periodic linear stochastic delay-differential equation of the form

$$\begin{aligned} \mathrm{d}\mathbf{x}_t = &\big(\mathbf{A}(t)\mathbf{x}_t + \mathbf{B}(t)\mathbf{x}_{t-\tau(t)} + \mathbf{c}(t)\big)\,\mathrm{d}t \\ &+ \big(\boldsymbol{\alpha}(t)\mathbf{x}_t + \boldsymbol{\beta}(t)\mathbf{x}_{t-\tau(t)} + \boldsymbol{\sigma}(t)\big)\,\mathrm{d}W_t, \end{aligned} \tag{R2.1}$$

where $\mathbf{x}_t$ is the $\mathbb{R}^d$-valued state variable at time t, $\mathbf{x}_{t-\tau(t)}$ denotes the delayed state at time $t-\tau(t)$, W_t is a standard Wiener process and $\mathbf{A}(t)$, $\mathbf{B}(t)$, $\boldsymbol{\alpha}(t)$, $\boldsymbol{\beta}(t) \in \mathbb{R}^{d\times d}$ are T-periodic coefficient matrices, $\mathbf{c}(t)$, $\boldsymbol{\sigma}(t) \in \mathbb{R}^d$ are T-periodic additive vectors and $\tau(t) > 0,\ t \in [0,T]$ is the T-periodic time delay. Stochastic semidiscretization of (R2.1) gives the $(r+1)d$ dimensional periodic stochastic map of the form

$$\mathbf{y}_{n+1} = (\mathbf{F}(n) + \mathbf{G}_n)\,\mathbf{y}_n + (\mathbf{f}(n) + \mathbf{g}_n)\,, \tag{R2.2}$$

where r is the delay resolution. The second moment stability and the steady-state first and second moments of (R2.1) can be approximated by the moment mappings of (R2.2).

To estimate the first moment stability and the steady-state first moment, the stability and the fixed point of the first moment map

$$\bar{\mathbf{y}}(n+p) = \mathbf{F}^{(n,p)}\bar{\mathbf{y}}(n) + \mathbf{f}^{(n,p)},$$

has to be considered, where p is the discrete time period.

To estimate the second moment stability and the steady-state second moment, the stability and the fixed point of the second moment map

$$\bar{\bar{\mathbf{y}}}(n+p) = \mathbf{H}^{(n,p)}\bar{\bar{\mathbf{y}}}(n) + \overline{\mathbf{h}\bar{\mathbf{y}}}^{(n,p)} + \overline{\bar{\mathbf{f}}\bar{\mathbf{g}}}^{(n,p)}$$

has to be considered.

The convergence rate of the approximation can be increased if a q-th order Lagrange polynomial is fitted on the delayed state during the stochastic semidiscretisation. When approximating the stability and stationary moments the stochastic semidiscretisation has orders of magnitudes faster convergence rate compared to the full discretisation method or to Monte-Carlo simulations.

Corresponding sections:

- Secs. 3.1-3.2
- Secs. 4.1-4.3

Corresponding publications:

- Journal Papers
  - [83] H. T. Sykora, D. Bachrathy. *Stochastic Semidiscretization Method: Second Moment Stability Analysis of Linear Stochastic Periodic Dynamical Systems with Delays*. Applied Mathematical Modelling, 88:933 – 950, 2020. ISSN 0307-904X
  - [87] H. T. Sykora, D. Bachrathy, and G. Stepan. *Stochastic semi-discretization for linear stochastic delay differential equations*. International Journal for Numerical Methods in Engineering, 119(9):879–898, 2019
- Conference Papers
  - [81] Sykora Henrik, Bachrathy Dániel, *A fehér zaj hatása lineáris, késleltetett, PD szabályozás stabilitási tulajdonságaira*, XXVI. Nemzetközi Gépészeti Konferencia (OGÉT) (Marosvásárhely, 2018.04.26-29.)

- Conference Talks
  [86] Sykora Henrik T, Bachrathy D., Stépán G. *Lineáris sztochasztikus késleltetett rendszerek szemi-diszkretizációja*, XIII. Magyar Mechanikai Konferencia (XIII. MaMeK) - Miskolc, Magyarország, 2019
  [88] Henrik T Sykora, Dániel Bachrathy, Gábor Stépán, *Stochastic Semi-Discretization for Stochastic Systems With Delay*, SIAM Conference on Applications of Dynamical Systems (DS19) - Minisymposium: When Stochasticity Meets Delay: Rendezvous in Infinite Dimension, Snowbird, USA, 2019

- Conference Poster
  [82] Henrik T Sykora, Dániel Bachrathy, *An effective method to investigate stochastic delayed systems in Julia*, JuliaCon Poster session, London, UK, 2018.08.07-11.
  [89] H. T Sykora, G. Fodor, D. Hajdu, D. Bachrathy, *Solving Periodic Stochastic Problems with Delays with the Help of Julia*, JuliaCon Poster session, Baltimore, US, 2019.07.22-26.
- Software
  StochasticSemiDiscretizationMethod.jl
  github.com/HTSykora/StochasticSemiDiscretizationMethod.jl

Main Result 3

Thesis statement 3a: Approximation of the steady-state first and second moments of stochastically delayed systems with additive noise

Consider the linear delay differential equaiton with stochastic delays and additive noise in the form

$$\begin{aligned} \mathrm{d}\mathbf{x}_t = &\big(\mathbf{A}\mathbf{x}_t + \mathbf{B}\mathbf{x}_{t-\tau_0} + \mathbf{B}_\mathrm{s}\mathbf{x}_{t-\tau_{\mathrm{s},t}}\big)\mathrm{d}t \\ &+ (\bar{\tau}_\mathrm{s} - \tau_{\mathrm{s},t})\,\boldsymbol{\sigma}_\tau \mathrm{d}t + \boldsymbol{\sigma}\mathrm{d}W_t, \end{aligned} \tag{R3.1}$$

where $\mathbf{x}_t$ is the $\mathbb{R}^d$-valued state variable at time t, $\mathbf{x}_{t-\tau_0}$ and $\mathbf{x}_{t-\tau_\mathrm{s}(t)}$ denotes the delayed state at time $t-\tau_0$ and $t-\tau_\mathrm{s}(t)$, respectively, W_t is a standard Wiener process, $\mathbf{A}$, $\mathbf{B}$, $\mathbf{B}_s \in \mathbb{R}^{d\times d}$ are the constant coefficient matrices, $\boldsymbol{\sigma}_\tau$, $\boldsymbol{\sigma} \in \mathbb{R}^d$ are the constant additive vectors and $\tau_0 > 0$ is the constant time delay. The stochastic time delay $\tau_{\mathrm{s},t}$ is assumed to stay constant for a holding time T_τ before potentially taking on a new value from a finite set $\{\tau_1, \tau_2, \ldots, \tau_{J_\tau} \in \mathbb{R} : 0 < \tau_1 < \tau_2 < \ldots < \tau_{J_\tau}\}$.

The steady-state first and second moments of system (R3.1) can be approximated by the moment mappings of the following periodic stochastic map

$$\mathbf{z}_{k+1} = \mathbf{K}_k\mathbf{z}_k + \mathbf{l}_k,$$

which can be obtained by stochastic semidiscretisation. To estimate the steady-state first moment, the fixed point of the first moment map

$$\bar{\mathbf{z}}(k+1) = \overline{\mathbf{K}}\bar{\mathbf{z}}(k) + \bar{\mathbf{l}}_\tau,$$

while to estimate the steady-state second moment, the fixed point of the second moment map

$$\bar{\bar{\mathbf{z}}}(k+1) = \overline{\overline{\mathbf{K}}}\bar{\bar{\mathbf{z}}}(k) + \bar{\mathbf{k}}\bar{\mathbf{z}}(k) + \left(\bar{\bar{\mathbf{l}}}_\tau + \bar{\bar{\mathbf{l}}}_W\right)$$

has to be considered.

Thesis statement 3b: Periodic steady-state first and second moments of stochastically delayed systems with additive noise

Consider the linear delay differential equation with stochastic delays and additive noise in the form of (R3.1). If the stochastic delay is described by the above stochastic switching process, the system (R3.1) has T_τ-periodic steady-state first and second moments, however, if $T_\tau < \tau_1$, the periodic first moment becomes zero.

Corresponding sections:

- Sec. 3.3
- Sec. 5.4

Corresponding publications:

- Journal Papers
  - [92] H. T. Sykora, M. Sadeghpour, J. I. Ge, D. Bachrathy, and G. Orosz. *On the moment dynamics of stochastically delayed linear control systems*. International Journal of Robust and Nonlinear Control, 2020.
- Conference Poster
  - [82] Henrik T Sykora, Dániel Bachrathy, *An effective method to investigate stochastic delayed systems in Julia*, JuliaCon Poster session, London, UK, 2018.08.07-11.

Main Result 4

Through a series of examples it is shown, that a small amount of noise excitation, that is an inherent property of all engineering systems, does not influence stability properties significantly, however, near the stability border it can lead to large amplitude stochastic vibrations. These vibrations can grow to an extent, that the mathematical model describing the system is not valid any more, due to inevitable saturation, even in the stable parameter domain.

> **Thesis statement 4: Stationary second moment charts**
>
> When analysing a dynamical system describing an engineering problem in terms of robustness against external excitations, stationary second moment charts of a state variable is a more appropriate measure of the actual physical process than the stability depicted on traditional stability charts.

There are examples given for these quantities, such as the standard deviation of the stochastically excited displacement of the cutting tool, corresponding to the surface roughness or the standard deviation of the velocity of a connected vehicle corresponding to the passenger comfort and the fuel consumption.

Furthermore, an improvement in stability properties does not necessarily lead to a superior system in terms of the robustness against external effects. It is demonstrated through the second moment chart of turning with spindle speed variation (SSV), that the SSV increases the stability of the turning process, however, in terms of the resulting surface roughness the cutting process might become worse. Similar demonstration is given through the control design of a connected automated vehicle, where the harmful effect of the stochastic packet drops are eliminated at the cost of a minor deterioration of the size of the stable parameter domain.

Corresponding sections:

- Secs. 5.1-5.4

Corresponding publications:

- Journal Papers
  - [83] H. T. Sykora, D. Bachrathy. *Stochastic Semidiscretization Method: Second Moment Stability Analysis of Linear Stochastic Periodic Dynamical Systems with Delays*. Applied Mathematical Modelling, 88:933 – 950, 2020. ISSN 0307-904X
  - [92] H. T. Sykora, M. Sadeghpour, J. I. Ge, D. Bachrathy, and G. Orosz. *On the moment dynamics of stochastically delayed linear control systems*. International Journal of Robust and Nonlinear Control, 2020.
- Conference Papers
  - [81] Sykora Henrik, Bachrathy Dániel, *A fehér zaj hatása lineáris, késleltetett, PD szabályozás stabilitási tulajdonságaira*, XXVI. Nemzetközi Gépészeti Konferencia (OGÉT) (Marosvásárhely, 2018.04.26-29.)
  - [84] H. T. Sykora, D. Bachrathy, and G. Stepan. *A theoretical investigation of the effect of the stochasticity in the material properties on the chatter detection during turning*. 29th Conference on Mechanical Vibration and Noise, 8, 2017.99
- Conference Poster
  - [82] Henrik T Sykora, Dániel Bachrathy, *An effective method to investigate stochastic delayed systems in Julia*, JuliaCon Poster session, London, UK, 2018.08.07-11.
  - [89] Henrik T Sykora, Gergő Fodor, Dávid Hajdu, Dániel Bachrathy, *Solving Periodic Stochastic Problems with Delays with the Help of Julia*, JuliaCon Poster session, Baltimore, US, 2019.07.22-26.

Main Result 5

During the measurement of the cutting force, large variations can be experienced in the measured signal, but these fluctuations are usually attributed to the quality of the measurements and only the average force is considered as the base for fitting the cutting parameters. However, these variations are orders of magnitude larger than it could be explained as a measurement noise.

There are high speed phenomena during cutting, such as chip fragmentation, inhomogeneities in material quality, shear plane oscillation, rough surface of the workpiece, friction, etc. These phenomena play important role in the amplitude of the forced vibrations, influencing the surface quality of the manufactured product and the detection of chatter. There are ways to model these variances in the cutting force, e.g. using sophisticated finite element method to compute the chip formation and the chip thickness accumulation or using a shear zone model. However, the results of these methods are very sensitive to the values of the numerous and hardly measurable parameters, are often compromised by numerical difficulties and is computationally very expensive.

Thesis statement 5: Stochastic cutting force model

The stochastic cutting force model of the form

$$F_t = \bar{F}(1 + \sigma_F \Gamma_t),$$

where

$$\mathrm{d}\Gamma_t = -\mu_1 \Gamma_t \mathrm{d}t + \sqrt{2\mu_1}\mathrm{d}W_t,$$

efficiently models the effects of the high frequency phenomena on the cutting force.

The cutting force measurements during orthogonal turning tests validate the stochastic cutting force model, thus the large amplitude noise is an inherent component of the cutting force, and is not related to a measurement noise.

Furthermore, a white noise approximation Γ_t of the stochastic variations in the cutting force can be given in the form

$$F_t = \bar{F}(1 + \sigma_0 \Gamma_t),$$

where $\sigma_0 = \sqrt{2}\sigma_F / \sqrt{\mu_1}$.

Corresponding sections:

- Sec. 6.1

Corresponding publications:

- Journal Papers
  - [27] G. Fodor, H. T. Sykora, and D. Bachrathy. *Stochastic Modeling of the Cutting Force in Turning Processes*. The International Journal of Advanced Manufacturing Technology, 111(1-2):213–226, 2020.
- Conference Papers
  - [85] H. T. Sykora, D. Bachrathy, and G. Stepan. *Gaussian noise process as cutting force model for turning*. Procedia CIRP, 77:94–97, 2018
- Conference Talks
  - [26] Fodor G., Sykora Henrik T, Bachrathy D., *Forgácsolóerő modellezése sztochasztikus folyamatokkal esztergálás során*, XIII. Magyar Mechanikai Konferencia (XIII. MaMeK) - Miskolc, Magyarország, 2019
- Conference Poster
  - [89] Henrik T Sykora, Gergő Fodor, Dávid Hajdu, Dániel Bachrathy, *Solving Periodic Stochastic Problems with Delays with the Help of Julia*, JuliaCon Poster session, Baltimore, US, 2019.07.22-26.

Main Result 6

Thesis statement 6a: Chatter peak growth due to noise-induced resonance

The stochastic model of milling explains that the growth of the so-called chatter peak in the Fourier transform of the measured vibration signals during a milling operation in the stable machining parameter domain, which leads to uncertain experimental chatter detection, is the result of the noise-induced resonance.

Thesis statement 6b: Chatter peak growth and the stationary second moment

The height of the chatter peak in the Fourier transform of the measured vibration signals during a milling operation behaves similar to the steady-state second moment of the relative displacement of the cutting tool and workpiece during machine tool vibrations. Thus, both can predict the onset of chatter based on measurements in the stable parameter domain.

The theoretical predictions produced by the basic stochastic milling model are validated with an extremely high-resolution milling experiment. The measured results show similar tendencies, but the magnitudes are also close to their calculated counterparts.

Corresponding sections:

- Sec. 5.3
- Sec. 6.2

Corresponding publications:

- Journal Papers

  [90] H. T. Sykora, D. Hajdu, Z. Dombovari and D. Bachrathy. *Chatter detection during milling utilising the stochastic cutting force induced resonance*. Preprint

- Conference Papers

  [84] H. T. Sykora, D. Bachrathy, and G. Stepan. *A theoretical investigation of the effect of the stochasticity in the material properties on the chatter detection during turning*. 29th Conference on Mechanical Vibration and Noise, 8, 2017.99

Bibliography

[1] M. Abramowitz and I. A. Stegun. *Handbook of Mathematical Functions with Formulas, Graphs, and Mathematical Tables*. Dover, New York, ninth dover printing, tenth gpo printing edition, 1964.

[2] Y. Altintas. *Manufacturing Automation: Metal Cutting Mechanics, Machine Tool Vibrations, and CNC Design*. Cambridge University Press, Cambridge, 2 edition, 2012.

[3] Y. Altintas and A. Ber. *Manufacturing Automation: Metal Cutting Mechanics, Machine Tool Vibrations, and CNC Design*, volume 54. 2001. ISBN 0521650291. ISSN 00036900. 384 pp.

[4] Y. Altintas and P. K. Chan. In-process detection and suppression of chatter in milling. *International Journal of Machine Tools and Manufacture*, 32(3):329–347, jun 1992.

[5] L. Arnold. *Stochastic Differential Equations: Theory and Applications*. R. Oldenbourg Verlag, Munich, 1973. ISBN 0-471-03359-6. ISSN 0036-1445.

[6] D. Bachrathy. Julia package: Mdbm.jl, v0.1.5, 2019. URL `https://github.com/bachrathyd/MDBM.jl`.

[7] D. Bachrathy and G. Stépán. Bisection method in higher dimensions and the efficiency number. *Periodica Polytechnica Mechanical Engineering*, 56(2):81, 2012. ISSN 0324-6051.

[8] C. T. Baker and E. Buckwar. Exponential stability in p-th mean of solutions, and of convergent euler-type solutions, of stochastic delay differential equations. *Journal of Computational and Applied Mathematics*, 184(2):404–427, dec 2005.

[9] R. Bellman. On the computational solution of differential-difference equations. *Journal of Mathematical Analysis and Applications*, 2(1):108 – 110, 1961. ISSN 0022-247X.

[10] S. Beregi, S. S. Avedisov, D. Takács, C. R. He, and G. Orosz. On the resiliance of connected automated vehicles. *IEEE Transaction on Intelligent Vehicles, submitted*, 2019.

[11] S. Berezvai, T. G. Molnar, A. Kossa, D. Bachrathy, and G. Stepan. Numerical and experimental investigation of contact length during orthogonal cutting. *Materials Today: Proceedings*, 12:329–334, 2019.

[12] J. Bezanson, A. Edelman, S. Karpinski, and V. B. Shah. Julia: A Fresh Approach to Numerical Computing. *SIAM Review*, 59(1):65–98, jan 2017. ISSN 0036-1445.

[13] E. Buckwar. Introduction to the numerical analysis of stochastic delay differential equations. *Journal of Computational and Applied Mathematics*, 125(1):297 – 307, 2000. ISSN 0377-0427. Numerical Analysis 2000. Vol. VI: Ordinary Differential Equations and Integral Equations.

[14] E. Buckwar, R. Kuske, B. L'Esperance, and T. SOO. Noise-sensitivity in machine tool vibrations. *International Journal of Bifurcation and Chaos*, 16(08):2407–2416, aug 2006. ISSN 0218-1274.

[15] E. Buckwar, R. Kuske, B. L'esperance, and T. Soo. Noise-sensitivity in machine tool vibrations. *International Journal of Bifurcation and Chaos*, 16(08):2407–2416, 2006.

[16] S. A. Campbell. *Time Delays in Neural Systems*, pages 65–90. Springer Berlin Heidelberg, Berlin, Heidelberg, 2007. ISBN 978-3-540-71512-2.

[17] W. Cao, Z. Zhang, and G. E. Karniadakis. Numerical Methods for Stochastic Delay Differential Equations Via the Wong–Zakai Approximation. *SIAM Journal on Scientific Computing*, 37(1):A295–A318, jan 2015. ISSN 1064-8275.

[18] W. Cao, Z. Zhang, and G. E. Karniadakis. Numerical methods for stochastic delay differential equations via the wong–zakai approximation. *SIAM Journal on Scientific Computing*, 37(1):A295–A318, jan 2015.

[19] M. B. G. Cloosterman, N. van de Wouw, W. P. M. H. Heemels, and H. Nijmeijer. Stability of networked control systems with uncertain time-varying delays. *IEEE Transactions on Automatic Control*, 54(7):1575–1580, July 2009.

[20] D. Coppersmith and S. Winograd. Matrix multiplication via arithmetic progressions. *Journal of Symbolic Computation*, 9(3):251–280, mar 1990.

[21] G. I. Depetri, F. A. C. Pereira, B. Marin, M. S. Baptista, and J. C. Sartorelli. Dynamics of a parametrically excited simple pendulum. *Chaos: An Interdisciplinary Journal of Nonlinear Science*, 28(3):033103, mar 2018.

[22] F. Desprez, J. J. Dongarra, and B. Tourancheau. Performance study of LU factorization with low communication overhead on multiprocessors. *Parallel Process. Lett.*, 5:157–169, 1995.

[23] Z. Dombovari, D. A. Barton, R. E. Wilson, and G. Stepan. On the global dynamics of chatter in the orthogonal cuttingmodel. *International Journal of Non-Linear Mechanics*, 46 (1):330 – 338, 2011. ISSN 0020-7462.

[24] O. Elbeyli, J. Q. Sun, and G. Ünal. A semi-discretization method for delayed stochastic systems. *Communications in Nonlinear Science and Numerical Simulation*, 10(1):85–94, 2005. ISSN 10075704.

[25] R. Faassen, E. Doppenberg, N. Wouw, van de, J. Oosterling, and H. Nijmeijer. Online detection of the onset and occurrence of machine tool chatter in the milling process. In *CIRP 2nd International Conference on High Performance Cutting*, pages paper–no. 23, 2006.

[26] G. Fodor, H. T. Sykora, and D. Bachrathy. Forgácsolóerő modellezése sztochasztikus folyamatokkal esztergálás során. *XIII. Magyar Mechanikai Konferencia (XIII. MaMeK) - Miskolc, Magyarország*, 2019.

[27] G. Fodor, H. T. Sykora, and D. Bachrathy. Stochastic modeling of the cutting force in turning processes. *The International Journal of Advanced Manufacturing Technology*, 111 (1-2):213–226, sep 2020.

[28] J. I. Ge, S. S. Avedisov, C. R. He, W. B. Qin, M. Sadeghpour, and G. Orosz. Experimental validation of connected automated vehicle design among human-driven vehicles. *Transportation Research Part C*, 91:335–352, 2018.

[29] J. I. Ge and G. Orosz. Data-driven parameter estimation for optimal connected cruise control. In *2017 IEEE 56th Annual Conference on Decision and Control (CDC)*. IEEE, dec 2017.

[30] M. M. Gomez, M. Sadeghpour, M. R. Bennett, G. Orosz, and R. M. Murray. Stability of systems with stochastic delays and applications to genetic regulatory networks. *SIAM Journal on Applied Dynamical Systems*, 15(4):1844–1873, jan 2016. ISSN 1536-0040.

[31] S. Guillouzic, I. L'Heureux, and A. Longtin. Small delay approximation of stochastic delay differential equations. *Physical Review E*, 59(4):3970–3982, apr 1999.

[32] C. Gupta, J. M. López, R. Azencott, M. R. Bennett, K. Josić, and W. Ott. Modeling delay in genetic networks: From delay birth-death processes to delay stochastic differential equations. *The Journal of Chemical Physics*, 140(20):204108, 2014.

[33] D. Hajdu, J. I. Ge, T. Insperger, and G. Orosz. Robust stability of connected cruise controllers. In *Stability, Control and Application of Time-delay Systems*, pages 163–184. Elsevier, 2019.

[34] D. J. Higham. An algorithmic introduction to numerical simulation of stochastic differential equations. *SIAM Review*, 43(3):525–546, jan 2001.

[35] Z. Hu and F. Deng. Robust h_∞ control for networked systems with transmission delays and successive packet dropouts under stochastic sampling. *International Journal of Robust and Nonlinear Control*, 27(1):84–107, 2017.

[36] T. Insperger, J. Munoa, M. a. Zatarain, and G. Peigné. Unstable islands in the stability chart of milling processes due to the helix angle. In *CIRP 2nd international conference on high performance cutting, Vancouver, Canada*, pages 12–13, 2006.

[37] T. Insperger and G. Stépán. Semi-discretization method for delayed systems. *International Journal for Numerical Methods in Engineering*, 55(5):503–518, 2002. ISBN 1097-0207. ISSN 00295981.

[38] T. Insperger and G. Stépán. Stability analysis of turning with periodic spindle speed modulation via semidiscretization. *Journal of Vibration and Control*, 10:1835–1855, 12 2004.

[39] T. Insperger and G. Stépán. *Semi-Discretization for Time-Delay Systems*, volume 178 of *Applied Mathematical Sciences*. Springer, New York, NY, 2011. ISBN 978-1-4614-0334-0.

[40] T. Insperger, G. Stepan, P. Bayly, and B. Mann. Multiple chatter frequencies in milling processes. *Journal of Sound and Vibration*, 262(2):333–345, apr 2003. ISBN 0022-460X. ISSN 0022460X.

[41] T. Insperger, G. Stépán, and J. Turi. On the higher-order semi-discretizations for periodic delayed systems. *Journal of Sound and Vibration*, 313(1):334 – 341, 2008. ISSN 0022-460X.

[42] ISO 1302:2002, Geometrical Product Specifications (GPS) — Indication of surface texture in technical product documentation. Standard, February, 2002.

[43] F. A. Khasawneh and E. Munch. Chatter detection in turning using persistent homology. *Mechanical Systems and Signal Processing*, 70-71:527–541, mar 2016. ISSN 08883270.

[44] F. A. Khasawneh and E. Munch. *Utilizing Topological Data Analysis for Studying Signals of Time-Delay Systems*, pages 93–106. Springer International Publishing, Cham, 2017. ISBN 978-3-319-53426-8.

[45] R. Khasminskii. *Stochastic Stability of Differential Equations*. Springer, Berlin Heidelberg, 2012. ISBN 978-3-642-23279-4. ISSN 0172-4568.

[46] A. K. Kiss, D. Hajdu, D. Bachrathy, and G. Stepan. Operational stability prediction in milling based on impact tests. *Mechanical Systems and Signal Processing*, 103:327–339, mar 2018.

[47] P. E. Kloeden, E. Platen, and H. Schurz. *Numerical Solution of SDE Through Computer Experiments*. Universitext. Springer Berlin Heidelberg, Berlin, Heidelberg, 1994. ISBN 978-3-540-57074-5.

[48] M. M. Klosek and R. Kuske. Multiscale Analysis of Stochastic Delay Differential Equations. *Multiscale Modeling & Simulation*, 3(3):706–729, jan 2005. ISSN 1540-3459.

[49] K. Konishi, H. Kokame, and N. Hara. Delayed feedback control based on the act-and-wait concept. *Nonlinear Dynamics*, 63(3):513–519, feb 2011. ISSN 1573-269X.

[50] R. Krtolica, Ü. Özgüner, H. Chan, H. Göktaş, J. Winkelman, and M. Liubakka. Stability of linear feedback systems with random communication delays. *International Journal of Control*, 59(4):925–953, 1994.

[51] E. Kuljanic, M. Sortino, and G. Totis. Multisensor approaches for chatter detection in milling. *Journal of Sound and Vibration*, 312(4-5):672–693, may 2008.

[52] R. Kuske. Multiple-scales approximation of a coherence resonance route to chatter. *Computing in Science & Engineering*, 8(3):35–43, may 2006. ISSN 1521-9615.

[53] R. Kuske. Competition of Noise Sources in Systems with Delay: The Role of Multiple Time Scales. *Journal of Vibration and Control*, 16(7-8):983–1003, jun 2010. ISBN 1077-5463. ISSN 1077-5463.

[54] D. S. Lemons and A. Gythiel. Paul langevin's 1908 paper "on the theory of brownian motion" ["sur la théorie du mouvement brownien," c. r. acad. sci. (paris) 146, 530–533 (1908)]. *American Journal of Physics*, 65(11):1079–1081, nov 1997.

[55] M. C. Mackey and I. G. Nechaeva. Solution moment stability in stochastic differential delay equations. *Physical Review E*, 52(4):3366–3376, oct 1995. ISSN 1063-651X.

[56] X. Mao. Exponential stability of equidistant euler–maruyama approximations of stochastic differential delay equations. *Journal of Computational and Applied Mathematics*, 200(1): 297–316, mar 2007.

[57] X. Mao. *Stochastic differential equations and applications*. Horwood Pub, Chichester, 2008. ISBN 9781904275343.

[58] H. Meerkamm. *Technical Pocket Guide*. Shaeffler Technologies AG & Co. KG, Herzogenaurach, Germany, 2018.

[59] J. Munoa, X. Beudaert, Z. Dombovari, Y. Altintas, E. Budak, C. Brecher, and G. Stepan. Chatter suppression techniques in metal cutting. *CIRP Annals*, 65(2):785 – 808, 2016. ISSN 0007-8506.

[60] J. Nilsson, B. Bernhardsson, and B. Wittenmark. Stochastic analysis and control of real-time systems with random time delays. *Automatica*, 34(1):57–64, 1998.

[61] B. Øksendal. *Stochastic Differential Equations*. Springer, Berlin, Heidelberg, 2003. ISBN 978-3-540-04758-2. ISSN 10577149.

[62] G. Orosz. Connected cruise control: modelling, delay effects, and nonlinear behaviour. *Vehicle System Dynamics*, 54(8):1147–1176, 2016.

[63] G. Orosz, B. Krauskopf, and R. E. Wilson. Traffic jam dynamics in a car-following model with reaction-time delay and stochasticity of drivers. *IFAC Proceedings Volumes*, 39(10): 199–204, 07 2006. ISBN 9783902661111.

[64] G. Orosz, R. E. Wilson, and G. Stépán. Traffic jams: dynamics and control. *Philosophical Transactions of the Royal Society of London A: Mathematical, Physical and Engineering Sciences*, 368(1928):4455–4479, 2010. ISSN 1364-503X.

[65] V. Y. Pan and Z. Q. Chen. The complexity of the matrix eigenproblem. In *Proceedings of the thirty-first annual ACM symposium on Theory of computing - STOC '99*. ACM Press, 1999.

[66] J. Prohaszka and J. Dobranszky. The role of an anisotropy of the elastic moduli in the determination of the elastic limit value. *Materials Science Forum - MATER SCI FORUM*, 414-415:311–316, 01 2003.

[67] J. Prohaszka, A. G. Mamalis, M. Horvath, J. Nyiro, and J. Dobranszky. Effect of microstructure on the mirror-like surface quality of fcc and bcc metals. *Materials and Manufacturing Processes*, 21(8):810–818, 2006.

[68] W. B. Qin, M. M. Gomez, and G. Orosz. Stability and frequency response under stochastic communication delays with applications to connected cruise control design. *IEEE Transactions on Intelligent Transportation Systems*, 18(2):388–403, Feb 2017. ISSN 1524-9050.

[69] W. B. Qin and G. Orosz. Scalable stability analysis on large connected vehicle systems subject to stochastic communication delays. *Transportation Research Part C: Emerging Technologies*, 83:39–60, oct 2017.

[70] D. Quevedo, E. Silva, and G. Goodwin. Control over unreliable networks affected by packet erasures and variable transmission delays. *Selected Areas in Communications, IEEE Journal on*, 26:672 – 685, 06 2008.

[71] C. Rackauckas and Q. Nie. Adaptive methods for stochastic differential equations via natural embeddings and rejection sampling with memory. *Discrete & Continuous Dynamical Systems - B*, 22(7):2731–2761, 2017.

[72] C. Rackauckas and Q. Nie. DifferentialEquations.jl – a performant and feature-rich ecosystem for solving differential equations in julia. *Journal of Open Research Software*, 5, may 2017.

[73] M. Sadeghpour and G. Orosz. On the stability of continuous-time systems with stochastic delay: applications to gene regulatory circuits. Volume 6: 10th International Conference on Multibody Systems, Nonlinear Dynamics, and Control(46391):V006T10A078, 2014.

[74] L. E. Shaikhet. *Lyapunov functionals and stability of stochastic functional differential equations*. Springer, Cham, Switzerland New York, 2013. ISBN 978-3-319-00100-5.

[75] L. Shampine and S. Thompson. Solving DDEs in matlab. *Applied Numerical Mathematics*, 37(4):441–458, jun 2001.

[76] T. Shardlow and P. Kloeden. The milstein scheme for stochastic delay differential equations without using anticipative calculus. *Stochastic Analysis and Applications*, 30(2):181–202, 2012. ISSN 0736-2994.

[77] R. Song and Q. Zhu. Stability of linear stochastic delay differential equations with infinite markovian switchings. *International Journal of Robust and Nonlinear Control*, 28(3):825–837, 2018.

[78] G. Stépán. *Retarded dynamical systems: stability and characteristic functions*, volume 210 of *Research Notes in Mathematics Series*. John Wiley & Sons, Inc., New York, NY, 1989. ISBN 0-582-03932-0. ISSN 0470213353 (Wiley). viii+151 pp.

[79] G. Stépán. Delay-differential equation models for machine tool chatter. *Nonlinear Dynamics of Material Processing and Manufacturing*, pages 165–192, 1998.

[80] H. T. Sykora. Julia Package: StochasticSemiDiscretizationMethod.jl, v0.3.3, 2019. URL `https://github.com/HTSykora/StochasticSemiDiscretizationMethod.jl`.

[81] H. T. Sykora and D. Bachrathy. A fehér zaj hatása lineáris, késleltetett, pd szabályozás stabilitási tulajdonságaira. *XXVI. Nemzetközi Gépészeti Konferencia (OGéT) Kiadványa*, pages 438 — 441, 2017.

[82] H. T. Sykora and D. Bachrathy. An effective method to investigate stochastic delayed systems in julia. *Juliacon 2018 Poster session, London, UK, 2018.08.07-11.*, 2018.

[83] H. T. Sykora and D. Bachrathy. Stochastic semidiscretization method: Second moment stability analysis of linear stochastic periodic dynamical systems with delays. *Applied Mathematical Modelling*, 88:933 – 950, 2020.

[84] H. T. Sykora, D. Bachrathy, and G. Stepan. A theoretical investigation of the effect of the stochasticity in the material properties on the chatter detection during turning. *29th Conference on Mechanical Vibration and Noise*, pages 1 – 5, 2017.

[85] H. T. Sykora, D. Bachrathy, and G. Stepan. Gaussian noise process as cutting force model for turning. *Procedia CIRP*, 77:94–97, 2018.

[86] H. T. Sykora, D. Bachrathy, and G. Stépán. Lineáris sztochasztikus késleltetett rendszerek szemi-diszkretizációja. *XIII. Magyar Mechanikai Konferencia (XIII. MaMeK) - Miskolc, Magyarország*, 2019.

[87] H. T. Sykora, D. Bachrathy, and G. Stepan. Stochastic semi-discretization for linear stochastic delay differential equations. *International Journal for Numerical Methods in Engineering*, 119(9):879–898, apr 2019.

[88] H. T. Sykora, D. Bachrathy, and G. Stépán. Stochastic semi-discretization for stochastic systems with delay. *SIAM Conference on Applications of Dynamical Systems (DS19) - Minisymposium: When Stochasticity Meets Delay: Rendezvous in Infinite Dimension, Snowbird, USA*, 2019.

[89] H. T. Sykora, G. Fodor, D. Hajdu, and D. Bachrathy. Solving periodic stochastic problems with delays with the help of julia. *Juliacon 2019 Poster session, Baltimore, US, 2019.07.22-26.*, 2019.

[90] H. T. Sykora, D. Hajdu, D. Bachrathy, and Z. Dombóvári. Chatter formation during milling due to stochastic noise induced resonance. *Preprint*.

[91] H. T. Sykora, V. Rackauckas, Christopher, D. Widmann, and D. Bachrathy. Stochasticdelaydiffeq.jl - an integrator interface for stochastic delay differential equations in julia. *Submitted to ENOC 2020*, 2020.

[92] H. T. Sykora, M. Sadeghpour, J. I. Ge, D. Bachrathy, and G. Orosz. On the moment dynamics of stochastically delayed linear control systems. *International Journal of Robust and Nonlinear Control*, 30(18):8074–8097, 2020.

[93] H. T. Sykora, W. V. Wedig, D. Bachrathy, and G. Stepan. Approximation of Top Lyapunov Exponent of Stochastic Delayed Turning Model Using Fokker-Planck Approach. *Proceedings of the 9th European Nonlinear Dynamics Conference*, 2017.

[94] J. Tlusty and L. Spacek. *Self-excited vibrations on machine tools*. Nakl. CSAV, Prague, Czech Republic, 1954.

[95] S. Tobias. *Machine-tool Vibration*. Blackie, 1965.

[96] L. N. Trefethen. *Spectral Methods in MATLAB*. SIAM, Philadelphia, 2000. ISBN 978-0-89871-465-4.

[97] V. V. Sur la théorie mathématique des phénomènes héréditaires. *J Math Pure Appl*, 7: 149–192, 1928.

[98] W. V. Wedig. Vertical Dynamics of Riding Cars under Stochastic and Harmonic Base Excitations. In *IUTAM Symposium on Chaotic Dynamics and Control of Systems and Processes in Mechanics*, volume 122, pages 371–381. Springer-Verlag, Berlin/Heidelberg.

[99] T. YaZ. The systems with delayed feedback. *Avtomatika i Telemekhanika*, 7:107–129, 1928.

[100] S. Yi, S. Duan, P. Nelson, and A. Ulsoy. The Lambert W function approach to time delay systems and the LambertW_DDE toolbox. *IFAC Proceedings Volumes*, 45(14):114–119, jun 2012.